



Differential electrochemical mass spectrometry (DEMS) studies of nitrite reduction catalyzed by polyoxometallates, silver electrode, and ionic liquid-based hybrid materials

Yulin Zhou

► To cite this version:

Yulin Zhou. Differential electrochemical mass spectrometry (DEMS) studies of nitrite reduction catalyzed by polyoxometallates, silver electrode, and ionic liquid-based hybrid materials. Theoretical and/or physical chemistry. Université de Strasbourg, 2022. English. NNT : 2022STRAF021 . tel-04368447

HAL Id: tel-04368447

<https://theses.hal.science/tel-04368447>

Submitted on 1 Jan 2024

HAL is a multi-disciplinary open access archive for the deposit and dissemination of scientific research documents, whether they are published or not. The documents may come from teaching and research institutions in France or abroad, or from public or private research centers.

L'archive ouverte pluridisciplinaire **HAL**, est destinée au dépôt et à la diffusion de documents scientifiques de niveau recherche, publiés ou non, émanant des établissements d'enseignement et de recherche français ou étrangers, des laboratoires publics ou privés.

ÉCOLE DOCTORALE DES SCIENCES CHIMIQUES

Institut de Chimie, UMR 7177

THÈSE présentée par:

Yulin ZHOU

soutenue le : **10 Novembre 2022**

pour obtenir le grade de : **Docteur de l'Université de Strasbourg**

Discipline / Spécialité : Chimie

**Études par spectrométrie de masse électrochimique
différentielle (DEMS) de la réduction des nitrites catalysée par
les polyoxométallates, une électrode d'argent et des matériaux
hybrides à base de liquide ionique**

THÈSE dirigée par :

M. RUHLMANN Laurent

Professeur, Université de Strasbourg

Co-directeur du thèse :

M. BONNEFONT Pierre-Antoine

Maitre de conférences, Université de Strasbourg

Rapporteurs :

Mme DEBIEMME-CHOUVY Catherine

Directrice de recherche, Sorbonne Université

M. COSTENTIN Cyrille

Professeur, Université Grenoble Alpes

Autres membres du jury :

M. MELIN Frédéric

Maitre de conférences, Université de Strasbourg

M. MIALANE Pierre

Professeur, Université de Versailles Saint-Quentin-en-Yveline

Membre invité :

Mme BADETS Vasilica

Maitre de conférences, Université de Strasbourg

Remerciements

Je tiens tout d'abord à remercier tous les membres du jury d'avoir accepté d'évaluer cette thèse :

- Prof. Laurent RUHLMANN, Université de Strasbourg
- Dr. Pierre-Antoine BONNEFONT, Université de Strasbourg
- Prof. Catherine DEBIEMME-CHOUVY, Sorbonne Université
- Prof. M. Cyrille COSTENTIN, Université Grenoble Alpes
- Dr. Frédéric MELIN, Université de Strasbourg
- Prof. Pierre MIALANE, Université Versailles - Saint-Quentin

Je tiens à remercier le Chinese Scholarship Council qui a fourni le soutien financier pour étudier et vivre en France.

Je tiens à exprimer ma gratitude au Dr Vasilica Badets pour son aimable soutien au cours de l'étude de cette recherche. Au cours de mes études, elle me donne de la patience et de l'expérience pour m'aider à résoudre beaucoup de problèmes. Et elle m'a vraiment beaucoup aidé à rédiger la thèse pendant ma période difficile. Merci.

Je tiens à exprimer ma gratitude au Pr Laurent Ruhlmann. Il a une attitude rigoureuse et un dévouement professionnel à la recherche scientifique.

Je tiens à exprimer ma gratitude au Dr Antoine Bonnefont pour son aide dans la partie calcul cinétique et ses conseils et commentaires professionnels et rigoureux sur mon travail. Son aide a été très importante pour améliorer la discussion des résultats.

Je tiens à remercier Dr Anzel Falch et d'autres personnes pour leur aide lors de mon échange d'un mois en Afrique du Sud.

Je tiens à remercier mes collègues du groupe de recherche qui ont partagé le même laboratoire avec moi surtout au début de ma thèse.

Je tiens à remercier mes amis de m'avoir accompagné ces trois dernières années.

Résumé

1) Introduction

La réduction électrochimique du nitrite ou de l'acide nitreux est catalysée, entre autres, par les polyoxométallates (POMs), une classe d'agrégats d'oxydes métalliques inorganiques solubles notamment en milieu aqueux. Différents POMs ont été testés, allant de petits polyanions de types Keggin et Wells-Dawson [1] à des structures plus complexes (telles que des tétramères dérivés de POM du type Wells-Dawson, des structures de type couronne [2] et même des composés hybrides organiques - inorganiques [3]). Dans la plupart des cas, les études sont réalisées en milieu aqueux en fonction du pH et les performances électrocatalytiques sont présentées comme la variation du courant catalytique avec la concentration en nitrite ou en acide nitreux présent dans le milieu. La catalyse est réalisée souvent en phase homogène [4-10] mais de nombreux exemples en phase hétérogène existent aussi [11-25].

Un problème important dans la réduction électrochimique du nitrite est d'identifier les produits de réaction. Le nitrite est le premier produit obtenu à partir de la réduction du nitrate et les deux composés sont connus comme des polluants environnementaux du fait de leurs utilisations comme conservateurs alimentaires. Ainsi, des recherches sont menées pour transformer ces deux espèces en composés inoffensifs ou en produits d'intérêt industriel. Parmi la diversité des produits possibles (ammoniac, hydroxylamine, monoxyde d'azote, protoxyde d'azote, etc.) et l'azote (N_2) qui apparaît comme l'option la plus respectueuse de l'environnement, tandis que NH_3 est un produit industriel valorisable et N_2O peut être utilisé pour des applications médicales. De ce point de vue, disposer d'une technique analytique capable d'identifier rapidement en un seul test un maximum de produits devient un outil de caractérisation important.

La spectrométrie de masse électrochimique différentielle (DEMS) est une technique analytique capable d'identifier la formation *in situ* de produits gazeux au cours d'un seul balayage de potentiel. Une corrélation directe entre le potentiel électrochimique appliqué et la formation de produits peut être obtenue. Cette technique a été utilisée pour étudier les réductions des nitrites et des nitrates catalysées par les métaux nobles à la fois dans des conditions acides et alcalines [26, 27]. Alors que seules les espèces gazeuses, telles que NO, NO_2 , N_2O et N_2 sont mesurées avec le DEMS, certaines techniques complémentaires doivent être utilisées afin de bien comprendre le mécanisme de la réaction. Ainsi, une électrode à disque rotatif et une électrolyse en masse ont été utilisées pour confirmer la présence d'hydroxylamine et d'ammonium, et les spectroscopies FTIR et ATR-SEIRAS (spectroscopie d'absorption infrarouge à réflexion totale atténuée) peuvent être utilisées pour mesurer les intermédiaires adsorbés liés au NO. Sur les métaux nobles et les conditions acides, l'une des observations les plus importantes est que le NO issu de la décomposition de HNO_2 est réduit aux hauts potentiels. Le produit est N_2O sur la base de la réaction entre le NO en phase solution et le NO adsorbé. Par la suite, à des potentiels inférieurs, HNO_2 est directement réduit en produits hydrogénés (NH_2OH , NH_3). Ceci est observé pour des électrodes de Ru, Rh [28], Pd, Pt [29] mais pas pour l'Ir, où seule la réduction de NO en N_2O est enregistrée. Pour les métaux Cu, Ag et Au, la principale différence est que HNO_2 est réduit en NO puis ensuite réduit en N_2O . L'explication principale est que l'adsorption de NO sur ces métaux est faible

et, de cette manière, NO peut être détecté en solution [26]. Jusqu'à présent, il n'existe qu'un seul exemple d'utilisation du DEMS pour la caractérisation de la réduction des nitrites catalysée par le polyoxométallate à base de molybdène $[\text{SiMo}_{12}\text{O}_{40}]^{4-}$ [30].

Dans cette optique, le travail effectué dans cette thèse est axé sur l'étude de l'électroréduction des nitrites à l'aide de différent type de POM en utilisant la technique DEMS. Dans une première partie, l'étude présente la dépendance des produits gazeux par rapport aux propriétés électrochimiques des POMs sélectionnés. La modélisation microcinétique a été utilisée pour établir une hiérarchie des efficacités électrocatalytiques d'une série de POM du type Keggin où la charge du POM a été modulée. Dans une deuxième partie, la catalyse en tandem entre les POMs et une électrode de travail en argent a été étudiée. Cette partie fait le lien entre la catalyse homogène (utilisant uniquement des POM en solution), décrite dans la première partie, et la catalyse hétérogène (utilisant uniquement des électrodes métalliques), décrite dans la littérature. La dernière partie décrit la catalyse hétérogène réalisée par une série de POM hybride obtenus en remplaçant les contre-cations par un cation issu du liquide ionique. Cette étude est originale car elle complète les très rares études existantes dans la littérature.

2) Résultats et Discussions

2.1) Études DEMS de l'électroréduction des nitrites catalysée par une série de POM de type Keggin

Nous avons étudié l'influence de la charge et des potentiels redox d'une série de polyoxométallates (POM) appartenant à la famille Keggin sur la réduction électrochimique du nitrite ou de l'acide nitreux (NO_2^- ou HNO_2). Nous nous sommes concentrés sur la dépendance de la formation de produits gazeux au regard des propriétés redox des POMs. Malgré plusieurs études sur la réduction des nitrites catalysée par les POM, un nombre limité d'étude analyse les produits de réaction. Par exemple, Nadjo et al. ont montré que le NO est converti en N_2O par une série de POM réduits [31]. Ces études ont été réalisées sous forme d'électrolyse dans laquelle les POMs ont été réduits avant l'ajout de nitrite. Néanmoins, le mécanisme de réaction et la relation entre la structure des POM et l'activité de réaction ne sont toujours pas clairs. Ainsi, la spectroscopie de masse électrochimique différentielle (DEMS) a été utilisée pour suivre la formation de produits gazeux en fonction du potentiel appliqué. Les signaux mesurés sont ceux des produits gazeux majeurs, soit m/z 31 (^{15}NO), m/z 46 ($^{15}\text{N}_2\text{O}$) et m/z 30 ($^{15}\text{N}_2$). Ces signaux ne sont pas quantitatifs. Ainsi, un autre paramètre est requis afin de comparer différents ensembles de données. Pour cette raison, le potentiel d'apparition correspondant au potentiel auquel le produit commence à se former a été choisi. La définition de ce potentiel d'apparition est spécifique aux données DEMS, elle est donc différente de la définition utilisée pour les expériences en voltammétrie cyclique. Le potentiel d'apparition a été choisi comme le potentiel correspondant au signal égal à une valeur deux fois supérieure au bruit du signal DEMS.

Les résultats montrent que les produits gazeux (NO et N_2O) se forment à pH 2 et 5 par la réaction de HNO_2 ou NO_2^- avec le POM réduit. Seul le NO est détecté lorsque le POM ($[\text{PW}_{12}\text{O}_{40}]^{3-}$, $[\text{SiW}_{12}\text{O}_{40}]^{4-}$, $[\text{BW}_{12}\text{O}_{40}]^{5-}$) subit la première réduction (réduction mono-électronique, Figure 1a). Cependant, N_2O est obtenu avec NO dès que le POM subit une réduction biélectronique. Le potentiel de la première vague de réduction du POM est corrélé à sa charge, la réduction étant plus facile si le POM est moins chargé. Par conséquent la

production de NO et/ou de N₂O apparaît à un potentiel inférieur pour [PW₁₂O₄₀]³⁻ et [SiW₁₂O₄₀]⁴⁻ par rapport à [BW₁₂O₄₀]⁵⁻ et [H₂W₁₂O₄₀]⁶⁻ (Figure 1b).

Pour mieux comprendre l'influence du pH sur le mécanisme de réaction, une analyse DEMS a été réalisée entre pH 1 et pH 5 en utilisant [SiW₁₂O₄₀]⁴⁻ comme catalyseur. Le potentiel d'apparition de NO et de N₂O est présenté dans le Tableau 1. La première réduction du POM (E⁰) se déplace légèrement vers des potentiels plus positifs avec l'augmentation du pH. Le potentiel d'apparition du NO suit cette tendance, passant progressivement de 0,193 V *vs* RHE à pH 1 à 0,340 à pH 5. Le potentiel d'apparition du N₂O reste quasiment inchangé entre pH 1 et pH 3, soit -0,160 V *vs* RHE. Ensuite, il diminue soudainement à -0,27 V *vs* RHE pour pH 4 et à -0,350 à pH 5. Compte tenu de ces données et du pK_a du couple HNO₂/NO₂⁻ égal à 3,3, on peut conclure que la réaction entre le POM mono-réduit (i.e. [SiW^VW^{VI}₁₁O₄₀]⁵⁻) et HNO₂ (entre pH 1 et pH 3) est plus rapide que celle entre le POM mono-réduit et NO₂⁻ (entre pH 4 et pH 5). En effet, le produit de la réaction est du NO. Très probablement, une concentration minimale est nécessaire avant que la formation ultérieure de N₂O puisse être observée. Si l'étude est menée à pH 4 ou à pH 5, la réaction est lente, la concentration de NO est faible et donc le N₂O n'est observé qu'à une surtension plus élevée (c'est-à-dire uniquement lorsque le [SiW₂^VW^{VI}₁₂O₄₀]⁶⁻ est déjà formé). De plus, la réaction de réduction implique des protons, ainsi une modification du pH peut affecter la cinétique de la réaction.

Tableau 1. Potentiel d'apparition du NO et N₂O quand [SiW₁₂O₄₀]⁴⁻ est utilisé comme catalyseur.

pH	E ⁰ pour [SiW ₁₂ O ₄₀] ⁴⁻ / [SiW ₁₂ O ₄₀] ⁵⁻ (V <i>vs.</i> RHE)	NO		N ₂ O	
		Potentiel d'apparition (V <i>vs.</i> RHE)	Vague POM (nombre d'électrons)	Potentiel d'apparition (V <i>vs.</i> RHE)	Vague POM (nombre d'électrons)
1	0,099	0,193	I ^{ère} (1e ⁻)	-0.169	II ^{ème} (1e ⁻)
2	0,116	0,198	I ^{ère} (1e ⁻)	-0.155	II ^{ème} (1e ⁻)
3	0,175	0,256	I ^{ère} (1e ⁻)	-0.165	II ^{ème} (1e ⁻)
4	0,213	0,246	I ^{ère} (1e ⁻)	-0.270	III ^{ème} (2e ⁻)
5	0,251	0,340	I ^{ère} (1e ⁻)	-0.350	III ^{ème} (2e ⁻)

Les résultats des études DEMS indiquent une plage de potentiel où la réaction catalytique ne produit que du monoxyde d'azote (NO). Cela a permis le développement d'un modèle microcinétique qui simule avec succès les courbes expérimentales courant-potentiel. A partir de ce modèle, la valeur de la constante de vitesse k_c de la réaction entre le POM réduit (éq. 1) et HNO₂ ou NO₂⁻ en solution (éq. 2 et éq. 3) et la valeur du TOF ont pu être calculées (Figure 1c). Aux faibles surtensions, les valeurs de TOF sont décroissantes suivant le potentiel redox de première réduction du POM : [PW₁₂O₄₀]³⁻ > [SiW₁₂O₄₀]⁴⁻ > [BW₁₂O₄₀]⁵⁻ alors qu'avec une forte surtension les TOF sont dominés par k_c suivant un ordre inversé. A pH 5, les valeurs de k_c sont environ 70 fois plus faibles qu'à pH 2, ce qui est attribué à la diminution de la concentration en protons au sein de la solution et à la répulsion électrostatique entre le POMⁿ⁻ et le NO₂⁻ chargés négativement.

Enfin, le mécanisme de formation de N₂O mis en évidence par l'expérience DEMS peut être provisoirement discuté (Figure 1c). Les résultats expérimentaux du DEMS démontrent (i) que N₂O est produit lors de la deuxième vague de réduction du POM et l'injection de 2 électrons et (ii) que la formation de N₂O est concomitante à la consommation

de NO. Ainsi, l'étape de réaction importante à considérer est la seconde réduction du POM⁻ en POM²⁻ (éq. 4). En supposant que le POM²⁻ biréduit réagit de manière externe avec NO, l'étape suivante de réaction pourrait impliquer la réduction de NO en HNO catalysée par POM²⁻ (éq. 5). Il convient de mentionner que la valeur du potentiel standard de NO/HNO est encore débattue. Récemment, il a été montré que NO peut être converti en HNO par H₂S, des alcools aromatiques ou des thiols, ce qui serait en accord avec le potentiel redox $E_{\text{HNO/NO}}^0 = -0,11 \text{ V}$ [32]. Comme les potentiels redox du couple POM⁻/POM²⁻ sont inférieurs à -0,1 V pour [SiW₁₂O₄₀]⁴⁻, [BW₁₂O₄₀]⁵⁻ et [PW₁₂O₄₀]³⁻, un transfert d'électrons de sphère externe entre POM²⁻ et NO est thermodynamiquement possible. Enfin, la production de N₂O à partir de HNO pourrait se produire par une réaction complexe qui peut être écrite de manière simplifiée comme le montre l'équation 6 (cf. Figure 1). L'ensemble du processus catalytique est schématisé sur la Figure 1d.

Afin de vérifier si ce mécanisme est toujours vrai pour d'autres POMs, nous avons étendu les études DEMS aux POMs de type Keggin à base de molybdène (Mo) car le potentiel de réduction standard formel de ces composés est plus positif par rapport aux POM à base de tungstène (W) analogues. Aussi, nous avons étendu les mesures DEMS aux POMs du type Dawson car ces composés présentent plusieurs vagues de réduction biélectronique dans des conditions acides. Il a été observé que pour tous ces POMs le potentiel de début de formation de N₂O est de -0,2 V vs RHE ce qui correspond au mécanisme proposé via un intermédiaire HNO.

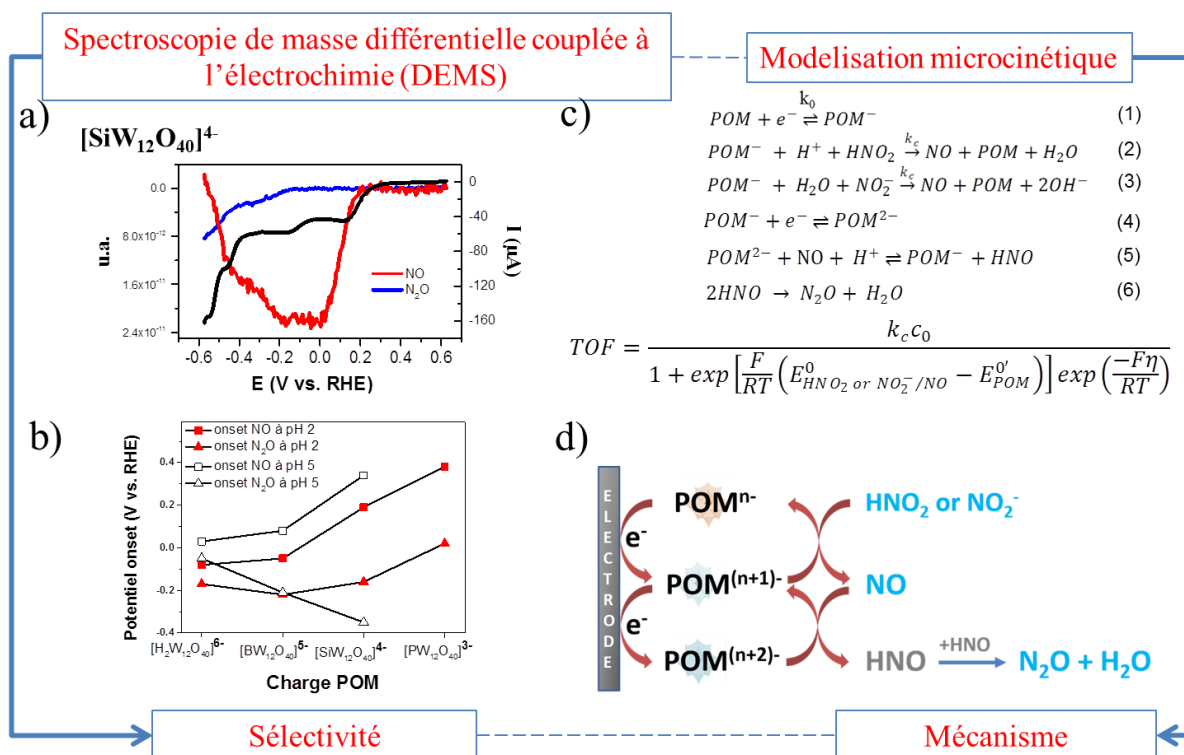


Figure 1. a) Analyse DEMS de la réduction des nitrites catalysée par K₄[SiW₁₂O₄₀] en solution ; b) Potentiel d'apparition de N₂O obtenu à partir d'une analyse DEMS à différentes électrodes ; c) Équations des réactions chimiques entre les POM et le nitrite et équation utilisée pour calculer la valeur du TOF ; d) Schéma du mécanisme proposé pour la réduction des nitrites catalysée par les POMs en solution.

L'oxyde nitrique (NO) est l'un des principaux oxydes d'azote et il est très facile à oxyder par le dioxygène pour former du NO₂. NO et NO₂ peuvent aussi facilement réagir pour former HNO₂ en solution. NO peut également être formé à partir de la dismutation de HNO₂. L'équilibre entre HNO₂ et NO₂⁻ est défini par le pK_a qui est égal à 3,3. Ainsi, la composition exacte d'un système NO/HNO₂/NO₂⁻/NO₂ est très dépendante de la présence du dioxygène dissous, du pH et de la concentration totale de nitrite. De plus, le NO est un produit intermédiaire de la réduction des nitrites catalysée par les POM. La réduction du NO catalysée par certains POM a été rapportée [7, 33]. Dans un rapport intéressant, lorsque [SiMo₁₂O₄₀]⁴⁻ a été utilisé comme catalyseur immobilisé [24] les auteurs ont observé le même comportement catalytique pour la réduction du NO par rapport à la réduction des nitrites. Dans ce cas, l'électrolyte était du Na₂SO₄ 0,2 M à pH 2 et la concentration totale de nitrite était de 10 mM. Ces conditions sont très similaires à nos expériences. Les auteurs n'avaient aucune explication pour les résultats trouvés et ils n'excluent pas la possibilité que l'espèce redox réelle soit NO⁺.

Dans cette optique, nous avons cherché à utiliser le DEMS pour étudier la réduction de NO catalysée par certains POM Keggin à base de W. Dans le montage expérimental, l'argon est barboté dans l'électrolyte pour éliminer les traces d'oxygène. De plus, un récipient contenant du NaOH a été utilisé comme piège à NO₂ qui pourrait éventuellement se former malgré les efforts pour éliminer l'oxygène par barbotage avec l'argon. Comme mentionné précédemment, il est difficile de connaître la concentration exacte de NO dissous. Ainsi, en augmentant le temps de barbotage, une quantité croissante de NO dissous a été obtenue, bien que la concentration réelle ne soit pas connue. Avant de réaliser des expériences DEMS, nous avons tracé la voltamétrie cyclique en présence de [SiW₁₂O₄₀]⁴⁻. Comme rapporté par Keita et al., nous observons le même comportement catalytique pour la réduction du NO que pour la réduction des nitrites. En détail, l'intensité du courant de la première vague de réduction de [SiW₁₂O₄₀]⁴⁻ augmente avec le temps de bullage de NO. Cette vague ne porte qu'un seul électron de réduction, ainsi la réduction de NO devrait générer une espèce contenant un atome d'azote avec un état d'oxydation +1. L'intensité du courant des autres vagues augmente également avec le temps de bullage du NO, suggérant une réduction supplémentaire de cette espèce. Des mesures DEMS ont été effectuées pour trouver les produits gazeux. Il convient de mentionner que l'isotope ¹⁴N a été utilisé dans ces études car il s'agit du seul gaz ¹⁴NO disponible. La conséquence en est que le signal de m/z = 44 est surveillé, mais cela correspond également au N₂O et au CO₂. Dans cette situation, la sensibilité de détection du N₂O est plus faible en raison d'un signal de base plus élevé. À des fins de comparaison, différents POM de Keggin à base de W ont été utilisés dans cette étude, à savoir [H₂W₁₂O₄₀]⁶⁻, [BW₁₂O₄₀]⁵⁻ et [SiW₁₂O₄₀]⁴⁻. Afin d'avoir une concentration constante en NO, un temps de bullage de 20 minutes a été fixé. L'intensité de courant enregistrée dans ce cas est similaire à celle obtenue lorsque 1 mM de nitrite est réduit.

Le résultat le plus frappant est l'apparition d'un signal m/z 30 positif directement lors de la première vague de réduction de tous les POMs. Cela signifie la formation d'oxyde nitrique (NO). La seule explication plausible est l'existence de quelques traces de dioxygène dans la cellule DEMS, conduisant à la formation de NO₂ dissous et donc à la formation de HNO₂. Ensuite, cet acide nitreux est réduit par les POM lors de la première vague pour former du monoxyde d'azote (NO). Cette hypothèse peut être vérifiée en surveillant le signal DEMS de NO₂, m/z = 46. Une corrélation claire entre la formation de NO et la consommation de NO₂ est observée. Cela suggère que NO₂ est consommé dans la réaction avec NO pour former HNO₂, comme décrit ci-dessus. Tous ces résultats sont tout à fait préliminaires et des mesures

impliquant un nombre plus grand de POMs et des paramètres expérimentaux plus variés doivent être effectuées avant qu'une conclusion sur le mécanisme de réaction puisse être tirée. Néanmoins, les résultats sont suffisamment intrigants pour nous encourager à mener d'autres expériences à l'avenir.

2.2) Études DEMS de l'électroréduction des nitrites catalysée par des POMs et/ou une électrode de travail en argent

Comme vu dans la première partie de cette thèse, les produits gazeux issus de l'électroréduction des nitrites catalysés par les POMs sont le monoxyde d'azote (NO) et le protoxyde d'azote (N₂O). Cela est similaire aux résultats décrits dans la littérature lorsque des électrodes d'or et d'argent sont utilisées comme catalyseurs hétérogènes. Sachant que la structure des POMs peut être facilement ajustée pour incorporer une variété de métaux nobles et de transition sous forme d'hétéroatomes, on pourrait étudier l'activité électrocatalytique de telles molécules.

Dans cette optique, nous avons tout d'abord étudié la synergie de la combinaison entre les POMs classiques de type Keggin présents en solution (électrocatalyse homogène) et l'électrode d'argent (électrocatalyse hétérogène). La spectrométrie de masse électrochimique différentielle (DEMS) a été utilisée pour mesurer les produits gazeux (NO, N₂O et N₂) à pH 1. Les études catalytiques ont été effectuées par l'emploi d'une électrode d'argent seule (Figure 2a). Les résultats ont été comparés à l'électrocatalyse homogène menées avec un polyoxométallates de type Keggin seuls en solution en présence de HNO₂ ou NO₂⁻ (en utilisant une électrode de carbone vitreux) et avec à la fois le même type de POM en solution et une électrode d'argent (Figure 2b). Alors que la réduction de HNO₂ en NO est similaire pour les trois systèmes catalytiques, la réduction suivante de NO en N₂O apparaît à une surtension inférieure lorsque l'électrode d'argent est utilisée avec les POMs en solution. Quatre POMs du type Keggin ont été testés, différant par leur comportement redox électrochimique : (NH₄)₆[H₂W₁₂O₄₀], K₅[BW₁₂O₄₀], K₄[SiW₁₂O₄₀] et Na₃[PW₁₂O₄₀]. Nous avons observé que la réduction du NO en N₂O est effectuée en tandem par l'argent et les POMs tant que la première réduction du POM apparaît dans une plage de potentiel où l'argent seul ne catalyse pas la réaction (c'est-à-dire quand le potentiel de réduction des POMs est suffisamment positif). Ceci n'est valable que pour deux POMs : K₄[SiW₁₂O₄₀] et Na₃[PW₁₂O₄₀]. Les potentiels de début de formation de N₂O sont présentés dans la Figure 2b. Ce potentiel est maintenant thermodynamiquement défavorable à l'existence de l'intermédiaire HNO (comme décrit dans la partie 1, Figure 1d). Ainsi, un autre mécanisme doit être considéré pour expliquer la formation de N₂O. Nous suggérons ici la contribution de l'argent pour adsorber le NO et favoriser la formation de N₂O via un dimère de NO. Ce mécanisme se produit déjà sur l'argent seul mais à des potentiels plus négatifs (-0,25 V / RHE) lorsque la seule source de NO aqueux est la dismutation de HNO₂. La concentration de NO ainsi obtenue est estimée grossièrement à 1 mM après 30 minutes de dismutation pour une solution de 20 mM de HNO₂. En présence de POM, la concentration de NO aqueux est augmentée en raison de la réduction catalytique de HNO₂. Ainsi, le potentiel de réduction de NO en N₂O est déplacé vers des potentiels plus positifs. La Figure 2d décrit ce mécanisme basé sur une synergie entre les POM et l'électrode d'argent.

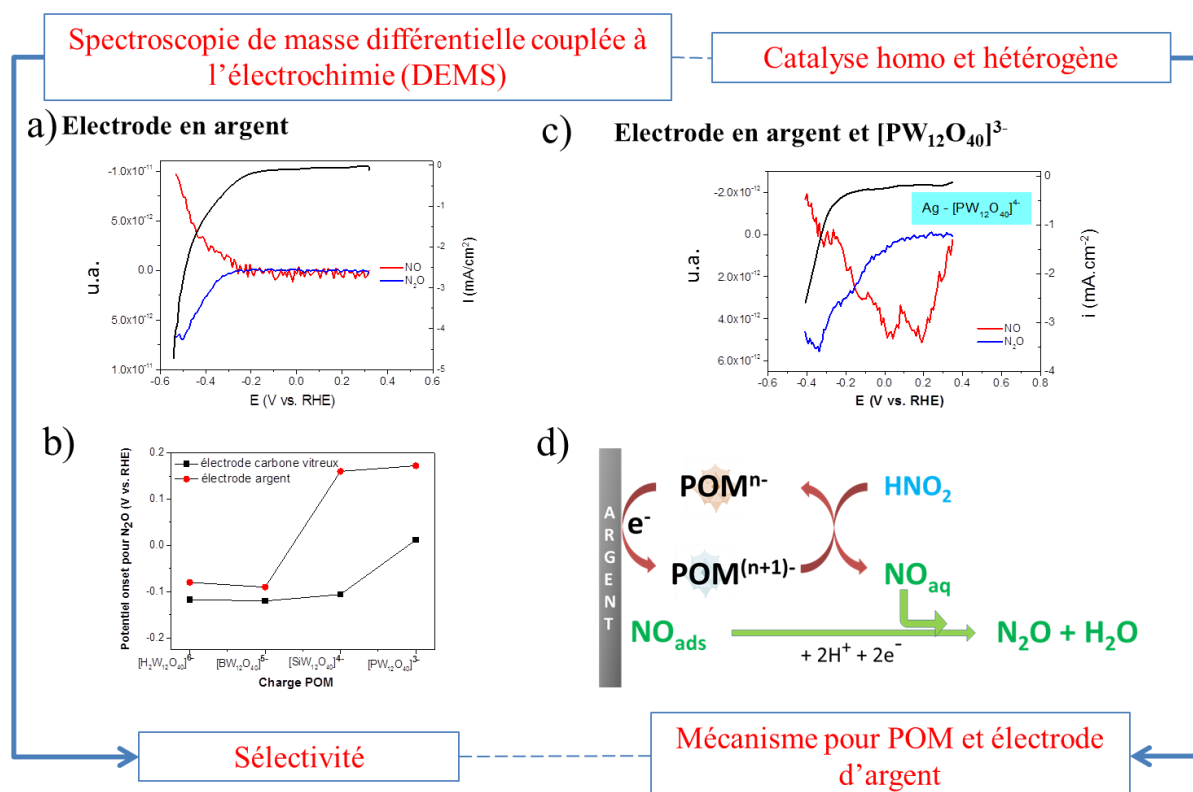


Figure 2. Analyse DEMS de la réduction des nitrites catalysée par une électrode d'argent ; b) Potentiel d'apparition de N_2O obtenu à partir d'une analyse DEMS avec différentes électrodes de travail ; c) Analyse DEMS de la réduction des nitrites catalysée par une électrode d'argent et le POM $\text{Na}_3[\text{PW}_{12}\text{O}_{40}]$ en solution ; d) Schéma du mécanisme proposé pour la réaction tandem de réduction des nitrites catalysé à la fois par les POMs en solution et l'électrode d'argent.

L'interaction particulière entre les POMs et l'argent a été décrite dans la littérature. La capacité des POMs à agir à la fois comme agent réducteur et stabilisant dans la production de nanoparticules d'argent est bien documentée [34]. Les nanoparticules $\text{Ag}@\text{POMs}$ obtenues sont stables pendant plusieurs mois et la microscopie électronique à transmission cryogénique (Cryo-MET) à haute résolution a montré la présence de molécules de POM entourant les nanoparticules métalliques [35]. Ainsi, nous avons synthétisé des nanoparticules $\text{Ag}@\text{POMs}$ en utilisant $(\text{NH}_4)_6[\text{H}_2\text{W}_{12}\text{O}_{40}]$, et $\text{K}_4[\text{SiW}_{12}\text{O}_{40}]$. Nous avons utilisé ces nanoparticules, dispersées en solution, comme catalyseurs pour la réduction des nitrites. Cependant, nous avons observé que ces particules précipitaient rapidement lors des mesures DEMS. Nous avons donc dans un second temps, utilisé la pectine comme stabilisant, mais les données DEMS n'ont montré aucune formation d'oxyde nitrique (NO) et la formation de N_2O a été détecté à un potentiel beaucoup plus faible ($-0,4 \text{ V} / \text{RHE}$). Afin d'améliorer cette étude, ces nanoparticules d' $\text{Ag}@\text{POMs}$ doivent être immobilisées sur la surface de l'électrode. Cela devrait offrir une bien meilleure stabilité et éliminera le besoin d'un deuxième stabilisateur qui bloque la surface active.

2.3) Études DEMS de l'électroréduction des nitrites catalysée par des hybrides liquides ioniques-POM

Dans cette dernière partie, nous avons étudié la catalyse hétérogène de réduction des

nitrites effectuée par des POM immobilisés. Différentes techniques d'immobilisation sont décrites dans la littérature pour une grande variété de POM. Nous avons choisi d'immobiliser nos POMs en utilisant la réaction avec un liquide ionique, le bromure de 1-butyl-3-vinylimidazolium (BrBVIM). La réaction donne un sel insoluble qui est mélangé avec de la poudre de carbone et du Nafion afin de préparer une encre (Figure 3d). Cette encre est déposée sur des électrodes de carbone vitreux et l'activité de ces encres pour la réduction des nitrites est ensuite mesurée. La réaction entre les POMs et un liquide ionique a été proposée dans le cadre de plusieurs travaux [9], mais seul le POM de type Keggin à base de molybdène ($H_3[PMo_{12}O_{40}]$) a été utilisé dans le développement de capteurs pour la réduction des nitrites [12].

Nous avons caractérisé différents hybrides BVIM-POM (BVIM = 1-butyl-3-vinylimidazolium) par FT-IR, ATG et DRX pour nous assurer que la structure des POMs est préservée dans le matériau final. La teneur en eau des matériaux hybrides est réduite de manière dépendante du POM. Par exemple, pour $(BVIM)_6[H_2W_{12}O_{40}]$ et $(BVIM)_4[SiW_{12}O_{40}]$ la large bande à 3400 cm^{-1} (FT-IR) a presque complètement disparu. Ce phénomène a été observé pour d'autres matériaux hybrides liquides POM-ioniques, comme celui résultant de l'appariement $[H_4PW_{18}O_{62}]^{7-}$ ou $[P_2W_{18}O_{60}]^{6-}$ avec le cation 1-butyl-3-méthylimidazolium $[BMIM]^+$ [13]. Mais pour $(BVIM)_5[BW_{12}O_{40}]$ et $(BVIM)_3[PW_{12}O_{40}]$ l'eau est toujours présente, notamment dans le second composé. La raison n'est pas claire, mais on peut noter que les POM parents de ces deux composés contiennent initialement un nombre plus élevé de molécules d'eau de constitution, tel que déterminé à partir de l'analyse ATG.

Le comportement thermogravimétrique du BVIM, des POMs parents et des matériaux hybrides a été mesuré. La courbe ATG du BVIMBr montre une perte de poids totale commençant à $300\text{ }^{\circ}\text{C}$ et se terminant à $600\text{ }^{\circ}\text{C}$. Ceci est attribué à la décomposition du liquide ionique. L'analyse thermique de tous les POMs parents montre une perte de masse initiale à partir de $100\text{ }^{\circ}\text{C}$ et jusqu'à $300\text{ }^{\circ}\text{C}$ correspondant à la perte d'eau puisque tous les POMs contiennent des molécules d'eau de constitution. De plus, cette analyse donne la possibilité de calculer exactement combien de molécules d'eau sont présentes. On obtient $(NH_4)_6[H_2W_{12}O_{40}]*4H_2O$, $K_5[BW_{12}O_{40}]*7H_2O$, $K_4[SiW_{12}O_{40}]*4H_2O$ et $Na_3[PW_{12}O_{40}]*12H_2O$. Ainsi, la perte d'eau représente respectivement 3%, 4%, 2% et 7%. Cela se produit en deux étapes pour tous les POM sauf pour $K_4[SiW_{12}O_{40}]*4H_2O$ pour lequel une seule étape est visible. Au-dessus de $300\text{ }^{\circ}\text{C}$ une légère décomposition lente des POMs est observée, sauf pour $(NH_4)_6[H_2W_{12}O_{40}]*3H_2O$ pour lequel une décomposition nette de 300 à $400\text{ }^{\circ}\text{C}$ (pic endothermique), représentant 4 % de perte de masse est observée. Ceci est probablement associé à la décomposition du cation ammonium qui l'accompagne avant la décomposition de l'anion Keggin. Pour tous les matériaux hybrides, la stabilité thermique est améliorée car aucune perte de masse n'est observée jusqu'à $300\text{ }^{\circ}\text{C}$. Cela s'explique par le fait qu'il n'y a pratiquement pas d'eau disponible dans les matériaux hybrides. Ceci corrobore avec les spectres FT-IR qui montrent une nette diminution de la teneur en eau (*vide supra*). Au-dessus de $300\text{ }^{\circ}\text{C}$, une perte de poids significative d'environ 24 %, 20 %, 16 % et 13 % est observée pour les matériaux hybrides. Ceci est associé à la décomposition du cation organique et correspond au pourcentage théorique du cation dans les matériaux BVIM-POM.

L'analyse par diffraction des rayons X a été réalisée sur la poudre des POM parents et des matériaux hybrides. Les résultats montrent que les sels de Keggin purs ont une structure mieux définie par rapport aux matériaux hybrides BVIM-POM. Cela peut s'expliquer par les modifications de la structure secondaire des POM induites par le liquide ionique. Ces

changements s'expliquent par la suppression des molécules d'eau de constitution mais aussi par le remplacement des petits cations (NH_4^+ , K^+ , Na^+) par un cation plus volumineux (BVIM^+). Un comportement similaire a été observé pour d'autres exemples de matériaux hybrides, tels que ceux obtenus à partir des POM de type Dawson $\text{K}_7[\text{H}_4\text{PW}_{18}\text{O}_{62}]$ et $\text{K}_6[\text{P}_2\text{W}_{18}\text{O}_{62}]$ et du tétrafluoroborate de 1-butyl-3-méthylimidazolium. Particulièrement pour $(\text{BVIM})_3[\text{PW}_{12}\text{O}_{40}]$ la structure est complètement amorphe.

Les mesures électrochimiques avec un montage standard à trois électrodes ont été effectuées afin de montrer que le comportement redox des BVIM-POM hybrides immobilisés est similaire à celui des POMs parents (à l'exception de $(\text{BVIM})_3[\text{PW}_{12}\text{O}_{40}]$ qui a un comportement particulier). Nous avons ensuite mené plusieurs expériences de contrôle pour comprendre l'influence du support carboné et du liquide ionique sur les performances électrocatalytiques finales des matériaux hybrides.

Tout d'abord, à partir de l'analyse DEMS, nous avons observé que le support de carbone seul permet la formation de N_2O à un potentiel assez positif (0,05 V *vs* RHE) (Figure 3a). Cette valeur est trop positive pour soutenir le mécanisme de réduction de l'oxyde nitrique via l'intermédiaire HNO (comme décrit dans la première partie). Il a été remarqué également que le début de la catalyse était réalisé à un potentiel beaucoup plus positif que celui obtenu avec une électrode en carbone vitreux (-0,15 V *vs* RHE). Ce résultat est très inattendu car dans la littérature les matériaux carbonés sont toujours modifiés par d'autres composés afin d'augmenter leurs performances électrocatalytiques. De plus, lorsque la réduction des nitrites a été étudiée au niveau de l'électrode de carbone avec le BVIM en solution, une légère diminution du potentiel d'apparition du N_2O a été observée (-0,01 V *vs* RHE).

Enfin, le potentiel d'apparition de N_2O obtenu avec les matériaux hybrides BVIM-POMs (BVIM = 1-butyl-3-vinyl imidazolium) a été mesuré à une valeur de potentiel plus positive, le potentiel étant légèrement dépendant du type de POM utilisé (Figure 3b et c). On peut noter que le courant catalytique est plus élevé pour ces matériaux. A ce stade, le mécanisme exact de formation de N_2O qui pourrait expliquer ces résultats n'est pas connu. Un mécanisme possible impliquerait une réaction entre un NO lié en surface avec un NO dissous dans un transfert proton-électron simultané. L'intermédiaire supposé est un dimère, $\text{HN}_2\text{O}_{2,\text{ads}}$ et sa formation serait l'étape déterminante de la vitesse de la catalyse. Alors que ce mécanisme a été proposé pour les électrodes métalliques et aussi pour les POM portant un hétéroatome métallique (par exemple, Fe), il est assez difficile d'imaginer qu'un NO lié en surface puisse exister sur un support de carbone ou de carbone modifié avec des BVIM-POM ne portant pas d'hétéroatome métallique. Très probablement, d'autres techniques spectroscopiques (telles que l'Infrarouge à transformée de Fourier opérando) devraient être utilisées pour clarifier le mécanisme.

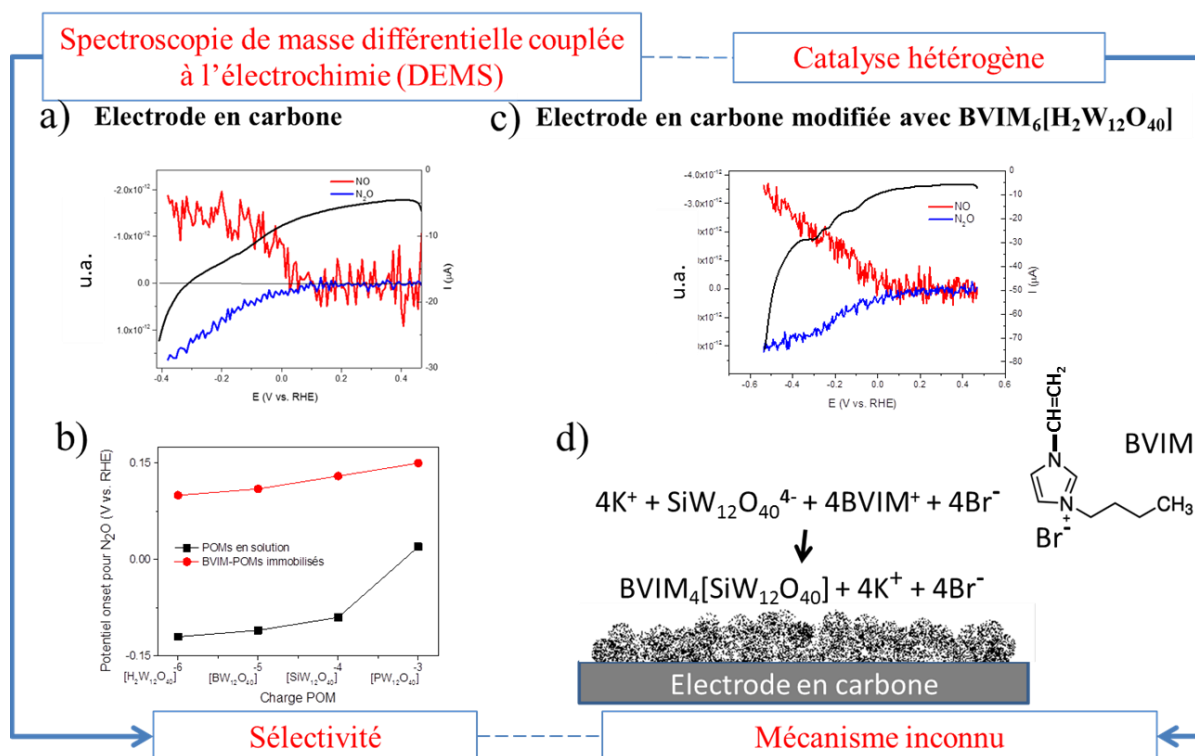


Figure 3. a) Analyse DEMS de la réduction des nitrites au niveau d'une électrode en carbone ; b) Analyse DEMS de la réduction des nitrites sur une électrode de carbone modifiée avec l'hybride $\text{BVIM}_6[\text{H}_2\text{W}_{12}\text{O}_{40}]$ immobilisé ; c) Potentiel d'apparition de N_2O obtenu à partir d'une analyse DEMS à différentes électrodes ; d) Équation de la réaction chimique entre le POM $\text{K}_4[\text{SiW}_{12}\text{O}_{40}]$ et le liquide ionique le bromure de 1-butyl-3-vinyl imidazolium (BVIM) formant le composé insoluble $\text{BVIM}_4[\text{SiW}_{12}\text{O}_{40}]$ qui est ensuite immobilisé sur une électrode de carbone. (BVIM = 1-butyl-3-vinyl imidazolium).

3) Conclusion générale

Cette thèse porte sur l'étude de la réduction des nitrites par la technique de spectrométrie de masse électrochimique différentielle (DEMS). La réaction est catalysée par trois systèmes différents : i) divers polyoxométallates de type Keggin et Dawson en solution (catalyse homogène) ; ii) quatre polyoxométallates de type Keggin libres en solution et une électrode d'argent (catalyse tandem mixte homogène et hétérogène), et enfin iii) quatre POMs de type Keggin modifiés avec un liquide ionique et immobilisés sur électrode de carbone (catalyse hétérogène).

Les résultats remarquables suivants ont été obtenus : i) deux produits gazeux (NO et N_2O) sont obtenus à partir de la réduction des nitrites et leur potentiel d'apparition dépend du comportement électrochimique des POMs étudiés ; le mécanisme réactionnel de formation de N_2O est commun à tous les POMs et fait intervenir un intermédiaire HNO ; ii) les POMs en solution et une électrode de travail en argent effectuent une catalyse en tandem pour la réduction des nitrites ce qui abaisse la surtension pour la formation de N_2O en utilisant peut-être un dimère NO comme intermédiaire ; iii) les matériaux hybrides immobilisés, obtenus à partir de POMs et d'un liquide ionique, conservent leur comportement électrochimique et leur activité électrocatalytique vis-à-vis de la réduction des nitrites mais le mécanisme est encore inconnu et reste à étudier.

Les perspectives suivantes sont proposées : i) étendre la modélisation microcinétique à

plus de POMs pour hiérarchiser leur efficacité électrocatalytique ; ii) utiliser des nanoparticules d'argent stabilisées par des POM comme catalyseurs hétérogènes immobilisés pour la réduction des nitrites ; iii) utiliser plusieurs techniques spectroscopiques complémentaires pour comprendre le mécanisme de réduction des nitrites catalysée par des matériaux hybrides obtenus à partir de POM et de liquide ionique ; iv) utiliser différents liquides ioniques pour l'obtention de ces matériaux hybrides et étudier leur influence sur le comportement électrocatalytique pour la réduction des nitrites ; et enfin tester ces systèmes vis-à-vis de la réduction des nitrates.

4) Références

- [1] Keita B.; Abdeljalil E.; Nadjo L.; Contant R.; Belgiche R.; First examples of efficient participation of selected metal-ion-substituted heteropolyanions in electrocatalytic nitrate reduction, *Electrochem. Commun.* 3 (2001) 56–62.
- [2] Imar S.; Maccato C.; Dickinson C.; Laffir F.; Vagin M.; McCormac T.; Enhancement of Nitrite and Nitrate Electrocatalytic Reduction through the Employment of Self-Assembled Layers of Nickel- and Copper-Substituted Crown-Type Heteropolyanions, *Langmuir* 31 (2015) 2584–2592.
- [3] Liu H.; He P.; Li Z.; Sun C.; Shi L.; Liu Y.; Zhu G.; Li J.; An ionic liquid-type carbon paste electrode and its polyoxometalate-modified properties, *Electrochem. Commun.* 7 (2005) 1357–1363.
- [4] Dong, S.; Xi, X.; Tian, M., Study of the electrocatalytic reduction of nitrite with silicotungstic heteropolyanion. *Journal of Electroanalytical Chemistry* 1995, 385 (2), 227-233.
- [5] Toth, J. E.; Anson, F. C., Electrocatalytic reduction of nitrite and nitric oxide to ammonia with iron-substituted polyoxotungstates. *Journal of the American Chemical Society* 1989, 111 (7), 2444-2451.
- [6] McCormac, T.; Fabre, B.; Bidan, G., Part II. Role of pH and the transition metal for the electrocatalytic reduction of nitrite with transition metal substituted Dawson type heteropolyanions. *Journal of Electroanalytical Chemistry* 1997, 427 (1-2), 155-159.
- [7] Ruhlmann, L.; Genet, G., Wells–Dawson-derived tetrameric complexes $\{K_{28}H_8[P_2W_{15}Ti_3O_{60.5}]_4\}$ electrochemical behaviour and electrocatalytic reduction of nitrite and of nitric oxide. *Journal of Electroanalytical Chemistry* 2004, 568, 315-321.
- [8] Xi, X.; Dong, S., Electrocatalytic reduction of nitrite using Dawson-type tungstodiphosphate anions in aqueous solutions, adsorbed on a glassy carbon electrode and doped in polypyrrole film. *Journal of Molecular Catalysis A: Chemical* 1996, 114 (1-3), 257-265.
- [9] Naseer, R.; Mal, S. S.; Kortz, U.; Armstrong, G.; Laffir, F.; Dickinson, C.; Vagin, M.; McCormac, T., Electrocatalysis by crown-type polyoxometalates multi-substituted by transition metal ions; Comparative study. *Electrochimica Acta* 2015, 176, 1248-1255.
- [10] Belhouari, A.; Keita, B.; Nadjo, L.; Contant, R., Efficient conversion of NO into N₂O by selected electroreduced heteropolyanions. *New Journal of Chemistry* 1998, 22 (2), 83-86.
- [11] Boussema, F.; Haddad, R.; Ghandour, Y.; Belkhiria, M. S.; Holzinger, M.; Maaref, A.; Cosnier, S., Polyoxometalate $[PMo_{11}O_{39}]^{7-}$ / carbon nanocomposites for sensitive amperometric detection of nitrite. *Electrochimica Acta* 2016, 222, 402-408.
- [12] Huang, B.-Q.; Wang, L.; Shi, K.; Xie, Z.-X.; Zheng, L.-S., A new strategy for the fabrication of the phosphor polyoxomolybdate modified electrode from ionic liquid solutions

- and its electrocatalytic activities. *Journal of Electroanalytical Chemistry* 2008, 615 (1), 19-24.
- [13] Ammam, M.; Fransaer, J., Synthesis and characterization of hybrid materials based on 1-butyl-3-methylimidazolium tetrafluoroborate ionic liquid and Dawson-type tungstophosphate $K_7[H_4PW_{18}O_{62}] \cdot 18H_2O$ and $K_6[P_2W_{18}O_{62}] \cdot 13H_2O$. *Journal of Solid State Chemistry* 2011, 184 (4), 818-824.
- [14] (a) Haghighi, B.; Hamidi, H.; Gorton, L., Formation of a robust and stable film comprising ionic liquid and polyoxometalate on glassy carbon electrode modified with multiwalled carbon nanotubes: Toward sensitive and fast detection of hydrogen peroxide and iodate. *Electrochimica Acta* 2010, 55 (16), 4750-4757; (b) Feizy, S.; Haghighi, B., A survey on the effect of ionic liquid on electrochemical behavior and electrocatalytic activity of a phosphomolybdic acid-ionic liquid-MWCNT-modified glassy carbon electrode. *Journal of Solid State Electrochemistry* 2019, 23 (5), 1339-1350.
- [15] Wang, R.; Jia, D.; Cao, Y., Facile synthesis and enhanced electrocatalytic activities of organic-inorganic hybrid ionic liquid polyoxometalate nanomaterials by solid-state chemical reaction. *Electrochimica acta* 2012, 72, 101-107.
- [16] Wang, B.; Cheng, L.; Dong, S., Construction of a heteropolyanion-modified electrode by a two-step sol-gel method and its electrocatalytic applications. *Journal of Electroanalytical Chemistry* 2001, 516 (1-2), 17-22.
- [17] Chen, S.; Xiang, Y.; Banks, M. K.; Xu, W.; Peng, C.; Wu, R., Polyoxometalate-coupled graphene nanohybrid via gemini surfactants and its electrocatalytic property for nitrite. *Applied Surface Science* 2019, 466, 110-118.
- [18] Imar, S.; Yaqub, M.; Maccato, C.; Dickinson, C.; Laffir, F.; Vagin, M.; McCormac, T., Nitrate and Nitrite Electrocatalytic Reduction at Layer-by-Layer Films Composed of Dawson-type Heteropolyanions Mono-substituted with Transitional Metal Ions and Silver Nanoparticles. *Electrochimica Acta* 2015, 184, 323-330.
- [19] Sahraoui, Y.; Chaliaa, S.; Maaref, A.; Haddad, A.; Jaffrezic-Renault, N., An electrochemical nitrite sensor based on a multilayer film of polyoxometalate. *Journal of Sensor Technology* 2013, 3 (03), 84.
- [20] Shan, Y.; Yang, G.; Sun, Y.; Pang, S.; Gong, J.; Su, Z.; Qu, L., ITO electrode modified by self-assembling multilayer film of polyoxometallate on poly (vinyl alcohol) nanofibers and its electrocatalytic behavior. *Electrochimica acta* 2007, 53 (2), 569-574.
- [21] Zhang, D.; Ma, H.; Chen, Y.; Pang, H.; Yu, Y., Amperometric detection of nitrite based on Dawson-type vanodotungstophosphate and carbon nanotubes. *Analytica Chimica Acta* 2013, 792, 35-44.
- [22] Zhang, L.; Li, S.; Zhang, Z.; Tan, L.; Pang, H.; Ma, H., Facile fabrication of reduced graphene oxide and Keggin-type polyoxometalates nanocomposite film for high performance electrocatalytic oxidation of nitrite. *Journal of Electroanalytical Chemistry* 2017, 807, 97-103.
- [23] Wang, Q.; Khungwa, J.; Li, L.; Liu, Y.; Wang, X.; Wang, S., Fabrication of polyoxometalate/GO/PDDA hybrid nanocomposite modified electrode and electrocatalysis for nitrite ion, ascorbic acid and dopamine. *Journal of Electroanalytical Chemistry* 2018, 824, 91-98.
- [24] Keita, B.; Belhouari, A.; Nadjo, L.; Contant, R., Electrocatalysis by polyoxometalate/polymer systems: reduction of nitrite and nitric oxide. *Journal of Electroanalytical Chemistry* 1995, 381 (1-2), 243-250.
- [25] Cao, F.; Guo, S.; Ma, H.; Gong, J., ITO Electrode Modified by α - $K_6[P_2W_{18}O_{62}]$ Hybrid Nanofibers for Nitrite Determination. *Electroanalysis* 2012, 24 (2), 418-424.

- [26] Duca M.; B. van der Klugt, Koper M.T.M.; Electrocatalytic reduction of nitrite on transition and coinage metals, *Electrochimica Acta* 68 (2012) 32–43.
- [27] (a) Duca, M.; Cucarella, M. O.; Rodriguez, P.; Koper, M. T., Direct reduction of nitrite to N₂ on a Pt (100) electrode in alkaline media. *Journal of the American Chemical Society* 2010, 132 (51), 18042-18044; (b) Duca, M.; Figueiredo, M. C.; Climent, V.; Rodriguez, P.; Feliu, J. M.; Koper, M. T., Selective catalytic reduction at quasi-perfect Pt (100) domains: a universal low-temperature pathway from nitrite to N₂. *Journal of the American Chemical Society* 2011, 133 (28), 10928-10939.
- [28] Duca, M.; Van Der Klugt, B.; Hasnat, M.; Machida, M.; Koper, M., Electrocatalytic reduction of nitrite on a polycrystalline rhodium electrode. *Journal of Catalysis* 2010, 275 (1), 61-69
- [29] Duca, M.; Kavvadia, V.; Rodriguez, P.; Lai, S.; Hoogenboom, T.; Koper, M., New insights into the mechanism of nitrite reduction on a platinum electrode. *Journal of Electroanalytical Chemistry* 2010, 649 (1-2), 59-68
- [30] Debiemme-Chouvy C.; Cachet H.; Folcher G.; Deslouis C.; Electrocatalytic Reduction of HNO₂ by a Silicomolybdate Polyanion: A Differential Electrochemical Mass Spectrometry Study, *Electroanalysis* 19 (2007) 259–262.
- [31] Belhouari, A.; Keita, B.; Nadjo, L.; Contant, R., Efficient conversion of NO into N₂O by selected electroreduced heteropolyanions. *New Journal of Chemistry* 1998, 22 (2), 83-86
- [32] Flores-Santana W.; Salmon D.J.; Donzelli S.; Switzer C.H.; Basudhar D.; Ridnour L.; Cheng R.; Glynn S.A.; Paolucci N.; Fukuto J.M.; Miranda K.M.; Wink D.A.; The Specificity of Nitroxyl Chemistry Is Unique Among Nitrogen Oxides in Biological Systems, *Antioxid. Redox Signal.* 14 (2011) 1659–1674.
- [33] Ruhlmann, L.; Nadjo, L.; Canny, J.; Contant, R.; Thouvenot, R., Di-and Tetranuclear Dawson-Derived Sandwich Complexes: Synthesis, Spectroscopic Characterization, and Electrochemical Behavior. *European Journal of Inorganic Chemistry* 2002, 2002 (4), 975-986
- [34] Troupis A.; Hiskia A.; Papaconstantinou E.; Synthesis of Metal Nanoparticles by Using Polyoxometalates as Photocatalysts and Stabilizers, *Angew. Chem. Int. Ed.* 41 (2002) 1911–1914.
- [35] Keita B.; Liub T.; Nadjo L.; Synthesis of remarkably stabilized metal nanostructures using polyoxometalates, *J. Mater. Chem.* 19 (2009) 19–33.

Content

List of Abbreviations	1
Introduction	4
Chapter I: Introduction and literature review	7
1.1 Polyoxometalates.....	8
1.1.1 Structures and properties of polyoxometalates.....	8
1.1.1.1 Structure of polyoxometalates.....	8
1.1.1.2 Synthesis of polyoxometalates	9
1.1.1.3 Redox behavior of polyoxometalates	11
1.1.2 Polyoxometalates applications.....	11
1.1.2.1 Photocatalytic properties of polyoxometalates	12
1.1.2.2 Electrocatalytic properties of polyoxometalates	14
1.2 Differential Electrochemical Mass Spectroscopy (DEMS)	17
1.2.1 DEMS experimental setup.....	17
1.2.1.1 The electrochemical cell	17
1.2.1.2 The membrane inlet system	19
1.2.1.3 The mass spectrometer	20
1.2.2 DEMS applications	20
1.2.2.1 DEMS detection of carbonaceous species	21
1.2.2.2 DEMS detection of nitrogen-based species	21
1.3 NO ₂ ⁻ and NO ₃ ⁻ : environmental pollutants and removal strategies.....	23
1.3.1 Nitrite (nitrate) pollution in water resources	23
1.3.1.1 Sources of nitrite (nitrate) in water.....	23
1.3.1.2 Hazards of nitrite (nitrate).....	24
1.3.2 Methods for nitrite (nitrate) removal.....	25
1.3.2.1 Physical methods for nitrite (nitrate) removal	25
1.3.2.2 Biological methods for nitrite (nitrate) removal	26
1.3.2.3 Chemical methods for nitrite (nitrate) removal.....	27
1.4 Electrochemical reduction of NO _x species.....	29
1.4.1 DEMS studies of NO ₃ ⁻ electrochemical reduction.....	30
1.4.2 DEMS studies of NO electrochemical reduction.....	33
1.4.3 DEMS studies of NO ₂ ⁻ electrochemical reduction.....	34
1.4.4 Polyoxometalates as catalysts for electroreduction of NO ₂ ⁻	36
1.4.4.1 POM-based homogeneous catalysis of NO ₂ ⁻ electrochemical reduction	37
1.4.4.2 POM-based heterogeneous catalysis of NO ₂ ⁻ electrochemical reduction.....	40
1.5 DEMS studies of POM-based catalysis of electrochemical reduction of nitrite.....	47
1.6 References	47
Chapter II: Nitrite electroreduction catalyzed by Keggin and Dawson polyoxometalates	62
2.1 Introduction	63
2.2 Electrochemical properties of POMs on GC electrode.....	65
2.2.1 Electrochemical properties of W-based Keggin POMs	65
2.2.2 Electrochemical properties of Mo-based Keggin and W-based Dawson POMs	70

2.3 Nitrite reduction catalyzed by POMs – Cyclic voltammetry studies	76
2.3.1 W-based Keggin POMs as catalysts for nitrite reduction	76
2.3.2 Mo-based Keggin POMs as catalysts for nitrite reduction.....	83
2.3.3 W-based Dawson POMs as catalysts for nitrite reduction	85
2.4 Nitrite reduction catalyzed by POMs – DEMS studies	87
2.4.1 Nitrite reduction catalyzed by W-based Keggin POMs – DEMS studies	88
2.4.2 Nitrite reduction catalyzed by Mo-based Keggin POMs – DEMS studies	94
2.4.3 Nitrite reduction catalyzed by Dawson POMs – DEMS studies	95
2.4.4 Comparison of NO and N ₂ O onset potentials for all studied POMs.....	98
2.5 Investigation of other products of nitrite reduction catalyzed by POMs	100
2.5.1 DEMS detection of NH ₃ (NH ₄ ⁺).....	100
2.5.2 Detection of hydroxylamine (NH ₂ OH) by UV-Vis.....	101
2.6 Reduction of nitric oxide (NO) catalyzed by POMs	104
2.7 Kinetic studies of nitrite reduction catalyzed by POMs	106
2.8 Conclusion.....	114
2.9 References	115
Chapter III: Nitrite electroreduction catalyzed by a series of Keggin polyoxometalates and Ag materials.....	120
3.1 Introduction	121
3.2 Cyclic voltammetry studies.....	122
3.2.1 Electrochemical properties of Ag electrode.....	122
3.2.2 Electrochemical and electrocatalytic properties of POMs on Ag electrode	124
3.3 DEMS studies of nitrite reduction	129
3.3.1 Catalysis by Ag electrode alone.....	129
3.3.2 Catalysis by Keggin POMs and Ag electrode.....	133
3.4 Nitrite reduction catalyzed by Ag nanoparticles stabilized by POMs (Ag@POM)	141
3.4.1 Synthesis of Ag@POM nanoparticles	141
3.4.1.1 Synthesis of Ag@POM nanoparticles using photoreduced POM.....	141
3.4.1.2 Synthesis of Ag@POM using electroreduced POM.....	145
3.4.2 DEMS analysis of nitrite reduction catalyzed by Ag@POM	148
3.4.2.1 Performance of Ag@[SiW ₁₂ O ₄₀] ⁴⁻ prepared by photoreduction.....	148
3.4.2.2 Performance of Ag@[SiW ₁₂ O ₄₀] ⁴⁻ prepared by electroreduction.....	150
3.5 Conclusion.....	155
3.6 References	156
Chapter IV: Nitrite electroreduction catalyzed by hybrid compounds of Keggin polyoxometalates and 1-butyl-3-vinylimidazolium	159
4.1 Introduction	160
4.2 Synthesis of hybrid compounds BVIM-POM.....	160
4.3 Characterization of BVIM-POM.....	161
4.3.1 FT-IR characterization of BVIM-POM.....	161
4.3.2 TGA characterization of BVIM-POM.....	165
4.3.3 XRD characterization of BVIM-POM	167
4.4 Preparation of BVIM-POM/C electrodes	169
4.5 Electrochemical behavior of GC/C/BVIM-POM electrodes	170
4.6 Electrocatalytic behavior of GC/C/BVIM-POM electrodes	173
4.7 DEMS analysis of nitrite reduction catalyzed by GC/C/BVIM-POM electrodes.....	179

4.8 Conclusion.....	185
4.9 References	185
Conclusion	187
Appendix.....	189

List of Abbreviations

ATR-SEIRAS	Attenuated total reflectance surface-enhanced infrared absorption spectroscopy
BMIM	1-n-Butyl-3-methylimidazolium tetrafluoroborate (BMIM⁺BF₄⁻)
BMIMBF ₄	1-n-Butyl-3-methylimidazolium tetrafluoroborate
BVIM	1-butyl-3-vinylimidazolium
CV	Cyclic voltammogram
C ₁₂ Py	N-dodecyl pyridinium hexafluorophosphate ([C₁₂Py][PF₆])
CNT	Carbon nanotube
CAT	Catalytic efficiency
DEMS	Differential electrochemical mass spectrometry
DMSO	Dimethylsulfoxide
D _p	The diffusion coefficient of the POM,
D _N	The diffusion coefficient of the nitrite (or nitrous acid)
EMIMBF ₄	1-methyl-3-methylimidazolium tetrafluoroborate
EMIMBr	1-methyl-3-methylimidazolium bromide
EQCM	Electrochemical quartz crystal microbalance
FTIR	Fourier-transform infrared spectroscopy
F	Faraday constant: 96485 C mol⁻¹
GO	Graphene oxide
Gem	Gemini surfactants
GC	Glass carbon
HOMO	Highest occupied molecular orbital
HER	Hydrogen evolution reaction
IL	Ionic liquid
ITO	Indium tin oxide

IC	Ion chromatography
k_c	Kinetic constant
LUMO	Lowest unoccupied molecular orbital
MWCNT	Multi-wall carbon nanotubes
MOF	Metal organic frameworks
MSCV	Mass Spectroscopic Cyclic Voltammogram
NRR	N₂ reduction
NitER	Nitrite electrochemical reduction
η	Overpotential
Ox-SWCNT	Oxidized single-walled carbon nanotubes
OCP	Open Circuit Potential
OLEMS	Online Electrochemical Mass Spectrometry
OER	Oxygen evolution reaction
PCL	Polycaprolactone
PBS	Polybutylene succinate
PVP	Poly-vinylpyridine
POMs	Polyoxometalates
PVA	Poly-vinylalcohol
PDDA	Poly-diallyldimethylammonium chloride
PSS	Poly(styrenesulfonate)
PEI	Poly(ethyleneimine)
PANI	Polyaniline
PAH	Poly(allylamine hydrochloride)
PPy	Polypyrrole film
$P_4W_{30}Cd_4$	$[Cd_4(H_2O)_2(P_2W_{15}O_{56})_2]^{16-}$
$P_4W_{30}Mn_4$	$[Mn_4(H_2O)_2(P_2W_{15}O_{56})_2]^{16-}$
$P_4W_{30}Zn_4$	$[Zn_4(H_2O)_2(P_2W_{15}O_{56})_2]^{16-}$

PIL	Polymerized ionic liquid
R	The ideal gas constant: $8.314 \text{ J.K}^{-1}\text{mol}^{-1}$
rGO	Reduced graphene oxide
RHE	Reversible hydrogen electrode
SCE	Saturated Calomel Electrode
TGA	Thermal gravimetric analysis
TOF	Turnover frequency
UV-Vis	Ultra Violet Visible
WIG	Wax impregnated graphite
WOC	Water-oxidizing complex
XRD	X-ray Powder Diffraction

Introduction

Conversion of NO_x species (nitrate, nitrite, nitric oxide, etc.) to harmless products such as nitrogen or useful chemicals such as ammonia and nitrous oxide is highly desirable to discard these environmental pollutants in an efficient manner. Amongst various techniques, electrochemical methods are quite clean as they require less external chemical adjuvants. In order to decrease the energy input, various electrochemical catalysts are investigated. One class of catalysts are the inorganic metal-oxides clusters named polyoxometalates (POMs). POMs can carry out reversible multi-electron transfer reactions without any change of their structure showing good stability.¹ In addition, POMs have high proton mobility, strong Brønsted acidity, high solubility, and are stable in acid environment.² The number of POMs is continuously increasing, as the knowledge about their chemical properties becomes richer. In this view, all new POMs are tested for various electrochemical reactions, including NO_x reduction. Various POMs, ranging from small compounds from Keggin and Dawson types to more complex structures (such as Wells-Dawson-derived tetramers, crown-type structures), and even organic-inorganic hybrids have been tested. Nevertheless, the vast majority of the studies are concerned about the electrocatalytic performance but not focused on the actual obtained products. The mechanism of nitrite electroreduction is still unclear owing to lack of real-time product analysis.³ From these points of view, disposing of an analytical technique able to rapidly identify in a single test as many products as possible becomes an important characterization tool.

In this view, the work performed in this thesis is focused on the study of nitrite electroreduction using a diversity of POMs and DEMS technique. Differential electrochemical mass spectrometry (DEMS) is an analytical technique able to identify the *in situ* formation of gaseous products during one single potential scan. A direct correlation between the applied electrochemical potential and products formation is obtained. This technique has been extensively used for deciphering the mechanism when noble and transition metals are acting as catalysts,⁴ but barely no publication was found for the study of POMs catalysts.⁵ This is the main purpose of the work described in this thesis. The results are organized in three main parts.

In the first part one (chapter 3), as many as eleven different POMs from the Keggin and Dawson family have been tested. The idea is to use archetypal POMs and refine the knowledge of their catalytic performance by study the influence of their global charge and redox potential on the obtained products. Due to their selectivity for the conversion of nitrite to nitric oxide at low overpotential, a microkinetic model allowed the computation of the rate constant and turnover frequency for the first time.

In the second part (chapter 4), a mixed homogeneous and heterogeneous catalysis by using POMs in solution and silver as working electrode. This metal was chosen due to the known existing interactions between POMs and silver, for example Ag@POMs nanoparticles.⁶ DEMS data unraveled the tandem catalysis between the two catalysts, with much reduced overpotential for the conversion of nitric oxide to nitrous oxide.

POMs are also thought as a kind of transferable building blocks for functional materials. Polyoxometalate-based molecular and composite materials show unique performance.⁷ In the final part (chapter 5) new hybrid materials were obtained by replacing innate cations of the POMs with an organic cation issued from an ionic liquid. These hybrid materials were tested

in a heterogeneous catalysis after the immobilization on glassy carbon electrodes. DEMS data were quite surprising as the overpotential of nitric oxide conversion to nitrous oxide is also very much reduced.

In summary, this thesis reports and compares a series of POMs and hybrid POMs materials performance for the electrocatalytic reduction of nitrite. The reaction mechanism and influencing factors such as pH, substrate, POM structure, and synergy between POMs and Ag or ionic liquid organic cation are discussed.

Reference

1. (a) Chai, D.; Gómez-García, C. J.; Li, B.; Pang, H.; Ma, H.; Wang, X.; Tan, L., Polyoxometalate-based metal-organic frameworks for boosting electrochemical capacitor performance. *Chemical Engineering Journal* **2019**, *373*, 587-597; (b) Lu, B.; Li, S.; Pan, J.; Zhang, L.; Xin, J.; Chen, Y.; Tan, X., pH-controlled assembly of five new organophosphorus Strandberg-type cluster-based coordination polymers for enhanced electrochemical capacitor performance. *Inorganic chemistry* **2020**, *59* (3), 1702-1714; (c) Wang, X.-L.; Tian, Y.; Chang, Z.-H.; Lin, H., A Series of Polyoxometalate-Based Metal-Bis (pyridyl-tetrazole) Complexes with High Electrocatalytic Activity for Hydrogen Evolution Reaction in Alkaline and Acid Media. *ACS Sustainable Chemistry & Engineering* **2020**, *8* (41), 15696-15702.
2. Huang, B.; Yang, D.-H.; Han, B.-H., Application of polyoxometalate derivatives in rechargeable batteries. *Journal of Materials Chemistry A* **2020**, *8* (9), 4593-4628.
3. (a) Dong, S.; Xi, X.; Tian, M., Study of the electrocatalytic reduction of nitrite with silicotungstic heteropolyanion. *Journal of Electroanalytical Chemistry* **1995**, *385* (2), 227-233; (b) Toth, J. E.; Anson, F. C., Electrocatalytic reduction of nitrite and nitric oxide to ammonia with iron-substituted polyoxotungstates. *Journal of the American Chemical Society* **1989**, *111* (7), 2444-2451; (c) McCormac, T.; Fabre, B.; Bidan, G., Part II. Role of pH and the transition metal for the electrocatalytic reduction of nitrite with transition metal substituted Dawson type heteropolyanions. *Journal of Electroanalytical Chemistry* **1997**, *427* (1-2), 155-159; (d) Ruhlmann, L.; Genet, G., Wells-Dawson-derived tetrameric complexes $\{K_{28}H_8[P_2W_{15}Ti_3O_{60.5}]_4\}$ electrochemical behaviour and electrocatalytic reduction of nitrite and of nitric oxide. *Journal of Electroanalytical Chemistry* **2004**, *568*, 315-321; (e) Naseer, R.; Mal, S. S.; Kortz, U.; Armstrong, G.; Laffir, F.; Dickinson, C.; Vagin, M.; McCormac, T., Electrocatalysis by crown-type polyoxometalates multi-substituted by transition metal ions; Comparative study. *Electrochimica Acta* **2015**, *176*, 1248-1255; (f) Xi, X.; Dong, S., Electrocatalytic reduction of nitrite using Dawson-type tungstodiphosphate anions in aqueous solutions, adsorbed on a glassy carbon electrode and doped in polypyrrole film. *Journal of Molecular Catalysis A: Chemical* **1996**, *114* (1-3), 257-265.
4. (a) Duca, M.; Van Der Klugt, B.; Hasnat, M.; Machida, M.; Koper, M., Electrocatalytic reduction of nitrite on a polycrystalline rhodium electrode. *Journal of Catalysis* **2010**, *275* (1), 61-69; (b) Duca, M.; Kavvadia, V.; Rodriguez, P.; Lai, S.; Hoogenboom, T.; Koper, M., New insights into the mechanism of nitrite reduction on a platinum electrode. *Journal of Electroanalytical Chemistry* **2010**, *649* (1-2), 59-68; (c) Duca, M.; Van der Klugt, B.; Koper, M., Electrocatalytic reduction of nitrite on transition and coinage metals. *Electrochimica Acta* **2012**, *68*, 32-43.
5. Debiemme-Chouvy, C.; Cachet, H.; Folcher, G.; Deslouis, C., Electrocatalytic reduction of HNO_2 by a silicomolybdate polyanion: a differential electrochemical mass spectrometry study. *Electroanalysis: An International Journal Devoted to Fundamental and Practical Aspects of Electroanalysis* **2007**, *19* (2□3), 259-262.
6. Costa-Coquelard, C.; Schaming, D.; Lampre, I.; Ruhlmann, L., Photocatalytic reduction of Ag_2SO_4 by the Dawson anion $\alpha-[P_2W_{18}O_{62}]^{6-}$ and tetracobalt sandwich complexes. *Applied Catalysis B: Environmental* **2008**, *84* (3-4), 835-842.

7. (a) Ueda, T., Electrochemistry of polyoxometalates: from fundamental aspects to applications. *ChemElectroChem* **2018**, 5 (6), 823-838; (b) Sartorel, A.; Carraro, M.; Scorrano, G.; Zorzi, R. D.; Geremia, S.; McDaniel, N. D.; Bernhard, S.; Bonchio, M., Polyoxometalate embedding of a tetraruthenium (IV)-oxo-core by template-directed metalation of $[\gamma\text{-SiW}_{10}\text{O}_{36}]^{8-}$: a totally inorganic oxygen-evolving catalyst. *Journal of the American Chemical Society* **2008**, 130 (15), 5006-5007; (c) Haber, J.; Matachowski, L.; Mucha, D.; Stoch, J.; Sarv, P., New Evidence on the Structure of Potassium Salts of 12-Tungstophosphoric Acid, $\text{K}_x\text{H}_{1(3-x)}\text{PW}_{12}\text{O}_{40}$. *Inorganic chemistry* **2005**, 44 (19), 6695-6703; (d) R  ther, T.; Hultgren, V. M.; Timko, B. P.; Bond, A. M.; Jackson, W. R.; Wedd, A. G., Electrochemical investigation of photooxidation processes promoted by sulfo-polyoxometalates: coupling of photochemical and electrochemical processes into an effective catalytic cycle. *Journal of the American Chemical Society* **2003**, 125 (33), 10133-10143.

Chapter I: Introduction and literature review

1.1 Polyoxometalates

Polyoxometalates (POMs) are a series of metal oxide cluster anions. The first POM was reported in 1826 by Berzelius¹ and series of new POMs are produced afterwards. The Keggin-type and the Wells-Dawson-type POMs are most common and well-studied structures. POMs can carry out reversible multi-electron transfer reactions without any change of their structure showing good stability.² Mo and W-based POMs show remarkable photochemical and photophysical properties in heterogeneous photo(electro)catalysis. In addition, POMs have high proton mobility, strong Brønsted acidity, high solubility, and are stable in acid environment.³ Therefore polyoxometalates have been widely explored also as sensing materials for many years.⁴ At the same time, POMs are thought as a kind of transferable building blocks for functional materials. Polyoxometalate-based molecular and composite materials show unique performance.⁵

1.1.1 Structures and properties of polyoxometalates

1.1.1.1 Structure of polyoxometalates

Polyoxometalates are transition metal oxide clusters with various topological structures.^{3-4, 6} The most common structures of POMs are Keggin⁷ and Wells-Dawson,⁸ which have been most widely studied,⁹ besides Lindqvist,¹⁰ Anderson-Evans,¹¹ and Preyssler structures (Silverton-type¹² and Waugh-type¹³) (Figure 1.1.1). There are also numerous fascinating cluster architectures such as annular, sphere, and wheel-shaped structures.¹⁴ The d^0 or d^1 metal ions are bridged via oxygen atoms through co-angle, co-edge, or co-planar mode.¹⁵ $[X_xM_yO_z]^{n-}$ is the general formula of POM anions. M represents transition metals (such as Mo^{VI} , W^{VI} , $V^{V,VI}$, Nb^V , or Ta^V) and X is the heteroatom (such as P, Si, Ge, Se, B or Sb).¹⁶ POMs can be divided into isopolyanions and heteropolyanions depending whether there are heteroatoms. Isopolyoxometalates are only composed of same metal oxyacid ions, such as $[W_6O_{19}]^{2-}$ or $[V_{10}O_{28}]^{6-}$, and possess high symmetry and negative charge.^{9, 17} Heteropolyoxometalates have both metal oxyacid ions and heteroatoms. Some POMs comprise phosphorous or sulfur, e.g. in the form of tetrahedral SO_4^{2-} .¹⁸ In addition, recently new classes of hybrid species were produced from the covalent functionalization of traditional POM architectures.¹⁹ Due to POMs' structure, most of the compounds are highly soluble in different kinds of polar solvents including water. Electrostatic forces, covalent and non-covalent interactions, and hydrogen bonding between POMs and solvents explain their solubility. Furthermore, the change of nature of the counter cations can change drastically the solubility. For instance, Li^+ or Na^+ counter cations lead the POM to be soluble in aqueous solution, while TBA counter cations allow the POM to be soluble in an organic medium.



Figure 1.1.1 Six typical structures of polyoxometalates: Keggin, Wells-Dawson, Lindqvist, Anderson-Evans, Silverton, and Waugh.

Keggin POMs

The first reported Keggin structure was 12-tungstophosphoric acid $\text{H}_3[\text{PW}_{12}\text{O}_{40}]$.²⁰ Since that, many Keggin structures have been discovered and have been distinguished by the metal ions, heteroatoms, and isomerism type. The general formula of them is $[\text{XM}_{12}\text{O}_{40}]^{n-}$. XO_4 tetrahedrons are composed by W or Mo. The charge “ $n-$ ” depends on the heteroatom and it ranges from -2²¹ to -7²². Keggin POMs have five isomers. As shown in Figure 1.1.2, depending on the amounts (from 0 to 4) of M_3O_{13} triads undergoing 60° rotations, Keggin POMs isomers are divided into α (original), β , γ , δ and ϵ isomers.²³ Apart from the molecular structure, the electrostatic repulsion is different between these units. The most stable fully oxidized anion is α -type, then by the order: β , γ , δ , ϵ . Reduced α and β -Keggin-type POMs can be synthesized electrochemically²⁴ or hydrothermally²⁵. However, reduced δ and ϵ -Keggin POMs are only prepared by hydrothermal synthesis when bounded to a transition metal ion.²⁶ Compared with oxidized Keggin POMs, the reduced states have eternal delocalized electrons, which stabilize the structure to prevent addenda atom substitution. To stabilize highly charged Keggin POMs cationic groups can be used for capping.

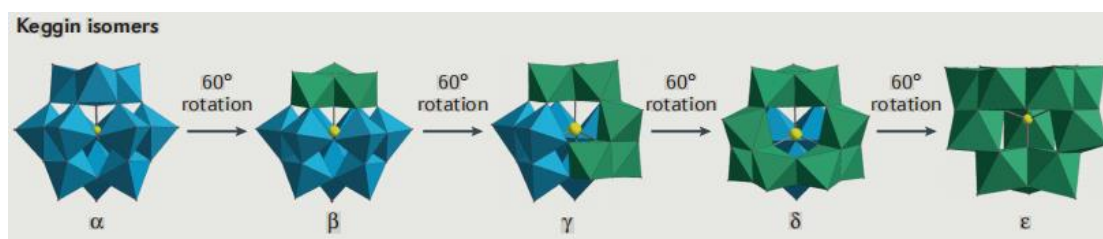
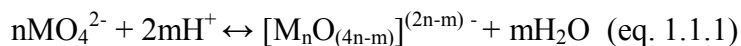


Figure 1.1.2 Keggin structure and its isomers.²³

1.1.1.2 Synthesis of polyoxometalates

The synthesis of most POMs is performed in several steps.²⁷ Raw materials are commercially cheap. The crucial step is to adjust the pH of solution because different values will lead to different products. For example, normal POM can be prepared in acidic condition, while the lacunary POMs (such as lacunary Keggin- or Dawson-type POMs) can be synthesized in alkaline solution.²⁸ The formation of POMs is based on a polycondensation between several oxometalate ions upon protonation with conventional inorganic acids (equation 1.1.1). Condensation of oxometallic groups can occur also around the heteroatom, yielding heteropolyanions (*vide supra*) (Figure 1.1.3).



During the synthesis, several parameters must be taken into account: 1) pH, 2) concentration/type of metal oxide anion, 3) ionic strength, 4) heteroatom type/concentration, 5) presence of additional ligands, 6) reducing agent, and 7) temperature of reaction and processing (e.g. microwave, hydrothermal, refluxing). Each POM is stable in a certain pH range where its proportion is maximum. The molecular ratio M/X is generally close to the stoichiometric ratio, but, in some cases, an excess of the heteroatom is necessary. For some metastable species a careful control of the temperature is necessary. In some cases, the stability is improved by addition to the aqueous solution of solvents such as ethanol, dioxane or acetonitrile. In hydrothermal methods, the pressure is a few bars, but this parameter is not very important.

As explained before, the counter cations impact the stability and solubility of POMs in solution. Except the common oxyacid salts (such as Na^+ , K^+ , Li^+ , NH_4^+ and Cs^+), organic cations also can be used. For example, alkylammonium (e.g. tetramethylammonium and tetrabutylammonium) salts are chosen to improve POMs' stability in organic solvents.²⁹ The kinetic or thermodynamic stability of final product strongly depends on the nature of the heteroatom and the alkaline cations present in the solution. During synthesis, the formation of complexes between the vacant heteropolyoxotungstates and the alkaline cations strongly depends on the size of the coordination site and the one of cations. Thus, these are the main factors controlling the stability. The role of cations is also to avoid parallel condensation or hydrolysis reaction.

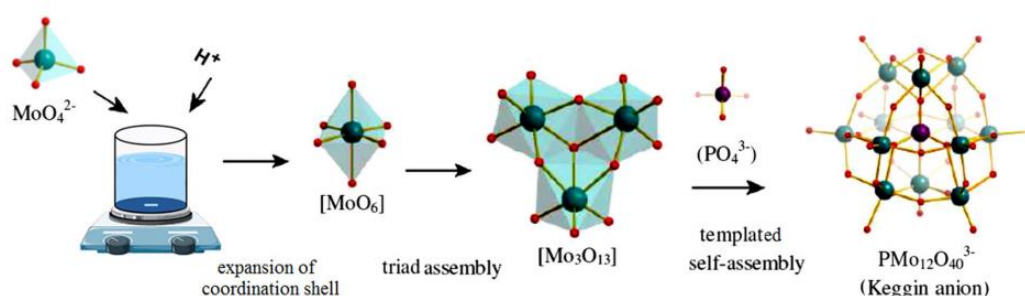


Figure 1.1.3 Schematic of self-assembly synthesis of $[\text{PMo}_{12}\text{O}_{40}]^{3-}$, a Keggin type POM. MoO_4^{2-} was used as a tetrahedral precursor which accepts two oxo ligands in acidic conditions and turns to MoO_6 intermediate. In the next step, Mo_3O_{13} subunits were constructed and finally in the presence of PO_4^{3-} , as a template, the assembly of the tetrahedral Keggin cluster was performed which led to $[\text{PMo}_{12}\text{O}_{40}]^{3-}$ construction. (C. Streb, Ph.D. Thesis, Glasgow University 2008.)

For the isolation of POMs in solid state, the choice of the suitable cation is essential and several trials are necessary. Different species are often present in the solution and isolation of the desired one is possible only if there are large differences in the solubility. If the acid form of the POM is stable, it can be isolated by extraction by etheroxide. Subsequently, the etheroxide is decomposed by addition of water. Finally, after removing the ether, the acid is recrystallized in water.³⁰

1.1.1.3 Redox behavior of polyoxometalates

Most Keggin-type and the Wells-Dawson-type POMs are redox active. Multi-electron transfers reversibly occur in multi-steps, yielding reduced species with a blue color in solution. Hence reduced POMs are called “heteropolyblue”. During voltammetric studies, POMs present a series of redox peaks.^{5a, 31} The redox behavior of Keggin-type POMs is highly acid-dependent.³² The potential of reduced POMs is more positive with higher Lewis acidity. The highly charged reduced forms are stronger Lewis bases than their oxidized form.^{5a, 31b, 33} The number of exchanged electrons in one wave can strongly depend on the potential. For example, the first reversible reduction ($2e^-$) potential of $[\text{SiMo}^{\text{VI}}_{12}\text{O}_{40}]^{4-}$ shifts to more negative potential with higher pH. The $2e^-$ wave can split into two $1e^-$ waves. At pH 2.4, there is a first wave corresponding to formation of $[\text{SiMo}^{\text{V}}\text{Mo}^{\text{VI}}_{11}\text{O}_{40}]^{5-}$, while at pH 9.5 and 13, there are the second and third wave for $[\text{SiMo}^{\text{V}}_2\text{Mo}^{\text{VI}}_{10}\text{O}_{40}]^{6-}$ and $[\text{SiMo}^{\text{V}}_3\text{Mo}^{\text{VI}}_9\text{O}_{40}]^{7-}$ respectively.³⁴ Dawson-type POMs have similar performance, however their process is more complex compared with Keggin-type POMs. For example, $[\text{S}_2\text{M}_{18}\text{O}_{62}]^{4-}$ can be reduced to $[\text{S}_2\text{M}_{18}\text{O}_{62}]^{10-}$ (M= Mo or W). There are 6 electrons transferred within six well-defined reversible one-electron-transfer processes.

The heteroatom is also influencing the redox potential. It has been shown that the apparent formal potential for one-electron redox reaction depend on the overall negative charge of the polyanion. This total charge is influenced by the heteroatom. For a higher total charge of the polyanion, the potential shifts to more negative values, as explained by the repulsion of charges.³⁵ In the case of polyanions bearing the same total charge, and protons not interfering in the electron transfer, the size of the heteroatom influences the redox potential as well. For example, within a given Keggin family, such as $[\text{XW}_{12}\text{O}_{40}]^{q-}$, where X = B, Al or Ga, the POM with the smaller atom (i.e. B) has the more negative redox potential. Density functional theory was used to compute the electrostatic potential created by each internal anionic unit in a fragment-like approach. They show that internal XO_4^{q-} units affect differently the tungstate oxide cage. Smaller atoms (with smaller atomic number) produce a more negative potential in the surroundings and thus a poorer capacity to accept electrons.^{35b}

Heteropolymolybdates $[\text{XMo}_{12}\text{O}_{40}]^{n-}$ are reduced more easily than heteropolytungstates $[\text{XW}_{12}\text{O}_{40}]^{n-}$. Mixed-addenda POMs can be formed by the substitution of one or more tungsten or molybdenum by another addenda ion like W, Mo or V. In the one-electron reduction, the electron is localized on the more reducible atom. For example, for $[\text{PW}^{\text{VI}}_{11}\text{V}^{\text{V}}\text{O}_{40}]^{4-}$ the electron will be accepted by vanadium, giving $[\text{PW}^{\text{VI}}_{11}\text{V}^{\text{IV}}\text{O}_{40}]^{5-}$, because the oxidizing ability follows the order: $\text{V(V)} > \text{Mo(VI)} > \text{W(VI)}$.^{32b}

1.1.2 Polyoxometalates applications

Polyoxometalates have been explored for their unique properties for 100 years. Nowadays, POMs are widely applied in magnetism, catalysis, gas absorption, photochemistry, biochemistry, and energy storage.³⁶ Herein, the use of POMs in photocatalysis and electrocatalysis is introduced briefly.

1.1.2.1 Photocatalytic properties of polyoxometalates

POMs have strong light absorption in UV range and they have been widely studied as photocatalysts for removal of organic and inorganic contaminants (Figure 1.1.4). POMs' photocatalytic behavior is similar to common semiconductors. Under the light irradiation, when the light energy is higher than or equal to the band gap energy between the highest occupied molecular orbital (HOMO) and lowest unoccupied molecular orbital (LUMO) of the polyanion, the charge is transferred from oxygen (or others) to the POMs' transition metal.³⁷ The photogenerated electrons and holes can work as electron donors and electron acceptors during the reaction, due to their strong photoreductive or photooxidative abilities.

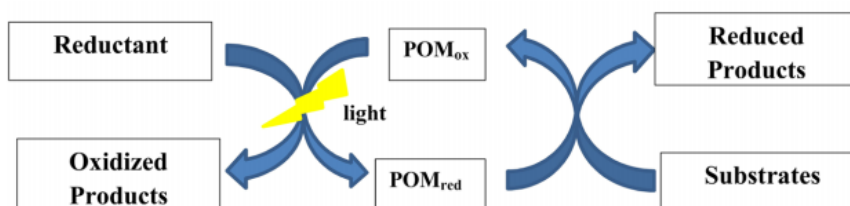


Figure 1.1.4 Homogeneous photocatalysis involving POMs.²⁷

POMs have demonstrated their photocatalytic ability in degradation of different organic pollutants such as dyes, phenol, chlorophenols, chloroacetic acids, and pesticides.³⁸ The solution pH and light intensity are the main experimental parameters. In the removal of organic molecules from wastewater, $[\text{Mn}_3(\text{H}_2\text{O})_3(\text{SbW}_9\text{O}_{33})_2]^{12-}$, synthesized by Yu et al., shows outstanding photocatalytic activity without Mn^{2+} and manganese oxide residual. Hori et al. applied $\text{H}_4[\text{SiW}_{12}\text{O}_{40}]$ to decompose bio-accumulative surfactants (such as hydro perfluoro carboxylic acids) by photocatalysis.³⁹ Keggin-type POMs have been compared for degradation of organic pollutants by Hu and Xu.⁴⁰ In water at pH 1.0 under UV light irradiation, the removal efficiency is decreasing as such: $\text{H}_3[\text{PW}_{12}\text{O}_{40}] > \text{H}_4[\text{SiW}_{12}\text{O}_{40}] > \text{H}_4[\text{GeW}_{12}\text{O}_{40}] > \text{H}_3[\text{PMo}_{12}\text{O}_{40}]$.

POMs only can work as photocatalyst under UV irradiation due to the high energy gap between the HOMO and LUMO orbitals. As a result, commonly available visible light can't be used as a light source, thus limiting POMs' performance.⁴¹ There are various methods to reduce the energy band gap. For example, doping POMs with dye molecules or coupling with other metal oxides. Keggin-type POM / metallic silver / titania ($\text{H}_3[\text{PW}_{12}\text{O}_{40}]/\text{Ag-TiO}_2$) can be activated in both UV and visible light irradiation, synthesized by the sol-gel hydrothermal method. Sulfamethoxazole, a typical pharmaceutical pollutant, can be removed by this photocatalyst under Xe lamp condition ($320 \text{ nm} < \lambda < 680 \text{ nm}$).⁴² Compared with Ag-TiO_2 , $\text{H}_3[\text{PW}_{12}\text{O}_{40}]/\text{Ag-TiO}_2$ has higher conversion of sulfamethoxazole. There is a synergy between POM and TiO_2 . The transfer of electrons from the Keggin-type POM to oxygen atoms also exist and improve the catalysis performance.⁴³

POMs are excellent photocatalysts, however their high solubility limits their reusability and separation from the reaction mixture.⁴¹ Therefore, the immobilization of POMs is widely studied. There are various supporting organic or inorganic materials, such as active carbon, functionalized polymers, resins and electrodes, which have been used for preventing POMs

from dissolution. Different methods include solidification by embedding in polymers, self-assembled surfactant-encapsulated POMs, layered double hydroxides and Langmuir-Blodgett films.⁴⁴

POMs are also able to reduce metal ions in a photocatalytic reaction. As early as 1952, Chalkley had tried to use one-electron-reduced Keggin tungstophosphate, $[\text{PW}_{12}\text{O}_{40}]^{4-}$, to reduce silver ions to metallic silver.⁴⁵ In 2002, mono-reduced Keggin-type POM $[\text{PW}_{12}\text{O}_{40}]^{4-}$ and $[\text{SiW}_{12}\text{O}_{40}]^{5-}$ were firstly used for the photocatalytic reduction of Ag, Au, Pt and Pd metal ions to nanoparticles by Papaconstantinou and his co-workers. The formation of metal nanoparticles can be followed by UV-visible spectroscopy (Figure 1.1.5). During the reduction, propan-2-ol or 2,4-dichlorophenol are the sacrificial electrons donors. POMs also stabilize the formed nanoparticles.⁴⁶

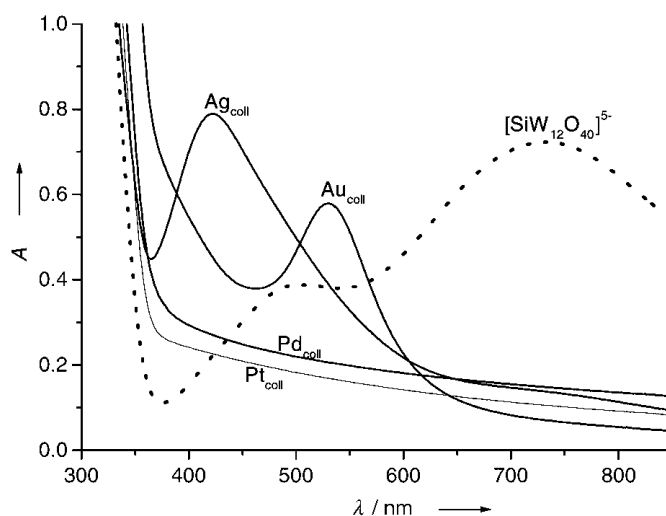
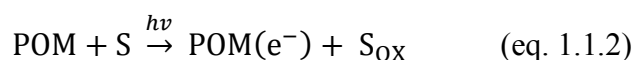


Figure 1.1.5 UV absorption spectra of metal nanoparticles (Ag, Au, Pd, Pt) in colloidal solution, obtained after thermal reaction of photogenerated $[\text{SiW}_{12}\text{O}_{40}]^{5-}$ (about 0.35 mM), with the corresponding metal ions (Ag^+ , Pd^{2+} , $[\text{Pt}^{\text{IV}}\text{Cl}_6]^{2-}$ (0.1 mM) or $[\text{Au}^{\text{III}}\text{Cl}_4]^-$ (1 mM)).⁴⁶

The mechanism of the photocatalytic reduction includes two steps: a) light excited POM oxidizes the organic (electrons donor) to form reduced POM (equation 1.1.2); b) reduced POM are reoxidized by metal ions (equation 1.1.3).⁴⁷



During the reaction, if the ionic strength is low, the reduced metal appears as nanoparticles evenly distributed and forming a colloidal solution (equation 1.1.4). In this process, POMs serve both as photocatalysts-reducing reagents and stabilizers.



Photocatalytic reduction of Ag^+ by the Dawson-type POM $\alpha\text{-}[\text{P}_2\text{W}_{18}\text{O}_{62}]^{6-}$ was reported by Isabelle Lampre and Laurent Ruhlmann team.⁴⁸ It has been proposed that a new reaction mechanism for the photocatalytic reduction of silver ions to form nanoparticles in the presence of photoreduced POMs. In fact, the direct reaction is not thermodynamically possible because the potential of Ag^+/Ag^0 couple is -1.75 V vs. NHE, a much lower value than

any redox potential of reduced POMs. But, the potential of clusters of silver containing a reduced number of atoms is rather positive $\text{Ag}_n^+/\text{Ag}_n^0$ 0.4 V vs. NHE. Thus, it was suggested that reduction process can be initiated by the alcohol radical produced during illumination (step 1 and 2 in Figure 1.1.6). Association and coalescence reactions of the Ag^+ ions and initial silver clusters (step 3) lead then to the formation of silver particles. When the clusters become sufficient large, their redox potential is also higher and thus, their reduction by the photoreduced POMs is possible (step 4). Moreover, the charge and size of the polyoxometalate have an influence on the size and stability of the formed silver particles, and the structure of POMs also affects the kinetics of the reduction processes.

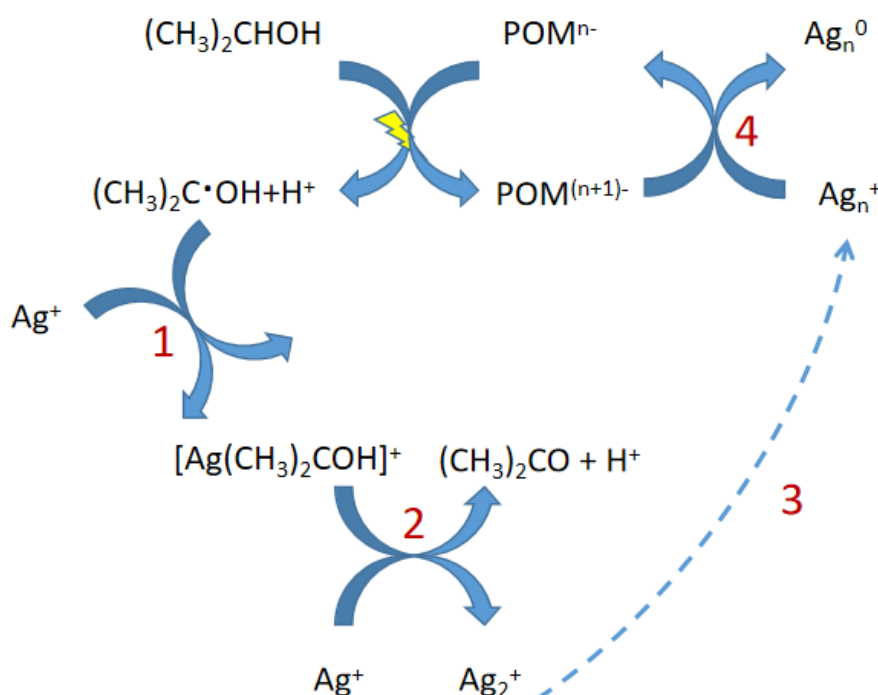


Figure 1.1.6. Proposed mechanism for the photoreduction of silver ions to produce silver nanoparticles in the presence of photoreduced POMs.

1.1.2.2 Electrocatalytic properties of polyoxometalates

POMs have excellent redox activity. Both the reduced and oxidized state are stable and undergo multiple reversible electron transfer without decomposition.^{32b} Furthermore, this ability can be finely tuned by changing the structure or composition. For example, POMs can be modified by redox-active metals to obtain effective POM-based electrocatalysts.^{32b}. Herein we describe some examples about the use of POMs as catalysts for HER, OER, ORR. Nitrite electroreduction will be discussed in chapter 1.4 “Electrochemical reduction of NO_x species”.

Hydrogen evolution reaction (HER)

In 1985, Keita and Nadjo reported the first POM-based electrocatalyst for HER, i.e. $[\text{SiW}_{12}\text{O}_{40}]^{4-}$,⁴⁹ but the efficiency is debatable due to the presence of trace amounts of Pt from

anodic dissolution.^{32b, 50} Lacunary $[\text{SiW}_{11}\text{O}_{39}]^{8-}$ (abbreviated SiW_{11}), parent $[\text{SiW}_{12}\text{O}_{40}]^{4-}$, and $[\text{P}_2\text{W}_{18}\text{O}_{62}]^{6-}$ POMs with extremely low Pt loadings were prepared as active HER electrodes by Zhang et al. In comparison to the electrode without POM, the mixed electrode has better HER performance and stability.⁵⁰ Metal substituted POMs, such as Ru-substituted⁵¹ and Co-substituted⁵² were also explored. Pd^0 nanostructures encapsulated POMs are reported in 2010.⁵³ Metal organic frameworks (MOF) were also used in conjunction with POMs. Qin et al and Nohra et al. used the POM ϵ - $[\text{PMo}^{\text{V}}_8\text{Mo}^{\text{VI}}_4\text{O}_{40}\text{Zn}_4]$ (Zn- ϵ -Keggin unit) to prepare different novel POM@MOFs with high electroactivity for HER.⁵⁴

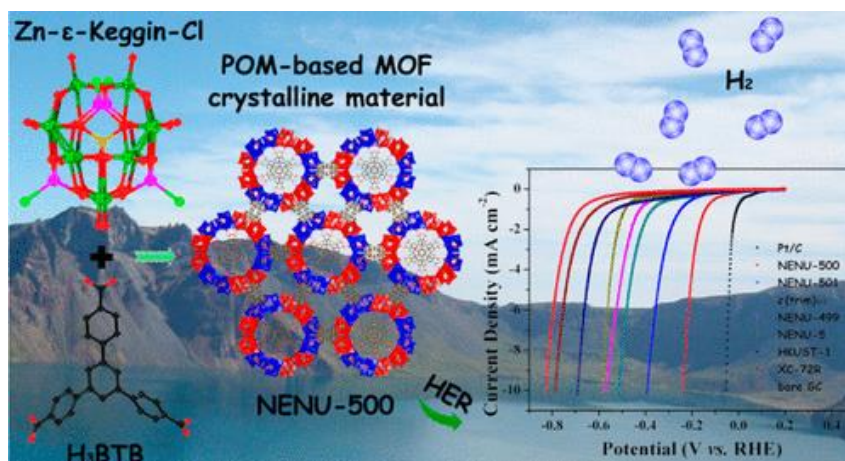


Figure 1.1.7 Polyoxometalate (POM)-based metal–organic frameworks (MOFs) ϵ - $[\text{PMo}^{\text{V}}_8\text{Mo}^{\text{VI}}_4\text{O}_{40}\text{Zn}_4]$ (Zn- ϵ -Keggin unit) were employed as electrocatalysts for the hydrogen evolution reaction (HER) owing to the combination of the redox activity of a POM unit and the porosity of a MOF.^{54a}

Carbon nanomaterials were also applied to tune the HER activity for the Preyssler-type POM $\text{K}_{12.5}\text{Na}_{1.5}[\text{NaP}_5\text{W}_{30}\text{O}_{110}]$ ⁵⁵ and Keggin-type POM $[\text{PW}_{11}\text{MO}_{39}]^{5-}$ (M: Co, Ni,⁵⁶ and/or Cu)⁵⁷.

Oxygen evolution reaction (OER):

In 2004, Howells et al reported the first POM-based OER electrocatalyst i.e. $[\text{Ru}^{\text{III}}_2\text{Zn}_2(\text{H}_2\text{O})_2(\text{ZnW}_9\text{O}_{34})_2]$. In 2008, it was shown that the hydrolytically stable complex $[\text{Ru}_4\text{O}_4(\text{OH})_2(\text{H}_2\text{O})_4](\gamma\text{-SiW}_{10}\text{O}_{36})_2]^{10-}$ (Figure 1.1.8a) displays a good catalytic activity for the rapid oxidation of H_2O to O_2 in aqueous solution at pH 7.⁵⁸ The tetra-Co-substituted $[\text{Co}_4(\text{H}_2\text{O})_2(\text{PW}_9\text{O}_{34})_2]^{10-}$ (abbreviated $\text{Co}_4\text{-POM}$) was tested as OER electrocatalyst by Stracke and Finke.⁵⁹ During the reaction, unexpected CoO_x compound could be formed because of decomposition of $\text{Co}_4\text{-POM}$. CoO_x is also an electrocatalyst for OER and it is difficult to distinguish which one is a dominant catalyst. In a 2013 study by Hill and co-workers, additional evidence is provided to show that Co_4POM (Figure 1.1.8b) is the active water-oxidizing complex (WOC) in the presence of $\text{Ru}(\text{III})(\text{bpy})_3^{3+}$.⁶⁰ Another interesting cobalt polyoxometalate system is $[\text{Co}_9(\text{H}_2\text{O})_6(\text{OH})_3(\text{HPO}_4)_2(\text{PW}_9\text{O}_{34})_3]^{16-}$ (Co_9POM , Figure 1.1.8c) since it is a trimeric analogue of the Co_4POM dimer. In a study by Galan-Mascaro and co-workers, bulk electrolysis of the Co_9POM at 1.41 V vs. NHE resulted in the formation of a catalytic film on the electrode in pH 7 sodium phosphate buffer.⁶¹ Due to the observed instability of the Co_9POM under oxidizing conditions and the similar onset potential for the catalytic current, it is also possible that the Co_9POM is simply being converted into a

transiently stable CoO_x catalyst. Controls with authentic CoO_x are needed to rule out, or support, this possibility.

Relatively robust polydentate POM ligands are used to stabilize transition metal oxide clusters for OER. Thus, Co and Ru substituted POMs were reported as catalysts for OER, with various carbon nanomaterials as supports.⁶²

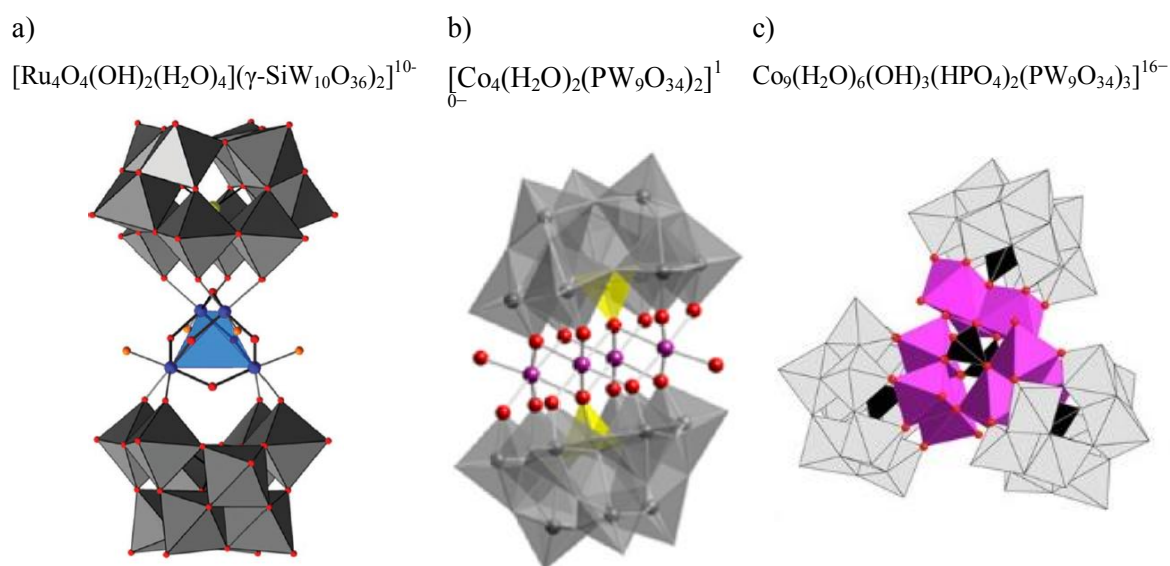


Figure 1.1.8 a) Ball-and-stick representation highlighting the $[\text{Ru}_4(\mu\text{-O})_4(\mu\text{-OH})_2(\text{H}_2\text{O})_4]^{6+}$ core (Ru blue, m-O red, O (H₂) orange; hydrogen atoms omitted for clarity) and the slightly distorted $[\text{Ru}_4]$ tetrahedron (transparent blue). The polytungstate fragments are shown as gray polyhedra, and Si as yellow spheres; b) Ball-and-stick representation of $[\text{Co}_4(\text{H}_2\text{O})_2(\text{PW}_9\text{O}_{34})_2]^{1-}$: Co pink, O red, polytungstate fragments are shown as gray polyhedra, and P as yellow tetrahedra, hydrogen atoms omitted for clarity; c) Ball-and-stick representation of $\text{Co}_9(\text{H}_2\text{O})_6(\text{OH})_3(\text{HPO}_4)_2(\text{PW}_9\text{O}_{34})_3]^{16-}$: Co pink, O red, polytungstate fragments are shown as gray polyhedral.

Oxygen reduction reaction (ORR)

In 1997, Dawson-type POM $[\text{P}_2\text{W}_{18}\text{O}_{62}]^{6-}$ was immobilized on graphite electrode and used for the first time as ORR catalyst.⁶³ Same as for HER and OER, transition metal substituted POMs are used for ORR. A series of transition-metal-substituted Wells–Dawson ($[\text{P}_2\text{W}_{17}\text{M}^n\text{O}_{62}]^{(12-n)-}$; $\text{M} = \text{W}^{\text{VI}}, \text{Fe}^{\text{II}}, \text{Co}^{\text{II}}, \text{Ru}^{\text{II}}$) and Keggin ($[\text{PW}_{12}\text{O}_{40}]^{3-}$ and $[\text{PCo}^{\text{II}}(\text{H}_2\text{O})\text{W}_{11}\text{O}_{39}]^{5-}$) anions were tested as co-catalysts with Au, Pd, and Pt electrodes.⁶⁴ Nobel metal nanoparticles, such as Pt⁶⁵, Pd⁶⁶, and Au⁶⁷ were also combined with various POMs such as, $[\text{PW}_{12}\text{O}_{40}]^{3-}$, $[\text{PMo}_{12}\text{O}_{40}]^{3-}$, $[\text{P}_2\text{Co}(\text{H}_2\text{O})\text{W}_{17}\text{O}_{61}]^{8-}$ and the wheel-shaped $\text{V}^{\text{V}}\text{--}\text{V}^{\text{IV}}$ mixed-valence tungstovanadate $[\text{P}_8\text{W}_{48}\text{O}_{184}(\text{V}_4^{\text{V}}\text{V}_2^{\text{IV}}\text{O}_{12}(\text{H}_2\text{O})_2)_2]^{32-}$.⁶⁸ Furthermore, liquid-catalyst fuel cells (LCFC) reported that POM in solution is the electrocatalyst.⁶⁹

1.2 Differential Electrochemical Mass Spectroscopy (DEMS)

1.2.1 DEMS experimental setup

Compared with the Electrochemical Mass Spectroscopy (EMS) invented by Bruckenstein⁷⁰ in the early seventies, the vacuum system was improved by Wolter and Heitbaum at 1984 by the introduction of a differential pumping setup. As a result, the time constant is decreased and on-line detection of volatile products is possible.⁷¹ The technique is named Differential Electrochemical Mass Spectroscopy (DEMS). Nowadays, DEMS is a mature technology which can measure gaseous and volatile products of electrochemical reactions quantitatively and sensitively. The main parts of DEMS equipment are the electrochemical cell, the membrane inlet system (that separates the liquid phase from the vacuum) and the mass spectrometer.

1.2.1.1 The electrochemical cell

The electrochemical cell normally consists of working, counter and reference electrodes, and the cell is always divided into anode chamber and cathode chamber to avoid possible contamination from counter reaction. Working electrode chamber has a specific design to match the membrane inlet system. For a fast transfer of a species from the working electrode surface to the membrane, the distance shouldn't be too long. The variety of setups is based on this criterion. The conventional cell has the electrocatalyst layer, e.g. Pt, sputtered onto the membrane (Figure 1.2.1a). While the time constant is the theoretically the lowest, the mechanical stability is not so good. If the thickness of the membrane or of the electrode is increased, the time constant is increased as well. The second disadvantage is the limitation to use only those metals that can be sputtered on the membrane.

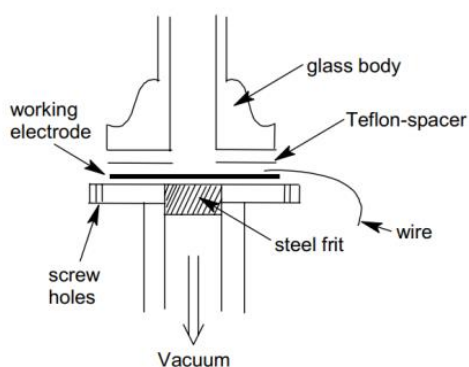
The use of DEMS for an increasing number of electrochemical reactions has stimulated the development of different experimental setups. One of the main changes is the position of the working electrode that is no longer attached to the membrane. This has paved the way to coupling DEMS with other techniques. The working electrode is either placed in the same compartment with the membrane ("thin-layer cell") or placed in different compartments, this last setup being called "dual thin-layer cell".

The use of thin-layer cell has allowed the use of single crystals electrodes in a hanging meniscus configuration⁷² and even the use of a rotating disc electrode.⁷³ The dual thin-layer was used to combine DEMS and electrochemical quartz crystal microbalance (EQCM) to measure volatile products and deposited (or dissolved) species simultaneously (Figure 1.2.1b).⁷⁴ A coupling with in-situ FT-IR analysis was also shown.⁷⁵ The electrolyte flow rate, the volume of compartments and electrode and membrane surfaces are optimized to reduce the residence time and increase the time constant.

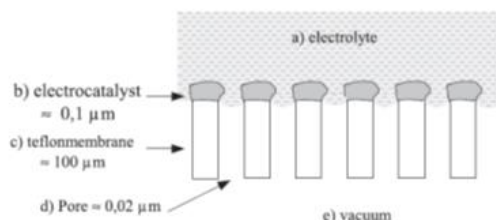
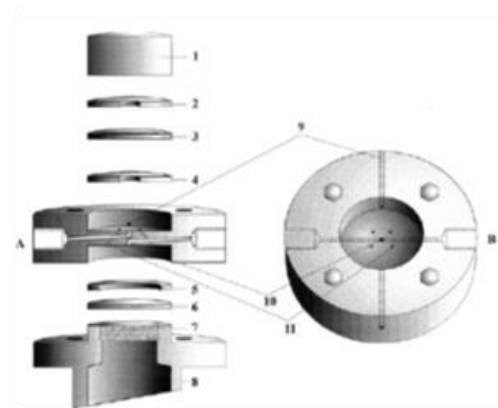
In some particular cell designs, the amounts of volatile species are very low and, thus, differential pumping is not necessary. The technique is called Online Electrochemical Mass

Spectrometry (OLEMS) but the results are very similar to DEMS and sometimes confusion between the techniques is possible. In OLEMS, a PTFE capillary covered with a PTFE membrane is used as inlet to mass spectrometer (Figure 1.2.1c). In most of cases, the capillary is placed at a small distance from the working electrode. In a particular design, the capillary was placed inside the glassy carbon electrode, through a hole in the middle. The catalytic ink was placed on the electrode and membrane.⁷⁶

a)

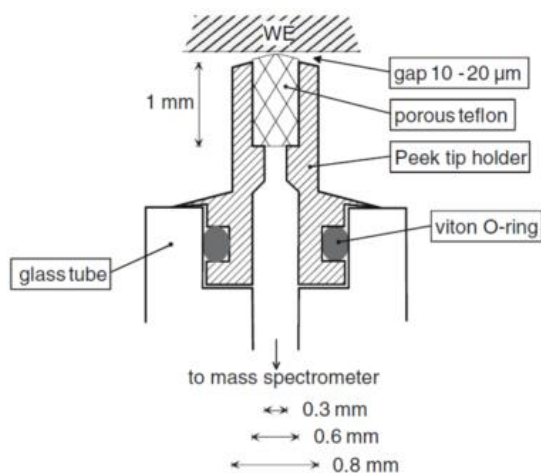


b)



DEMS/EQCM assembly: (1) Kel-F support; (2) Kalrex gasket; (3) quartz crystal; (4, 5) Teflon gaskets; (6) porous Teflon membrane; (7) stain-less steel frit; (8) stainless steel connection to MS; (9) capillaries for contact wires; (10) inlet-outlet capillaries; (11) connecting capillaries. (A) side view of Kel-F body of the cell; (B) top view of the cell.

c)



d)

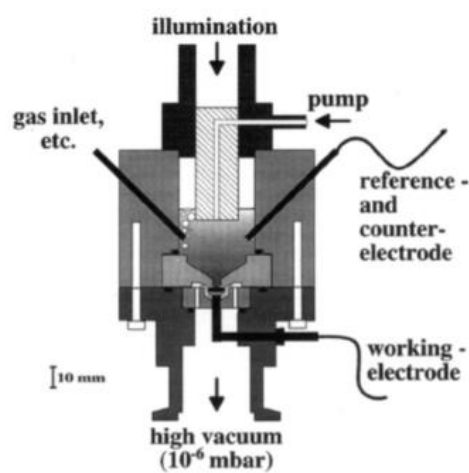


Figure 1.2.1 a) The conventional cell for DEMS⁷⁷; b) DEMS-EQCM coupling⁷⁴; c) OLEMS setup⁷⁶; d) Photoelectrochemical DEMS.⁷⁸

Study of photoelectrochemical reactions with DEMS is possible but examples are scarce. In early 1993, the group of Bogdanoff described a cell design in which TiO₂ is sputtered on the Teflon membrane and illumination is brought from the top of the cell.⁷⁹ Later, the group has developed a cell in which massive electrodes can be used (Figure 1.2.1d).⁷⁸

1.2.1.2 The membrane inlet system

One of the first membrane inlet setup is described in Figure 1.2.2. The first joint (1) of the glass body is connected to the ionization chamber of the mass spectrometer. The second joint (2) is connected to the electrochemical cell. On the top of the glass body, there is a glass frit (B) which has to withstand the atmospheric pressure. The thin porous teflon membrane (C) is tightened onto the glass frit. A teflon shrinking tube (D) keeps the membrane tight. On the membrane the catalyst layer (E) with connecting wire (F) is deposited.⁸⁰

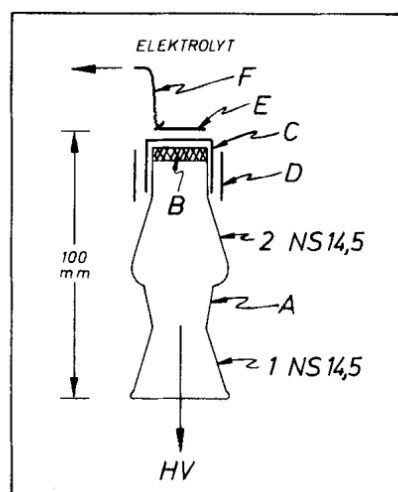


Figure 1.2.2 A conventional membrane inlet system⁸⁰

Nowadays, a variety of designs exists. Nevertheless, the Teflon membrane is still irreplaceable. The characteristics of the membrane must be selected in order to keep a certain vapor pressure of the electrode in the primary vacuum chamber. Therefore, the contact angle of water on Teflon, the surface tension of water, the pore size, porosity and pumping speed are used for calculating a maximum acceptable surface of the membrane. Thus, a typical Teflon membrane is 75 μm thick, it has a nominal pore width of 20 nm with a porosity of 50% and a surface of 0.5 cm^2 .⁷⁷ In this case, the membrane meets the following requirements:

- i) high mechanical strength (it withstands the difference in the pressure between electrolyte (about 1000 mbar) and the vacuum ($< 10^{-4}$ mbar))
- ii) hydrophobicity (to avoid leaking of electrolyte)
- iii) porosity (to allow a good sensitivity)
- iv) permeability (to allow a fast flow of molecules and avoid time consuming diffusion resistance)

Non-porous membranes can prevent water reaching the vacuum, however the response time is usually more than 10 s. Recently, the surface of the membrane was considerably reduced using a pin-hole inlet. The pin-hole (several micrometers in diameter) is covered with a Teflon membrane and brought about few micrometers distance of the center surface of the electrode. In this manner, a high signal-to-noise ratio of the DEMS signals is achieved. The setup was used for the study of electroreduction of acetylene on platinum single crystals. It was shown that Pt (110) has a higher activity than Pt (111) and Pt (100).⁸¹ The disadvantage of this inlet is the risk to sample products from a larger volume than the small cylindrical

volume between the pin-hole and the electrode surface. The planar diffusion of product away from the electrode is superposed with the spherical diffusion to the pin-hole head. This leads to larger response time.

1.2.1.3 The mass spectrometer

A scheme of a typical mass spectrometer of a DEMS setup is difficult to illustrate here because of the large variety of home-made systems. Nevertheless, some common observations and recommendations can be made.⁷⁷

i) The time constant should be low. This is calculated based on the volume of the ionization chamber and the pumping speed. For example, with a volume of 1 L and a pumping speed of 200 L/s, a value of 5 ms is obtained.

ii) The pressure of the analyzer chamber must be lower than 10^{-5} mbar. A turbomolecular pump at 50 L/s is sufficient.

iii) Two pumping stages can be defined by the use of a rotary pump that sets the pressure at about 10^{-2} mbar and followed by the turbomolecular pump. In this configuration, the ionization source is placed in a chamber with a much lower volume, so that the time constant is kept low.

iv) The condensation of some species in the gas inlet should be avoided by supplying heat to this inlet.⁸² The vacuum chambers should be free of any compound related to the reaction participant. Flushing the chambers with argon before the experiments can remove some contaminants.

v) Any change in the incoming flow of species should be quickly detected.

vi) The ionization chamber should accept a high partial pressure from H₂O. Despite the hydrophobic character, there is still a large amount of electrolyte evaporating and going through the membrane.

1.2.2 DEMS applications

DEMS is still mainly used only in research laboratories due to the lack of commercially available setup (very recently, Hiden Analytical (England) and SpectroInlets (Denmark) started to commercialize DEMS setups). DEMS is an effective tool for studying heterogeneous catalysis in liquid phase. Electrochemical reactants, products and volatile intermediates can be detected quantitatively after external calibration. The faradic efficiency of different products is obtained in real-time. In comparison to gas chromatography, DEMS is faster and more sensitive. When single crystal electrodes are used, DEMS results can be obtained before their deterioration by contaminants. Combining Cyclic Voltammetry and DEMS, the so-called Mass Spectroscopic Cyclic Voltammograms (MSCV) are recorded. A direct relation between the electrode potential and the presence of a volatile species is obtained. Other electrochemical techniques, such as chronoamperometry can be used. Herein we briefly give some examples about DEMS utilization for detection of carbonaceous species and nitrogen-based species.

1.2.2.1 DEMS detection of carbonaceous species

Multiple carbon species can be detected in a DEMS setup. Nevertheless, the detection of some molecular fragments is not always possible due to fragments of water molecule, i.e. $m/z = 18, 17, 16$ corresponding to fragmentation ions H_2O^+ , OH^+ and O^+ respectively. These fragments establish a high baseline of DEMS signal as water is the molecule in the highest concentration, thus decreasing the sensitive towards fragments of same m/z but coming from another molecule. For example, detection of CH_4 would require monitoring the fragment $m/z=16$. This is easily replaced by fragment CH_3^+ , $m/z=15$, that has a 90% relative intensity compared to the molecular fragment. The inconvenient is the possibility to obtain this fragment from other molecules, such as ethane, methanol and ethanol. Thus, an external technique, such as gas chromatography, is required to establish the exact sources of this fragment. Another example is the possibility to directly detect CO issued from an electrochemical reaction in the presence of CO_2 . In fact, fragmentation of CO_2 inside the ionization chamber creates CO^+ with 10% of relative intensity. While this value seems low, the concentration of dissolved CO_2 in bicarbonate solution is 34 mM and, thus, the generated background signal of CO^+ is finally quite high. A recent publication proposes to reduce the eV (voltage) of the ionization filament in order to considerably reduce the fragmentation of CO_2 .⁸³

The use of DEMS for study the electroreduction of CO_2 goes back to 1992, when M. Fujihira and T. Noguchi analyzed H_2 and CO products using a stationary gas permeable Au electrode.⁸⁴ Since then, many examples of the use of DEMS for understanding the mechanism of CO_2 reduction have been published.⁸⁵ A remarkable work is done by the group of M.T. Koper in which experimental results supports the pH dependent mechanism with the formation of methane mainly on Cu (111) and a carbon monoxide dimer on Cu (100).⁸⁶ The increasing popularity of DEMS has pushed mass spectrometer suppliers to commercialize an electrochemical cell specially designed for CO_2 reduction by the group of A. Bell.⁸⁷ Nevertheless, the authors thoroughly explain why ethanol and propanol DEMS signals cannot be deconvoluted (mainly due the presence of similar main fragments and low values for secondary fragments) without the use of an external detection by liquid chromatography.

DEMS studies have helped understanding the mechanism of other electrochemical reactions such as: methanol oxidation⁸⁸, ethanol oxidation⁸⁹, CO oxidation⁹⁰ and electrodesorption of organic molecules (biphenyl and cyclohexylbenzene)⁹¹.

1.2.2.2 DEMS detection of nitrogen-based species

Nitrogen atom is contained by abundant volatile compounds: NO_2 , NO , N_2O , N_2 , N_2H_4 , NH_3 and so on. Most of these compounds are easily detected with DEMS and a large number of related research articles are published. The subjects are related to NO_3^- ⁹² and NO_2^- reduction⁹³, N_2 reduction (NRR), NH_3 and N_3^- oxidation⁹⁴. Some general remarks should be taken into account.

Atmospheric nitrogen can induce a high background signal that could lower the sensitivity of detection for N_2 issued from the electrochemical reaction. The use of isotope compounds is thus very important. For example, the use of $^{15}\text{N}_2$ is indispensable for rigorous study of ammonia production from NRR because ammonia can be found in air, ion-conducting membrane and human breath. Moreover, nitrates, nitrites, amines, nitrogen oxides can be found in the feed gas stream and the catalysts itself.⁹⁵ The use of isotope allows an unambiguous proof for the fixation of molecular nitrogen.

Another issue is the similarity of m/z fragments between N_2O and CO_2 (44), both having m/z equal to 44. Thus, atmospheric CO_2 could induce a high background signal that could lower the sensitivity of detection for N_2O . The use of ^{15}N in NO_2^- or NO_3^- eliminates this interference as the product $^{15}\text{N}_2\text{O}$ has now an $m/z=46$ fragment. Moreover, if molecular nitrogen is formed, this will be in the form of $^{15}\text{N}_2$ and thus easily distinguishable from atmospheric $^{14}\text{N}_2$. On the other hand, if ammonia is detected by DEMS the use of ^{15}N leads to $^{15}\text{NH}_3$ that has the same $m/z=18$ fragment as water, so this molecular fragment cannot be used. Other fragments such as ^{15}N or ^{15}NH are still available but their fragmentation relative intensity is below 10%, thus the sensitivity is drastically reduced.

Nevertheless, the use of ^{15}N isotope in nitrogen-based species is very recent and a lot of earlier works used classical ^{14}N . Having a good DEMS experimental setup is the key for being able to monitor the formation of $^{14}\text{N}_2$, $^{14}\text{N}_2\text{O}$ besides ^{14}NO and $^{14}\text{NO}_2$. In this sense, the team of M.T. Koper team published a lot of articles on detection of nitrogen species electroreduction using OLEMS.⁹⁶ Figure 1.2.3, shows a typical Mass Spectroscopic Cyclic Voltammetry (MSCV) for nitrogen-based species.⁹⁷ More details about DEMS analysis of nitrate and nitrite electroreduction at different metal electrodes will be discussed in detail in chapter 1.4.

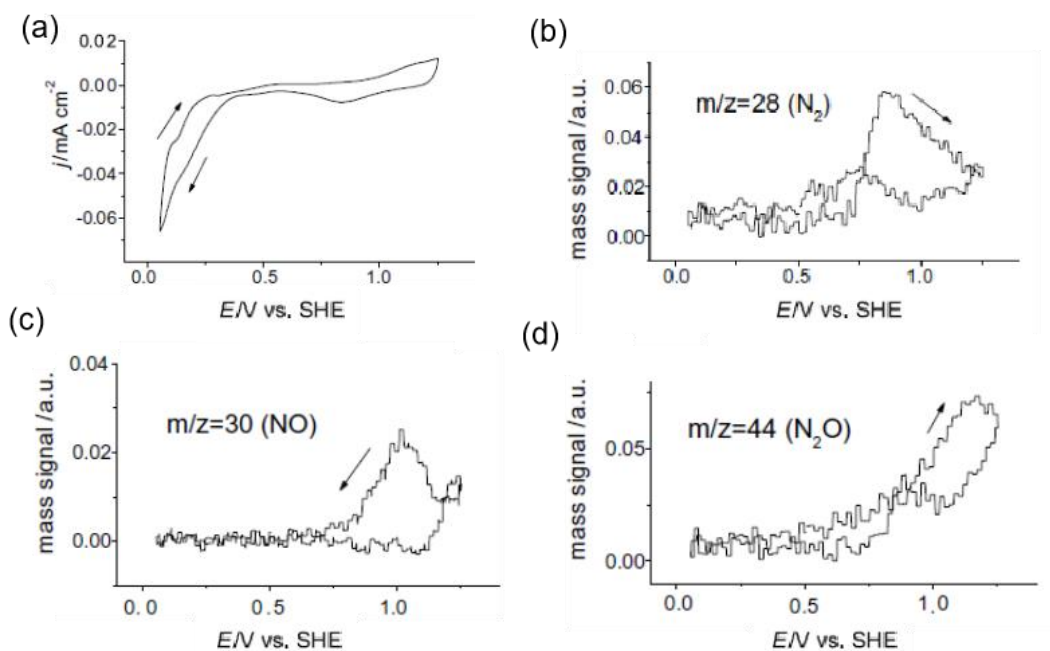


Figure 1.2.3 DEMS measurements of 2.7 M HNO_3 in 0.5 M H_2SO_4 . (a) Cyclic voltammetry at scan rate of 10 mV/s using a platinized electrode. DEMS signal of: N_2 $m/z = 28$ (b), NO $m/z = 30$ (c) and N_2O $m/z = 44$ (d).^{97a}

1.3 NO_2^- and NO_3^- : environmental pollutants and removal strategies

1.3.1 Nitrite (nitrate) pollution in water resources

The global freshwater content only accounts for 2.5% of the total water reserves, and the directly available one only accounts for 0.125%. At present, human activities have consumed 54% the total available freshwater resources and have caused groundwater pollution.⁹⁸ There is a variety of pollutants from industry and agriculture sewage and, as a result, the excess nitrogen will enter the water as nitrates, nitrites, amines, etc.⁹⁹ The pollution of nitrogenous compounds in water has become increasingly serious worldwide. For example, in United Kingdom and the United States, the concentration of groundwater nitrate is normally between 9.0-11.3 mg/L while in some seriously polluted area the concentration is 10 times higher than the WHO (world health organization) regulation (10.0 mg/L).¹⁰⁰ In France, the nitrate content in groundwater around Paris reaches 180.0 mg/L, which is not an underestimated problem.¹⁰¹

1.3.1.1 Sources of nitrite (nitrate) in water

a. Pollution caused by infiltration of domestic sewage and garbage

Urban domestic sewage and feces are an important source of groundwater pollution. In cities, underground water wells and septic tanks are used to discharge feces and domestic sewage. Sewage is decomposed by microorganisms in the soil to produce amino acids, which are ammoniated to produce ammonia, and then converted into nitrite in the presence of nitrifying bacteria, which infiltrate into the ground, causing pollution of soil, shallow underground water and deep water.

b. Pollution caused by nitrogenous fertilizers

The nitrogen content of groundwater increases year by year where nitrogen fertilizer is used for a long time. For example, according to a survey, nitrate and nitrite content in the groundwater continues to rise with 1.25 mg/L per year in China Beijing area, and the pollution area has exceeded 3000 km².¹⁰² Moreover, according to statistics, 55% to 60% of the nitrogen flowing into rivers and lakes comes from fertilizers.

c. Pollution caused by industrial wastewater

A large amount of organic wastewater and waste residue are released from paper, leather, and food modern industry. Some organic wastewater can flow into the ground through seepage wells and septic tanks, pollute the groundwater, and provide the necessary material for the synthesis of nitrite. Other mechanical and chemical industries also use a lot of nitrite-related raw materials every year. More than half of them finally get lost into the environment such as rivers, lakes, soil, atmosphere and groundwater.

d. Pollution from deposition of atmospheric nitrogen oxides

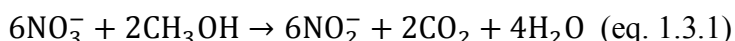
Nitrogen oxides can arise from combustion of coal, oil, natural gas, etc. Then, these compounds are released into the atmosphere. During photochemical processes, a part of nitrogen oxides is transformed into nitrite and nitrate. Oxidation reactions of nitrogen in the air are widespread. Under the action of lightning, oxygen and nitrogen in the air are combined to form nitrogen oxide compounds. Such compounds are dissolved after rain and are further oxidized to nitrate and nitrite. These substances settle down or fall to the ground surface, lakes, rivers, etc. with the rain. Finally, they enter into the groundwater. Generally, nitrate in rainfall does not exceed 0.2 ppm. Rainwater usually contains more ammonia, which pollutes water. According to Davey's research¹⁰³, only 2.5% of total nitrogen in drinking water comes from rainwater, but this proportion becomes larger and larger with social and economic development.

e. Pollution caused by improper usage of chloramine

Chloramine is used for the disinfection in the water delivery system. If improperly used, the concentration of nitrite in drinking water could exceed the critical accepted value.

f. Pollution from nitrate transformation

Under the condition of anaerobic environment, nitrate ions in water are converted into nitrite ions by the denitrifying bacteria. In this process, denitrifying bacteria use various organic substrates as electrons donor (equation 1.3.1, with methanol as carbon source).



Nitrification is the process of converting ammonium nitrogen into nitrate and nitrite under aerobic conditions. Nitrobacteria use CO_2 to oxidize ammonia to nitrite and obtain energy at the same time. This reaction can be inhibited by organic matter and promoted by ammonium salts and carbonates.

1.3.1.2 Hazards of nitrite (nitrate)

As a natural component of nitrogen cycle in ecosystems, nitrite is widely present in natural water. It has been extensively recognized that nitrite can cause direct or indirect harm to humans, animals and plants. Drinking water containing high concentration of nitrite is one of the main causes of methemoglobinemia (lack of oxygen in the tissue when hemoglobin (Fe^{2+}) is oxidized to methemoglobin (Fe^{3+}) by nitrites). Long-term ingestion can even lead to an increase in risk of liver and gastric cancer.¹⁰⁴ Excessive nitrate concentrations are also toxic to human health. Nitrate itself has no direct harm to the human body, but after it enters inside through various ways, it is converted into nitrite. Nitrite is toxic to the human body, and its harmfulness is about ten times higher than that of nitrate ions.¹⁰⁵ Figure 1.3.1 shows a schematic diagram of the transformation of nitrite and nitrate in the body.

In adult blood, there are some reductase enzymes that can reduce methemoglobin to hemoglobin. Therefore, methemoglobin's concentration can be controlled under 1% or less which doesn't affect the normal function of the human body. However, infants lack the reductase. Especially, infants under 4 months are very sensitive to the nitrite, so it is easy to

generate high concentrations of methemoglobin in their blood. When the methemoglobin concentration is higher than 1%, the infant will have blue baby disease, which can lead to mental retardation and even death.¹⁰⁶ At the same time, pregnant women, the elderly and the vulnerable are susceptible population.

Nitrite in water is not only harmful to humans, but also harmful to livestock, crops, fish, and aquatic organisms. When animals eat high-concentration nitrite-nitrogen feed or fish, they are exposed to several diseases and even death. If crops absorb the nitrogen from irrigation with high nitrogen content sewage water, the quality of amino acids and proteins in the grain is decreased. If nitrite and nitrogen content in the water continues to accumulate it results in eutrophication of the water, causing the algae and plankton to multiply. Hence, there is a large consumption of dissolved oxygen that deteriorates the ecological environment of the water and causes fish and other aquatic organism death.

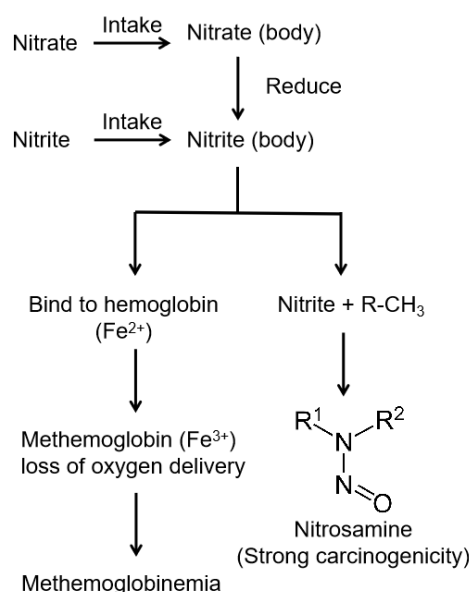


Figure 1.3.1 Schematic diagram of the transformation of nitrate and nitrous acid in the human body.

1.3.2 Methods for nitrite (nitrate) removal

The removal methods of nitrite mainly include physical methods, biological methods and chemical methods. They will be briefly described and compared in the following part.¹⁰⁷

1.3.2.1 Physical methods for nitrite (nitrate) removal

Physical methods are divided into stripping, ion exchange, reverse osmosis and electrodialysis.¹⁰⁸

a. Stripping

The stripping method consists in adjusting the wastewater pH to alkaline, and then insert air or steam, and strip the free ammonia to the atmosphere. In general, the pH needs to be

adjusted to above 11. Despite the high energy and alkali consumption, ammonia is only transferred from the liquid phase to the gas phase and doesn't convert into harmless substances. But without further treatment of the waste gas, it leads to atmospheric pollution.

b. Ion exchange

Ion exchange is one of the most widely used denitrification methods. It is based on the difference in the binding force between the charged particles in the solution and the ion exchanger. Nitrate removal is accomplished by anion exchange of chloride ions with nitrate ions in an anion exchange resin. Ion exchange technology is a relatively mature water treatment technology. It has the advantages of stability, rapidity and large processing capacity.¹⁰⁹ However, the current application range is still limited by the variety, the performance and cost of ion exchangers. The requirements for pretreatment are relatively high, and the regeneration of ion exchangers and the treatment of regeneration liquid are difficult.

c. Reverse osmosis

The reverse osmosis method uses appropriate pressure to make the solvent in the solution migrate through the semi-permeable membrane and prevent the passage of solute molecules. The method does not require the addition of chemicals during the treatment process. However, the semi-permeable membrane is easily damaged and fouled. In order to maintain the durability of the membrane, the treated water must be pretreated before use, and the reverse osmosis method cannot fundamentally degrade the nitrate. The more concentrated waste water still needs a secondary treatment. High cost and complexity of the process limit this method.

d. Electrodialysis

Under the direct current passing through the treated water to form an electric field, cation and anion are respectively separated by the selective permeability of the ion exchange membrane. Compared with the reverse osmosis, the electrodialysis has higher selectivity. Nevertheless, easily precipitating ion species will accumulate on the membrane surface thus blocking it and seriously affecting its lifetime. Electrodialysis has high operating costs, it is unsuitable for large-scale applications and its wastewater need secondary treatment.

In conclusion, physical methods for degrading nitrates in water are highly efficient and easy to operate. The process is automated and leads to a rapid improvement of water quality. Whereas the obvious disadvantage is that ion exchange resins and permeable membrane are expensive and have short service life. These physical methods are not selective, and the removal of nitrite and nitrate will also remove other ions together. Moreover, nitrate is not degraded. The physical methods can only transfer or concentrate the nitrite/nitrate, which requires further treatment of high saline wastewater.

1.3.2.2 Biological methods for nitrite (nitrate) removal

Biological methods convert nitrate into nitrogen in water via denitrifying bacteria. These microorganisms carry out denitrification redox process for their own survival and

reproduction with nitrate as electron acceptor. The specific transformation steps are $\text{NO}_3^- \rightarrow \text{NO}_2^- \rightarrow \text{NO} \rightarrow \text{N}_2\text{O} \rightarrow \text{N}_2$.¹¹⁰ The complete conversion of nitrate to nitrogen is achieved with few by-products and low cost. Biological denitrification is a relatively mature and widely used removal strategy.^{111,112} The biofilm carrier for denitrifying microorganisms are biodegradable polymers. A large number of natural and synthetic biopolymers, including wood chips, sawdust, seaweed, polycaprolactone (PCL), polybutylene succinate (PBS) and other materials, are favored for their low cost, large quantities, and good properties.¹¹³

Denitrifying bacteria reduce nitrate to nitrogen under anoxic conditions. When the dissolved oxygen concentration is low, they extract oxygen from nitrate, thereby converting nitrate to nitrogen. Under aerobic conditions, they can use oxygen for aerobic respiration because they are facultative anaerobes. There are many types of denitrifying bacteria, for example: *Achromobacter*, *Aerobacter*, *Alcaligenes*, *Bacillus*, *Flavobacterium*, *Micrococcus*, *Pseudomonas*, *Proteus* and *Thiobacillus*, etc.¹¹⁴

A method of combining electrochemical and biological methods can effectively remove nitrite in water. Sun Hao Ming et al. utilize electrode-biofilm method to remove nitrite by combining the electrode biofilm in conjunction with existing nitrite denitrification techniques.¹¹⁵ In an intermittent reactor, NO_2^- removal rate can reach 90% and the pH of the reactor is stable.

Biological methods achieved higher efficiency than that of physical methods. However, the whole process is time consuming. The growth of involved microorganisms is greatly affected by the wastewater environment (concentration of dissolved oxygen, pH, temperature). If the external conditions are not suitable to these microorganisms, there will be the incomplete nitrification that can generate nitrogen oxides and nitrite. After treatment, bacterial pollution, organic matter residues, and intermediate product accumulation can cause secondary pollution of the water. Therefore, the water processed by the biological method always requires an extra treatment, that limits the application of this technology.

1.3.2.3 Chemical methods for nitrite (nitrate) removal

a. Chemical oxidation

Nitrogen in the nitrite ion is in an intermediate valence state. It can be oxidized and converted ideally into a less toxic or even non-toxic substance. Common oxidants are ozone, hydrogen peroxide, sodium hypochlorite and other strong oxidants. The method has a high reaction speed and high oxidation efficiency but most of the times the resulting oxidation product is still a pollutant. Hence, this method can only be used with small amounts of nitrite. When the concentration of the nitrite is too high (over 10 mg/L), the obtained nitrate concentration will be high, which isn't acceptable in lots of situations.

b. Chemical reduction on metals

This method requires alkaline conditions and an active metal. Currently common reducing metals are iron, aluminum, zinc, etc.¹¹⁶ The method is simple and has a higher reaction rate compared with biological denitrification method. But the active metal is easily

oxidized in solution and loses its activity. Moreover, the obtained products are not completely non-toxic. The metal oxides obtained after the reaction are a secondary pollution, making subsequent treatment more complex.¹¹⁷

c. Catalytic reduction

An emerging effective denitrification method in recent years is catalytic reduction denitrification, which includes photocatalytic method^{118,119}, liquid-phase catalytic reduction method and electrocatalytic method. Theoretically, the complete reduction of nitrate and nitrite to nitrogen can be achieved by appropriate catalysts and reaction conditions. It's important to explore and synthesize corresponding catalysts with high efficiency, high selectivity, and stable physical and chemical properties in this research field.

In the liquid-phase catalytic reduction, hydrogen or formic acid are used as reducing agents. In recent years, bimetallic catalysts including noble and transition metals show good performance. Li et al.¹²⁰ prepared a bimetallic catalyst Pd-Cu/ γ -Al₂O₃ and achieved 100% nitrate reduction efficiency.

Comparison of different methods:

- Chemical oxidation method has the advantages of simple equipment and cheap, but it cannot completely remove nitrogen compound in the water. It is ideal for the treatment of low nitrite content underground water. Especially, the high-efficiency ozone oxidation method has its incomparable advantages.
- Chemical reduction method can reduce nitrite to harmless nitrogen, but it requires high temperature, it is expensive, and the existing technology cannot completely remove nitrite.
- Membrane separation, ion exchange and other physical methods concentrate the nitrite in the waste liquid, and the removed nitrite returns to the environment unchanged, which is likely to cause secondary pollution. In addition, these methods are not selective for nitrite removal, other possible required substances are also removed, and the investment is relatively large.
- Biological method has the characteristics of high efficiency and low consumption, but its huge investment makes this process to be used only in large-scale sewage treatment projects. During the process, denitrification bacteria are easily affected by temperature and other factors. After the treatment, a large amount of biological sludge still needs to be deal with.

d. Electrocatalytic reduction method

Electrocatalytic reduction is a new water treatment technology that combines electrochemical methods with catalytic techniques. Under the external current, the electrochemical reaction of removing nitrate and nitrite at the cathode can be achieved, without extra reducing agents. The electrochemical method has the advantages of simple operation, environmental friendly, low investment cost and no introduction of extra chemicals.¹²¹ It is suitable for different concentrations of nitrate and nitrite wastewater and has potential application prospects. As an emerging cleaning process, electrochemical water treatment technology, compared with other water treatment processes, has the following advantages:

i) Wide application and versatility. Electrochemical water treatment technology can not only degrade and transform pollutants including oxidize refractory organic pollutants, but it can also be combined with other water treatment processes. For example, electrochemical oxidation technology can be used as a pretreatment of biological methods, so that the refractory organic matter can be easily biodegraded or even mineralized after electrochemical oxidation.

ii) No secondary pollution. Electrochemical water treatment technology directly relies on electric current to transfer electrons between electrodes (or homogeneous electrocatalysts) and pollutants. There is no need to add redox agents, avoiding secondary pollution caused by adding chemicals.

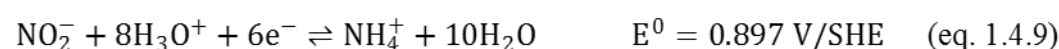
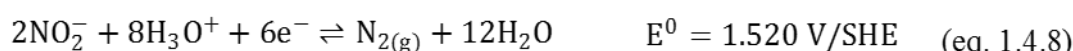
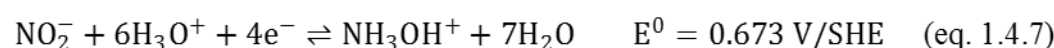
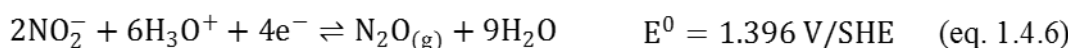
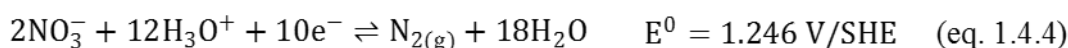
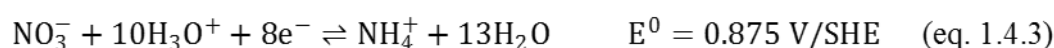
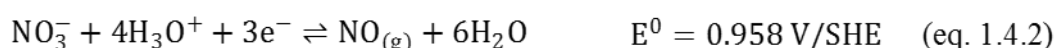
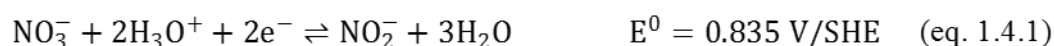
iii) Excellent controllability. The electrochemical treatment process is generally carried out under normal temperature and pressure, and can be realized by changing the current and voltage. Thus, the selectivity of reaction products can be improved.

iv) Economical. Electrochemical equipment is generally simple, small size, and have low operating costs.

However, electrocatalytic reduction has disadvantages such as low current efficiency, large energy consumption, electrode dissolution and passivation.

1.4 Electrochemical reduction of NO_x species

The most thermodynamically stable forms of nitrogen at pH values from 6 to 9 are N₂ and NH₃/NH₄⁺.¹²¹⁻¹²² The valence state of nitrogen varies from +5 to -3, and the main cathodic products issued from HNO₃ electrolysis are NO₂⁻, NO₂, NO, N₂O, N₂, NH₂OH, NH₄⁺ and NH₂NH₂. NO₂⁻ is a common intermediate and N₂ is the ideal harmless product. Equations 1.4.1-9 lists the electrochemical reduction reactions both of nitrate and nitrite anions.¹²³



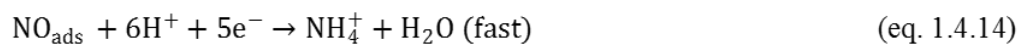
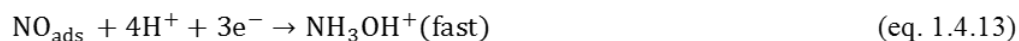
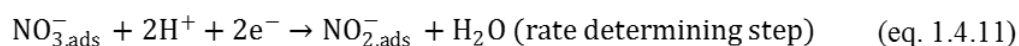
However, the actual reactions are very complex. The mechanism mainly depends on the cathode material, the applied cathode potential, the pH of the solution and the presence of

other anions.¹²⁴ Hydrogen evolution is the main side reaction, i.e. $2\text{H}_2\text{O} + 2\text{e}^- \rightarrow \text{H}_2 + 2\text{OH}^-$. The main anodic reaction is the evolution of oxygen, when there is no other ions ($4\text{OH}^- \rightarrow \text{O}_2 + 2\text{H}_2\text{O} + 4\text{e}^-$).¹²⁵

We will resume here how DEMS technique has helped understanding the mechanism and thus contribute to set a hierarchy of best catalysts. It is worth to notice that, in most cases, DEMS was used in conjunction with *in-situ* Fourier transformed infra-red spectroscopy, *ex-situ* liquid chromatography, rotating-disk electrode and stripping voltammetry experiments. Most of this work was performed by the group of M.T. Koper but other examples will be also given. An important part of these studies is dedicated to the electroreduction of nitric oxide (NO) because this is a decisive reaction intermediate. Some studies are dedicated to electroreduction of nitrous oxide (N_2O) as this is the last step in the nitrite (nitrate) reduction with molecular nitrogen as product.¹²⁶

1.4.1 DEMS studies of NO_3^- electrochemical reduction

The reduction of nitrate at low concentrations has been thoroughly investigated and the following mechanism was formulated (eq. 1.4.10-14):



The rate determining step is nitrate reduction to nitrite (1.4.11). Subsequent nitrite reduction leads to adsorbed NO (1.4.12). The adsorption of NO depends on the metal and leads to different performances and products. To desorb, NO_{ads} can react either with protons or with another NO molecule from the solution phase, if this molecule is available. This later mechanism will lead to solution phase N_2O (1.4.15-17) (vide infra).

In 2002, the performance of eight different polycrystalline electrodes for nitrate electroreduction was compared for relatively low nitrate concentration (0.1 M).⁹⁶ Based on cyclic voltammetry experiments, the activities decrease in the order Rh, Ru, Ir, Pd and Pt, and for the coinage metals, in the order Cu, Ag, Au. DEMS analysis showed no formation of N_2O and N_2 for all the metals and only the formation of gaseous NO for Cu electrode (Figure 1.4.1b). This experimental observation was important in order to ascribe NO_{ads} reduction to either hydroxylamine or ammonia (eq. 1.4.13 or 1.4.14). This is agreement with high chemisorption energy of NO on most of metals, except Cu.⁹⁶ Thus NO_{ads} could desorb from Cu and form some NO in solution (NO_{sol}), detected by DEMS. Interestingly, N_2O was not found with Cu electrode (Figure 1.4.1) as one could expect (eq. 1.4.17). This is explained by the lack of stability of copper electrode that gets oxidized by the $\text{NO} + \text{HNO}_3$ solution. Moreover, a palladium electrode covered by a full monolayer of Cu displays formation of

N_2O , probably due to higher stability of underpotential deposited Cu compared to bulk Cu.⁹⁶ This explains also why a PdCu bimetallic catalyst is selective for the reduction of nitrate to N_2 .¹²⁷ On Cu site, nitrate is reduced to N_2O whereas on Pd site N_2O is reduced to N_2 .

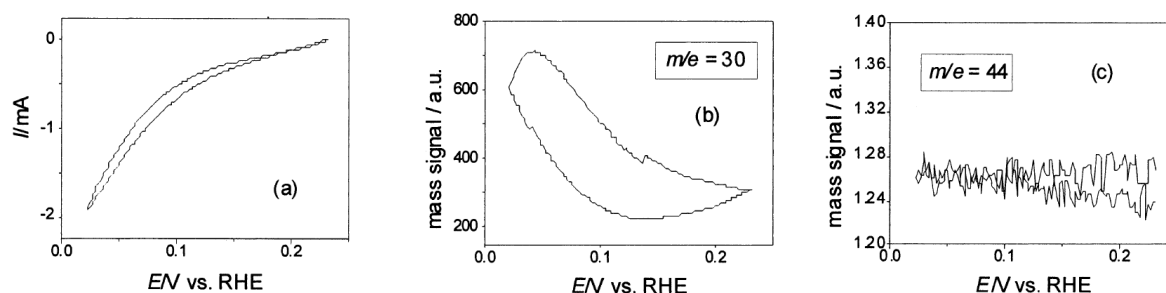


Figure 1.4.1 DEMS measurements on a Cu electrode in 0.1 M NaNO_3 and 0.5 M H_2SO_4 . a) Cyclic voltammogram; b) DEMS signal for $m/z=30$ (NO); c) DEMS signal for $m/z = 44$ (N_2O).⁹⁶

DEMS studies helped understanding the influence of nitrate (> 4 M) and acid concentration on the electrocatalytic reduction of nitrate on platinum. In highly acidic solutions, there is the autocatalytic indirect reduction of nitrate, i.e. the true electroactive species is NO^+ , issued from the decomposition of HNO_3 .⁹⁷ The NO^+ is reduced to NO_{sol} that reacts to HNO_3 to produce again NO^+ . This is supported by the formation of large amounts of NO in solution. It can be observed that the NO and NO_2 signals appears in the same time (as they are related to multiple gas phase reactions), suggesting that they are related to the same mechanism (Figure 1.4.2). The signal of N_2O appears at more negative potentials and it is correlated to the decrease of NO signal. This suggests that N_2O is formed from the electroreduction of NO. The signal of N_2 is barely higher than the baseline, suggesting that this is not a major product. Thus, at high potentials NO_{ads} starts to react with NO_{sol} , terminating the autocatalytic cycle and generating N_2O .

Nitrate reduction was studied also in alkaline conditions using DEMS^{92b} and different electrodes (platinum black, platinum single crystals, copper single crystals)¹²⁸. It has been found that Pt (100) is inactive for nitrate under alkaline conditions. Cu (100) and Cu (111) catalyze NO_3^- reduction to hydroxylamine. Then, bimetallic systems of Pt (100) electrode modified by Cu (Cu/Pt (100)) and Rh (Rh/Pt (100)) were explored.¹²⁹ Rh/Pt (100) has ammonia as the main product, and N_2 is the main product of Cu/Pt (100). The Cu sites catalyze NO_3^- to NO_2^- , and the Pt (100) sites catalyze NO_2^- to N_2 , though in different potential windows.

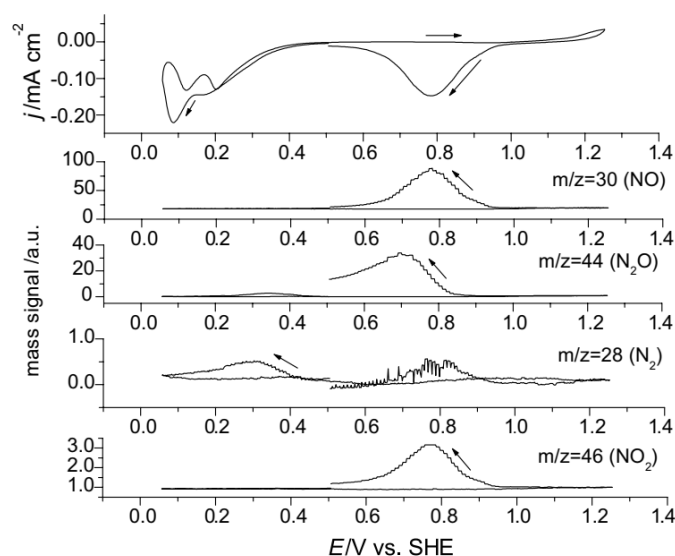


Figure 1.4.2 DEMS analysis of nitrogen-based species for nitrate reduction in 4.1 M HNO_3 in 0.5 M H_2SO_4 . Other experimental conditions: scan rate: 10 mV/s; platinized platinum gauze electrode.

A strategy to activate electrodes for nitrate reduction is the use of promoters. For example, germanium was electrodeposited on Pt electrodes surface.¹³⁰ The surface-adsorbed Ge is presumably $(\text{GeH})_{\text{ads}}$ and/or $(\text{GeH}_2)_{\text{ads}}$ or hydroxylated or oxidized state at more positive potentials. Germanium absorption prevents inhibitors (such as sulfate, hydrogen) from the surface rather than promoting nitrate reduction. In fact, the breaking of N-O bond is limited because the sites for NO lying flat on the surface are less abundant. Thus, in acidic environment and low concentrations of nitrate (0.1 M), the main product is hydroxylamine.

In acid solution Sn can effectively promote the activity of Pt electrode for nitrate reduction through catalyzing the reduction to nitrite at a PtSn ensemble site.¹³¹ N_2O is the dominant product on a PtSn electrode with an intermediate coverage of Sn, and it is consequently reduced to N_2 gas on the remaining free Pt sites. At high Sn coverage, NO_{ads} formation is blocked and NO_{sol} becomes the main product. On the other hand, Rh itself is already a very active catalyst for nitrate reduction. Therefore, Sn-modified Rh/C nanoparticles were used for the electrocatalytic reduction of nitrate.¹³² The modified Rh follows a similar change of activity and selectivity as modified Pt.

In 2013, ion chromatography (IC) was combined with voltammetry to quantitatively explore the possible ionic products. As a result, the formation of hydroxylamine and ammonia are detected by IC. Surface Sn species not only promote the conversion of nitrate to nitrite but also selectively catalyze nitrite/NO reduction to hydroxylammonium.¹³³ Later, the performance of a series of p-Block Metal (including Ge and Sn) modified Pt electrodes for electrocatalytic reduction of nitrate is compared.¹³⁴ The result is shown in the Figure 1.4.3. In perchloric acid, tin, cadmium, indium, and gallium were all active promoters for nitrate reduction. For tin modified electrode, the product distribution depends on the surface coverage, both in perchloric acid and sulfuric acid.


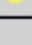

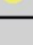

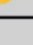










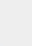











Group →	12	13	14	15
Period ↓				
4	Zn  	Ga  	Ge  	As  
5	Cd  N ₂ O 	In  N ₂ O 	Sn  NO, N ₂ O  NO, N ₂ O	Sb  
6		Tl  	Pb  N ₂ O 	Bi  
Perchloric acid	 Promoted	 Weakly promoted	 Not promoted	
Sulfuric acid	 Promoted	 Weakly promoted	 Not promoted	

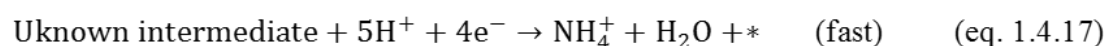
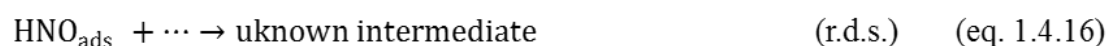
Figure 1.4.3 Promoting effect and product distribution along the sites of p-block elements for modified Pt electrode.¹³⁴

1.4.2 DEMS studies of NO electrochemical reduction

Two distinct mechanisms exist for the reduction of NO. The first one concerns the reduction of adsorbed NO in a clean electrolyte, while the second one concerns the continuous reduction of NO in solution. For both mechanisms, many DEMS studies were performed on transition and coinage metals, especially in acidic solution and some in alkaline conditions.

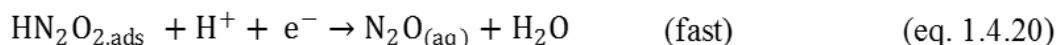
For the reduction of NO_{ads}, DEMS studies revealed that neither N₂O nor N₂ are formed. Thus, the formation of ammonia is hypothesized. From cyclic voltammetry studies combined with infrared spectroscopy, several conclusions have been drawn:

- NO_{ads} reduction is not surface sensitive¹³⁵, although one reported paper suggest that Pt (100) is more active for breaking the N-O bond¹³⁶.
- Neither the adsorption strength nor the N-O bond breaking plays a role in the reaction rate.
- The protonation of NO_{ads} is the rate determining step. From a Tafel slope of 60 mV/decade, an EC mechanism is suggested. The first electron-proton transfer is at equilibrium (eq. 1.4.15) resulting in the formation of HNO_{ads} as intermediate. The second reaction step is the chemical rate-determining step and involves the breaking of N-O bond (eq. 1.4.16). Most probably this step requires a free neighboring site (*).



For the continuous reduction of NO in solution, DEMS studies showed that transition metals (Pt, Pd, Rh, Ir, Rh, Au) promote the formation of N₂O at high potentials while N₂ is formed at intermediate potentials and NH₄⁺ at low potentials (although Au forms very little

NH_3 and N_2).¹³⁵ From Tafel slope analysis, the pH dependence and the kinetic order in NO solution concentration, a mechanism based on the formation of a weakly adsorbed NO dimer was suggested (eq. 1.4.18-20). The existence of this intermediate is indirectly proved by the fact that the reaction is not very metal-dependent. Thus a weakly adsorbed intermediate must be involved and the role of surface-bond NO is not so important.¹³⁵



The general scheme in Figure 1.4.4 is summarizing NO reduction on metal electrodes. It must be emphasized that silver was very little studied.¹³⁷ It was found that NO reduction in 0.5 M Na_2SO_4 using a silver electrode has a faradic efficiency for N_2O , NH_3 , N_2 and H_2 of 26%, 53%, 0% and 8.5 % respectively. Thus, the suggested scheme may not apply to silver.

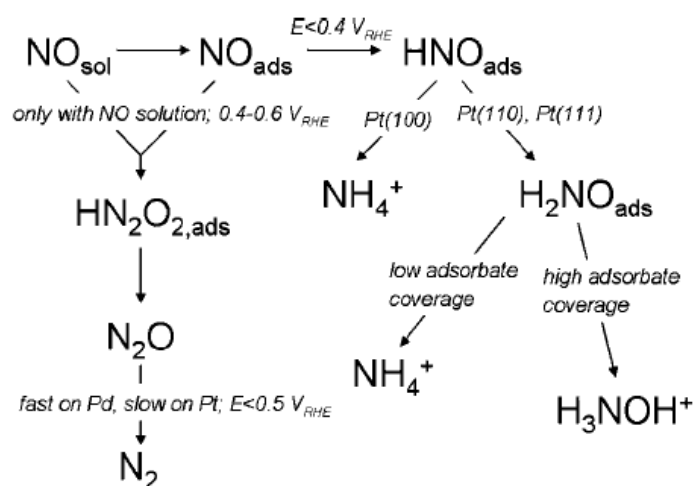
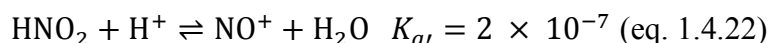
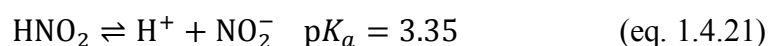


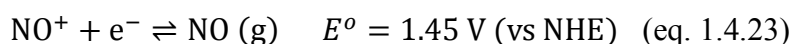
Figure 1.4.4 General scheme for NO reduction on most metal electrodes.¹³⁸

1.4.3 DEMS studies of NO_2^- electrochemical reduction

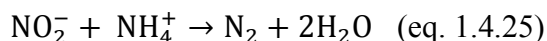
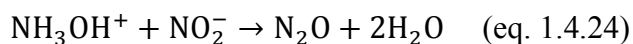
Nitrite is one of the more reactive compounds from nitrogen cycle. Before discussing its reduction, one must consider some equilibrium reactions, mainly in acidic conditions. Firstly, there are two acid-base reactions that lead to the formation of nitrosonium NO^+ :



In a solution of pH 1, 10 mM of nitrite (NO_2^-) contains 9.9 mM HNO_2 , 0.1 mM NO_2^- and 2×10^{-7} mM NO^+ . But in highly acidic conditions, the concentration of NO^+ becomes significant and this ion is the main electroactive form of nitrite. The equilibrium potential for the redox reaction of NO^+ and NO is 1.45 V vs NHE.¹³⁹ Thus, the electroactive species highly depends on pH: NO_2^- in alkaline and neutral, HNO_2 in mild acidic and NO^+ in highly acidic.



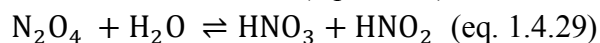
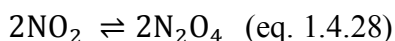
Secondly, in acidic conditions HNO_2 participates to some solution phase reactions with hydroxylammonium or ammonium:



Finally, there are the decomposition (disproportionation) reactions that are prominent when the solution is agitated and the concentration of HNO_2 is high.



It is worth to mention here that the reddish gas NO_2 converts to the colorless gas N_2O_4 which disproportionates to nitrous acid and nitric acid. This reaction has a very high equilibrium constant $8.5 \cdot 10^8$ but in highly acidic conditions of HNO_2 and HNO_3 some N_2O_4 and NO_2 can be formed.



DEMS analysis was used many times for studying the electrochemical reduction of nitrite both on noble and coinage metals, in alkaline and acidic conditions. While only gaseous species, such as NO , NO_2 , N_2O and N_2 are measured with DEMS, some complementary techniques have to be used in order to fully understand the reaction mechanism. Thus, rotating disk electrode and bulk electrolysis were used to confirm the presence of hydroxylamine and ammonium, and FTIR and ATR-SEIRAS (attenuated total reflectance surface-enhanced infrared absorption spectroscopy) were used to measure NO-related adsorbed intermediates.

On noble metals and acidic conditions, one of the most important observations is that NO issued from the decomposition of HNO_2 is reduced at high potentials. The product is N_2O based on the reaction between the solution phase NO and adsorbed NO (vide supra). Subsequently, at lower potentials HNO_2 is directly reduced to hydrogenated products (NH_3^+OH , NH_4^+). This is observed for Ru , Rh^{140} (Figure 1.4.5a), Pd , Pt^{141} but not for Ir , where only the NO reduction to N_2O is recorded. For coinage metals (Cu , Ag , Au), the main difference is that HNO_2 is reduced to NO that is subsequently reduced to N_2O . The main explanation is that coinage metals have a weak NO adsorption. Thus, NO can be found in solution. Figure 1.4.5b shows DEMS analysis on Au electrode. In the negative going sweep, NO is the first gaseous product around 0.5 V vs. RHE, well before any N_2O is detected. The onset of N_2O formation is 0.4 V vs. RHE. Both gaseous products disappear when hydrogen evolution appears, thus some hydrogenated products are expected in this potential range (< -0.2 V vs. RHE). In the positive going sweep, NO signal is largely diminished while N_2O peak is only slightly shifted to more positive values. The decrease in the NO peak is explained by the NO consumption for the formation of N_2O (the rate of NO formation is lower than the rate of its consumption). In the negative going sweep, the local partial pressure of NO remains high because NO formation happens before its consumption, so NO accumulation is possible.¹⁴²

In alkaline media, no gaseous products were recorded by DEMS analysis. The rate determining step is the first electron transfer that converts NO_2^- to NO . This is strongly adsorbed and further reduced to ammonia. The order of activity of polycrystalline metals is $\text{Rh} \sim \text{Ru} > \text{Pt} > \text{Ir}$ while Ag and Au do not selectively reduce NO_2^- (the reaction happens simultaneously with hydrogen evolution). The nitrite reduction is sensitive to surface structure and a change in selectivity is observed. For example the direct electroreduction of NO_2^- to N_2 on the $\text{Pt}(100)$ electrode in 0.1 M NaOH was reported and N_2O and ammonia are excluded as possible reaction intermediates by CV and DEMS experiments.¹⁴³

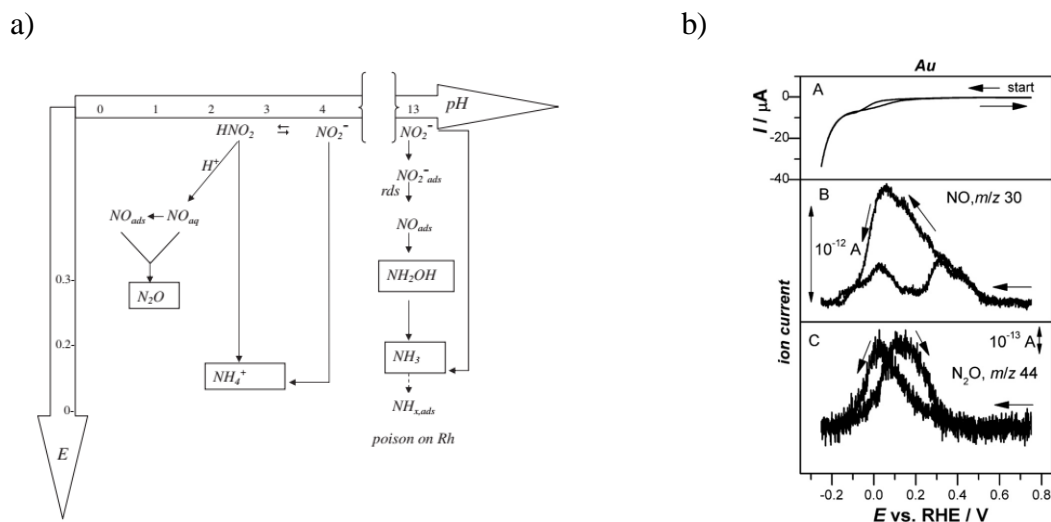


Figure 1.4.5 a) Mechanistic pathways for nitrite reduction at a polycrystalline Rh electrode as a function of pH and E.¹⁴⁰ b) DEMS analysis of HNO_2 reduction on gold.¹⁴²

1.4.4 Polyoxometalates as catalysts for electroreduction of NO_2^-

A polyoxometalate (POM) is a metal-oxygen cluster compound composed of transition metal ions linked by oxygen. POMs have excellent redox activity. Both the reduced and oxidized state have high stability and undergo reversible multiple electron transfer reactions without degradation.^{32b} Furthermore, this ability can be finely tuned by changing their structure or composition. POMs can act as homogeneous or heterogeneous catalysts, as well as a bifunctional catalyst for the transfer of protons and electrons. POMs have been widely used for catalyzing nitrite electrochemical reduction and much less for nitrate electrochemical reduction for which they are mostly inactive. **We introduce here the abbreviation “NitER” for “nitrite electrochemical reduction”.**

The following chapters are divided between the homogeneous and heterogeneous catalysis, with a chronological description of the used POMs. Tables 1.4.2 and 1.4.3 summarize the type of POMs, the immobilization technique (for heterogeneous catalysis), the catalytic efficiency and the reaction products (if the information is available). It is worthwhile to mention that earlier studies concern POMs with a rather simple structure, while later studies are based on more sophisticated POMs or POMs containing a transition metal.

1.4.4.1 POM-based homogeneous catalysis of NO_2^- electrochemical reduction

In 1995, the archetypal Keggin POM $[\text{SiW}_{12}\text{O}_{40}]^{4-}$ is used as electrocatalyst for nitrite reduction by Shaojun Dong.¹⁴⁴ Three redox processes are observed with two one-electron and one two-electron redox peaks in aqueous solutions. The nitrite reduction is explored from pH -0.6 to 4. By only cyclic voltammetry the reaction products cannot be identified. The electrocatalytic activity is computed by the difference between the peak current in solution with and without nitrite. The first waves show good electrocatalytic activities only in acidic solution with pH lower than 2. Figure 1.4.6 shows the CV (cyclic voltammogram) of POM after the addition of different concentration of nitrite in 0.5 M H_2SO_4 . The peak current is proportional to the nitrite concentration. For pH higher than 4, only the third wave of $[\text{SiW}_{12}\text{O}_{40}]^{4-}$ has electrocatalytic activity for NitER.

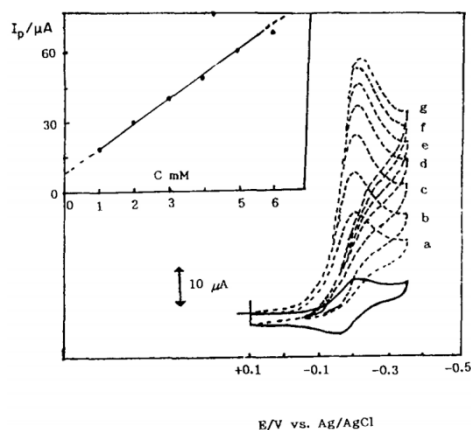


Figure 1.4.6 Cyclic voltammogram of 1 mM $[\text{SiW}_{12}\text{O}_{40}]^{4-}$ in 0.5 M H_2SO_4 solution (solid line) and after the addition of NO_2^- (dash line): (a) 1 mM, (b) 2 mM, (c) 3 mM, (d) 4 mM, (e) 5 mM, (f) 6 mM and (g) 7 mM.

Very interestingly, couple of years before (in 1989), a detailed study by Toth & Anson describes the catalysis of NitER by lacunary Keggin $[\text{SiW}_{11}\text{O}_{39}]^{8-}$ in which one tungsten atom and its oxo group located at the periphery of the anion is replaced by iron. Compared with archetypal $[\text{SiW}_{12}\text{O}_{40}]^{4-}$, the lacunary POM has no catalytic activity, while the $[\text{Fe}^{\text{III}}\text{SiW}_{11}\text{O}_{39}]^{5-}$ is reducing NO_2^- to NH_4^+ in a concerted multiple-electron step. The mechanism involves the formation of nitrosyl complex $[\text{Fe}^{\text{II}}(\text{NO})\text{SiW}_{11}\text{O}_{39}]^{6-}$. Moreover, the overpotential of NitER is decreased by replacing Si with Ge, P and As, respectively. Ammonia was measured by ion chromatography and faradic efficiency of 35, 22, 49 and 35 % respectively obtained at pH 4 in an acetate buffer.¹⁴⁵

The first use of a Dawson POM was reported in 1996. The archetypal $[\text{P}_2\text{W}_{18}\text{O}_{62}]^{6-}$, at pH lower than 3, displays two reversible one-electron waves, followed by two reversible two-electron waves. The addition of nitrite induced an increase in the current of the cathodic waves and a decrease in the one of the anodic waves, but in a pH dependent manner. For pH < 3, the first wave is catalytic, while for pH > 3, only the 5th reduction wave is catalytic (the redox behavior of POMs alone is now composed of four reversible one-electron waves followed by a two-electron wave). An improvement of the catalytic behavior at higher pH (4.5) was obtained by the substitution of lacunary Dawson-type POM with Fe^{III} and Cu^{II} , in a lesser extent (i.e. only for concentration of nitrite 20 times higher than that with Co^{II} and Ni^{II}). Meanwhile, substitution with Mn^{II} and Mn^{III} has no effect.¹⁴⁶

Later, Ruhlmann's group has tested Wells–Dawson-derived tetrameric complexes $K_{28}H_8[P_2W_{15}Ti_3O_{60.5}]_4$ as homogeneous electrocatalysts both for electrocatalytic reduction of nitrite and of nitric oxide.¹⁴⁷ $K_{28}H_8[P_2W_{15}Ti_3O_{60.5}]_4$ was formed by the reaction of trivacant α - $[P_2W_{15}O_{56}]^{12-}$ with titanyl at low pH. The electrochemical behavior of the tetrameric complexes in aqueous solution has been investigated at various pHs, and the electrocatalytic activity is greatly influenced by pH. When the pH is higher than 3.5, there is no catalytic effect because pK_a of nitrous acid is close to this value, thus a charge repulsion appears. Therefore, it's supposed that the dominant reactant is HNO_2 rather than NO_2^- . When nitric oxide (NO) was used as reactant, an electrocatalytic reaction is observed even at pH 4.57 (Figure 1.4.7).

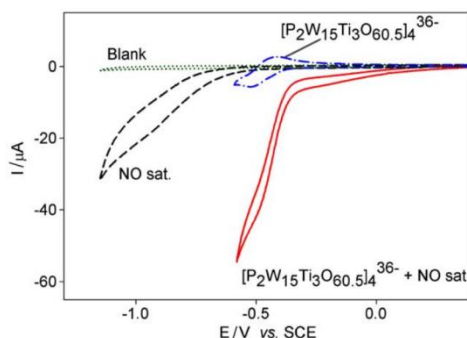


Figure 1.4.7 Cyclic voltammetry in 0.5 M Na_2SO_4/H_2SO_4 solution at pH 4.57 deaerated with pure argon at a scan of 20 mV s^{-1} . (a) Dotted line: Blank electrolyte without POMs or NO; (b) Short dash: electrolyte saturated with NO; (c) Dash dotted line: electrolyte with POMs; (d) Full line: electrolyte with POMs and saturated NO.¹⁴⁷

In order to compare different POMs, an equation for the catalytic activity is proposed, based on the increase of the reduction current of the POM first wave in the presence of nitrite (eq. 1.4.30). Compared with α - $[P_2W_{18}O_{62}]^{6-}$ or best previously reported POM catalyst $[FeSiW_{11}O_{39}]^{5-}$, $K_{28}H_8[P_2W_{15}Ti_3O_{60.5}]_4$ shows outstanding performance as shown in Table 1.4.1.

$$CAT = 100\% \times \frac{I_P(POM, NaNO_2) - I_P(POM)}{I_P(POM)} \quad (\text{eq. 1.4.30})$$

Table 1.4.1 Comparison of catalytic efficiencies for nitrite reduction using different polyoxometalates and various pH values.

pH	CAT/% (First $W^{VI/V}$ reduction wave)		
	α - $[P_2W_{18}O_{62}]^{6-}$	$[FeSiW_{11}O_{39}]^{5-}$	$[P_2W_{15}Ti_3O_{60.5}]_4^{36-}$
0.56	370	153 (Partial decomposition)	187
1.77	95	160	81
2.50	43	100	28
3.00	21	76	6
3.50	4	67	0

Even larger POMs were tested in 2015. The crown precursor ($K_{28}Li_5[H_7P_8W_{48}O_{184}]$) (denoted P_8W_{48}) was used for obtaining Co, Fe and Ni substituted compounds. These

compounds were more efficient for NitER at pH 4.5 than the precursor, with the increasing catalysis from Co, Ni and Fe. For Co substituted compound, the electrocatalytic activity is observed only for relatively high concentration of nitrite (> 3 mM).

Different POMs have been tested also for the reduction of nitric oxide. Pure gas was bubbled in the solution containing previously reduced POM (the reduction potential corresponds to the first one electron or two electrons wave). All studied POMs convert NO to N₂O with a 100% yield. The authors suggest the existence of an adduct between the NO and POM but without further experimental evidence. It is worthwhile to mention that both W and Mo based POMs as well as iron substituted POMs were used in this study. Table 1.4.3 summarize the electrolysis potential and the catalytic efficiency of these catalysts.

Table 1.4.2 Summary of POMs used in homogeneous catalysis of NO₂⁻ electrochemical reduction

POM	Electrocatalytic potential (V vs. RHE)	Reaction product	Ref.
Keggin POMs			
[SiW ₁₂ O ₄₀] ⁴⁻	0.059	N.D.	¹⁴⁴
[FeSiW ₁₁ O ₃₉] ⁵⁻	-0.275	NH ₄ ⁺	¹⁴⁵
[FeGeW ₁₁ O ₃₉] ⁵⁻	-0.248		
[FePW ₁₁ O ₃₉] ⁵⁻	-0.225		
[FeAsW ₁₁ O ₃₉] ⁵⁻	-0.213		
Dawson POMs			
α ₂ -[P ₂ W ₁₈ O ₆₂] ⁶⁻	0.307	N.D.	¹⁴⁸
α ₂ -[Cu ^{II} P ₂ W ₁₇ O ₆₁] ⁸⁻	0.107	N.D.	¹⁴⁶
α ₂ -[Ni ^{II} P ₂ W ₁₇ O ₆₁] ⁸⁻	0.087		
α ₂ -[Co ^{II} P ₂ W ₁₇ O ₆₁] ⁸⁻	0.067		
α ₂ -[Fe ^{III} P ₂ W ₁₇ O ₆₁] ⁷⁻	0.017		
Crown POMs			
(K ₂₈ Li ₅ [H ₇ P ₈ W ₄₈ O ₁₈₄])	-0.275	N.D.	¹⁴⁹
(K ₁₂ Li ₁₆ Co ₂ [Co ₄ (H ₂ O) ₁₆ P ₈ W ₄₈ O ₁₈₄])	-0.273		
(K ₁₄ Li ₈ Ni ₃ [Ni ₄ (H ₂ O) ₁₆ (P ₈ W ₄₈ O ₁₈₄)(WO ₂ (H ₂ O) ₂])	-0.272		
(Li ₄ K ₁₆ [P ₈ W ₄₈ O ₁₈₄ Fe ₁₆ (OH) ₂₈ (H ₂ O) ₄])	-0.274		
Well-Dawson POMs			
K ₂₈ H ₈ [P ₂ W ₁₅ Ti ₃ O _{60.5}] ₄	-0.029	N.D.	¹⁴⁷

N.D. not determined

Table 1.4.3 Summary of W and Mo Based POMs used in the homogeneous catalysis of NO reduction to N₂O.¹⁵⁰

POMs	Electrocatalytic potential (V vs. RHE)	Catalytic efficiency
W-based POMs (1 electron reduced POM)		
α_1 -[P ₂ MoW ₁₇ O ₆₁] ⁷⁻	0.40	1150
[P ₂ W ₁₈ O ₆₂] ⁶⁻	0.24	900
[SiW ₁₂ O ₄₀] ⁴⁻ , α_2 -[P ₂ W ₁₇ O ₆₁] ¹⁰⁻ , α_2 -[Fe ^{III} P ₂ W ₁₇ O ₆₁] ⁷⁻	n.p	n.p
Mo-based POMs (2 electrons reduced POM)		
[P ₂ Mo ₁₈ O ₆₂] ⁶⁻	0.62	475
[SiMo ₁₂ O ₄₀] ⁴⁻	0.48	1160
[P ₂ W ₁₂ Mo ₆ O ₆₂] ⁶⁻	0.35	344
[P ₂ W ₁₄ Mo ₄ O ₆₂] ⁶⁻ , [P ₂ W ₁₅ Mo ₃ O ₆₂] ⁶⁻ , α_2 -[P ₂ MoW ₁₇ O ₆₁] ⁷⁻ , α_2 - [Fe ^{III} P ₂ Mo ₂ W ₁₅ O ₆₁] ⁷⁻ , α_2 - [P ₂ Mo ₂ W ₁₅ O ₆₁] ¹⁰⁻	n.p.	n.p.

n.p. = not published

1.4.4.2 POM-based heterogeneous catalysis of NO₂⁻ electrochemical reduction

Most of POMs are highly soluble in different kinds of polar solvents including water. For extending POM-based applications and recyclability, immobilization techniques are necessary. In order to better describe the high number of published examples, we have classified the immobilization techniques as following: i) adsorption; ii) layer-by-layer via electrostatic interactions; iii) entrapment in polymer or other matrices. In most of the cases, carbon-based materials (Vulcan carbon powder, graphite, glassy carbon, carbon nanotubes) were used as support. The obtained composite material is used a sensor for nitrite detection (mostly via its reduction, but some nitrite oxidation-based examples can be found). Thus, results are often reported in terms of the limit of detection, i.e. the lowest concentration of nitrite that can generate a reduction current, and in terms of linear range, i.e. the domain of nitrite concentration where the reduction current varies proportional with the concentration. It is very important to mention that no particular attention is given to the reaction product. A high variety of POMs, ranging from Keggin to Dawson and Crown structures, both W and Mo-based compounds, was tested. The majority of examples are in acidic conditions (pH 1 to 2) and in sulfate-based electrolyte.

1) Immobilization of POMs via adsorption

This technique is probably the first and the simplest one, because it involves dropping a POM containing solution on the support. A recent example is the immobilization of lacunary Keggin [PMo₁₁O₃₉]⁷⁻ on a glassy carbon previously modified with either oxidized single walled carbon nanotubes or reduced graphene oxide. The sensors were used for nitrite

reduction at a potential corresponding to the second wave of the POM, with a linear range up to 14 mM in 0.1 M H₂SO₄.¹⁵¹ Nevertheless, the deposit lacks of stability and the immobilized amount is quite little. Moreover, POMs are highly soluble and thus they can easily dissolve in the electrolyte. One solution is to first immobilize another compound on the substrate and then realize an electrostatic interaction between this compound and POM. Another solution is to reduce the solubility of the POMs by replacing its native cation with another one. Some examples concern the use of ionic liquids (IL) as cations that are able to precipitate POMs. The obtained salt is further adsorbed on the support.

For example, Xie et al, immobilized H₃[PMo₁₂O₄₀] on GC electrode after its reaction with the 1-n-Butyl-3-methylimidazolium tetrafluoroborate (BMIM⁺BF₄⁻). The modified POM electrode shows high stability and electrocatalytic property on nitrite reduction.¹⁵² In another example, hybrid materials K[BMIM]₆[H₄PW₁₈O₆₂] and K₂[BMIM]₄[P₂W₁₈O₆₂] are formed by reaction between BMIM⁺BF₄⁻ and K₇[H₄P₂W₁₈O₆₂], K₆[P₂W₁₈O₆₂].¹⁵³ Although the materials were not tested for nitrite reduction, the example is still interesting for showing the insolubility of these materials, the only good solvent being dimethylsulfoxide (DMSO). From cyclic voltammetry, it was found that the reduction peak potentials shift towards negative values, which could be due to decrease of acidity compared with classic Dawson POM anions. A final example is the use of N-dodecyl pyridinium hexafluorophosphate ([C₁₂Py⁺][PF₆]) for preparing a hybrid material with [PMo₁₂O₄₀]³⁻.¹⁵⁴ The GC electrode surface was previously modified with MWCNTs, and then the electrode was dipped in an acetonitrile-based solution containing [PMo₁₂O₄₀]³⁻ anions and C₁₂Py⁺ cation. The obtained sensor had good analytical performances for nitrite reduction, but also for detection of BrO₃⁻, ClO₃⁻, IO₄⁻, IO₃⁻ and H₂O₂.

As a huge number of ionic liquids (IL) are available, one may inquire if there is an influence of the type of IL on the electrochemical behavior of the immobilized POM and on the performance of the sensor. A recent study demonstrated that IL having lower ionic volume display higher conductivities. Thus, the sensor prepared with [PMo₁₂O₄₀]³⁻ and 1-methyl-3-methylimidazolium tetrafluoroborate (EMIMBF₄) showed higher currents than the one prepared with BMIMBF₄. Moreover, the nanoparticles of the solid compound obtained with EMIMBF₄ are more homogeneous compared those obtained with 1-methyl-3-methylimidazolium bromide (EMIMBr).¹⁵⁵

II) Immobilization of POMs via layer-by-layer with electrostatic interactions

This method was widely used due to the native anionic structure of the POM bearing multiple negative charges that could be used in electrostatic interactions with a positively charged substrate.

Shaojun Dong used a two-step sol-gel method to prepare [P₂W₁₈O₆₂]⁶⁻-modified electrode.¹⁵⁶ The electrostatic interaction between [P₂W₁₈O₆₂]⁶⁻ anion and -NH₃⁺ was used to immobilize the [P₂W₁₈O₆₂]⁶⁻ on electrode surface. The ammonia group was contained inside the gel because 3-aminopropyltrimethoxysilane was used as precursor. The gel stability was improved by mixing it with a copolymer formed from poly-vinylalcohol (PVA) and poly-vinylpyridine (PVP). The sensor was applied both for BrO₃⁻ and NO₂⁻ detection. In latter case,

a LOD of 5 μM and a linear range between 0.02 to 34 mM were obtained by chronoamperometry at -0.1 V vs. RHE (corresponding to the first wave of the POM).

Carbon carriers are good load substrates due to their excellent electrical conductivity. A novel graphene oxide (GO)-polyoxometalate (POM) nanohybrid is prepared using gemini surfactants (Gem) as stabilizers. Gemini surfactants contain two cationic groups, two hydrophobic chains and a spacer, thus providing more binding sites than simple cationic surfactant (such as dodecyl trimethyl ammonium bromide). As a result, $\text{H}_3[\text{PMo}_{11}\text{VO}_{40}]$ is uniformly distributed on the surface of GO because of the anion exchange between the POM anions and Gem counter anions (Br^-). The construction of the sensor is shown in Figure 1.4.8. Electron conductivity is ameliorated by the immobilization POMs on GO nanosheets, and the stability of this nanohybrid is improved by the Gem. Therefore, the Gem-GO-POM nanohybrid has excellent electrochemical activity for nitrite oxidation and stability.¹⁵⁷

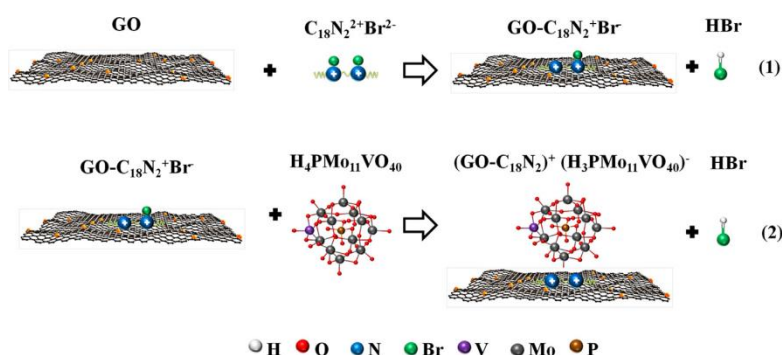


Figure 1.4.8 Anion exchange reaction between Gem and POM on graphene.¹⁵⁷

Shahzad Imar developed several sensors with lacunary Dawson-type POM $\text{K}_{10}[\text{P}_2\text{W}_{17}\text{O}_{61}]$ mono-substituted with transitional metal ions Fe^{3+} , Cu^{2+} , Ni^{2+} . The initial modification of glassy carbon electrode is achieved by its immersion in poly-diallyldimethylammonium chloride (PDDA). The Cu-substituted POM showed no electrocatalytic activity both for nitrite and nitrate. Moreover, the GC/PDDA/POM is further assembled with polymer-stabilized Ag nanoparticles. The use of AgNPs led to higher sensitivity and the possibility to achieve both nitrite and nitrate reduction in slightly acidic media (pH 4.5).¹⁵⁸

Another positively charged molecule that was used for POM immobilization is poly (allylamine hydrochloride). The mono-lacunary Keggin anion $[\text{SiW}_{11}\text{O}_{39}]^{8-}$ was thus fixed on the GC electrode. The sensor displayed a dynamic range up to 3.6 mM of NO_2^- in 0.1 M H_2SO_4 .¹⁵⁹ Indium tin oxide (ITO) electrodes were also used as substrates for POMs immobilization. A first example is the ITO modified by electrospinning of PVA. The electrode is dipped in PDDA solution to create a positive charge at the surface. Then the electrode is immersed in a $[\text{P}_2\text{W}_{18}\text{O}_{62}]^{6-}$ solution and used for nitrite reduction.¹⁶⁰ In another example, ITO electrode was modified with PEI/PSS/[PDDA/POM-CNT]_n (PSS = poly(styrenesulfonate), PEI=poly(ethyleneimine)). The purpose the PEI/PSS precursor layer is to minimize possible interference from the substrate and to form a more uniformly charged surface. The used POM is the vanadium-substituted Dawson $[\text{P}_2\text{VW}_{17}\text{O}_{62}]^{7-}$. The sensor was used for the electrocatalytic oxidation of nitrite, based on the $\text{V}^{\text{V}}/\text{V}^{\text{IV}}$ redox couple.¹⁶¹ In fact, this redox couple has been used in some other examples of sensors based on electrocatalytic oxidation of

nitrite. Mo-based Keggin POMs such as $[\text{PMo}_{11}\text{VO}_{40}]^{4-}$ ¹⁶² and $[\text{PMo}_{10}\text{V}_2\text{O}_{40}]^{5-}$ ¹⁶³ were immobilized on reduced graphene oxide (rGO) modified with PDDA.

III) Immobilization of POMs via entrapment in polymer or other matrices.

Various polymers have been used for the entrapment of POMs. One of the first example is polyaniline (PANI), a conducting polymer within a certain potential range.¹⁶⁴ Thus, the selection of POMs depends mainly on the redox potential that must be located within this potential range (i.e. 0.01 to 0.9 V vs. RHE). A suitable choice is SiMo_{12} which shows several well-defined redox peaks and has a very good catalytic efficiency for nitrite reduction. When this POM is in solution, a second order rate constant for nitrite reduction of $1.6 \cdot 10^3 \text{ M}^{-1} \text{ s}^{-1}$ was obtained. After immobilization, $[\text{SiMo}_{12}\text{O}_{40}]^{4-}$ retained a good electrocatalytic behavior with a catalytic efficiency (CAT, see eq. 1.4.30) of about 130%. Figure 1.4.9a displays the CV of PANI/ SiMo_{12} in the absence and presence of nitrite. One can observe that the reduction current in the presence of nitrite increases directly at the starting potential (0.5 V vs. SCE), well before the first reduction wave of $[\text{SiMo}_{12}\text{O}_{40}]^{4-}$. The authors did not make any comment about this behavior. In the same time, this behavior was not observed when $[\text{P}_2\text{Mo}_{18}\text{O}_{62}]^{6-}$ was immobilized within a PANI polymer (Figure 1.4.9b), but the concentration of nitrite in this experiment is reduced by half. More interestingly, it is the fact that the authors have replaced nitrite solution with nitric oxide (NO) saturated solution and recorded CV with PANI/ $[\text{SiMo}_{12}\text{O}_{40}]^{4-}$. They have observed **exactly the same** catalytic behavior. Thus, they cannot exclude that, even when nitrite solution is used, the real reactive species is nitric oxide, issued from the disproportionation reaction of HNO_2 . When performing large scale electrolysis at a potential 100 mV negative to the first redox wave of $[\text{SiMo}_{12}\text{O}_{40}]^{4-}$, with either NaNO_2 or NO as starting reagent, the only found product was N_2O . Besides this POM, $[\text{P}_2\text{W}_{18}\text{O}_{62}]^{6-}$ was studied as well and the authors affirm obtaining similar results.¹⁴⁸

On the other hand, $[\text{SiMo}_{12}\text{O}_{40}]^{4-}$ is not a good candidate for immobilization within PANI because its first reduction wave is already beyond the limit of conductivity of the polymer, i.e. -0.035 V vs. RHE. Another POM, $[\text{P}_2\text{VW}_{17}\text{O}_{62}]^{7-}$ has the first redox peak at a too positive potential to be used with PANI. For this reason, the incorporation of $[\text{SiW}_{12}\text{O}_{40}]^{4-}$ and $[\text{P}_2\text{VW}_{17}\text{O}_{62}]^{7-}$ into poly(4-vinylpyridine) (PVP), a non-conducting polymer, has been tested. The immobilization did not alter the redox behavior of these POMs neither their electrocatalytic activity for nitrite reduction.

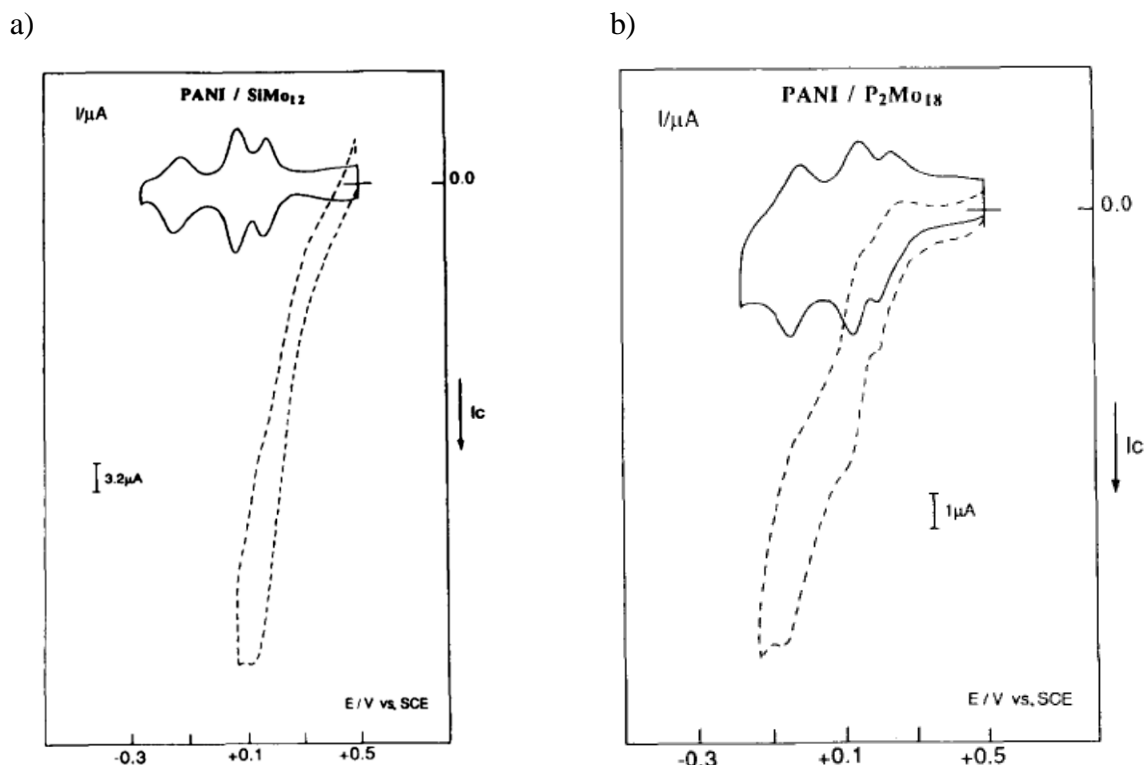
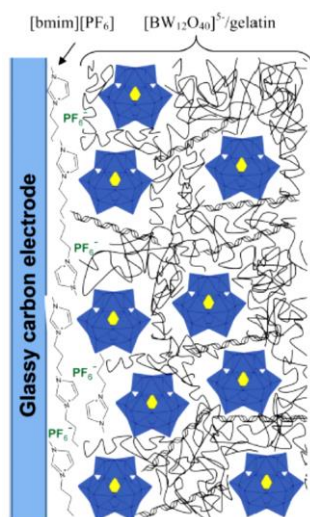


Figure 1.4.9 Cyclic voltammetry of a) $[\text{SiMo}_{12}\text{O}_{40}]^{4-}$ and b) $[\text{P}_2\text{Mo}_{18}\text{O}_{62}]^{6-}$ immobilized with polyaniline (PANI) in the absence of nitrite (black line) and in the presence of nitrite (dash line). Experimental conditions: 0.2 M $\text{Na}_2\text{SO}_4 + \text{H}_2\text{SO}_4$ (pH 2), scan rate, 5 mV s^{-1} , (a) 10^{-2} M NaNO_2 and (b) $5 \cdot 10^{-3}$ M NaNO_2 .

Papaconstantinou used functionalization electrode with Dawson POMs $[\text{P}_2\text{Mo}_{18}\text{O}_{62}]^{6-}$ and $[\text{P}_2\text{W}_{18}\text{O}_{62}]^{6-}$ for nitrite reduction.⁶³ The POMs were mixed with methyl methacrylate polymeric matrix and graphite powders and the slurry was dropped on wax impregnated graphite (WIG) electrode with evaporation. The redox behavior of $[\text{P}_2\text{Mo}_{18}\text{O}_{62}]^{6-}$ was conserved while the redox behavior of $[\text{P}_2\text{W}_{18}\text{O}_{62}]^{6-}$ changes from one two-electrons wave to two one-electron waves with a shift at more negative potentials. At 0.5 M H_2SO_4 , the reduction of nitrite is detected, but only starting with the second wave and this is very different from the behavior in solution. By comparing this study with the one of immobilization with PANI (and even PVP), we can notice that the immobilization matrix has a tremendous influence on the electrocatalytic behavior towards nitrite reduction.

Electrospinning of a mixture of poly(vinyl-alcohol) and $[\text{P}_2\text{W}_{18}\text{O}_{62}]^{6-}$ was used to obtain nanofibers onto the surface of an ITO electrode.¹⁶⁵ The redox behavior of $[\text{P}_2\text{W}_{18}\text{O}_{62}]^{6-}$ was quite altered because the first two one-electron waves are not clearly separated. The electroreduction of nitrite was performed only in 0.1 M H_2SO_4 with an upper limit of nitrite concentration of 1.5 mM. A very recent example is the development of a quite complex electrode for nitrite detection. A bionanocomposite is obtained via electrostatic reaction between Keggin POM $[\text{BW}_{12}\text{O}_{40}]^{5-}$ and gelatin solution (Figure 1.4.10). This hybrid hydrogel is deposited on a GC previously modified with an ionic liquid, i.e. 1-n-Butyl-3-methylimidazolium (BMIM) hexafluorophosphate. The role of IL is to increase the charge transfer rate.¹⁶⁶

a)



b)

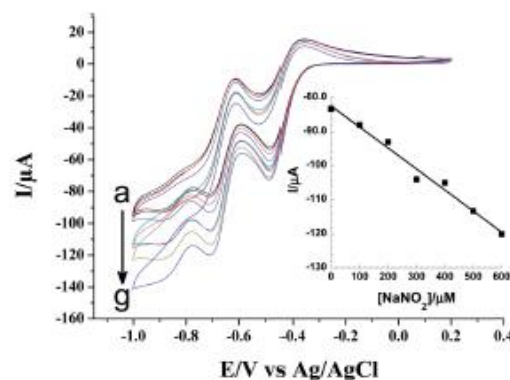


Figure 1.4.10 a) Scheme of a glassy carbon electrode modified with an ionic liquid layer and a gelatin-POM complex. The used POM is $[\text{BW}_{12}\text{O}_{40}]^{5-}$. b) Cyclic voltammetry for different additions of nitrite. Experimental conditions: 0.5 M Na_2SO_4 pH 3, from a to g is 0, 100, 200, 300, 400, 500, 600 μM of nitrite. Inset: calibration current obtained at -0.72 V vs. Ag/AgCl.¹⁶⁶

In conclusion, Table 1.4.4 briefly summarizes the variation of immobilization techniques and experimental conditions employed for heterogeneous catalysis of nitrite reduction by POMs.

Table 1.4.4 Summary of immobilization techniques of various POMs for developing sensor for nitrite detection.

Immobilization	POM	Type of POM	Experimental conditions regarding NO ₂ ⁻ reduction	Ref.
Immobilization via adsorption				
GC/ox-SWCNT or rGO/POM	[PMo ₁₁ O ₃₉] ⁷⁻	Keggin	pH 1, 0.1 M H ₂ SO ₄ , NO ₂ ⁻ up to 14 mM	151
GC/BMIM-POM	[PMo ₁₂ O ₄₀] ³⁻		pH 0, 0.5 M H ₂ SO ₄ , NO ₂ ⁻ up to 3.5 mM	152
GC/MWCNT/C ₁₂ Py-POM	[PMo ₁₂ O ₄₀] ³⁻		pH 1.1, 0.5 M Na ₂ SO ₄ , NO ₂ ⁻ up to 23 mM	154
CPE/EMIM-POM	[PMo ₁₂ O ₄₀] ³⁻		pH -0.3, 1 M H ₂ SO ₄ , NO ₂ ⁻ up to 10 mM	155
Immobilization of POMs via layer-by-layer with electrostatic interactions				
GC/PAH/POM	[SiW ₁₁ O ₃₉] ⁸⁻	Keggin	pH 0.7, 0.1 M H ₂ SO ₄ , NO ₂ ⁻ up to 3.6 mM	159
ITO/PEI/PSS/PDDA/POM	[P ₂ VW ₁₇ O ₆₅] ⁷⁻		pH 7, 0.05 M phosphate buffer saline, NO ₂ ⁻ up to 2.13 mM (*)	161
GC/PEI/rGO-PDDA/POM	[PVMo ₁₁ O ₄₀] ⁴⁻		pH 7, 0.2 M phosphate buffer saline, NO ₂ ⁻ up to 1.2 mM (*)	162
GC/PEI/rGO-PDDA/POM	[PV ₂ Mo ₁₀ O ₄₀] ⁵⁻		pH 1, H ₂ SO ₄ , NO ₂ ⁻ up to 3	163

			mM (*)	
GC/PVA-PVP-NH ₄ ⁺ /POM	[P ₂ W ₁₈ O ₆₂] ⁶⁻	Dawson	pH 0, 0.5 M H ₂ SO ₄ , NO ₂ ⁻ up to 34 mM	156
GC/PDDA/POM/AgNPs	[Fe ^{III} P ₂ W ₁₇ O ₆₁] ⁸⁻ α_2 -[Cu ^{II} ₂ W ₁₇ O ₆₁] ⁸⁻ α_2 -[Ni ^{II} P ₂ W ₁₇ O ₆₁] ⁸⁻		pH 4.5, up to 1 mM NO ₂ ⁻ and NO ₃ ⁻	158
ITO/PVA/PDDA/POM	[P ₂ W ₁₈ O ₆₂] ⁶⁻		pH 0.7, 0.1 M H ₂ SO ₄ , NO ₂ ⁻ up to 40 mM	160
Immobilization of POMs via entrapment in polymer or other matrices				
GC/PANI/POM	[SiMo ₁₂ O ₄₀] ⁴⁻	Keggin	pH 2, 0.2 M Na ₂ SO ₄ + H ₂ SO ₄ , 10 ⁻² M NaNO ₂	164
GC/PVP/POM	[SiW ₁₂ O ₄₀] ⁴⁻		pH 2, 0.2 M Na ₂ SO ₄ + H ₂ SO ₄ , 5*10 ⁻² M NaNO ₂	164
GC/BMIM/gelatin-POM	[BW ₁₂ O ₄₀] ⁵⁻		pH 3, 0.5 M Na ₂ SO ₄ , NO ₂ ⁻ up to 600 μM	166
GC/PANI/POM	[P ₂ Mo ₁₈ O ₆₂] ⁶⁻	Dawson	pH 2, 0.2 M Na ₂ SO ₄ + H ₂ SO ₄ , 5*10 ⁻³ M NaNO ₂	164
GC/PVP/POM	[P ₂ W ₁₈ O ₆₂] ⁶⁻		pH 2, 0.2 M Na ₂ SO ₄ + H ₂ SO ₄ , 5*10 ⁻³ M NaNO ₂	164
GC/WIG/POM	[P ₂ W ₁₈ O ₆₂] ⁶⁻ , [P ₂ Mo ₁₈ O ₆₂] ⁶⁻		pH 0, 0.5 M H ₂ SO ₄ , NO ₂ ⁻ up to 240 mM	63
ITO/PVA/POM	[P ₂ W ₁₈ O ₆₂] ⁶⁻		pH 0.7, 0.1 M H ₂ SO ₄ , NO ₂ ⁻ up to 1.5 mM	165

rGO: Reduced graphene oxide

Ox-SWCNT: Oxidized single-walled carbon nanotubes

MWCNT: Multi-wall carbon nanotubes

C₁₂Py: N-dodecyl pyridinium hexafluorophosphate ([C₁₂Py][PF₆])

BMIM: 1-n-Butyl-3-methylimidazolium tetrafluoroborate (BMIM⁺BF₄⁻)

EMIM: 1-methyl-3-methylimidazolium tetrafluoroborate (EMIMBF₄)

PAH: Poly(allylamine hydrochloride)

ITO: Indium tin oxide

PEI: Poly(ethyleneimine)

PSS: Poly(styrenesulfonate)

PDDA: Poly-diallyldimethylammonium chloride

PVA: Poly (1-acetyloxiethylene)

PVP: Polyvinylpyrrolidone

PANI: Polyaniline

WIG: Wax impregnated graphite

(*) for nitrite electro-oxidation

1.5 DEMS studies of POM-based catalysis of electrochemical reduction of nitrite

Polyoxometalates have been extensively studied in the electrocatalytic reduction of nitrite. However, compared with all the information gathered on the reaction catalyzed by metals, the mechanism and identity of products are unclear. Thus, it appears that DEMS technique could be used to identify volatile products and give more insights on the mechanism of nitrite reduction catalyzed by POMs.

Surprisingly, there is only one published study in which DEMS was used for analyzing nitrite reduction by POM. The used POM is $[\text{SiMo}_{12}\text{O}_{40}]^{4-}$ and the study is performed with POM in solution as well as immobilized on platinum electrode via a polypyrrole film (PPy).¹⁶⁷ For $[\text{SiMo}_{12}\text{O}_{40}]^{4-}$ dissolved in solution, DEMS data shown only the reduction of HNO_2 to NO, with no signal of N_2O (Figure 1.5.1a). For $[\text{SiMo}_{12}\text{O}_{40}]^{4-}$ immobilized in the PPy film DEMS data show not only the reduction of HNO_2 to NO but also the reduction of NO to N_2O . In Figure 1.5.1b the potential is shifted from OCP to a potential corresponding to the first two-electrons reduction wave of the POM. A consumption of NO simultaneously with the production of N_2O is observed.

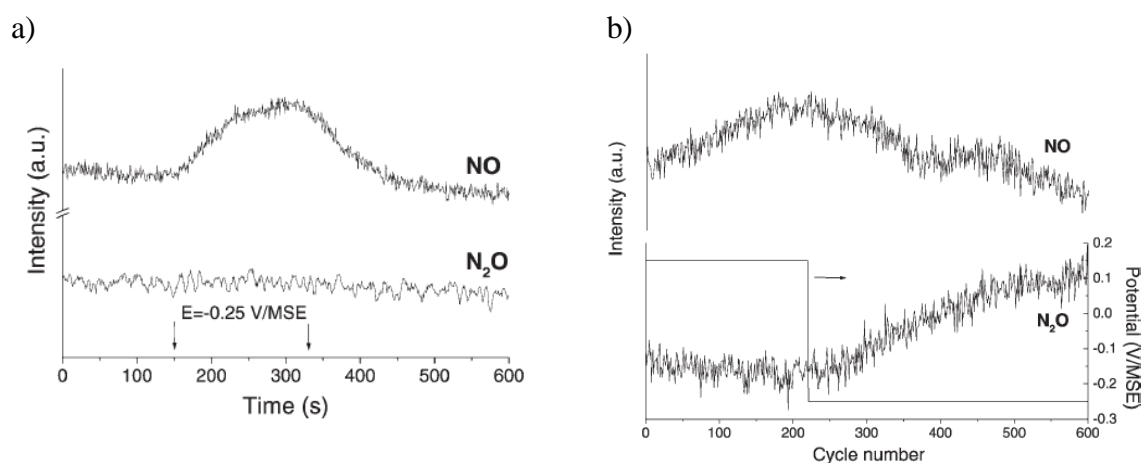


Figure 1.5.1 Mass spectrometer ion current corresponding to NO, $m/z = 30$ (top) and N_2O , $m/z = 44$ (bottom). a) A potential of -0.25 V/MSE was applied during 180 s for a Pt electrode with SiMo_{12} in solution. b) The potential of $\text{Pt/PPy}/[\text{SiMo}_{12}\text{O}_{40}]^{4-}$ electrode is decreased from open circuit to -0.25 V vs. MSE . Experimental conditions: $0.1 \text{ M H}_2\text{SO}_4$, (a) $1 \text{ mM } [\text{SiMo}_{12}\text{O}_{40}]^{4-}$ and (b) 0.01 M NaNO_2 .¹⁶⁷

1.6 References

1. Berzelius, J., The preparation of the phosphomolybdate ion $[\text{PMo}_{12}\text{O}_{40}]^{3-}$. *Pogg. Ann* **1826**, 6, 369-371.
2. (a) Chai, D.; Gómez-García, C. J.; Li, B.; Pang, H.; Ma, H.; Wang, X.; Tan, L., Polyoxometalate-based

- metal-organic frameworks for boosting electrochemical capacitor performance. *Chemical Engineering Journal* **2019**, 373, 587-597; (b) Lu, B.; Li, S.; Pan, J.; Zhang, L.; Xin, J.; Chen, Y.; Tan, X., pH-controlled assembly of five new organophosphorus Strandberg-type cluster-based coordination polymers for enhanced electrochemical capacitor performance. *Inorganic chemistry* **2020**, 59 (3), 1702-1714; (c) Wang, X.-L.; Tian, Y.; Chang, Z.-H.; Lin, H., A Series of Polyoxometalate-Based Metal-Bis (pyridyl-tetrazole) Complexes with High Electrocatalytic Activity for Hydrogen Evolution Reaction in Alkaline and Acid Media. *ACS Sustainable Chemistry & Engineering* **2020**, 8 (41), 15696-15702.
3. Huang, B.; Yang, D.-H.; Han, B.-H., Application of polyoxometalate derivatives in rechargeable batteries. *Journal of Materials Chemistry A* **2020**, 8 (9), 4593-4628.
4. (a) Ammam, M., Polyoxometalates: formation, structures, principal properties, main deposition methods and application in sensing. *Journal of Materials Chemistry A* **2013**, 1 (21), 6291-6312; (b) Gerth, H. U.; Rompel, A.; Krebs, B.; Boos, J.; Lanvers-Kaminsky, C., Cytotoxic effects of novel polyoxotungstates and a platinum compound on human cancer cell lines. *Anti-Cancer Drugs* **2005**, 16 (1), 101-106; (c) Hasenknopf, B., Polyoxometalates: introduction to a class of inorganic compounds and their biomedical applications. *Front. Biosci* **2005**, 10 (275), 10.2741; (d) Du, D.-Y.; Yan, L.-K.; Su, Z.-M.; Li, S.-L.; Lan, Y.-Q.; Wang, E.-B., Chiral polyoxometalate-based materials: From design syntheses to functional applications. *Coordination Chemistry Reviews* **2013**, 257 (3-4), 702-717.
5. (a) Ueda, T., Electrochemistry of polyoxometalates: from fundamental aspects to applications. *ChemElectroChem* **2018**, 5 (6), 823-838; (b) Sartorel, A.; Carraro, M.; Scorrano, G.; Zorzi, R. D.; Geremia, S.; McDaniel, N. D.; Bernhard, S.; Bonchio, M., Polyoxometalate embedding of a tetraruthenium (IV)-oxo-core by template-directed metalation of $[\gamma\text{-SiW}_{10}\text{O}_{36}]^{8-}$: a totally inorganic oxygen-evolving catalyst. *Journal of the American Chemical Society* **2008**, 130 (15), 5006-5007; (c) Haber, J.; Matachowski, L.; Mucha, D.; Stoch, J.; Sarv, P., New Evidence on the Structure of Potassium Salts of 12-Tungstophosphoric Acid, $\text{K}_x\text{H}_{(3-x)}\text{PW}_{12}\text{O}_{40}$. *Inorganic chemistry* **2005**, 44 (19), 6695-6703; (d) R  ther, T.; Hultgren, V. M.; Timko, B. P.; Bond, A. M.; Jackson, W. R.; Wedd, A. G., Electrochemical investigation of photooxidation processes promoted by sulfo-polyoxometalates: coupling of photochemical and electrochemical processes into an effective catalytic cycle. *Journal of the American Chemical Society* **2003**, 125 (33), 10133-10143.
6. Wang, D.; Liu, L.; Jiang, J.; Chen, L.; Zhao, J., Polyoxometalate-based composite materials in electrochemistry: state-of-the-art progress and future outlook. *Nanoscale* **2020**, 12 (10), 5705-5718.
7. Wang, H.; Hamanaka, S.; Nishimoto, Y.; Irle, S.; Yokoyama, T.; Yoshikawa, H.; Awaga, K., In operando X-ray absorption fine structure studies of polyoxometalate molecular cluster batteries: polyoxometalates as electron sponges. *Journal of the American Chemical Society* **2012**, 134 (10), 4918-4924.
8. Dhifallah, F.; Belkhiria, M. S.; Parent, L.; Leclerc, N.; Cadot, E., A series of octahedral first-row transition-metal ion complexes templated by wells-dawson polyoxometalates: synthesis, crystal structure, spectroscopic, and thermal characterizations, and electrochemical properties. *Inorganic Chemistry* **2018**, 57 (19), 11909-11919.
9. Long, D.-L.; Burkholder, E.; Cronin, L., Polyoxometalate clusters, nanostructures and materials: From self assembly to designer materials and devices. *Chemical Society Reviews* **2007**, 36 (1), 105-121.
10. Huang, B.; Wang, N.; Yang, K.; Ke, D.; Fang, Y.; Hu, X.; Wu, B.; Xiao, Z.; Wu, P.; Wei, Y., Stepwise syntheses and supramolecular assemblies of a series of polyoxovanadate hybrids with various architectures. *New Journal of Chemistry* **2018**, 42 (8), 5853-5858.
11. Wilson, E. F.; Miras, H. N.; Rosnes, M. H.; Cronin, L., Real-Time Observation of the Self-Assembly of Hybrid Polyoxometalates Using Mass Spectrometry. *Angewandte Chemie International Edition* **2011**, 50 (16), 3720-3724.
12. Luo, W.; Hu, J.; Diao, H.; Schwarz, B.; Streb, C.; Song, Y. F., Robust polyoxometalate/nickel foam

- composite electrodes for sustained electrochemical oxygen evolution at high pH. *Angewandte Chemie International Edition* **2017**, *56* (18), 4941-4944.
13. Jia, Y.; Zhang, J.; Zhang, Z.-M.; Li, Q.-Y.; Wang, E.-B., Metal-centered polyoxometalates encapsulated by surfactant resulting in the thermotropic liquid crystal materials. *Inorganic Chemistry Communications* **2014**, *43*, 5-9.
 14. (a) Yang, D.; Li, S.; Ma, P.; Wang, J.; Niu, J., Carboxylate-functionalized phosphomolybdates: ligand-directed conformations. *Inorganic Chemistry* **2013**, *52* (15), 8987-8992; (b) Niu, J.; Ma, P.; Niu, H.; Li, J.; Zhao, J.; Song, Y.; Wang, J., Giant polyniobate clusters based on $[\text{Nb}_7\text{O}_{22}]^{9-}$ units derived from a Nb_6O_{19} precursor. *Chemistry—A European Journal* **2007**, *13* (31), 8739-8748; (c) Mitchell, S. G.; Streb, C.; Miras, H. N.; Boyd, T.; Long, D.-L.; Cronin, L., Face-directed self-assembly of an electronically active Archimedean polyoxometalate architecture. *Nature Chemistry* **2010**, *2* (4), 308-312; (d) Reinoso, S.; Giménez-Marqués, M.; Galán-Mascarós, J. R.; Vitoria, P.; Gutiérrez-Zorrilla, J. M., Giant Crown-Shaped Polytungstate Formed by Self-Assembly of Ce(III) -Stabilized Dilacunary Keggin Fragments. *Angewandte Chemie* **2010**, *122* (45), 8562-8566; (e) Fang, X.; Kögerler, P.; Furukawa, Y.; Speldrich, M.; Luban, M., Molecular growth of a core-shell polyoxometalate. *Angewandte Chemie International Edition* **2011**, *50* (22), 5212-5216; (f) Hou, Y.; Nyman, M.; Rodriguez, M. A., Soluble heteropolyniobates from the bottom of group IA. *Angewandte Chemie* **2011**, *123* (52), 12722-12725; (g) Schäffer, C.; Todea, A. M.; Bögge, H.; Cadot, E.; Gouzerh, P.; Kopilevich, S.; Weinstock, I. A.; Müller, A., Softening of Pore and Interior Properties of a Metal-Oxide-Based Capsule: Substituting 60 Oxide by 60 Sulfide Ligands. *Angewandte Chemie International Edition* **2011**, *50* (51), 12326-12329; (h) Marrot, J.; Pilette, M. A.; Haouas, M.; Floquet, S.; Taulelle, F.; Lopez, X.; Poblet, J. M.; Cadot, E., Polyoxometalates paneling through $\{\text{Mo}_2\text{O}_2\text{S}_2\}$ coordination: cation-directed conformations and chemistry of a supramolecular hexameric scaffold. *Journal of the American Chemical Society* **2012**, *134* (3), 1724-1737.
 15. (a) Coronado, E.; Gómez-García, C. J., Polyoxometalate-based molecular materials. *Chemical reviews* **1998**, *98* (1), 273-296; (b) Li, J.-K.; Dong, J.; Wei, C.-P.; Yang, S.; Chi, Y.-N.; Xu, Y.-Q.; Hu, C.-W., Controllable synthesis of lindqvist alkoxopolyoxovanadate clusters as heterogeneous catalysts for sulfoxidation of sulfides. *Inorganic Chemistry* **2017**, *56* (10), 5748-5756; (c) Yin, P.; Li, D.; Liu, T., Solution behaviors and self-assembly of polyoxometalates as models of macroions and amphiphilic polyoxometalate-organic hybrids as novel surfactants. *Chemical Society Reviews* **2012**, *41* (22), 7368-7383; (d) Lv, H.; Geletii, Y. V.; Zhao, C.; Vickers, J. W.; Zhu, G.; Luo, Z.; Song, J.; Lian, T.; Musaev, D. G.; Hill, C. L., Polyoxometalate water oxidation catalysts and the production of green fuel. *Chemical Society Reviews* **2012**, *41* (22), 7572-7589.
 16. (a) Miras, H. N.; Yan, J.; Long, D.-L.; Cronin, L., Engineering polyoxometalates with emergent properties. *Chemical Society Reviews* **2012**, *41* (22), 7403-7430; (b) Zheng, S.-T.; Yang, G.-Y., Recent advances in paramagnetic-TM-substituted polyoxometalates (TM= Mn, Fe, Co, Ni, Cu). *Chemical Society Reviews* **2012**, *41* (22), 7623-7646; (c) Yue, Z.-C.; Shen, L.-X.; Wu, H.-H.; Li, X.-H.; Niu, Y.-Y., pH-dependent assembly of metal-organic hybrid compounds based on octamolybdates and a new flexible multidentate ligand. *CrystEngComm* **2013**, *15* (46), 9938-9948; (d) Modéc, B.; Brenčič, J. V.; Zubieta, J., The solvothermal synthesis and the crystal structure of polymeric N-methylpyridinium octamolybdate (VI), $(\text{Me-NC}_5\text{H}_5)_{4n}[\text{Mo}_8\text{O}_{26}]_n$. *Inorganic Chemistry Communications* **2003**, *6* (5), 506-512.
 17. King, R., Chemical applications of topology and group theory. 25. Electron delocalization in early-transition-metal heteropoly- and isopolyoxometalates. *Inorganic Chemistry* **1991**, *30* (23), 4437-4440.
 18. Richardt, P. J.; Gable, R. W.; Bond, A. M.; Wedd, A. G., Synthesis and Redox Characterization of the Polyoxo Anion, $\gamma^*[\text{S}_2\text{W}_{18}\text{O}_{62}]^{4-}$: A Unique Fast Oxidation Pathway Determines the Characteristic Reversible Electrochemical Behavior of Polyoxometalate Anions in Acidic Media. *Inorganic Chemistry* **2001**, *40* (4), 703-709.

19. (a) Proust, A.; Matt, B.; Villanneau, R.; Guillemot, G.; Gouzerh, P.; Izzet, G., Functionalization and post-functionalization: a step towards polyoxometalate-based materials. *Chemical Society Reviews* **2012**, *41* (22), 7605-7622; (b) Izzet, G.; Ishow, E.; Delaire, J.; Afonso, C.; Tabet, J.-C.; Proust, A., Photochemical activation of an azido manganese-monosubstituted Keggin polyoxometalate: On the road to a Mn (V)– nitrido derivative. *Inorganic Chemistry* **2009**, *48* (24), 11865-11870; (c) Izarova, N. V.; Vankova, N.; Heine, T.; Biboum, R. N.; Keita, B.; Nadj, L.; Kortz, U., Polyoxometalates made of gold: the polyoxoaurate $[\text{Au}^{\text{III}}_4\text{As}^{\text{V}}_4\text{O}_{20}]^{8-}$. *Angewandte Chemie International Edition* **2010**, *49* (10), 1886-1889.
20. Keggin, J., Structure of the crystals of 12-phosphotungstic acid. *Nature* **1933**, *132* (3331), 351-351.
21. Hori, T.; Himeno, S.; Tamada, O., Crystal structure of bis (tetra-n-butylammonium) dodecamolybdosulfate (VI)-(2-), $[\text{NBu}^n_4]_2[\text{SMo}_{12}\text{O}_{40}]$. *Journal of the Chemical Society, Dalton Transactions* **1996**, (10), 2083-2087.
22. WANG, J.-p.; Jie, L.; NIU, J.-y., Hybrid Tungstocuprate $[\text{Cu}(2, 2'\text{-bpy})_3]_2\text{H}_4[\text{CuW}_{12}\text{O}_{40}] \cdot 6\text{H}_2\text{O}$ Based on Keggin Polyoxoanion $[\text{CuW}_{12}\text{O}_{40}]^{6-}$ with Cu^{II} as Heteroatom. *Chemical Research in Chinese Universities* **2007**, *23* (3), 263-267.
23. Baker, L. C.; Figgis, J. S., New fundamental type of inorganic complex: hybrid between heteropoly and conventional coordination complexes. Possibilities for geometrical isomerisms in 11-, 12-, 17-, and 18-heteropoly derivatives. *Journal of the American Chemical Society* **1970**, *92* (12), 3794-3797.
24. (a) Barrows, J. N.; Jameson, G. B.; Pope, M. T., Structure of a heteropoly blue. The four-electron reduced. beta.-12-molybdophosphate anion. *Journal of the American Chemical Society* **1985**, *107* (6), 1771-1773; (b) Vu, T.; Bond, A. M.; Hockless, D. C.; Moubaraki, B.; Murray, K. S.; Lazarev, G.; Wedd, A. G., Electrochemical synthesis and structural and physical characterization of one-and two-electron-reduced forms of $[\text{SMo}_{12}\text{O}_{40}]^{2-}$. *Inorganic Chemistry* **2001**, *40* (1), 65-72.
25. (a) Tian, A.-X.; Hou, X.; Ying, J.; Liu, G.-C.; Yang, Y.; Ning, Y.-L.; Li, T.-J.; Wang, X.-L., A series of polyoxometalate-based compounds including infinite Ag belts and circles constructed by two tolyl-1 H-tetrazole isomers. *RSC Advances* **2015**, *5* (66), 53757-53765; (b) Zhang, C.; Lin, X.; Zhang, Z.; Long, L.-S.; Wang, C.; Lin, W., A hybrid polyoxometalate–organic molecular catalyst for visible light driven water oxidation. *Chemical Communications* **2014**, *50* (78), 11591-11594; (c) Yuan, M.; Li, Y.; Wang, E.; Tian, C.; Wang, L.; Hu, C.; Hu, N.; Jia, H., Modified polyoxometalates: hydrothermal syntheses and crystal structures of three novel reduced and capped Keggin derivatives decorated by transition metal complexes. *Inorganic chemistry* **2003**, *42* (11), 3670-3676; (d) Bakri, R.; Booth, A.; Harle, G.; Middleton, P. S.; Wills, C.; Clegg, W.; Harrington, R. W.; Errington, R. J., Rational addition of capping groups to the phosphomolybdate Keggin anion $[\text{PMo}_{12}\text{O}_{40}]^{3-}$ by mild, non-aqueous reductive aggregation. *Chemical Communications* **2012**, *48* (22), 2779-2781; (e) Dai, L.; Ma, Y.; Wang, E.; Lu, Y.; Xu, X.; Bai, X., Hydrothermal synthesis and crystal structure of two new α -Keggin derivatives decorated by transition metal complexes. *Transition metal chemistry* **2006**, *31* (3), 340-346; (f) Tian, A.-X.; Ning, Y.-L.; Ying, J.; Liu, G.-C.; Hou, X.; Li, T.-J.; Wang, X.-L., Subtly tuning one N site of benzyl-1 H-triazole ligands to build mono-nuclear subunits and tri-nuclear clusters to modify polyoxometalates. *CrystEngComm* **2015**, *17* (29), 5569-5578; (g) Chen, W.-H.; Mi, J.-X., A new redox-based approach for synthesizing a mixed-valence hybrid polymolybdate uncommonly bicapped by Cr (III) coordination complexes. *Polyhedron* **2015**, *85*, 117-123.
26. (a) López, X.; Poblet, J. M., DFT study on the five isomers of $\text{PW}_{12}\text{O}_{40}^{3-}$: Relative stabilization upon reduction. *Inorganic chemistry* **2004**, *43* (22), 6863-6865; (b) López, X.; Carbó, J. J.; Bo, C.; Poblet, J. M., Structure, properties and reactivity of polyoxometalates: a theoretical perspective. *Chemical Society Reviews* **2012**, *41* (22), 7537-7571; (c) Lopez, X.; Maestre, J. M.; Bo, C.; Poblet, J.-M., Electronic properties of polyoxometalates: A DFT study of $\alpha/\beta\text{-}[\text{XM}_{12}\text{O}_{40}]^n$ relative stability (M= W, Mo and X a main group element). *Journal of the American Chemical Society* **2001**, *123* (39), 9571-9576; (d) Müller, A.; Beugholt, C.; Kögerler, P.;

- Bögge, H.; Bud'ko, S.; Luban, M., $[\text{Mo}^{\text{V}}_{12}\text{O}_{30}(\mu_2\text{-OH})_{10}\text{H}_2\{\text{Ni}^{\text{II}}(\text{H}_2\text{O})_3\}_4]$, a highly symmetrical ε -Keggin unit capped with four NiII centers: synthesis and magnetism. *Inorganic Chemistry* **2000**, 39 (23), 5176-5177; (e) Dong, B.-X.; Wu, Y.-C.; Tian, H.; Liu, C.-B.; Liu, W.-L.; Teng, Y.-L., Synthesis, Crystal Structure and Electrochemical Properties of A New 2D Network Containing Linear $\{\varepsilon\text{-H}_2\text{PMo}^{\text{V}}_8\text{Mo}^{\text{VI}}_4\text{O}_{40}\text{Zn}_4\}_\infty$ Inorganic Chain. *Journal of Cluster Science* **2016**, 27 (1), 361-371; (f) Yu, H.-H.; Cui, X.-B.; Cui, J.-W.; Kong, L.; Duan, W.-J.; Xu, J.-Q.; Wang, T.-G., Hydrothermal synthesis and structural characterization of the first mixed molybdenum–tungsten capped-keggin polyoxometal complex: $\{[\text{Co}(\text{dien})]_4[(\text{As}^{\text{V}}\text{O}_4)\text{Mo}^{\text{V}}_8\text{W}^{\text{VI}}_4\text{O}_{33}(\mu_2\text{-OH})_3]\}\cdot 2\text{H}_2\text{O}$. *Dalton Transactions* **2008**, (2), 195-197; (g) Wang, W.; Xu, L.; Gao, G.; Liu, L.; Liu, X., The first ε -Keggin core of molybdo germanate in extended architectures of nickel (II) with N-donor ligands: Syntheses, crystal structures and magnetic properties. *CrystEngComm* **2009**, 11 (11), 2488-2493; (h) Cui, X. B.; Zheng, S. T.; Yang, G. Y., First Nickel (II) Cation Inclusion within the Mixed-valence Polyoxomolybdate Capped with Four $\text{Ni}^{\text{II}}(\text{en})(\text{H}_2\text{O})$ Groups: Hydrothermal Synthesis and Structure of $[\text{Mo}^{\text{V}}_8\text{Mo}^{\text{VI}}_4\text{O}_{30}(\mu_2\text{-OH})_6(\text{Ni}^{\text{II}}\text{O}_4)\{\text{Ni}^{\text{II}}(\text{en})(\text{H}_2\text{O})\}_4]$. *Zeitschrift für anorganische und allgemeine Chemie* **2005**, 631 (4), 642-644.
27. Long, D. L.; Tsunashima, R.; Cronin, L., Polyoxometalates: building blocks for functional nanoscale systems. *Angewandte Chemie International Edition* **2010**, 49 (10), 1736-1758.
28. (a) Li, Y.; Wang, S.; Tang, Z.; Bawa, M.; Ji, Y.; Wang, X.; Zhang, K., Visual detection of H_2O_2 and melamine based on $\text{PW}_{11}\text{MO}_{39}^{n-}$ ($\text{M} = \text{Cu}^{2+}, \text{Co}^{2+}, \text{Mn}^{2+}, \text{Fe}^{3+}$) and $\text{PW}_9\text{M}_3\text{O}_{34}^{n-}$ ($\text{M} = \text{Cu}^{2+}, \text{Co}^{2+}, \text{Mn}^{2+}, \text{Fe}^{3+}$). *New Journal of Chemistry* **2019**, 43 (46), 18018-18026; (b) Anyushin, A. V.; Kondinski, A.; Parac-Vogt, T. N., Hybrid polyoxometalates as post-functionalization platforms: from fundamentals to emerging applications. *Chemical Society Reviews* **2020**, 49 (2), 382-432; (c) Odyakov, V. F.; Zhizhina, E. G.; Rodikova, Y. A.; Gogin, L. L., $\text{Mo}\square\text{V}\square\text{Phosphoric}$ Heteropoly Acids and Their Salts: Aqueous Solution Preparation–Challenges and Perspectives. *European Journal of Inorganic Chemistry* **2015**, 2015 (22), 3618-3631.
29. Uchida, S., Frontiers and progress in cation-uptake and exchange chemistry of polyoxometalate-based compounds. *Chemical Science* **2019**, 10 (33), 7670-7679.
30. Borrás-Almenar, J. J.; Coronado, E.; Müller, A.; Pope, M., *Polyoxometalate molecular science*. Springer Science & Business Media: 2003; Vol. 98.
31. (a) Keita, B.; Bouaziz, D.; Nadjo, L., Solvent effects on the redox potentials of potassium $12\square$ tungstosilicate and $18\square$ tungstodiphosphate. *Journal of The Electrochemical Society* **1988**, 135 (1), 87; (b) Keita, B.; Nadjo, L., New aspects of the electrochemistry of heteropolyacids: part IV. Acidity dependent cyclic voltammetric behaviour of phosphotungstic and silicotungstic heteropolyanions in water and N, N-dimethylformamide. *Journal of electroanalytical chemistry and interfacial electrochemistry* **1987**, 227 (1-2), 77-98; (c) Keita, B.; Nadjo, L., New aspects of the electrochemistry of heteropolyacids: Part III. Further proof of minimal solvation and ion pairing of silicotungstic and phosphotungstic species in acidic concentrated aqueous solutions of alkali-metal salts. *Journal of electroanalytical chemistry and interfacial electrochemistry* **1987**, 230 (1-2), 267-271; (d) Keita, B.; Nadjo, L., Heterogeneous one-electron exchange of silicotungstic heteropolyanion in dimethylformamide. *Journal of electroanalytical chemistry and interfacial electrochemistry* **1987**, 219 (1-2), 355-363; (e) Keita, B.; Lucas, T.; Nadjo, L., New aspects of the electrochemistry of heteropolyacids: Reduction currents as a probe of solvent-electrolyte interactions. *Journal of electroanalytical chemistry and interfacial electrochemistry* **1986**, 208 (2), 343-356; (f) Pope, M. T.; Papaconstantinou, E., Heteropoly blues. II. Reduction of 2: 18-tungstates. *Inorganic Chemistry* **1967**, 6 (6), 1147-1152.
32. (a) Sun, H.-R.; Zhang, S.-Y.; Xu, J.-Q.; Yang, G.-Y.; Shi, T.-S., Electrochemical and in-situ UV-visible-near-IR and FTIR spectroelectrochemical characterisation of the mixed-valence heteropolyanion $\text{PMo}_{12}\text{O}_{40}^{n-}$ ($n = 4, 5, 6, 7$) in aprotic media. *Journal of Electroanalytical Chemistry* **1998**, 455 (1-2), 57-68; (b) Sadakane, M.; Steckhan, E., Electrochemical properties of polyoxometalates as electrocatalysts. *Chemical reviews* **1998**, 98 (1),

33. Zhang, J.; Bond, A. M.; Richardt, P. J.; Wedd, A. G., Voltammetric Reduction of α - and γ^* -[S₂W₁₈O₆₂]⁴⁻ and α -, β -, and γ -[SiW₁₂O₄₀]⁴⁻: Isomeric Dependence of Reversible Potentials of Polyoxometalate Anions Using Data Obtained by Novel Dissolution and Conventional Solution-Phase Processes. *Inorganic chemistry* **2004**, *43* (26), 8263-8271.
34. (a) Maksimovskaya, R. I., Molybdophosphate heteropoly blues: Electron-transfer reactions in aqueous solutions as studied by NMR. *Polyhedron* **2013**, *65*, 54-59; (b) Sanchez, C.; Livage, J.; Launay, J.; Fournier, M.; Jeannin, Y., Electron delocalization in mixed-valence molybdenum polyanions. *Journal of the American Chemical Society* **1982**, *104* (11), 3194-3202.
35. (a) Pope, M. T.; Varga Jr, G. M., Heteropoly blues. I. Reduction stoichiometries and reduction potentials of some 12-tungstates. *Inorganic Chemistry* **1966**, *5* (7), 1249-1254; (b) Mbomekallé, I.-M.; López, X.; Poblet, J. M.; Sécheresse, F.; Keita, B.; Nadjo, L., Influence of the heteroatom size on the redox potentials of selected polyoxoanions. *Inorganic chemistry* **2010**, *49* (15), 7001-7006.
36. (a) Chen, X.; Wang, Z.; Zhang, R.; Xu, L.; Sun, D., A novel polyoxometalate-based hybrid containing a 2D [CoMo₈O₂₆]_∞ structure as the anode for lithium-ion batteries. *Chemical Communications* **2017**, *53* (76), 10560-10563; (b) Prabhakaran, V.; Lang, Z.; Clotet, A.; Poblet, J. M.; Johnson, G. E.; Laskin, J., Controlling the activity and stability of electrochemical interfaces using atom-by-atom metal substitution of redox species. *ACS nano* **2018**, *13* (1), 458-466; (c) Yin, P.; Wu, P.; Xiao, Z.; Li, D.; Bitterlich, E.; Zhang, J.; Cheng, P.; Vezenov, D. V.; Liu, T.; Wei, Y., A double-tailed fluorescent surfactant with a hexavanadate cluster as the head group. *Angewandte Chemie International Edition* **2011**, *50* (11), 2521-2525; (d) Fu, D.-Y.; Zhang, S.; Qu, Z.; Yu, X.; Wu, Y.; Wu, L., Hybrid assembly toward enhanced thermal stability of virus-like particles and antibacterial activity of Polyoxometalates. *ACS applied materials & interfaces* **2018**, *10* (7), 6137-6145; (e) Liu, Y.; Zhao, S.-F.; Guo, S.-X.; Bond, A. M.; Zhang, J.; Zhu, G.; Hill, C. L.; Geletii, Y. V., Electrooxidation of ethanol and methanol using the molecular catalyst [$\{Ru_4O_4(OH)_2(H_2O)_4\}(\gamma-SiW_{10}O_{36})_2\}]^{10-}$. *Journal of the American Chemical Society* **2016**, *138* (8), 2617-2628; (f) Chen, J. J.; Ye, J. C.; Zhang, X. G.; Symes, M. D.; Fan, S. C.; Long, D. L.; Zheng, M. S.; Wu, D. Y.; Cronin, L.; Dong, Q. F., Design and Performance of Rechargeable Sodium Ion Batteries, and Symmetrical Li-Ion Batteries with Supercapacitor-Like Power Density Based upon Polyoxovanadates. *Advanced Energy Materials* **2018**, *8* (6), 1701021; (g) Liu, J.; Chen, Z.; Chen, S.; Zhang, B.; Wang, J.; Wang, H.; Tian, B.; Chen, M.; Fan, X.; Huang, Y., "Electron/ion sponge"-like V-based polyoxometalate: toward high-performance cathode for rechargeable sodium ion batteries. *ACS nano* **2017**, *11* (7), 6911-6920; (h) Chen, H.-Y.; Friedl, J.; Pan, C.-J.; Haider, A.; Al-Oweini, R.; Cheah, Y. L.; Lin, M.-H.; Kortz, U.; Hwang, B.-J.; Srinivasan, M., In situ X-ray absorption near edge structure studies and charge transfer kinetics of Na₆[V₁₀O₂₈] electrodes. *Physical Chemistry Chemical Physics* **2017**, *19* (4), 3358-3365; (i) Genovese, M.; Lian, K., Polyoxometalate modified inorganic-organic nanocomposite materials for energy storage applications: A review. *Current Opinion in Solid State and Materials Science* **2015**, *19* (2), 126-137; (j) Qiu, X.; Wang, L.; Fan, L.-Z., Immobilization of tungsten disulfide nanosheets on active carbon fibers as electrode materials for high performance quasi-solid-state asymmetric supercapacitors. *Journal of Materials Chemistry A* **2018**, *6* (17), 7835-7841.
37. Guo, Y.; Hu, C., Heterogeneous photocatalysis by solid polyoxometalates. *Journal of Molecular Catalysis A: Chemical* **2007**, *262* (1-2), 136-148.
38. Hiskia, A.; Troupis, A.; Antonaraki, S.; Gkika, E.; Papaconstantinou, P. K. E., Polyoxometallate photocatalysis for decontaminating the aquatic environment from organic and inorganic pollutants. *International Journal of Environmental Analytical Chemistry* **2006**, *86* (3-4), 233-242.
39. Hori, H.; Yamamoto, A.; Koike, K.; Kutsuna, S.; Murayama, M.; Yoshimoto, A.; Arakawa, R.,

- Photocatalytic decomposition of a perfluoroether carboxylic acid by tungstic heteropolyacids in water. *Applied Catalysis B: Environmental* **2008**, 82 (1-2), 58-66.
40. Hu, M.; Xu, Y., Photocatalytic degradation of textile dye X3B by heteropolyoxometalate acids. *Chemosphere* **2004**, 54 (3), 431-434.
 41. Hamadi, H.; Kooti, M.; Afshari, M.; Ghiasifar, Z.; Adibpour, N., Magnetic nanoparticle supported polyoxometalate: An efficient and reusable catalyst for solvent-free synthesis of α -aminophosphonates. *Journal of Molecular Catalysis A: Chemical* **2013**, 373, 25-29.
 42. Xu, L.; Wang, G.; Ma, F.; Zhao, Y.; Lu, N.; Guo, Y.; Yang, X., Photocatalytic degradation of an aqueous sulfamethoxazole over the metallic silver and Keggin unit codoped titania nanocomposites. *Applied Surface Science* **2012**, 258 (18), 7039-7046.
 43. Jin, H.; Wu, Q.; Pang, W., Photocatalytic degradation of textile dye X-3B using polyoxometalate-TiO₂ hybrid materials. *Journal of hazardous materials* **2007**, 141 (1), 123-127.
 44. (a) Liu, Y.; Murata, K.; Inaba, M., Liquid-phase oxidation of benzene to phenol by molecular oxygen over transition metal substituted polyoxometalate compounds. *Catalysis Communications* **2005**, 6 (10), 679-683; (b) Zhu, M.; Peng, J.; Pang, H.-J.; Zhang, P.-P.; Chen, Y.; Wang, D.-D.; Liu, M.-G.; Wang, Y.-H., Polyoxometalate immobilization in CuI/Ag-pz porous coordination polymers: The influences of them on the structural properties of frameworks. *Journal of Solid State Chemistry* **2011**, 184 (5), 1070-1078; (c) Kumar, D.; Landry, C. C., Immobilization of a Mo, V-polyoxometalate on cationically modified mesoporous silica: Synthesis and characterization studies. *Microporous and mesoporous materials* **2007**, 98 (1-3), 309-316; (d) Ruiz, V.; Suárez-Guevara, J.; Gomez-Romero, P., Hybrid electrodes based on polyoxometalate-carbon materials for electrochemical supercapacitors. *Electrochemistry Communications* **2012**, 24, 35-38.
 45. Chalkley, L., The extent of the photochemical reduction of phosphotungstic acid. *The Journal of Physical Chemistry* **1952**, 56 (9), 1084-1086.
 46. Troupis, A.; Hiskia, A.; Papaconstantinou, E., Synthesis of metal nanoparticles by using polyoxometalates as photocatalysts and stabilizers. *Angewandte Chemie International Edition* **2002**, 41 (11), 1911-1914.
 47. Troupis, A.; Gkika, E.; Hiskia, A.; Papaconstantinou, E., Photocatalytic reduction of metals using polyoxometallates: recovery of metals or synthesis of metal nanoparticles. *Comptes Rendus Chimie* **2006**, 9 (5-6), 851-857.
 48. Costa-Coquelard, C.; Schaming, D.; Lampre, I.; Ruhlmann, L., Photocatalytic reduction of Ag₂SO₄ by the Dawson anion α -[P₂W₁₈O₆₂]⁶⁻ and tetracobalt sandwich complexes. *Applied Catalysis B: Environmental* **2008**, 84 (3-4), 835-842.
 49. Keita, B.; Nadjo, L., Activation of electrode surfaces: Application to the electrocatalysis of the hydrogen evolution reaction. *Journal of electroanalytical chemistry and interfacial electrochemistry* **1985**, 191 (2), 441-448.
 50. Zhang, C.; Hong, Y.; Dai, R.; Lin, X.; Long, L.-S.; Wang, C.; Lin, W., Highly active hydrogen evolution electrodes via co-deposition of platinum and polyoxometalates. *ACS Applied Materials & Interfaces* **2015**, 7 (21), 11648-11653.
 51. Rong, C.; Pope, M. T., Lacunary polyoxometalate anions are pi-acceptor ligands. Characterization of some tungstosilicic acid (II, III, IV, V) heteropolyanions and their atom-transfer reactivity. *Journal of the American Chemical Society* **1992**, 114 (8), 2932-2938.
 52. Keita, B.; Kortz, U.; Holzle, L. R. B.; Brown, S.; Nadjo, L., Efficient hydrogen-evolving cathodes based on proton and electron reservoir behaviors of the phosphotungstate [H₇P₈W₄₈O₁₈₄]³³⁻ and the Co (II)-containing silicotungstates [Co₆(H₂O)₃₀{Co₉Cl₂(OH)₃(H₂O)₉(β -SiW₈O₃₁)₃}]⁵⁻ and [{Co₃(B- β -SiW₉O₃₃(OH))(B- β -SiW₈O₂₉(OH)₂)₂}]²²⁻. *Langmuir* **2007**, 23 (19), 9531-9534.

53. Biboum, R. N.; Keita, B.; Franger, S.; Nanseu Njiki, C. P.; Zhang, G.; Zhang, J.; Liu, T.; Mbomekalle, I.-M.; Nadjjo, L., Pd⁰@ polyoxometalate nanostructures as green electrocatalysts: illustrative example of hydrogen production. *Materials* **2010**, *3* (1), 741-754.
54. (a) Qin, J.-S.; Du, D.-Y.; Guan, W.; Bo, X.-J.; Li, Y.-F.; Guo, L.-P.; Su, Z.-M.; Wang, Y.-Y.; Lan, Y.-Q.; Zhou, H.-C., Ultrastable polymolybdate-based metal–organic frameworks as highly active electrocatalysts for hydrogen generation from water. *Journal of the American Chemical Society* **2015**, *137* (22), 7169-7177; (b) Nohra, B.; El Moll, H.; Rodriguez Albelo, L. M.; Mialane, P.; Marrot, J.; Mellot-Draznieks, C.; O’Keeffe, M.; Ngo Biboum, R.; Lemaire, J.; Keita, B., Polyoxometalate-based metal organic frameworks (POMOFs): structural trends, energetics, and high electrocatalytic efficiency for hydrogen evolution reaction. *Journal of the American Chemical Society* **2011**, *133* (34), 13363-13374.
55. Jiang, M.; Zhu, D.; Cai, J.; Zhang, H.; Zhao, X., Electrocatalytic hydrogen evolution and oxygen reduction on polyoxotungstates/graphene nanocomposite multilayers. *The Journal of Physical Chemistry C* **2014**, *118* (26), 14371-14378.
56. Ensafi, A. A.; Heydari-Soureshjani, E.; Jafari-Asl, M.; Rezaei, B., Polyoxometalate-decorated graphene nanosheets and carbon nanotubes, powerful electrocatalysts for hydrogen evolution reaction. *Carbon* **2016**, *99*, 398-406.
57. Ensafi, A. A.; Heydari-Soureshjani, E.; Rezaei, B., Nanostructure polyoxometalates containing Co, Ni, and Cu as powerful and stable catalysts for hydrogen evolution reaction in acidic and alkaline solutions. *International Journal of Hydrogen Energy* **2017**, *42* (8), 5026-5034.
58. Geletii, Y. V.; Botar, B.; Kögerler, P.; Hillesheim, D. A.; Musaev, D. G.; Hill, C. L., An all□inorganic, stable, and highly active tetraruthenium homogeneous catalyst for water oxidation. *Angewandte Chemie* **2008**, *120* (21), 3960-3963.
59. (a) Stracke, J. J.; Finke, R. G., Electrocatalytic Water Oxidation Beginning with the Cobalt Polyoxometalate [Co₄(H₂O)₂(PW₉O₃₄)₂]¹⁰⁻: Identification of Heterogeneous CoO_x as the Dominant Catalyst. *Journal of the American Chemical Society* **2011**, *133* (38), 14872-14875; (b) Stracke, J. J.; Finke, R. G., Water oxidation catalysis beginning with 2.5 μM [Co₄(H₂O)₂(PW₉O₃₄)₂]¹⁰⁻: Investigation of the true electrochemically driven catalyst at ≥ 600 mV overpotential at a glassy carbon electrode. *ACS Catalysis* **2013**, *3* (6), 1209-1219.
60. Vickers, J. W.; Lv, H.; Sumliner, J. M.; Zhu, G.; Luo, Z.; Musaev, D. G.; Geletii, Y. V.; Hill, C. L., Differentiating homogeneous and heterogeneous water oxidation catalysis: Confirmation that [Co₄(H₂O)₂(α-PW₉O₃₄)₂]¹⁰⁻ is a molecular water oxidation catalyst. *Journal of the American Chemical Society* **2013**, *135* (38), 14110-14118.
61. Soriano-Lopez, J.; Goberna-Ferron, S.; Vigara, L.; Carbo, J. J.; Poblet, J. M.; Galán-Mascarós, J. R., Cobalt polyoxometalates as heterogeneous water oxidation catalysts. *Inorganic chemistry* **2013**, *52* (9), 4753-4755.
62. (a) Ji, Y.; Huang, L.; Hu, J.; Streb, C.; Song, Y., Energy Environ. Sci., 2015, *8*, 776–789; (b) SS Wang and GY Yang. *Chem. Rev* **2015**, *115*, 4893-4962; (c) Toma, F. M.; Sartorel, A.; Iurlo, M.; Carraro, M.; Parisse, P.; Maccato, C.; Rapino, S.; Gonzalez, B. R.; Amenitsch, H.; Da Ros, T., Efficient water oxidation at carbon nanotube–polyoxometalate electrocatalytic interfaces. *Nature chemistry* **2010**, *2* (10), 826-831; (d) Toma, F. M.; Sartorel, A.; Iurlo, M.; Carraro, M.; Rapino, S.; Hooper□Burkhardt, L.; Da Ros, T.; Marcaccio, M.; Scorrano, G.; Paolucci, F., Tailored functionalization of carbon nanotubes for electrocatalytic water splitting and sustainable energy applications. *ChemSusChem* **2011**, *4* (10), 1447-1451; (e) Wu, J.; Liao, L.; Yan, W.; Xue, Y.; Sun, Y.; Yan, X.; Chen, Y.; Xie, Y., Polyoxometalates immobilized in ordered mesoporous carbon nitride as highly efficient water oxidation catalysts. *ChemSusChem* **2012**, *5* (7), 1207-1212; (f) Quintana, M.; Lopez, A. M.; Rapino, S.; Toma, F. M.; Iurlo, M.; Carraro, M.; Sartorel, A.; Maccato, C.; Ke, X.; Bittencourt, C., Knitting the catalytic pattern of artificial photosynthesis to a hybrid graphene nanotexture. *ACS nano* **2013**, *7* (1), 811-

- 817; (f) Guo, S.-X.; Liu, Y.; Lee, C.-Y.; Bond, A. M.; Zhang, J.; Geletii, Y. V.; Hill, C. L., Graphene-supported $[\{\text{Ru}_4\text{O}_4(\text{OH})_2(\text{H}_2\text{O})_4\}(\gamma\text{-SiW}_{10}\text{O}_{36})_2]^{10-}$ for highly efficient electrocatalytic water oxidation. *Energy & Environmental Science* **2013**, 6 (9), 2654-2663.
63. Papadakis, A.; Souliotis, A.; Papaconstantinou, E., Functionalization of electrodes with polyoxometalates $\text{P}_2\text{Mo}_{18}\text{O}_{62}^{6-}$ and $\text{P}_2\text{W}_{18}\text{O}_{62}^{6-}$. *Journal of Electroanalytical Chemistry* **1997**, 435 (1-2), 17-21.
64. Sankarraj, A. V.; Ramakrishnan, S.; Shannon, C., Improved oxygen reduction cathodes using polyoxometalate cocatalysts. *Langmuir* **2008**, 24 (3), 632-634.
65. (a) Chojak, M.; Kolary-Zurowska, A.; Wlodarczyk, R.; Miecznikowski, K.; Karnicka, K.; Palys, B.; Marassi, R.; Kulesza, P. J., Modification of Pt nanoparticles with polyoxometallate monolayers: competition between activation and blocking of reactive sites for the electrocatalytic oxygen reduction. *Electrochimica Acta* **2007**, 52 (18), 5574-5581; (b) Wlodarczyk, R.; Kolary-Zurowska, A.; Marassi, R.; Chojak, M.; Kulesza, P. J., Enhancement of oxygen reduction by incorporation of heteropolytungstate into the electrocatalytic ink of carbon supported platinum nanoparticles. *Electrochimica acta* **2007**, 52 (12), 3958-3964; (c) Hsu-Yao, T.; Browne, K. P.; Honesty, N.; Tong, Y. J., Polyoxometalate-stabilized Pt nanoparticles and their electrocatalytic activities. *Physical Chemistry Chemical Physics* **2011**, 13 (16), 7433-7438; (d) Renzi, M.; D'Angelo, G.; Marassi, R.; Nobili, F., Low platinum loading cathode modified with $\text{Cs}_3\text{H}_2\text{PMo}_{10}\text{V}_2\text{O}_{40}$ for polymer electrolyte membrane fuel cells. *Journal of Power Sources* **2016**, 327, 11-20; (e) Renzi, M.; Mignini, P.; Giuli, G.; Marassi, R.; Nobili, F., Rotating disk electrode study of $\text{Pt/Cs}_3\text{HPMo}_{11}\text{VO}_{40}$ composite catalysts for performing and durable PEM fuel cells. *international journal of hydrogen energy* **2016**, 41 (26), 11163-11173.
66. Xie, X.; Nie, Y.; Chen, S.; Ding, W.; Qi, X.; Li, L.; Wei, Z., A catalyst superior to carbon-supported-platinum for promotion of the oxygen reduction reaction: reduced-polyoxometalate supported palladium. *Journal of Materials Chemistry A* **2015**, 3 (26), 13962-13969.
67. Xin, J.; Lindenmuth, T.; Shannon, C., Electrocatalytic oxygen reduction at polyoxometalate/Au-nanoparticle hybrid thin films formed by layer-by-layer deposition. *Electrochimica acta* **2011**, 56 (24), 8884-8890.
68. Bao, Y.-Y.; Bi, L.-H.; Wu, L.-X., One-step synthesis and stabilization of gold nanoparticles and multilayer film assembly. *Journal of Solid State Chemistry* **2011**, 184 (3), 546-556.
69. (a) Liu, W.; Mu, W.; Deng, Y., High performance liquid catalyst fuel cell for direct biomass into electricity conversion. *Angewandte Chemie* **2014**, 126 (49), 13776-13780; (b) Wu, W.; Liu, W.; Mu, W.; Deng, Y., Polyoxymetalate liquid-catalyzed polyol fuel cell and the related photoelectrochemical reaction mechanism study. *Journal of Power Sources* **2016**, 318, 86-92.
70. Bruckenstein, S.; Gadde, R. R., Use of a porous electrode for in situ mass spectrometric determination of volatile electrode reaction products. *Journal of the American Chemical Society* **1971**, 93 (3), 793-794.
71. Wolter, O.; Heitbaum, J., Adsorption of CO on a porous Pt-electrode in sulfuric acid studied by DEMS. *Ber. Bunsenges. Phys. Chem. (Germany, Federal Republic of)* **1984**, 88 (1).
72. Hartung, T.; Schmiemann, U.; Kamphausen, I.; Baltruschat, H., Electrodesorption from single-crystal electrodes: analysis by differential electrochemical mass spectrometry. *Analytical chemistry* **1991**, 63 (1), 44-48.
73. Tegtmeier, D.; Heitbaum, J.; Heindrichs, A., Electrochemical on line mass spectrometry on a rotating electrode inlet system. *Berichte der Bunsengesellschaft für physikalische Chemie* **1989**, 93 (2), 201-206.
74. Jusys, Z.; Massong, H.; Baltruschat, H., A New Approach for Simultaneous DEMS and EQCM: Electro oxidation of Adsorbed CO on Pt and Pt-Ru. *Journal of the electrochemical Society* **1999**, 146 (3), 1093.
75. Heinen, M.; Chen, Y.; Jusys, Z.; Behm, R. J., In situ ATR-FTIRS coupled with on-line DEMS under controlled mass transport conditions—A novel tool for electrocatalytic reaction studies. *Electrochimica acta* **2007**, 52 (18), 5634-5643.

76. Guillén-Villafuerte, O.; García, G.; Arévalo, M. C.; Rodríguez, J. L.; Pastor, E., New insights on the electrochemical oxidation of ethanol on carbon-supported Pt electrode by a novel electrochemical mass spectrometry configuration. *Electrochemistry Communications* **2016**, *63*, 48-51.
77. Baltruschat, H., Differential electrochemical mass spectrometry. *Journal of the American Society for Mass Spectrometry* **2004**, *15* (12), 1693-1706.
78. Bogdanoff, P.; Friebe, P.; Alonso-Vante, N., A New Inlet System for Differential Electrochemical Mass Spectroscopy Applied to the Photocorrosion of p-InP (111) Single Crystals. *Journal of the Electrochemical Society* **1998**, *145* (2), 576.
79. Bogdanoff, P.; Alonso-Vante, N., On-line Determination via Differential Electrochemical Mass Spectroscopy (DEMS) of Chemical Products Formed in Photoelectrocatalytical Systems. *Berichte der Bunsengesellschaft für physikalische Chemie* **1993**, *97* (7), 940-943.
80. Wolter, O.; Heitbaum, J., Differential electrochemical mass spectroscopy (DEMS)—a new method for the study of electrode processes. *Berichte der Bunsengesellschaft für physikalische Chemie* **1984**, *88* (1), 2-6.
81. Gao, Y.; Tsuji, H.; Hattori, H.; Kita, H., New on-line mass spectrometer system designed for platinum-single crystal electrode and electroreduction of acetylene. *Journal of Electroanalytical Chemistry* **1994**, *372* (1-2), 195-200.
82. Ianniello, R.; Schmidt, V. M., A simplified DEMS set up for electrocatalytic studies of porous PtRu alloys. *Berichte der Bunsengesellschaft für physikalische Chemie* **1995**, *99* (1), 83-86.
83. Bondue, C. J.; Koper, M. T., A DEMS approach for the direct detection of CO formed during electrochemical CO₂ reduction. *Journal of Electroanalytical Chemistry* **2020**, *875*, 113842.
84. Fujihira, M.; Noguchi, T., A highly sensitive analysis of electrochemical reduction products of CO₂ on gold by new differential electrochemical mass spectroscopy (dems). *Chemistry letters* **1992**, *21* (10), 2043-2046.
85. (a) Kolbe, D.; Vielstich, W., Adsorbate formation during the electrochemical reduction of carbon dioxide at palladium—A DEMS study. *Electrochimica acta* **1996**, *41* (15), 2457-2460; (b) Kim, Y.-G.; Javier, A.; Baricuatro, J. H.; Torelli, D.; Cummins, K. D.; Tsang, C. F.; Hemminger, J. C.; Soriaga, M. P., Surface reconstruction of pure-Cu single-crystal electrodes under CO-reduction potentials in alkaline solutions: A study by seriatim ECSTM-DEMS. *Journal of Electroanalytical Chemistry* **2016**, *780*, 290-295; (c) Mora-Hernandez, J.; González-Suárez, W. I.; Manzo-Robledo, A.; Luna-Trujillo, M., A comparative differential electrochemical mass spectrometry (DEMS) study towards the CO₂ reduction on Pd, Cu, and Sn-based electrocatalyst. *Journal of CO₂ Utilization* **2021**, *47*, 101504.
86. Schouten, K. J. P.; Gallent, E. P.; Koper, M. T., The influence of pH on the reduction of CO and CO₂ to hydrocarbons on copper electrodes. *Journal of Electroanalytical Chemistry* **2014**, *716*, 53-57.
87. Clark, E. L.; Singh, M. R.; Kwon, Y.; Bell, A. T., Differential electrochemical mass spectrometer cell design for online quantification of products produced during electrochemical reduction of CO₂. *Analytical chemistry* **2015**, *87* (15), 8013-8020.
88. (a) Bagotzy, V.; Vassiliev, Y. B.; Khazova, O., Generalized scheme of chemisorption, electrooxidation and electroreduction of simple organic compounds on platinum group metals. *Journal of Electroanalytical Chemistry and Interfacial Electrochemistry* **1977**, *81* (2), 229-238; (b) Wang, H.; Löffler, T.; Baltruschat, H., Formation of intermediates during methanol oxidation: A quantitative DEMS study. *Journal of applied electrochemistry* **2001**, *31* (7), 759-765.
89. Nia, N. S.; Martucci, A.; Granozzi, G.; García, G.; Pastor, E.; Penner, S.; Bernardi, J.; Alonso-Vante, N.; Kunze-Liebhäuser, J., DEMS studies of the ethanol electro-oxidation on TiO₂C supported Pt catalysts—Support effects for higher CO₂ efficiency. *Electrochimica Acta* **2019**, *304*, 80-86.
90. Zinola, C.; Vasini, E. J.; Mueller, U.; Baltruschat, H.; Arvia, A. J., Detection of CO desorbing from the Ni

electrode surface by DEMS. *Journal of Electroanalytical Chemistry* **1996**, 415.

91. Löffler, T.; Drbálková, E.; Janderka, P.; Königshoven, P.; Baltruschat, H., Adsorption and desorption reactions of bicyclic aromatic compounds at polycrystalline and Pt (111) studied by DEMS. *Journal of Electroanalytical Chemistry* **2003**, 550, 81-92.
92. (a) Karabinas, P.; Wolter, O.; Heitbaum, J., Mechanistic studies with mass spectroscopic cyclic voltammetry: Anodic oxidation of hydroxylamine on Pt. *Berichte der Bunsengesellschaft für physikalische Chemie* **1984**, 88 (12), 1191-1196; (b) Wasmus, S.; Vasini, E.; Krausa, M.; Mishima, H.; Vielstich, W., DEMS-cyclic voltammetry investigation of the electrochemistry of nitrogen compounds in 0.5 M potassium hydroxide. *Electrochimica acta* **1994**, 39 (1), 23-31.
93. (a) Nishimura, K.; Machida, K.; Enyo, M., On-line mass spectroscopy applied to electroreduction of nitrite and nitrate ions at porous Pt electrode in sulfuric acid solutions. *Electrochimica acta* **1991**, 36 (5-6), 877-880; (b) Da Cunha, M.; De Souza, J.; Nart, F., Reaction pathways for reduction of nitrate ions on platinum, rhodium, and platinum– rhodium alloy electrodes. *Langmuir* **2000**, 16 (2), 771-777.
94. Dalmia, A.; Wasmus, S.; Savinell, R.; Liu, C., Electrochemical behavior of sodium azide at Pt and Au electrodes in sodium sulfate electrolyte: a DEMS study. *Journal of the Electrochemical Society* **1995**, 142 (11), 3735.
95. Andersen, S. Z.; Čolić, V.; Yang, S.; Schwalbe, J. A.; Nielander, A. C.; McEnaney, J. M.; Enemark-Rasmussen, K.; Baker, J. G.; Singh, A. R.; Rohr, B. A., A rigorous electrochemical ammonia synthesis protocol with quantitative isotope measurements. *Nature* **2019**, 570 (7762), 504-508.
96. Dima, G.; De Vooys, A.; Koper, M., Electrocatalytic reduction of nitrate at low concentration on coinage and transition-metal electrodes in acid solutions. *Journal of Electroanalytical Chemistry* **2003**, 554, 15-23.
97. (a) De Groot, M.; Koper, M., The influence of nitrate concentration and acidity on the electrocatalytic reduction of nitrate on platinum. *Journal of Electroanalytical Chemistry* **2004**, 562 (1), 81-94; (b) Schmid, G., Die autokatalytische Natur der kathodischen Reduktion von Salpetersäure zu salpetriger Säure I. Zur Deutung stationärer strom–Spannungs–Kurven. *Zeitschrift für Elektrochemie, Berichte der Bunsengesellschaft für physikalische Chemie* **1959**, 63 (9–10), 1183-1188; (c) Schmid, G.; Delfs, J., Die autokatalytische Natur der kathodischen Reduktion von Salpetersäure zu salpetriger Säure II. Der galvanostatische Einschaltvorgang. *Zeitschrift für Elektrochemie, Berichte der Bunsengesellschaft für physikalische Chemie* **1959**, 63 (9–10), 1192-1197; (d) Schmid, G., Die autokatalytische Natur der kathodischen Reduktion von Salpetersäure zu salpetriger Säure: III Mathematische Behandlung einer autokatalytischen Elektrodenreaktion 1. Ordnung. *Zeitschrift für Elektrochemie, Berichte der Bunsengesellschaft für physikalische Chemie* **1961**, 65 (6), 531-534.
98. Huan, H.; Hu, L.; Yang, Y.; Jia, Y.; Lian, X.; Ma, X.; Jiang, Y.; Xi, B., Groundwater nitrate pollution risk assessment of the groundwater source field based on the integrated numerical simulations in the unsaturated zone and saturated aquifer. *Environment International* **2020**, 137, 105532.
99. Ma, X.; Li, M.; Liu, X.; Wang, L.; Chen, N.; Li, J.; Feng, C., A graphene oxide nanosheet-modified Ti nanocomposite electrode with enhanced electrochemical property and stability for nitrate reduction. *Chemical Engineering Journal* **2018**, 348, 171-179.
100. (a) Spalding, R. F.; Exner, M. E., Occurrence of nitrate in groundwater—a review. *Journal of environmental quality* **1993**, 22 (3), 392-402; (b) Widory, D.; Kloppmann, W.; Chery, L.; Bonnin, J.; Rochdi, H.; Guinamant, J.-L., Nitrate in groundwater: an isotopic multi-tracer approach. *Journal of contaminant hydrology* **2004**, 72 (1-4), 165-188.
101. Hong, S.; Zhang, J.; Feng, C.; Zhang, B.; Ma, P., Enhancement of nitrate removal in synthetic groundwater using wheat rice stone. *Water Science and Technology* **2012**, 66 (9), 1900-1907.
102. jinxia, F.; jianjun, Z.; li, C., Prevention, evaluation and prediction method of groundwater nitrate pollution

in China. *Groundwater* **2006**, 28 (4), 58-62.

103. Davey, K., *An Investigation Into the Nitrate Pollution of the Chalk Borehole Water Supplies [of the North Lindsey Water Board]*. North Lindsey Water Board: 1970.

104. Pintar, K. D.; Slawson, R. M., Effect of temperature and disinfection strategies on ammonia-oxidizing bacteria in a bench-scale drinking water distribution system. *Water Research* **2003**, 37 (8), 1805-1817.

105. Al-Malack, M. H.; Ahmed, B. O., Effect of presence of chemical species on removal of phenol in electrocoagulation process. *Desalination and Water Treatment* **2016**, 57 (36), 16779-16789.

106. dongmei, Z. Study on Removal of Nitrate in Water by Electrochemical Catalytic Reduction. Qingdao University of Science and Technology, 2013.

107. (a) Schoeman, J.; Steyn, A., Nitrate removal with reverse osmosis in a rural area in South Africa. *Desalination* **2003**, 155 (1), 15-26; (b) Koyuncu, I., Effect of operating conditions on the separation of ammonium and nitrate ions with nanofiltration and reverse osmosis membranes. *Journal of Environmental Science and Health, Part A* **2002**, 37 (7), 1347-1359.

108. Jones, C. S.; Kim, S.-w.; Wilton, T. F.; Schilling, K. E.; Davis, C. A., Nitrate uptake in an agricultural stream estimated from high-frequency, in-situ sensors. *Environmental monitoring and assessment* **2018**, 190 (4), 1-16.

109. Shuai, Y.; Chun, X.; Zhenghu, C.; Xin, Y., Nano-zero valent iron coupled with hydrogen autotrophic denitrification to remove nitrate from water. *China water supply and drainage* **2019**, 35 (15), 43-47.

110. Wolf, I.; Russow, R., Different pathways of formation of N₂O, N₂ and NO in black earth soil. *Soil Biology and Biochemistry* **2000**, 32 (2), 229-239.

111. Peng, Y.; Zhu, G., Biological nitrogen removal with nitrification and denitrification via nitrite pathway. *Applied microbiology and biotechnology* **2006**, 73 (1), 15-26.

112. Yatong, X., Research on nitrogen removal by biological denitrification. *ACTA SCIENTIAE CIRCUMSTANTIAE* **1994**, 14, 4.

113. Wang, L.; Li, M.; Liu, X.; Feng, C.; Zhou, F.; Chen, N.; Hu, W., Mechanism and effectiveness of Ti-based nano-electrode for electrochemical denitrification. *International Journal of Electrochemical Science* **2017**, 12 (3), 1992-2002.

114. (a) Payne, W., Reduction of nitrogenous oxides by microorganisms. *Bacteriological reviews* **1973**, 37 (4), 409-452; (b) Jetten, M. S.; Horn, S. J.; van Loosdrecht, M. C., Towards a more sustainable municipal wastewater treatment system. *Water science and technology* **1997**, 35 (9), 171-180.

115. Weifeng, S.; Yaming, N.; Dewen, H., Research progress of electrolysis water treatment technology. *Chemical environmental protection* **2001**, 21 (1), 11-15.

116. (a) Choe, S.; Chang, Y.-Y.; Hwang, K.-Y.; Khim, J., Kinetics of reductive denitrification by nanoscale zero-valent iron. *Chemosphere* **2000**, 41 (8), 1307-1311; (b) Hansen, H. C. B.; Koch, C. B.; Nancke-Krogh, H.; Borggaard, O. K.; Sørensen, J., Abiotic nitrate reduction to ammonium: key role of green rust. *Environmental Science & Technology* **1996**, 30 (6), 2053-2056; (c) Murphy, A. P., Chemical removal of nitrate from water. *Nature* **1991**, 350 (6315), 223-225.

117. Chen, L.; Chen, X.; Zhou, Z.; Guo, S.; Zhao, Y.; Zhang, X., Studies on morphology, electrical and optical characteristics of Al-doped ZnO thin films grown by atomic layer deposition. *Journal of Semiconductors* **2018**, 39 (3), 033004.

118. Mack, J.; Bolton, J. R., Photochemistry of nitrite and nitrate in aqueous solution: a review. *Journal of Photochemistry and Photobiology A: Chemistry* **1999**, 128 (1-3), 1-13.

119. Kim, M.-S.; Lee, D.-W.; Chung, S.-H.; Kim, J. T.; Cho, I.-H.; Lee, K.-Y., Pd-Cu bimetallic catalysts supported on TiO₂-CeO₂ mixed oxides for aqueous nitrate reduction by hydrogen. *Journal of Molecular*

Catalysis A: Chemical **2014**, 392, 308-314.

120. Wanjun, L.; Deren, F.; Jinbo, Z., Removal of Nitrate from Water by Pd-Cu/ γ -Al₂O₃ Bimetallic Catalyst. *Industrial Catalysis (Chinese)* **2015**, 23 (5), 390-395.

121. Garcia-Segura, S.; Lanzarini-Lopes, M.; Hristovski, K.; Westerhoff, P., Electrocatalytic reduction of nitrate: Fundamentals to full-scale water treatment applications. *Applied Catalysis B: Environmental* **2018**, 236, 546-568.

122. Yang, J.; Sebastian, P.; Duca, M.; Hoogenboom, T.; Koper, M. T., pH dependence of the electroreduction of nitrate on Rh and Pt polycrystalline electrodes. *Chemical Communications* **2014**, 50 (17), 2148-2151.

123. Paidar, M.; Roušar, I.; Bouzek, K., Electrochemical removal of nitrate ions in waste solutions after regeneration of ion exchange columns. *Journal of Applied Electrochemistry* **1999**, 29 (5), 611-617.

124. Xu, H.-Y.; Wang, Y.; Shi, T.-N.; Zhao, H.; Tan, Q.; Zhao, B.-C.; He, X.-L.; Qi, S.-Y., Heterogeneous Fenton-like discoloration of methyl orange using Fe₃O₄/MWCNTs as catalyst: kinetics and Fenton-like mechanism. *Frontiers of Materials Science* **2018**, 12 (1), 34-44.

125. Jongprateep, O.; Sato, N.; Techapiesancharoenkij, R.; Surawathanawises, K., Electrocatalytic properties of calcium titanate, strontium titanate, and strontium calcium titanate powders synthesized by solution combustion technique. *Advances in Materials Science and Engineering* **2019**, 2019.

126. (a) Ebert, H.; Parsons, R.; Ritzoulis, G.; VanderNoot, T., The reduction of nitrous oxide on platinum electrodes in acid solution. *Journal of electroanalytical chemistry and interfacial electrochemistry* **1989**, 264 (1-2), 181-193; (b) Ahmadi, A.; Brace, E.; Evans, R. W.; Attard, G., Anion-surface interactions: Part II. Nitrous oxide reduction as a probe of anion adsorption on transition metal surfaces. *Journal of Electroanalytical Chemistry* **1993**, 350 (1-2), 297-316.

127. De Vooy, A.; Van Santen, R.; Van Veen, J., Electrocatalytic reduction of NO₃⁻ on palladium/copper electrodes. *Journal of Molecular Catalysis A: Chemical* **2000**, 154 (1-2), 203-215.

128. Pérez-Gallent, E.; Figueiredo, M. C.; Katsounaros, I.; Koper, M. T., Electrocatalytic reduction of Nitrate on Copper single crystals in acidic and alkaline solutions. *Electrochimica Acta* **2017**, 227, 77-84.

129. Chen, T.; Li, H.; Ma, H.; Koper, M. T., Surface modification of Pt (100) for electrocatalytic nitrate reduction to dinitrogen in alkaline solution. *Langmuir* **2015**, 31 (10), 3277-3281.

130. Dima, G.; Rosca, V.; Koper, M., Role of germanium in promoting the electrocatalytic reduction of nitrate on platinum: An FTIR and DEMS study. *Journal of electroanalytical chemistry* **2007**, 599 (2), 167-176.

131. Yang, J.; Duca, M.; Schouten, K. J. P.; Koper, M. T., Formation of volatile products during nitrate reduction on a Sn-modified Pt electrode in acid solution. *Journal of electroanalytical chemistry* **2011**, 662 (1), 87-92.

132. Siriwatcharapiboon, W.; Kwon, Y.; Yang, J.; Chantry, R.; Li, Z.; Horswell, S.; Koper, M., Promotion effects of Sn on the electrocatalytic reduction of nitrate at Rh nanoparticles. *ChemElectroChem* **2014**, 1 (1), 172-179.

133. Yang, J.; Kwon, Y.; Duca, M.; Koper, M. T., Combining voltammetry and ion chromatography: application to the selective reduction of nitrate on Pt and PtSn electrodes. *Analytical chemistry* **2013**, 85 (16), 7645-7649.

134. Yang, J.; Calle-Vallejo, F.; Duca, M.; Koper, M. T., Electrocatalytic Reduction of Nitrate on a Pt Electrode Modified by p-Block Metal Adatoms in Acid Solution. *ChemCatChem* **2013**, 5 (7), 1773-1783.

135. De Vooy, A.; Beltramo, G.; Van Riet, B.; Van Veen, J.; Koper, M., Mechanisms of electrochemical reduction and oxidation of nitric oxide. *Electrochimica Acta* **2004**, 49 (8), 1307-1314.

136. Rosca, V.; Koper, M. T., Mechanism of electrocatalytic reduction of nitric oxide on Pt (100). *The Journal of Physical Chemistry B* **2005**, 109 (35), 16750-16759.

137. Hara, K.; Kamata, M.; Sonoyama, N.; Sakata, T., Electrocatalytic reduction of NO on metal electrodes and gas diffusion electrodes in an aqueous electrolyte. *Journal of Electroanalytical Chemistry* **1998**, 451 (1-2), 181-186.

138. Rosca, V.; Duca, M.; de Groot, M. T.; Koper, M. T., Nitrogen cycle electrocatalysis. *Chemical Reviews* **2009**, *109* (6), 2209-2244.
139. Plieth, W.; Bard, A., Encyclopedia of Electrochemistry of the Elements. by *AJ Bard, Marcel Dekker, Inc. New York* **1978**, 8.
140. Duca, M.; Van Der Klugt, B.; Hasnat, M.; Machida, M.; Koper, M., Electrocatalytic reduction of nitrite on a polycrystalline rhodium electrode. *Journal of Catalysis* **2010**, *275* (1), 61-69.
141. Duca, M.; Kavvadia, V.; Rodriguez, P.; Lai, S.; Hoogenboom, T.; Koper, M., New insights into the mechanism of nitrite reduction on a platinum electrode. *Journal of Electroanalytical Chemistry* **2010**, *649* (1-2), 59-68.
142. Duca, M.; Van der Klugt, B.; Koper, M., Electrocatalytic reduction of nitrite on transition and coinage metals. *Electrochimica Acta* **2012**, *68*, 32-43.
143. (a) Duca, M.; Cucarella, M. O.; Rodriguez, P.; Koper, M. T., Direct reduction of nitrite to N₂ on a Pt (100) electrode in alkaline media. *Journal of the American Chemical Society* **2010**, *132* (51), 18042-18044; (b) Duca, M.; Figueiredo, M. C.; Climent, V.; Rodriguez, P.; Feliu, J. M.; Koper, M. T., Selective catalytic reduction at quasi-perfect Pt (100) domains: a universal low-temperature pathway from nitrite to N₂. *Journal of the American Chemical Society* **2011**, *133* (28), 10928-10939.
144. Dong, S.; Xi, X.; Tian, M., Study of the electrocatalytic reduction of nitrite with silicotungstic heteropolyanion. *Journal of Electroanalytical Chemistry* **1995**, *385* (2), 227-233.
145. Toth, J. E.; Anson, F. C., Electrocatalytic reduction of nitrite and nitric oxide to ammonia with iron-substituted polyoxotungstates. *Journal of the American Chemical Society* **1989**, *111* (7), 2444-2451.
146. McCormac, T.; Fabre, B.; Bidan, G., Part II. Role of pH and the transition metal for the electrocatalytic reduction of nitrite with transition metal substituted Dawson type heteropolyanions. *Journal of Electroanalytical Chemistry* **1997**, *427* (1-2), 155-159.
147. Ruhlmann, L.; Genet, G., Wells–Dawson-derived tetrameric complexes {K₂₈H₈[P₂W₁₅Ti₃O_{60.5}]₄} electrochemical behaviour and electrocatalytic reduction of nitrite and of nitric oxide. *Journal of Electroanalytical Chemistry* **2004**, *568*, 315-321.
148. Xi, X.; Dong, S., Electrocatalytic reduction of nitrite using Dawson-type tungstodiphosphate anions in aqueous solutions, adsorbed on a glassy carbon electrode and doped in polypyrrole film. *Journal of Molecular Catalysis A: Chemical* **1996**, *114* (1-3), 257-265.
149. Naseer, R.; Mal, S. S.; Kortz, U.; Armstrong, G.; Laffir, F.; Dickinson, C.; Vagin, M.; McCormac, T., Electrocatalysis by crown-type polyoxometalates multi-substituted by transition metal ions; Comparative study. *Electrochimica Acta* **2015**, *176*, 1248-1255.
150. Belhouari, A.; Keita, B.; Nadjio, L.; Contant, R., Efficient conversion of NO into N₂O by selected electroreduced heteropolyanions. *New Journal of Chemistry* **1998**, *22* (2), 83-86.
151. Boussema, F.; Haddad, R.; Ghandour, Y.; Belkhiria, M. S.; Holzinger, M.; Maaref, A.; Cosnier, S., Polyoxometalate [PMo₁₁O₃₉]⁷⁻ / carbon nanocomposites for sensitive amperometric detection of nitrite. *Electrochimica Acta* **2016**, *222*, 402-408.
152. Huang, B.-Q.; Wang, L.; Shi, K.; Xie, Z.-X.; Zheng, L.-S., A new strategy for the fabrication of the phosphor polyoxomolybdate modified electrode from ionic liquid solutions and its electrocatalytic activities. *Journal of Electroanalytical Chemistry* **2008**, *615* (1), 19-24.
153. Ammam, M.; Fransaer, J., Synthesis and characterization of hybrid materials based on 1-butyl-3-methylimidazolium tetrafluoroborate ionic liquid and Dawson-type tungstophosphate K₇[H₄PW₁₈O₆₂]·18H₂O and K₆[P₂W₁₈O₆₂]·13H₂O. *Journal of Solid State Chemistry* **2011**, *184* (4), 818-824.
154. (a) Haghighi, B.; Hamidi, H.; Gorton, L., Formation of a robust and stable film comprising ionic liquid and

polyoxometalate on glassy carbon electrode modified with multiwalled carbon nanotubes: Toward sensitive and fast detection of hydrogen peroxide and iodate. *Electrochimica Acta* **2010**, 55 (16), 4750-4757; (b) Feizy, S.; Haghighi, B., A survey on the effect of ionic liquid on electrochemical behavior and electrocatalytic activity of a phosphomolybdic acid-ionic liquid-MWCNT-modified glassy carbon electrode. *Journal of Solid State Electrochemistry* **2019**, 23 (5), 1339-1350.

155. Wang, R.; Jia, D.; Cao, Y., Facile synthesis and enhanced electrocatalytic activities of organic-inorganic hybrid ionic liquid polyoxometalate nanomaterials by solid-state chemical reaction. *Electrochimica acta* **2012**, 72, 101-107.

156. Wang, B.; Cheng, L.; Dong, S., Construction of a heteropolyanion-modified electrode by a two-step sol-gel method and its electrocatalytic applications. *Journal of Electroanalytical Chemistry* **2001**, 516 (1-2), 17-22.

157. Chen, S.; Xiang, Y.; Banks, M. K.; Xu, W.; Peng, C.; Wu, R., Polyoxometalate-coupled graphene nanohybrid via gemini surfactants and its electrocatalytic property for nitrite. *Applied Surface Science* **2019**, 466, 110-118.

158. Imar, S.; Yaqub, M.; Maccato, C.; Dickinson, C.; Laffir, F.; Vagin, M.; McCormac, T., Nitrate and Nitrite Electrocatalytic Reduction at Layer-by-Layer Films Composed of Dawson-type Heteropolyanions Mono-substituted with Transitional Metal Ions and Silver Nanoparticles. *Electrochimica Acta* **2015**, 184, 323-330.

159. Sahraoui, Y.; Chaliaa, S.; Maaref, A.; Haddad, A.; Jaffrezic-Renault, N., An electrochemical nitrite sensor based on a multilayer film of polyoxometalate. *Journal of Sensor Technology* **2013**, 3 (03), 84.

160. Shan, Y.; Yang, G.; Sun, Y.; Pang, S.; Gong, J.; Su, Z.; Qu, L., ITO electrode modified by self-assembling multilayer film of polyoxometallate on poly (vinyl alcohol) nanofibers and its electrocatalytic behavior. *Electrochimica acta* **2007**, 53 (2), 569-574.

161. Zhang, D.; Ma, H.; Chen, Y.; Pang, H.; Yu, Y., Amperometric detection of nitrite based on Dawson-type vanodotungstophosphate and carbon nanotubes. *Analytica Chimica Acta* **2013**, 792, 35-44.

162. Zhang, L.; Li, S.; Zhang, Z.; Tan, L.; Pang, H.; Ma, H., Facile fabrication of reduced graphene oxide and Keggin-type polyoxometalates nanocomposite film for high performance electrocatalytic oxidation of nitrite. *Journal of Electroanalytical Chemistry* **2017**, 807, 97-103.

163. Wang, Q.; Khungwa, J.; Li, L.; Liu, Y.; Wang, X.; Wang, S., Fabrication of polyoxometalate/GO/PDDA hybrid nanocomposite modified electrode and electrocatalysis for nitrite ion, ascorbic acid and dopamine. *Journal of Electroanalytical Chemistry* **2018**, 824, 91-98.

164. Keita, B.; Belhouari, A.; Nadjjo, L.; Contant, R., Electrocatalysis by polyoxometalate/vb polymer systems: reduction of nitrite and nitric oxide. *Journal of Electroanalytical Chemistry* **1995**, 381 (1-2), 243-250.

165. Cao, F.; Guo, S.; Ma, H.; Gong, J., ITO Electrode Modified by $\alpha\text{-K}_6[\text{P}_2\text{W}_{18}\text{O}_{62}]$ Hybrid Nanofibers for Nitrite Determination. *Electroanalysis* **2012**, 24 (2), 418-424.

166. Khadro, B.; Baroudi, I.; Goncalves, A.-M.; Berini, B.; Pegot, B.; Nouar, F.; Le, T. N. H.; Ribot, F.; Gervais, C.; Carn, F., Interfacing a heteropolytungstate complex and gelatin through a coacervation process: design of bionanocomposite films as novel electrocatalysts. *Journal of Materials Chemistry A* **2014**, 2 (24), 9208-9220.

167. Debiemme-Chouvy, C.; Cachet, H.; Folcher, G.; Deslouis, C., Electrocatalytic reduction of HNO_2 by a silicomolybdate polyanion: a differential electrochemical mass spectrometry study. *Electroanalysis: An International Journal Devoted to Fundamental and Practical Aspects of Electroanalysis* **2007**, 19 (2-3), 259-262.

Chapter II: Nitrite electroreduction catalyzed by Keggin and Dawson polyoxometalates

2.1 Introduction

Nitrite is the first product obtained from the reduction of nitrate, and both of them are environmental pollutants, although they are food preservatives. Thus, research is focused on converting them into products of industrial interest or harmless compounds. Among the various possible products, nitrogen is the most environmentally harmless, while NH_3 has an industrial value and N_2O is used in medicine or as extra oxidizer in engines for enhancing power output.

A large number of polyoxometalates (POMs) have been used to catalyze nitrite or nitrous acid electrochemical reduction. Among of them, Keggin- and Dawson-types polyoxometalate¹ and more complex structures such as Wells-Dawson-derived tetramers,² crown-type structures,³ and even organic-inorganic hybrids⁴ have been used. In early 1990s, $[\text{SiW}_{12}\text{O}_{40}]^{4-}$ was studied as homogeneous catalyst on electrolyte (for details, see chapter 1.4.3). In most of these studies the catalytic electroreduction is performed at different nitrite concentration and at different pH values. However, there is a lack of *in-situ* detection of the actual products and no correlation with the potential is made.

From this point of view, disposing of an analytical technique able to rapidly identify in a single test as many products as possible becomes an important characterization tool. Differential electrochemical mass spectrometry (DEMS) is an *in-situ* analytical technique which is able to identify gaseous products during one single potential scan. This technique has been already used for characterizing nitrite and nitrate electroreduction catalyzed by coinage and noble metals.⁵ There is only one report describing the use of DEMS for characterizing nitrite reduction catalyzed by Mo-based Keggin POM $[\text{SiMo}_{12}\text{O}_{40}]^{4-}$ (see chapter 1.5).⁶

The lack of thorough study about the correlation between POMs redox behavior and the products of nitrite reduction is the main motivation of the experiments described in this thesis. In the first chapter, various POMs were employed as homogeneous catalysts. We have selected W-based and Mo-based Keggin POMs and several Dawson POMs. In detail, we have first studied the influence of the charge and redox potential of a series of Keggin-type POMs ($[\text{PW}_{12}\text{O}_{40}]^{3-}$, $[\text{SiW}_{12}\text{O}_{40}]^{4-}$, $[\text{BW}_{12}\text{O}_{40}]^{5-}$, and $[\text{H}_2\text{W}_{12}\text{O}_{40}]^{6-}$) on the electrochemical reduction of nitrite or nitrous acid (NO_2^- or HNO_2) (Figure 3.1.1). These Keggin POMs are different by the central heteroatom, by the total negative charge and redox properties such as the potential of the reduction waves, the number of electrons involved in each wave, the number of waves and their pH dependence. Secondly, we have studied two Mo-based Keggin POMs, i.e. $([\text{PMo}_{12}\text{O}_{40}]^{3-})$, $[\text{SiMo}_{12}\text{O}_{40}]^{4-}$ (Figure 3.1.2) because these compounds have a more positive reduction potential and more exchanged electrons than their W-based Keggin analogs. Finally, we have studied a series of dimers sandwich Dawson POMs, i.e. $[\text{Cd}_4(\text{H}_2\text{O})_2(\text{P}_2\text{W}_{15}\text{O}_{56})_2]^{16-}$, $[\text{Mn}_4(\text{H}_2\text{O})_2(\text{P}_2\text{W}_{15}\text{O}_{56})_2]^{16-}$ and $[\text{Zn}_4(\text{H}_2\text{O})_2(\text{P}_2\text{W}_{15}\text{O}_{56})_2]^{16-}$ as well as parent Dawson α - $[\text{P}_2\text{W}_{18}\text{O}_{62}]^{6-}$ that were previously synthesized in our group (Figure 3.1.3).⁷ These compounds were chosen due to the higher number of exchanged electrons at a similar potential compared to W-based Keggin POMs.

The electrochemical behavior of all these compounds is described in detail in the first part of this chapter. Following, cyclic voltammetry measurements are described for nitrite reduction catalyzed by these compounds. Then, detailed DEMS analysis is described for the identification of gaseous products. Additional measurements of some possible liquid phase

products were achieved for one POM, $[\text{H}_2\text{W}_{12}\text{O}_{40}]^{6-}$. As nitric oxide was identified as a gaseous product, DEMS analysis was also performed for the reduction of nitric oxide in the absence of nitrite and catalyzed by three Keggin-type POMs, $[\text{SiW}_{12}\text{O}_{40}]^{4-}$, $[\text{BW}_{12}\text{O}_{40}]^{5-}$, and $[\text{H}_2\text{W}_{12}\text{O}_{40}]^{6-}$. Furthermore, from DEMS analysis, we have identified a certain potential range specific to each POM, where only nitric oxide is produced. This triggered a kinetic study in which the rate constant between the reduced POM and HNO_2 and turnover frequency (TOF) from nitrite to NO were computed. For this, a microkinetic model was developed and applied to the experimental data. Thus, we were able to classify our POMs based on the use of TOF and offer a very new way of discussing electrocatalytic properties of these compounds.

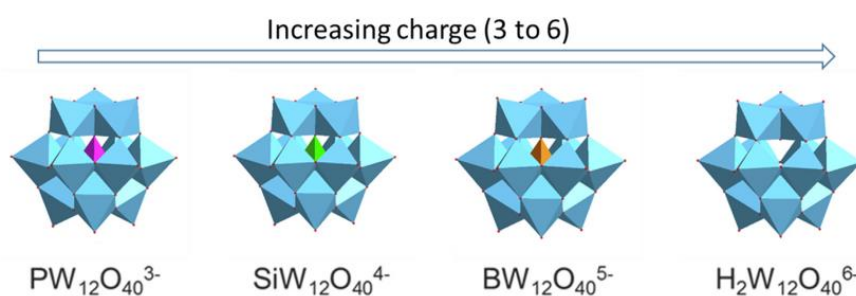


Figure 3.1.1 Coordination polyhedra structures of all studied W-based Keggin POMs. Oxygen atoms are depicted in red, blue polyhedra are formed by W atoms and central atoms (tetrahedra) is depicted in specific color (P pink, Si green, B orange, H no color).

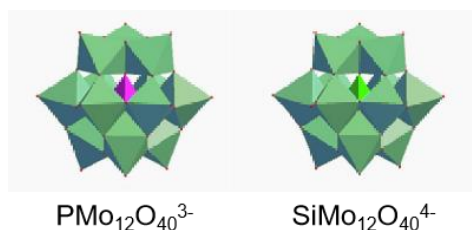


Figure 2.1.2 Coordination polyhedra structures of all studied Mo-based Keggin POMs. Oxygen atoms are depicted in red, green polyhedra are formed by Mo atoms and central atoms (tetrahedra) is depicted in specific color (P pink, Si light green).

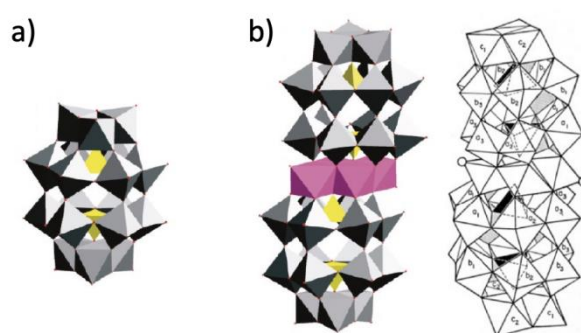


Figure 2.1.3 (a) Coordination polyhedra structure of Wells–Dawson POM $\alpha\text{-}[\text{P}_2\text{W}_{18}\text{O}_{62}]^{6-}$; (b) Coordination polyhedra structure of $[\text{M}_4(\text{H}_2\text{O})_2(\text{P}_2\text{W}_{15}\text{O}_{56})_2]^{16-}$ ($\text{M} = \text{Zn}^{2+}, \text{Cd}^{2+}, \text{Mn}^{2+}$). The four unlabeled central octahedra are the MO_6 edge-shared planar array; the open circles represent the two constitutional waters. The four shaded tetrahedra represent the PO_4 heterogroups. The two $[\text{P}_2\text{W}_{15}\text{O}_{56}]^{12-}$ units lie above and below the four central edge-shared octahedra and have eight symmetry-inequivalent (C_{2h}) W atoms labeled $a_1, a_2, a_3, b_1, b_2, b_3, c_1$, and c_2 .⁸

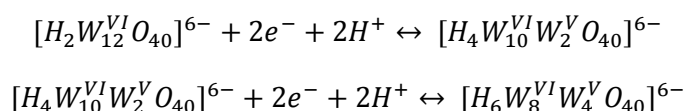
2.2 Electrochemical properties of POMs on GC electrode

2.2.1 Electrochemical properties of W-based Keggin POMs

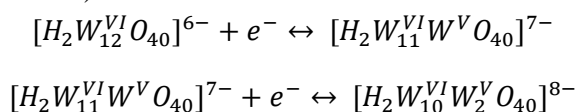
The electrochemical properties of $[\text{PW}_{12}\text{O}_{40}]^{3-}$, $[\text{SiW}_{12}\text{O}_{40}]^{4-}$, $[\text{BW}_{12}\text{O}_{40}]^{5-}$, and $[\text{H}_2\text{W}_{12}\text{O}_{40}]^{6-}$ were studied in solution with glassy carbon (GC) as working electrode, by using cyclic voltammetry. The electrochemical redox behavior of these POMs is well known in the literature. The potential of the first reduction is becoming more negative from $[\text{PW}_{12}\text{O}_{40}]^{3-}$, $[\text{SiW}_{12}\text{O}_{40}]^{4-}$, $[\text{BW}_{12}\text{O}_{40}]^{5-}$, and $[\text{H}_2\text{W}_{12}\text{O}_{40}]^{6-}$ that is contrary to their total charge.⁹ Repulsion of charges increases with the increase of the POMs total anionic charge which explains the shift of potential to more negative values.^{5f} The influence of pH on the redox behaviour will be discussed for every POM.

Cyclic voltammograms of $[\text{H}_2\text{W}_{12}\text{O}_{40}]^{6-}$ are displayed in Figure 2.2.1. Three reduction waves are observed in all pH solutions. From pH 1 to pH 4 the first two waves are reversible. The third wave is not reversible at any pH and no data can be found in literature about this wave. Moreover, this wave overlaps with the hydrogen evolution that makes data interpretation less precise. Thus, this wave will not be discussed in detail. In the first reduction wave two electrons are transferred. In fact, the transfer of the second electron is pH dependent and, in acid conditions, the potential shifts and overlaps with the transfer of the first electron. At pH 5, the two electrons wave splits into two one-electron waves (-0.119 V vs. RHE and -0.206 V vs. RHE) that overlap partially. A similar situation is observed for the second wave. This causes a decrease in the peak current intensities by half. In details, the peak current intensities of first and second wave are about -12 μA and -18 μA between pH 1 to pH 3 and decrease rapidly at pH 5 to -5.3 μA and -8.3 μA . The redox processes of $[\text{H}_2\text{W}_{12}\text{O}_{40}]^{6-}$ could be described as below:^{9b}

At pH 1-4:



At pH 5 (split of the first wave):

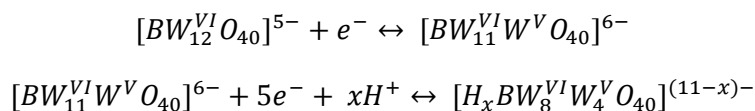


The coupled proton-electron transfer, i.e. the conversion of $[\text{H}_2\text{W}_{12}\text{O}_{40}]^{6-}$ to $[\text{H}_4\text{W}_{12}\text{O}_{40}]^{8-}$ was simulated with a model that takes into account the protonation equilibria. The success of the simulation proves that this coupled proton-electron exists.¹⁰ The variation of the redox potential of the first coupled proton-electron transfer with pH is shown in Figure 2.2.5a. Except the value at pH 1, that was probably subjected at some experimental error, the lack of variation of E^0 expressed in V vs. RHE with the pH confirms the involvement of protons in the electron transfer. Moreover, it indicates that the pKa of the reduced POM, $[\text{H}_4\text{W}_{10}^{\text{VI}}\text{W}_2^{\text{V}}\text{O}_{40}]^{6-}$ is higher than 4, but no data in literature can be found about this. In fact, pKa of fully oxidized POMs (such as $[\text{H}_2\text{W}_{12}^{\text{VI}}\text{O}_{40}]^{6-}$) are generally situated between 0 and 2, as these compounds are strong acids.¹¹ A peculiar behavior is observed for the second wave (Figure 2.2.5b) because the redox potential, in V vs. RHE, decreases as the pH increases. This

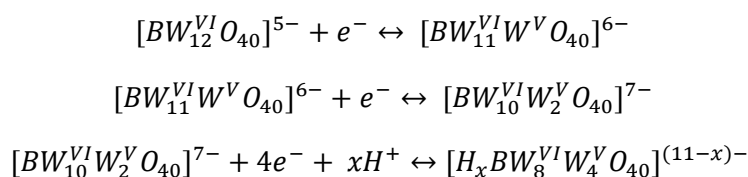
suggests that additional phenomena, such as solvation of the reduced POM $[H_4W_8^{VI}W_4^VO_{40}]^{6-}$ might influence the coupled proton-electron transfer. This is not the case of the other two POMs, $[BW_{12}O_{40}]^{6-}$ and $[SiW_{12}O_{40}]^{5-}$ for which the redox potential in V vs. RHE is increasing with the pH.

Cyclic voltammograms of $[BW_{12}O_{40}]^{5-}$ are displayed in Figure 2.2.2. The first peak corresponds to one electron transfer and is reversible in all pH solutions. The potential of the wave, expressed as V vs. RHE, shifts to more positive values as the pH increases (Figure 2.2.5a), but the current intensity remains the same (about -6 μ A). The second wave of $[BW_{12}O_{40}]^{5-}$ is one electron transfer and the third wave is four electrons transfer. But at pH 1 these two waves overlap to each other and also to hydrogen evolution. At pH 2 and pH 3, the separation between the second and third wave is visible, but the second wave appears as a shoulder. At pH 4 and 5, the second wave is clearly visible and reversible with the current intensity similar to first wave. At these pH values, the third wave is not visible because the CV was stopped at a potential not negative enough.⁹ The pKa of the reduced POM $[BW_{12}O_{40}]^{6-}$ may be situated around 1 or even less, suggesting the strong acid characters of this compound. The three redox processes can be described as below:

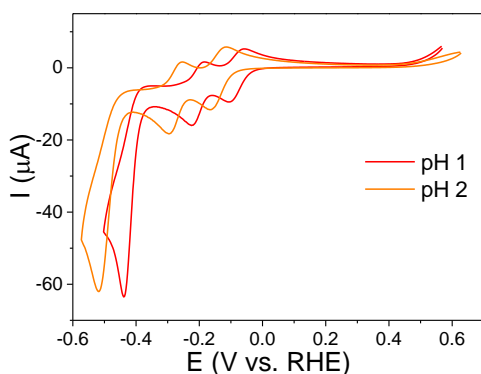
At pH 1:



At pH 2 - 5:



a) pH = 1 and 2



b) pH = 3, 4, and 5

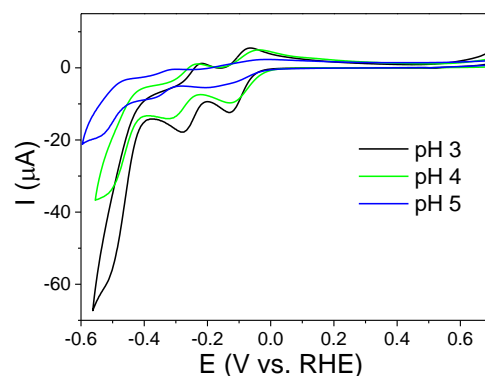
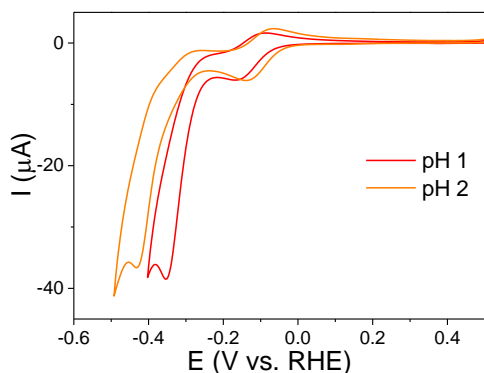


Figure 2.2.1 Cyclic voltammetry of $[H_2W_{12}O_{40}]^{6-}$ at a) pH 1 and pH 2; b) pH 3 to pH 5. Experimental conditions: working electrode, glassy carbon (GC); POM concentration, 1 mM; scan rate, 20 mVs^{-1} .

a) pH = 1 and 2



b) pH = 3, 4, and 5

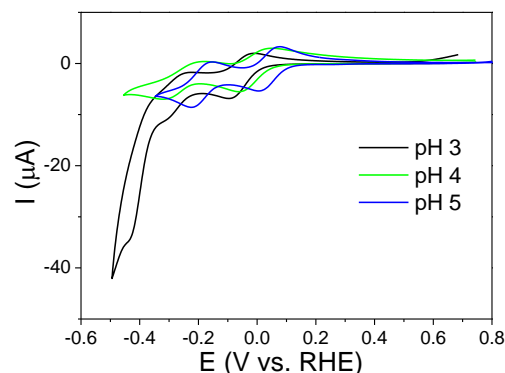
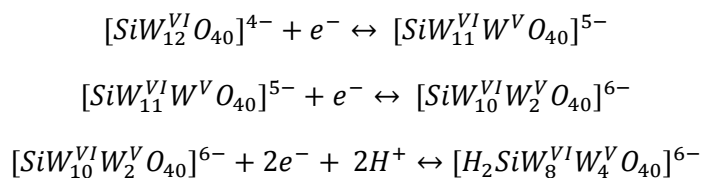
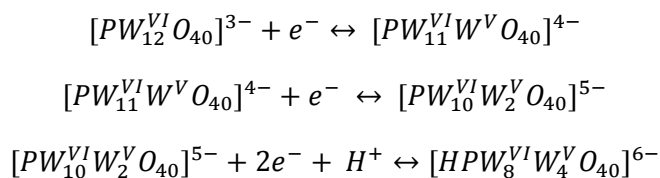


Figure 2.2.2 Cyclic voltammetry of $[\text{BW}_{12}\text{O}_{40}]^{5-}$ at a) pH 1 and pH 2; b) pH 3 to pH 5. Experimental conditions: working electrode, glassy carbon (GC); POM concentration, 1 mM; scan rate, 20 mVs^{-1}

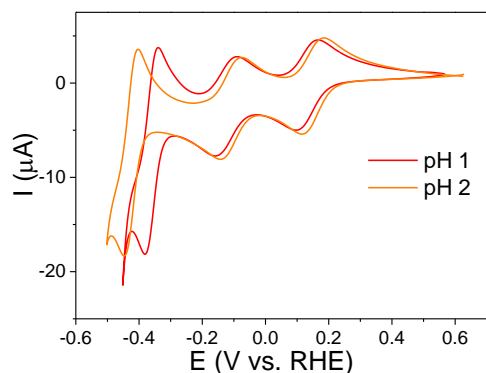
Cyclic voltammograms of $[\text{SiW}_{12}\text{O}_{40}]^{4-}$ are displayed in Figure 2.2.3. Three reduction peaks are observed in all pH buffer solution. The first two peaks are reversible with similar current intensities regardless of pH. Each peak corresponds to one electron transfer. The redox potential, in V vs. RHE, increases as the pH increases, as expected (Figure 2.2.5). The third wave is described in the literature as being pH depended and involving one transfer of two coupled protons-electrons. The current intensity of this wave is slightly higher than the double of the first wave, suggesting that hydrogen evolution reaction starts to overlap. The pK_a of the reduced POMs $[\text{SiW}_{12}\text{O}_{40}]^{5-}$ and $[\text{SiW}_{12}\text{O}_{40}]^{6-}$ are probably less than 1, suggesting the strong acid characters of these compounds. The three redox processes can be described as:¹²



Cyclic voltammograms of $[\text{PW}_{12}\text{O}_{40}]^{3-}$ are displayed in Figure 2.2.4. The first and second peaks of $[\text{PW}_{12}\text{O}_{40}]^{3-}$ are reversible with one electron transfer. The third peak has two electrons transfer, but the current intensity is slightly higher than the double of the current intensity of the first two wave, suggesting that hydrogen evolution reaction starts to overlap. This POM is not stable at pH higher than 1.7. The three redox processes could be described as:^{9b, 13}



a) pH = 1 and 2



b) pH = 3, 4, and 5

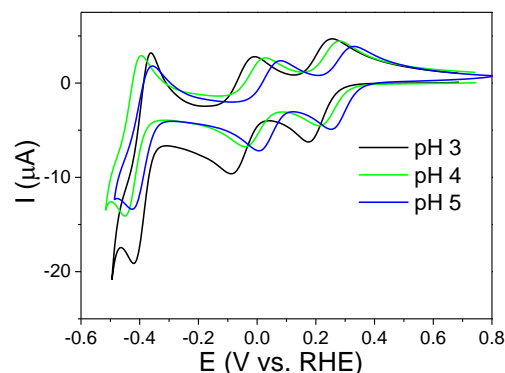


Figure 2.2.3 Cyclic voltammetry of $[\text{SiW}_{12}\text{O}_{40}]^{4-}$ at a) pH 1 and pH 2; b) pH 3 to pH 5. Experimental conditions: working electrode, glassy carbon (GC); POM concentration, 1 mM; scan rate, 20 mVs^{-1} .

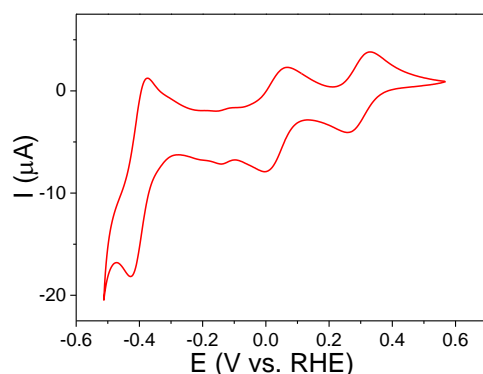


Figure 2.2.4 Cyclic voltammetry of $[\text{PW}_{12}\text{O}_{40}]^{3-}$ at pH 1. Experimental conditions: working electrode, glassy carbon (GC); POM concentration, 1 mM; scan rate, 20 mVs^{-1} .

The number and intensity of POMs waves are in agreement with previously published results. In the Table 2.2.1, the number of exchanged electrons and the apparent formal potential for each wave is presented (E^0 is the average potential of the anodic and cathodic waves in the cyclic voltammetry; the number of electrons is from cited references). A summary of the formal potential (E^0) of each wave and its variation with pH and the number of electrons of each wave are shown in Figure 2.2.5 and Figure 2.2.6. As a conclusion, except the splitting of the first wave of $[\text{H}_2\text{W}_{12}\text{O}_{40}]^{6-}$ at pH 5 and the overlap of the second and third waves of $[\text{BW}_{12}\text{O}_{40}]^{5-}$ at pH 1-2, all POMs have reversible first and second reduction processes. The first reduction peak of $[\text{PW}_{12}\text{O}_{40}]^{3-}$, $[\text{SiW}_{12}\text{O}_{40}]^{4-}$, $[\text{BW}_{12}\text{O}_{40}]^{5-}$ is one electron processes regardless the pH. The third wave is reversible only for $[\text{PW}_{12}\text{O}_{40}]^{3-}$ and $[\text{SiW}_{12}\text{O}_{40}]^{4-}$ and it overlaps with hydrogen evolution for $[\text{H}_2\text{W}_{12}\text{O}_{40}]^{6-}$ and $[\text{BW}_{12}\text{O}_{40}]^{5-}$.

Table 2.2.1 Details of redox behavior of studied POMs: formal potential and number of electrons⁹ for each wave at pH 2 and pH 5.

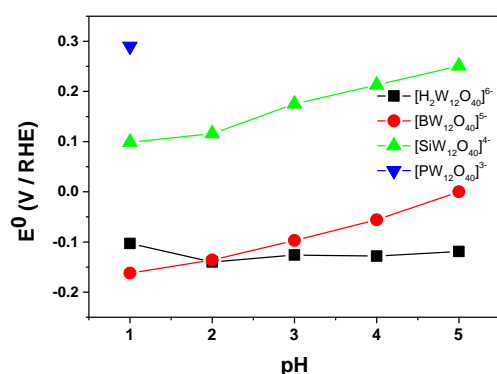
pH	POM	E ⁰ / V vs. RHE (no. of electrons)		
		I st wave	II nd wave	III rd wave
pH 1	[H ₂ W ₁₂ O ₄₀] ⁶⁻	- 0.103 (2e ⁻)	- 0.223 (2e ⁻)	-
	[BW ₁₂ O ₄₀] ⁵⁻	- 0.162 (1e ⁻)	- 0.351 (1+4e ⁻)	-
	[SiW ₁₂ O ₄₀] ⁴⁻	0.099 (1e ⁻)	-0.157 (1e ⁻)	-0.382 (2e ⁻)
	[PW ₁₂ O ₄₀] ^{3- a}	0.290 (1e ⁻)	0.030 (1e ⁻)	-0.400 (2e ⁻)
pH 2	[H ₂ W ₁₂ O ₄₀] ⁶⁻	- 0.140 (2e ⁻)	- 0.275 (2e ⁻)	-
	[BW ₁₂ O ₄₀] ⁵⁻	- 0.136 (1e ⁻)	- 0.330 (1e ⁻)	-0.433 (4e ⁻)
	[SiW ₁₂ O ₄₀] ⁴⁻	0.116 (1e ⁻)	-0.142 (1e ⁻)	-0.447 (2e ⁻)
pH 3	[H ₂ W ₁₂ O ₄₀] ⁶⁻	- 0.126 (2e ⁻)	- 0.279 (2e ⁻)	-
	[BW ₁₂ O ₄₀] ⁵⁻	- 0.097 (1e ⁻)	- 0.298 (1e ⁻)	- 0.431 (4e ⁻)
	[SiW ₁₂ O ₄₀] ⁴⁻	0.175 (1e ⁻)	- 0.085 (1e ⁻)	-0.423 (2e ⁻)
pH 4	[H ₂ W ₁₂ O ₄₀] ⁶⁻	- 0.128 (2e ⁻)	- 0.316 (2e ⁻)	-
	[BW ₁₂ O ₄₀] ⁵⁻	- 0.056 (1e ⁻)	- 0.317 (1e ⁻)	(4e ⁻) ^c
	[SiW ₁₂ O ₄₀] ⁴⁻	0.213 (1e ⁻)	- 0.040 (1e ⁻)	-0.448 (2e ⁻)
pH 5	[H ₂ W ₁₂ O ₄₀] ⁶⁻	- 0.119; -0.206 (1+1e ⁻) ^b	- 0.355 (1+1e ⁻) ^b	-
	[BW ₁₂ O ₄₀] ⁵⁻	0.00 (1e ⁻)	- 0.223 (1e ⁻)	(4e ⁻) ^c
	[SiW ₁₂ O ₄₀] ⁴⁻	0.251 (1e ⁻)	0.006 (1e ⁻)	-0.425 (2e ⁻)

a) [PW₁₂O₄₀]³⁻ is not stable for pH > 1.7

b) the waves are not well separated

c) not measured here

a) E⁰ of first wave



b) E⁰ of second wave

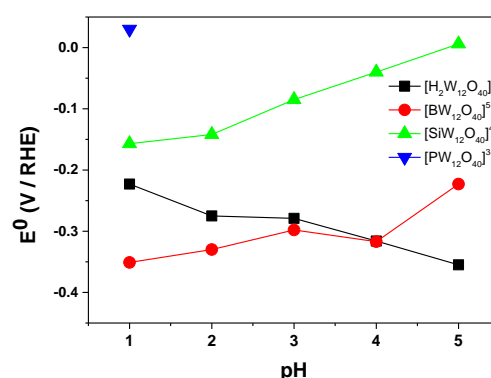


Figure 2.2.5 The formal potential (E⁰) of all waves of the four studied Keggin-type POMs as a function of pH (a) first wave; (b) second wave. The values are extracted from Figures 2.2.1 to 2.2.4. A missing point means that the wave is not present at that pH.

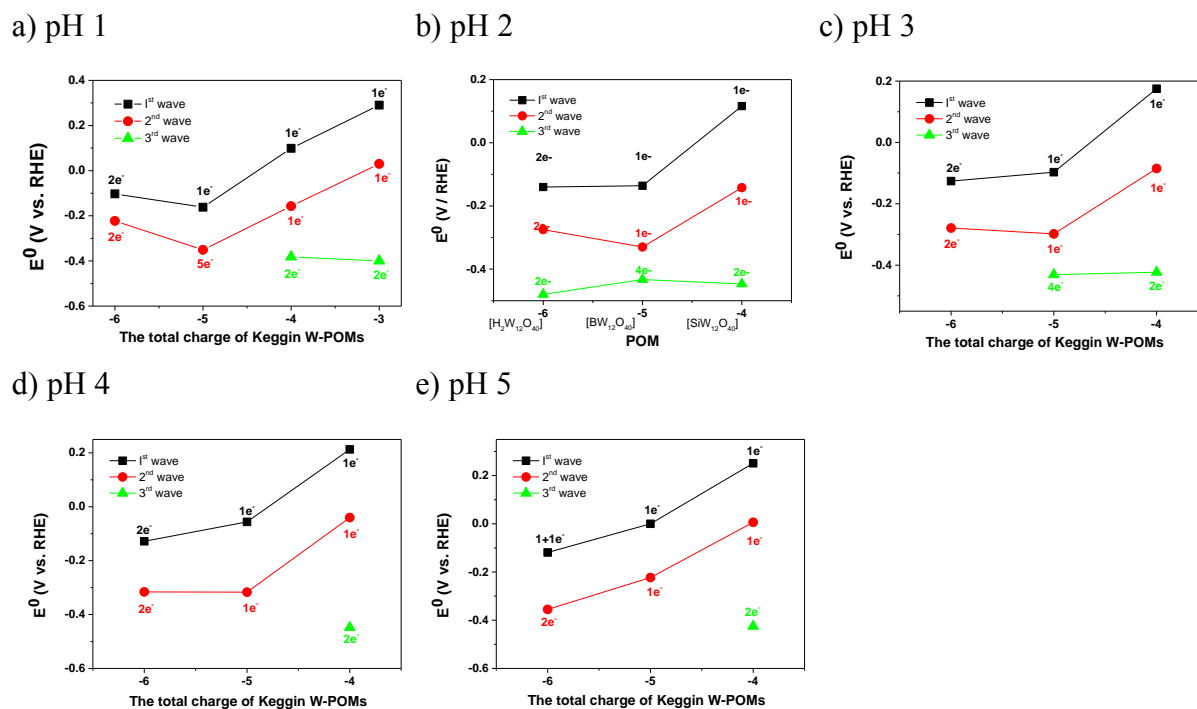


Figure 2.2.6 Formal potential (E^0) and number of electrons of each wave of the four studied Keggin W-POMs as a function of the total charge in different pH solutions (a) pH 1; (b) pH 2; (c) pH 3; (d) pH 4; (e) pH 5. Charge number: -3 is from $[\text{PW}_{12}\text{O}_{40}]^{3-}$; -4 is from $[\text{SiW}_{12}\text{O}_{40}]^{4-}$, -5 is from $[\text{BW}_{12}\text{O}_{40}]^{5-}$, and -6 is from $[\text{H}_2\text{W}_{12}\text{O}_{40}]^{6-}$. A missing point means that the wave is not present.

2.2.2 Electrochemical properties of Mo-based Keggin and W-based Dawson POMs

The electrochemical redox behavior of two Mo-based Keggin-type POMs, namely $\text{H}_4[\text{SiMo}_{12}\text{O}_{40}]$ and $\text{H}_3[\text{PMo}_{12}\text{O}_{40}]$ is depicted in Figure 2.2.7 as a function of pH and summarized in Table 2.2.2. It must be emphasized here that these POMs are commercially available as an aqueous solution of the acid form, with concentration given as weight percent of $[\text{MoO}_3]$ obtained by gravimetric analysis. For example, for $\text{H}_4[\text{SiMo}_{12}\text{O}_{40}]$ this value is between 18 to 22 %, thus the theoretical concentration of the further diluted POM in the working electrolyte has some degree of imprecision. While the redox behavior of $\text{H}_4[\text{SiMo}_{12}\text{O}_{40}]$ is similar to the one reported in the literature¹⁴, very few reports of $\text{H}_3[\text{PMo}_{12}\text{O}_{40}]$ exists and reported results are sometimes different.¹⁴⁻¹⁵ In detail, for $\text{H}_4[\text{SiMo}_{12}\text{O}_{40}]$ three reversible redox waves bearing two electrons each are observed at pH 1 and pH 2 (Figure 2.2.7a). At pH 5 (Figure 2.2.7b), we have observed two redox waves but with a much lower current intensity. This due to the decomposition of the POM. In fact, at pH 5, it was shown by ionic chromatography that 70% of the acid is decomposed.¹⁶ This is consistent with the decrease of the current intensity observed in our data at pH 5 compared with pH 1 or 2. Moreover, the signal is decreasing after each scan, suggesting that the compound is not stable at this pH.

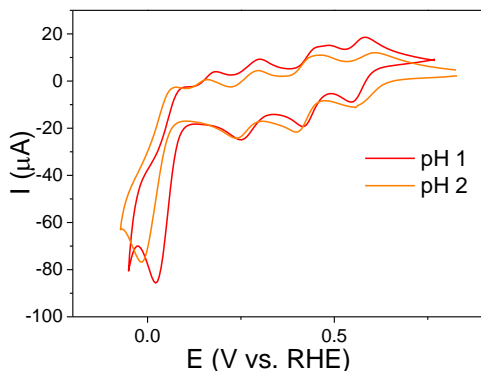
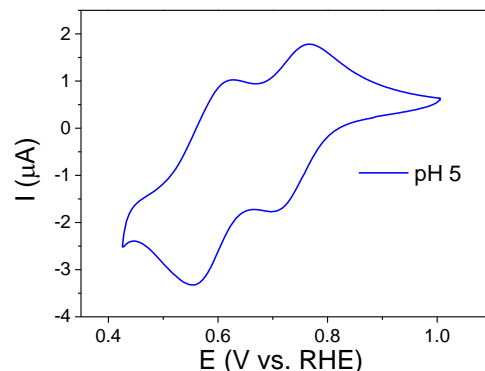
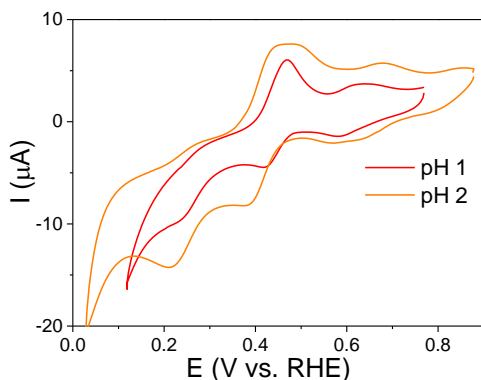
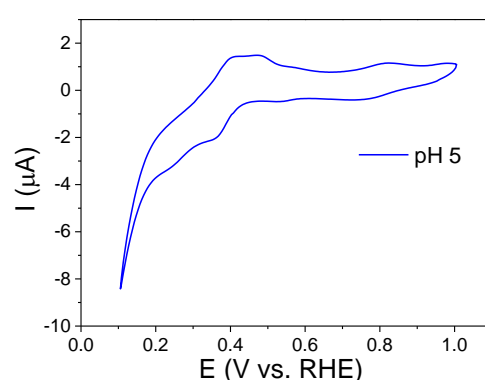
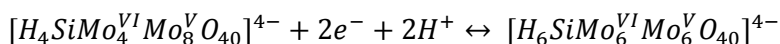
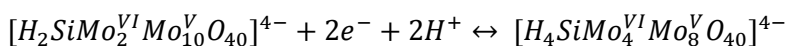
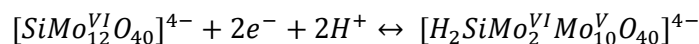
a) $H_4[SiMo_{12}O_{40}]$ pH 1 and 2b) $H_4[SiMo_{12}O_{40}]$ pH 5c) $H_3[PMo_{12}O_{40}]$ pH 1 and 2d) $H_3[PMo_{12}O_{40}]$ pH 5

Figure 2.2.7 Cyclic voltammetry of $[SiMo_{12}O_{40}]^{4-}$ a) at pH 1 and 2, b) at pH 5; $[PMo_{12}O_{40}]^{3-}$ at c) pH 1 and 2, d) at pH 5. Experimental conditions: working electrode, glassy carbon (GC); POM concentration, 1 mM; scan rate, 20 mVs⁻¹.

At pH 1 and 2, taking into account the instability of the compound for higher pH values, the three redox processes can be described as below.¹⁷ It must be noted that the pK_a of $H_4[SiMo_{12}O_{40}]$ was not reported, but this is a less strong acid than $H_3[PMo_{12}O_{40}]$.¹⁸ As a consequence, the actual redox species at pH 1 and 2 may be $H_4[SiMo_{12}O_{40}]$ and not $[SiMo_{12}O_{40}]^{4-}$. The notation of $[SiMo_{12}O_{40}]^{4-}$ used throughout this chapter is just for the sake of uniformity compared to the other POMs.



For $H_3[PMo_{12}O_{40}]$ at pH 1 and pH 2 multiple waves are visible but they are overlapping and not fully reversible. For comparison, Figure 2.2.8 shows three reported cyclic voltammetry studies from different research groups. The first wave is a two electrons wave that splits in two overlapping waves. This is common to our results and the reported ones. The explanation for this is not very clear, some authors suggesting the hydrolysis of the POM. The common observation is that the redox behavior is complex and sensitive to scan rate and concentration. The second wave is a two electrons reversible wave and the results are very similar between us and all reported works. Finally, for the third wave we observe the same irreversible

behavior as the one reported by R. Włodarczyk et al.^{14, 15b} On the contrary, the group of T. Matsui et al.^{15a} shows a very reversible third wave, but the experiments were conducted in the absence of any electrolyte and at high concentration of the POM (100 mM). This reinforces the observation that the behavior of $H_3[PMo_{12}O_{40}]$ is very sensitive to many experimental parameters. Taking into account the reported pKa values for the first protonation of this POM (pKa 2.4¹⁹), at pH 1, the redox processes could be described as below. The notation of $[PMo_{12}O_{40}]^{3-}$ used throughout this chapter is just for the sake of uniformity compared to the other POMs.

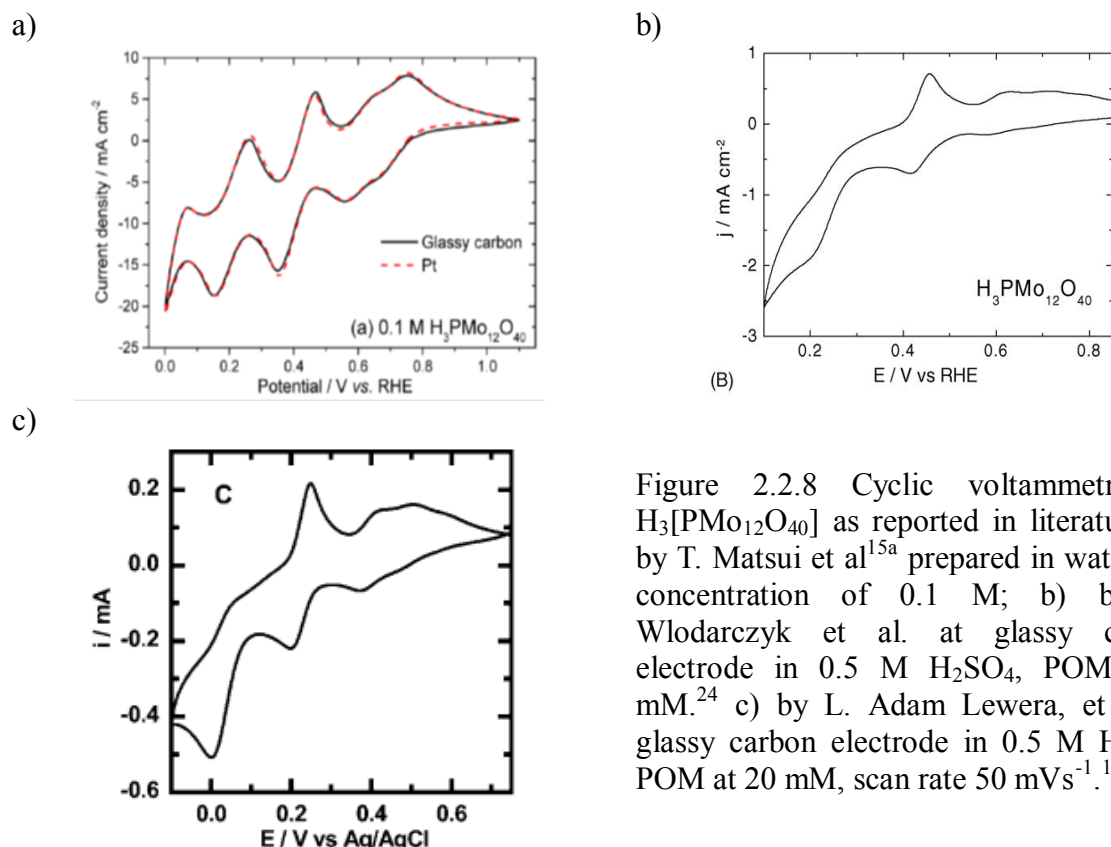
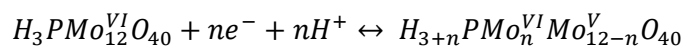


Figure 2.2.8 Cyclic voltammetry of $H_3[PMo_{12}O_{40}]$ as reported in literature: a) by T. Matsui et al.^{15a} prepared in water at a concentration of 0.1 M; b) by R. Włodarczyk et al. at glassy carbon electrode in 0.5 M H_2SO_4 , POM at 5 mM.²⁴ c) by L. Adam Lewera, et al. at glassy carbon electrode in 0.5 M H_2SO_4 , POM at 20 mM, scan rate 50 mVs⁻¹.^{15b}

Table 2.2.2 Formal potentials and number of electrons of each wave of $H_4SiMo_{12}O_{40}$ and $H_3PMo_{12}O_{40}$.

pH	POMs	E ⁰ / V vs. RHE (no. of electrons)			
		I st wave	II nd wave	III rd wave	IV th wave
pH 1	$[PMo_{12}O_{40}]^{3-}$	0.59 (2e ⁻)	0.42 (2e ⁻)	0.23 (2e ⁻)	–
	$[SiMo_{12}O_{40}]^{4-}$	0.55 (2e ⁻)	0.42 (2e ⁻)	0.25 (2e ⁻)	0.02
pH 2	$[PMo_{12}O_{40}]^{3-}$	0.63; 0.57 (1+1e ⁻)	0.38 (2e ⁻)	0.21 (2e ⁻)	–
	$[SiMo_{12}O_{40}]^{4-}$	0.55 (2e ⁻)	0.40 (2e ⁻)	0.25 (2e ⁻)	-0.01

An important observation is that the formal potentials of Mo-based Keggin POMs are more positive than their W-based analogous. Moreover, the presence of phosphate, rather than silicate tetrahedral unit Keggin type structure tends to shift redox reactions towards more

positive values. As a summary, Figure 2.2.9 displays the formal potential of all POMs studied in this thesis. By choosing both W and Mo-based Keggin POMs a wide span of formal potential with diverse number of electrons was covered.

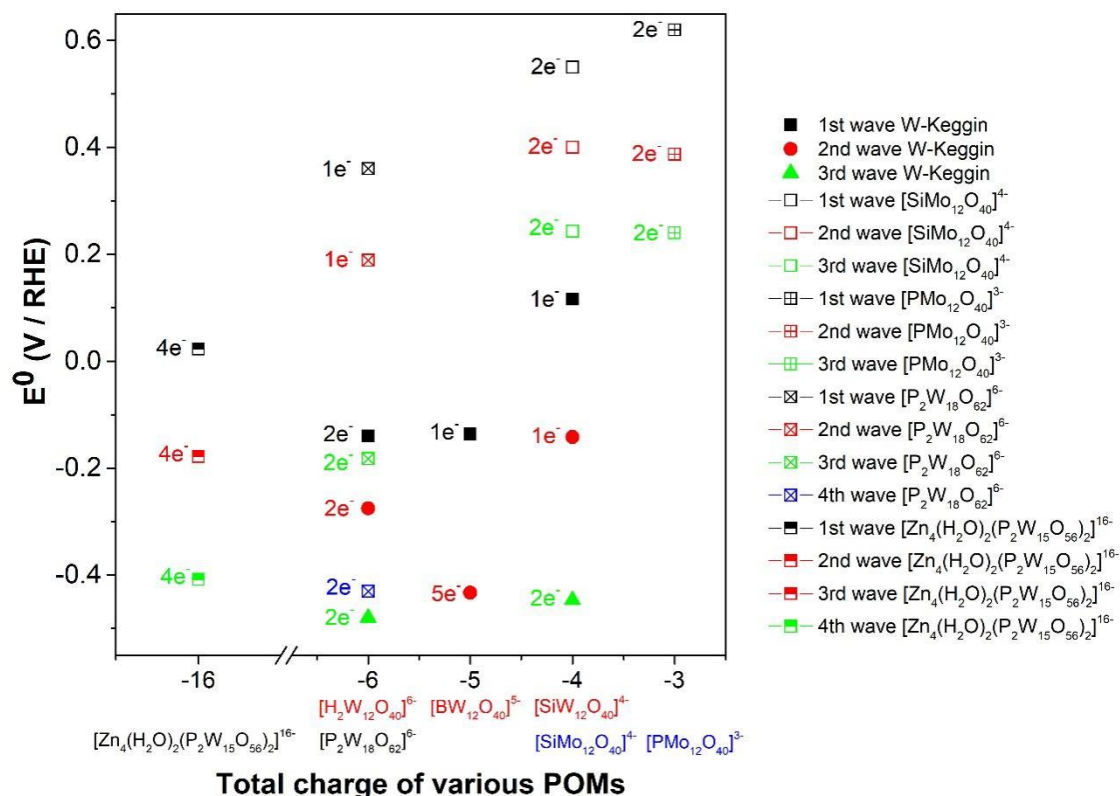
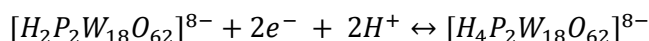
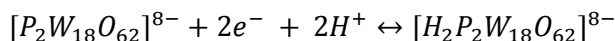
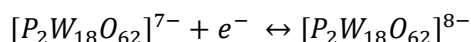
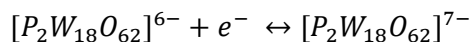
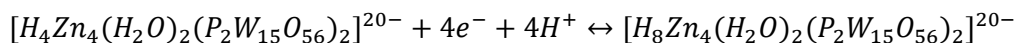
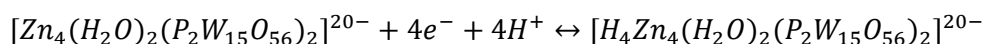
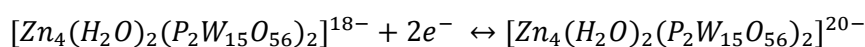
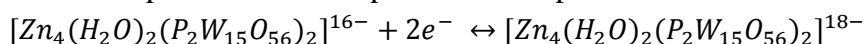


Figure 2.2.9 Comparisons of formal potential of all POMs studied in this work, at pH 2. Only $[PW_{12}O_{40}]^{3-}$ is missing due to its instability at pH > 1.7.

In order to increase even more the number of electrons transferred in a single wave we have completed our study by testing dimers sandwich Wells-Dawson-type POMs further described here in comparison with parent Wells-Dawson-type POM α - $[P_2W_{12}O_{62}]^{6-}$. A series of dimetal (2^+)-substituted dimer sandwich Dawson POMs, namely $Na_{16}[Zn_4(H_2O)_2(P_2W_{15}O_{56})_2]^{16-}$,^{8, 20} $Na_{16}[Cd_4(H_2O)_2(P_2W_{15}O_{56})_2]^{16-}$,⁸ and $Na_{16}[Mn_4(H_2O)_2(P_2W_{15}O_{56})_2]^{16-}$ ²¹ were synthesized by our group. The trivacant heteropoly ligand $[P_2W_{15}O_{56}]^{12-}$ is obtained from the Dawson-type polyoxometalate $[P_2W_{18}O_{62}]^{6-}$. On the action of metallic cations, metal-heteropolyanions that can be formulated as $[M_4(H_2O)_2(P_2W_{15}O_{56})_2]^{n-}$ (where $M = Mn^{II}, Fe^{III}, Co^{II}, Ni^{II}, Cu^{II}, Zn^{II}$, or Cd^{II} , and $n = 16$, except in the case of Fe^{III} , where $n = 12$) are obtained. These constitute an extensive series of compounds in which a tetranuclear cluster $[M_4O_{14}(H_2O)_2]$ is encapsulated between two trivacant fragments.^{8, 20, 22} Of the four metal atoms, two reside in a pseudooctahedral environment with one coordination site occupied by a labile water molecule, which can be replaced by other ligands.^{7, 23} Figure 2.2.10 shows the CV of dimers, $[Cd_4(H_2O)_2(P_2W_{15}O_{56})_2]^{16-}$ ($P_4W_{30}Cd_4$), $[Mn_4(H_2O)_2(P_2W_{15}O_{56})_2]^{16-}$ ($P_4W_{30}Mn_4$) and $[Zn_4(H_2O)_2(P_2W_{15}O_{56})_2]^{16-}$ ($P_4W_{30}Zn_4$) as well as parent α - $[P_2W_{18}O_{62}]^{6-}$. Parent Dawson POM α - $[P_2W_{18}O_{62}]^{6-}$ displays a well-known behavior of four consecutive redox waves bearing one, one, two and two electrons respectively (at pH 2). These redox processes are displayed below:²⁴



Tetranuclear Dawson-Derived Sandwich Complexes have analogous redox behavior (Figure 2.2.10e) at pH 2. They exhibit three consecutive redox peaks corresponding to four transferred electrons, but the waves split into two two-electron waves that partially overlap in a POM specific manner. The stability of these POMs at pH 1 is reduced and the redox behavior at pH 5 is very different. Thus, at pH 2, the four redox processes of $P_4W_{30}Zn_4$ can be described as below. The pKa of these compounds is comprised between 3.5 and 3.6.⁷



Reduction potential and electron numbers of each wave are summarized in Table 2.2.3. It can be observed that the reduction potentials of all these POMs happens are very similar. When comparing the dimers with the parent Dawson (Figure 2.2.10f) it can be seen that the last reduction happens at very similar potentials, suggesting that the reduction appears in the same position both on dimers and on the parent compounds and the surrounding environment has little impact.

In order to compare these Dawson POMs with the studied Keggin POMs, their formal potentials and electron numbers of each wave are displayed in Figure 2.2.9 (see before). It can be observed that parent Dawson has quite positive formal potential when compared to W-based Keggin POMs and a similar potential to the second and third waves of Mo-based Keggin POMs. Dimer Dawson POMs have similar potentials with the W-based Keggin POMs, while bearing a higher number of electrons.

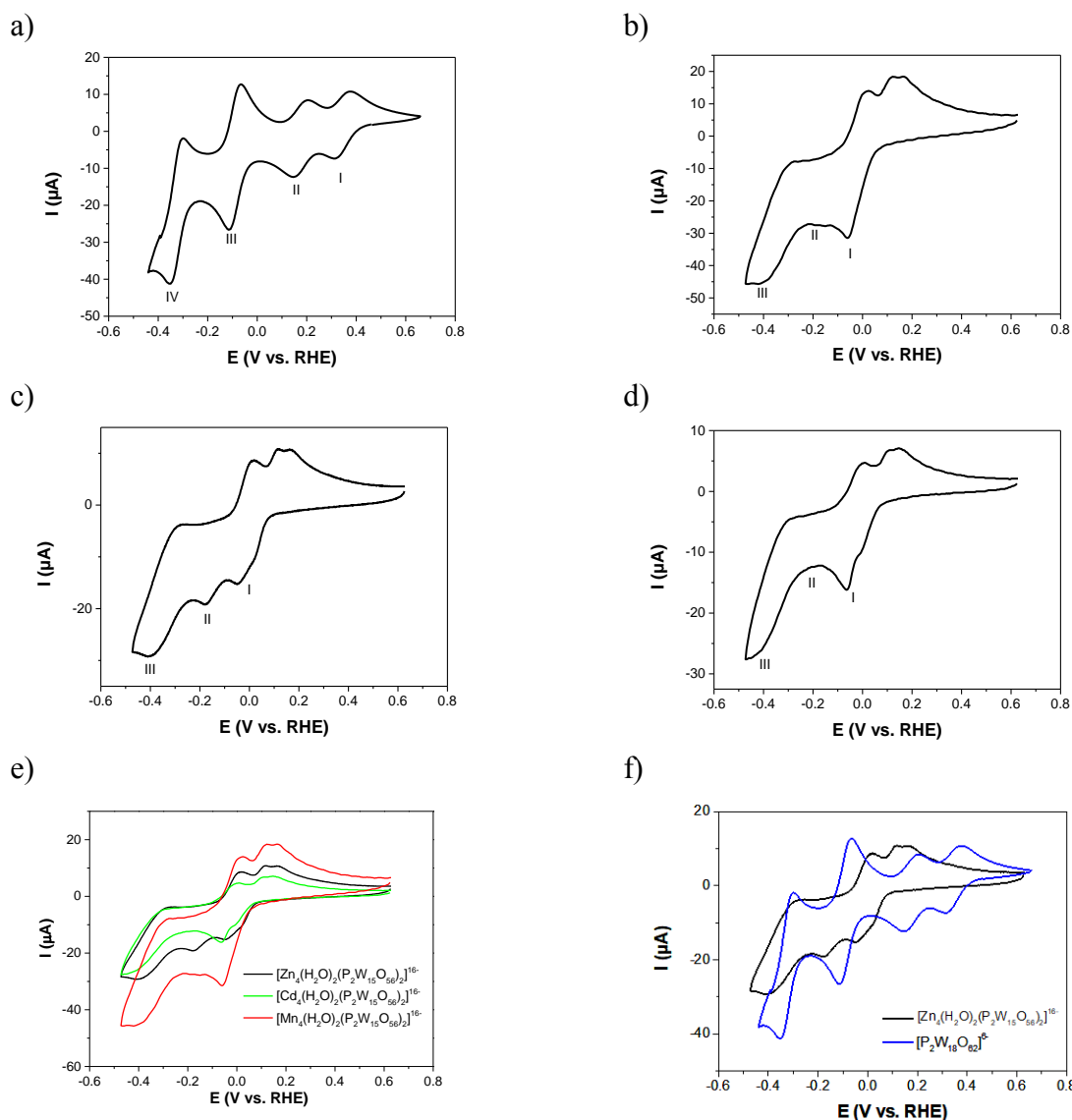


Figure 2.2.10 Cyclic voltammetry of Dawson POMs: a) α -[P₂W₁₈O₆₂]⁶⁻, b) [Mn₄(H₂O)₂(P₂W₁₅O₅₆)₂]¹⁶⁻; c) [Zn₄(H₂O)₂(P₂W₁₅O₅₆)₂]¹⁶⁻; d) [Cd₄(H₂O)₂(P₂W₁₅O₅₆)₂]¹⁶⁻; e) and f) comparisons. Experimental conditions: working electrode, glassy carbon (GC); POM concentration: 0.1 mM; scan rate: 20 mVs⁻¹; electrolyte, 0.5 M Na₂SO₄ + H₂SO₄ at pH 2.

Table 2.2.3 Dawson POMs reduction potential (V vs. RHE) and electron numbers of each peak

POMs	Peak potential (V vs. RHE)			
	peak 1	peak 2	peak 3	Peak 4
[Cd ₄ (H ₂ O) ₂ (P ₂ W ₁₅ O ₅₆) ₂] ¹⁶⁻	0.030 (2e ⁻) -0.083 (2e ⁻)	Not visible	-0.433 (4e ⁻)	
[Zn ₄ (H ₂ O) ₂ (P ₂ W ₁₅ O ₅₆) ₂] ¹⁶⁻	0.023 (2e ⁻) -0.047 (2e ⁻)	-0.178 (4e ⁻)	-0.408 (4e ⁻)	
[Mn ₄ (H ₂ O) ₂ (P ₂ W ₁₅ O ₅₆) ₂] ¹⁶⁻	-0.061 (4e ⁻)	-0.159 (2e ⁻) -0.193 (2e ⁻)	-0.330 (2e ⁻) -0.409 (2e ⁻)	
α -[P ₂ W ₁₈ O ₆₂] ⁶⁻	0.360 (1e ⁻)	0.189 (1e ⁻)	-0.182 (2e ⁻)	-0.430 (2e ⁻)

2.3 Nitrite reduction catalyzed by POMs – Cyclic voltammetry studies

2.3.1 W-based Keggin POMs as catalysts for nitrite reduction

Nitrite reduction catalyzed by a series of Keggin POMs at different pH values is described here. In the absence of POMs, GC electrode is not active towards nitrite reduction. But in the presence of POMs, the catalytic current starts already from POMs' first reduction wave. The current intensity increases with the concentration of nitrite, but one may inquire if the current intensity increases in the same manner irrespective the POM reduction state and pH. This will be analyzed in the following part, by describing the results for each POM. A general equation describing the catalytic reduction is expressed below, but the reaction products cannot be identified only from cyclic voltammetry measurements.

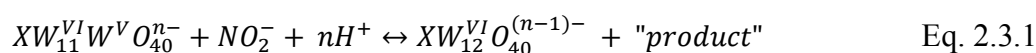
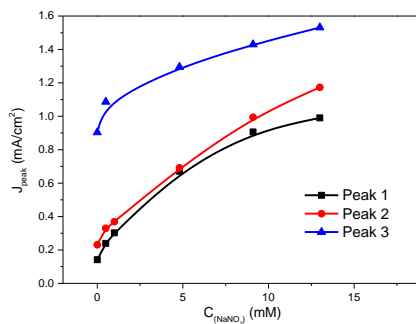
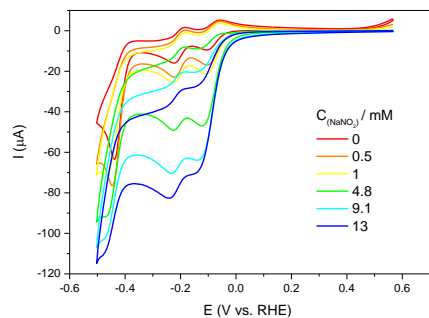


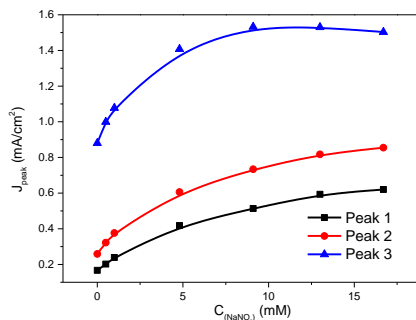
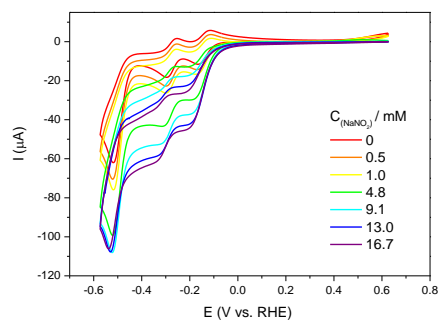
Figure 2.3.1 shows CV measurements for increasing concentration of nitrite in the presence $[H_2W_{12}O_{40}]^{6-}$ and the variation of current intensities with nitrite concentration in the pH range of 1 to 5. It can be observed that, at all pH values and for all three redox peaks, the current intensity increases with nitrite concentration, although not in a perfect linear manner. In almost all situations, the current intensity increases sharply for low concentration of nitrite (up to 5 mM). For higher concentrations, the current intensity increases but in a lesser extent. In the absence of nitrite, the current intensity of all peaks decreases with the increase of pH, especially for pH values higher than 3. Thus, a direct comparison of absolute values of current intensity in the presence of nitrite is not a good reasoning.

Another parameter that can be used as a comparison criterion is the onset potential of the catalytic reaction at POM's first reduction peak. This is arbitrarily defined as the potential where the current in the presence of nitrite becomes with 0.5 μA higher than in the absence of nitrite, i.e. E_{onset} where $|I_{HNO_2/NO_2^-} - I_{POM}| = 0.5 \mu A$. The concentration of 1 mM of nitrite was chosen, due to high catalytic activity observed at this value (as described before). In this way, the catalytic onset potentials are respectively at 0.076 V vs. RHE (pH 1), -0.051 V vs. RHE (pH 2), -0.011 V vs. RHE (pH 3), -0.078 V vs. RHE (pH 4), and -0.108 V vs. RHE (pH 5) for $[H_2W_{12}O_{40}]^{6-}$. The onset potential shifts to more negative values for higher pH values.

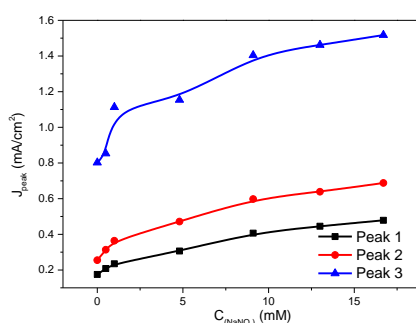
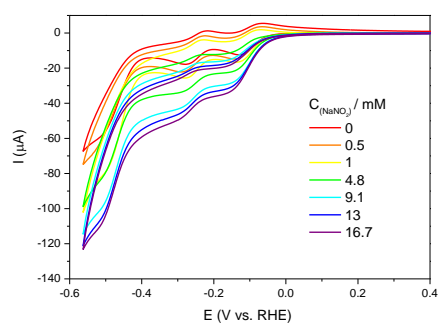
a) pH = 1



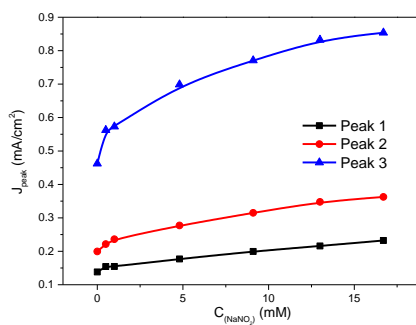
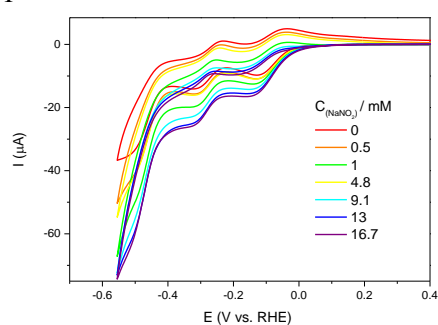
b) pH = 2



c) pH = 3



d) pH = 4



e) pH = 5

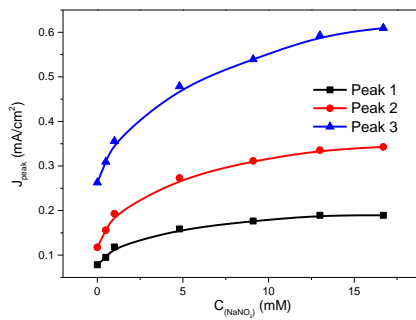
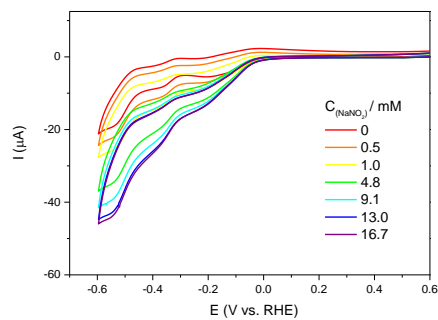
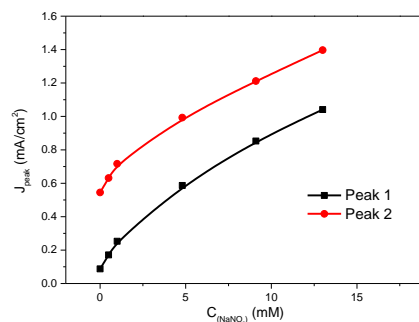
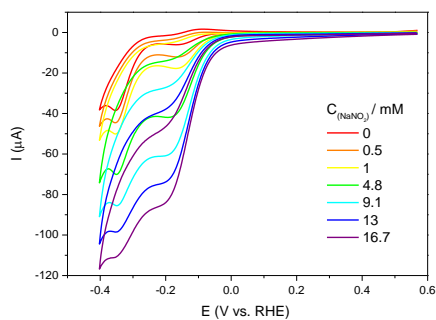


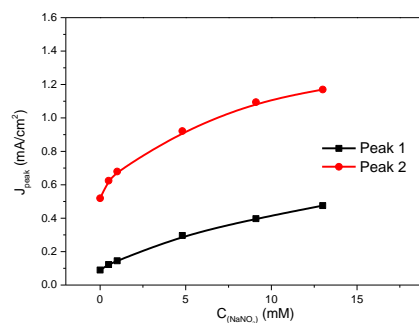
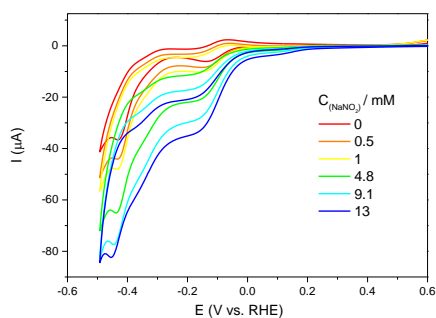
Figure 2.3.1 Cyclic voltammetry of $[\text{H}_2\text{W}_{12}\text{O}_{40}]^{6-}$ in the presence of different concentrations of nitrite (from 0 to 16.7 mM) at different pH values. Experimental

conditions: $[\text{H}_2\text{W}_{12}\text{O}_{40}]^{6-}$, 1 mM; working electrode, glassy carbon; scan rate, 20 mVs^{-1} ; a) pH 1, 0.5 M Na_2SO_4 ; b) pH 2, 0.5 M Na_2SO_4 ; c) pH 3, 0.3 M $\text{Na}_3[\text{C}_6\text{H}_5\text{O}_7]$; d) pH 4, 1 M CH_3COOLi ; e) pH 5, 1 M CH_3COOLi . Right panel: Current density of the three redox peaks of $[\text{H}_2\text{W}_{12}\text{O}_{40}]^{6-}$ as a function of nitrite concentration.

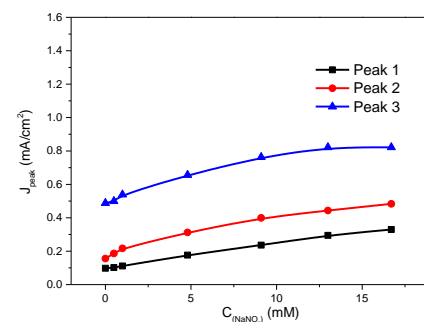
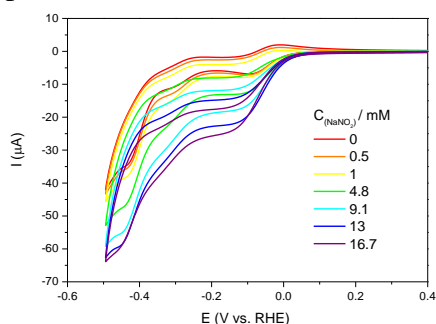
a) pH = 1



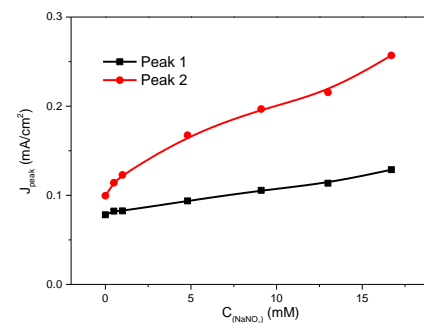
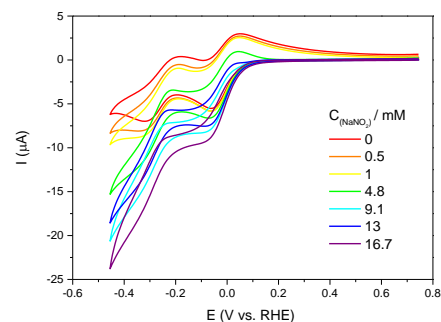
b) pH = 2



c) pH = 3



d) pH = 4



e) pH = 5

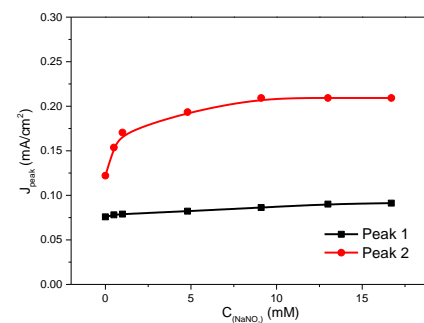
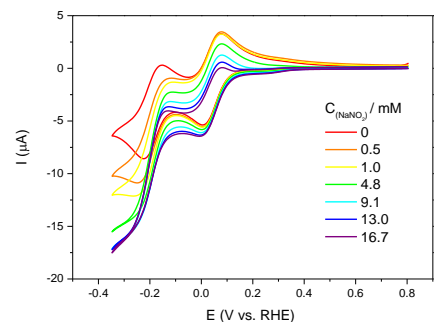
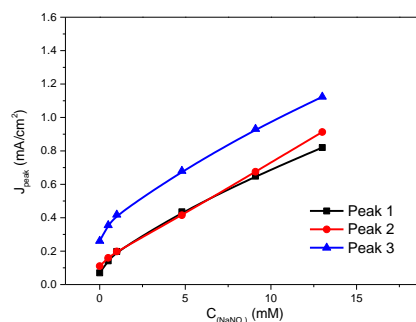
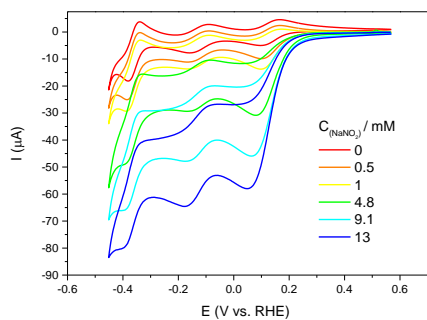


Figure 2.3.2 Cyclic voltammetry of $[\text{BW}_{12}\text{O}_{40}]^{5-}$ in the presence of different concentrations of nitrite (from 0 to 16.7 mM) at different pH values. Experimental conditions: $[\text{BW}_{12}\text{O}_{40}]^{5-}$, 1

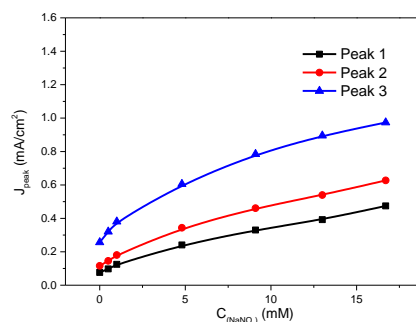
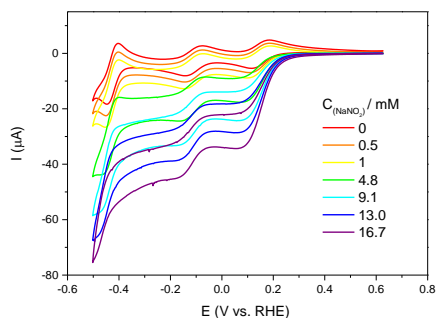
mM; working electrode, glassy carbon; scan rate, 20 mVs⁻¹; a) pH 1, 0.5 M Na₂SO₄; b) pH 2, 0.5 M Na₂SO₄; c) pH 3, 0.3 M Na₃[C₆H₅O₇]; d) pH 4, 1 M CH₃COOLi; e) pH 5, 1 M CH₃COOLi. Right panel: current density of the three (two) redox peaks of [BW₁₂O₄₀]⁵⁻ as a function of nitrite concentration.

Nitrite reduction current is observed on all three reduction waves of [SiW₁₂O₄₀]⁴⁻ and increases with the concentration of NaNO₂ added in solution (Figure 2.3.3). The group of Nadjo et al. has studied different POMs as homogeneous electrocatalysts including [SiW₁₂O₄₀]⁴⁻.²⁵ Their conclusion was that at pH 2, the catalyst is the reduced species [SiW^{VI}₁₁W^VO₄₀]⁵⁻, present at the first wave, and at pH 5, it is the multielectron reduced [H₂SiW^{VI}₈W^V₄O₄₀]⁶⁻, present at the third wave.¹² We have refined this study here by including more pH values. Compared with [H₂W₁₂O₄₀]⁶⁻ and [BW₁₂O₄₀]⁵⁻, proton concentration has more influence on catalytic behavior of [SiW₁₂O₄₀]⁴⁻. For example, at pH 4 and pH 5, the catalytic current intensities of peak 1 and peak 2 are varying very little with nitrite concentration. For peak 3 the variation of current intensity with the concentration is more obvious, but the absolute values are much lower than those at pH 1 and pH 2. Similar to [H₂W₁₂O₄₀]⁶⁻ and [BW₁₂O₄₀]⁵⁻, all absolute values of current intensity are much lower for pH ≥ 3. According to the definition of the onset potential, the obtained values (at the first wave) are respectively 0.264 V vs. RHE (pH 1), 0.225 V vs. RHE (pH 2) and 0.175 V vs. RHE (pH 3), while no onset potential cannot be found at pH 4 and pH 5 because the catalytic current of peak 1 is lower than the defined value of 0.5 μA.

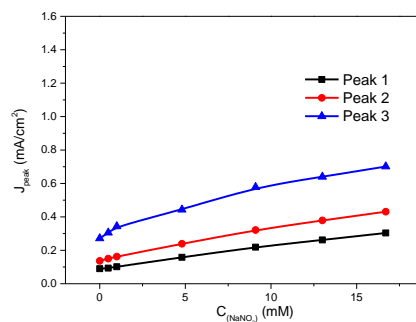
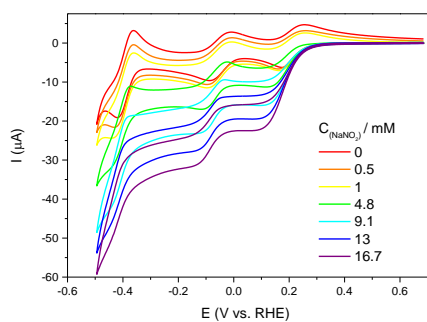
a) pH = 1



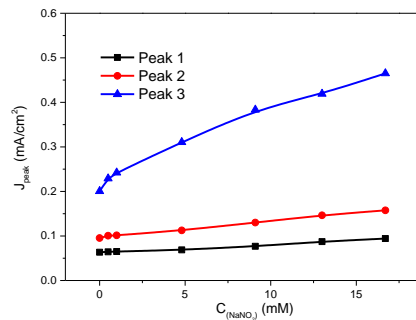
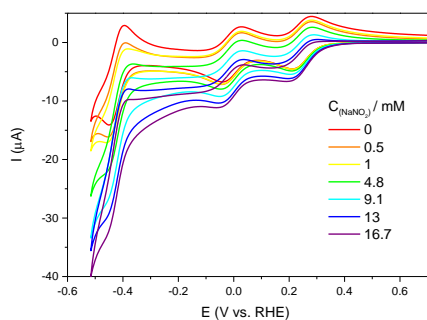
b) pH = 2



c) pH = 3



d) pH = 4



e) pH = 5

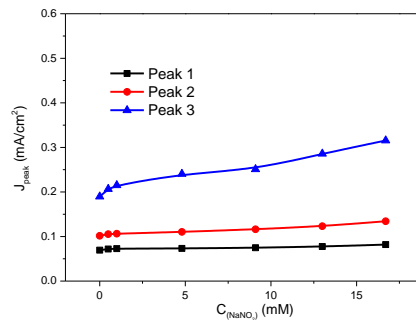
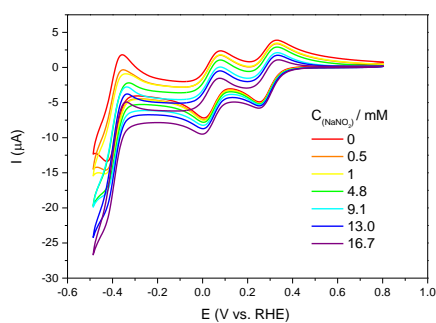


Figure 2.3.3 Cyclic voltammetry of $[\text{SiW}_{12}\text{O}_{40}]^{4-}$ in the presence of different concentrations of nitrite (from 0 to 16.7 mM) at different pH values. Experimental conditions: $[\text{SiW}_{12}\text{O}_{40}]^{4-}$, 1

mM; working electrode, glassy carbon; scan rate, 20 mVs⁻¹; a) pH 1, 0.5 M Na₂SO₄; b) pH 2, 0.5 M Na₂SO₄; c) pH 3, 0.3 M Na₃[C₆H₅O₇]; d) pH 4, 1 M CH₃COOLi; e) pH 5, 1 M CH₃COOLi. Right panel: Current density of the three (two) redox peaks of [SiW₁₂O₄₀]⁴⁻ as a function of nitrite concentration.

Different from other POMs, [PW₁₂O₄₀]³⁻ is only stable at pH lower than 1.7. Hence, the catalytic performance of [PW₁₂O₄₀]³⁻ was studied only at pH 1. Nitrite reduction current is observed on all three reduction waves of [PW₁₂O₄₀]³⁻ and increases with the concentration of NaNO₂ added in solution. (Figure 2.3.4a) The catalytic current increase almost linearly on the entire concentration range. According to definition of the onset potential, the obtained value (at the first wave) is respectively 0.454 V vs. RHE (pH 1).

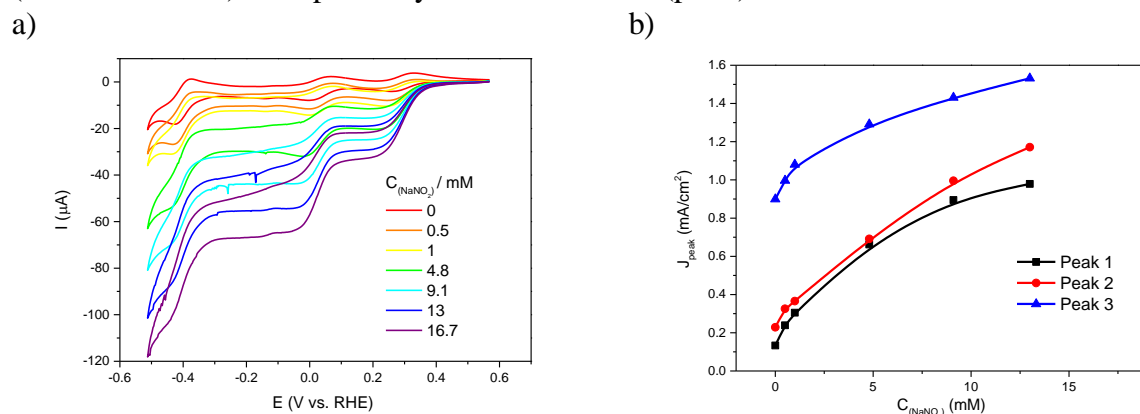


Figure 2.3.4 (a) Cyclic voltammetry of [PW₁₂O₄₀]³⁻ in the presence of different concentration of nitrite (from 0 to 16.7 mM) at pH 1. Experimental conditions: [PW₁₂O₄₀]³⁻, 1 mM; working electrode, glassy carbon; scan rate, 20 mVs⁻¹; electrolyte, pH 1 0.5 M Na₂SO₄. (b) Current density of the three redox peaks of [PW₁₂O₄₀]³⁻ as a function of nitrite concentration. Experimental conditions as in Figure 2.3.4a.

Comparison of four Keggin-type POMs:

From data shown in Figure 2.3.1 to Figure 2.3.4, a general observation can be made to all POMs. The catalytic activity greatly diminishes for pH higher than 3. Knowing that the pK_a of nitrous acid (HNO₂) is equal to 3.3, this suggests that the charge repulsion between POMs and nitrite ion (NO₂⁻) could be one cause for the diminished catalytic activity. Moreover, the reduction reaction is consuming protons; thus, an increase of pH will cause slower kinetics. While for [H₂W₁₂O₄₀]⁶⁻ all three reduction waves display catalytic activity for all pH values, for the other POMs only the third wave displays catalytic activity for all pH values. Thus, a good comparison for the POMs should be made either only for the third wave irrespective the pH, or at pH 1 (or pH 2) for the first and second wave. However, the number of electrons of each wave is POM dependent, thus one may inquire how this influences the catalytic activity and even the reaction products. It is worth to note that the stepwise reduction of HNO₂/NO₂⁻ to NO, N₂O and N₂ requires one, two and two electrons respectively. DEMS studies will be further described in order to correlate the reaction product to each catalytic wave of the POMs.

The onset potentials of nitrite reduction at the first wave of these four Keggin POMs are summarized in Table 2.3.1. The onset potential becomes more negative as the charge number of the POMs increases. Only [H₂W₁₂O₄₀]⁶⁻ have a catalytic activity for pH 4 and pH 5. For all POMs, the onset potential becomes more negative as the proton concentration decreases.

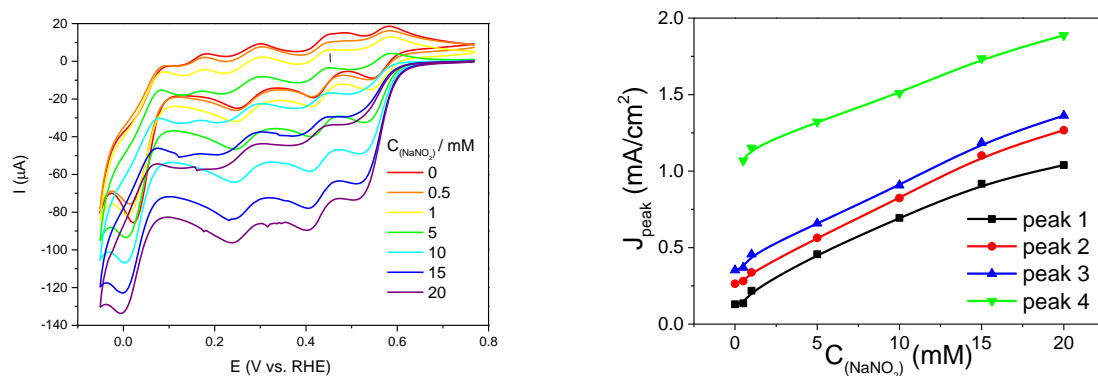
Table 2.3.1 Onset potential of nitrite reduction with different Keggin POMs at different pH values. (*: onset potential cannot be measured because the catalytic current is lower than the arbitrarily defined value of 0.5 μ A).

POM	Onset potential (V vs. RHE)				
	pH 1	pH 2	pH 3	pH 4	pH 5
[H ₂ W ₁₂ O ₄₀] ⁶⁻	0.076	-0.051	-0.011	-0.078	-0.108
[BW ₁₂ O ₄₀] ⁵⁻	0.037	0.076	-0.07	*	*
[SiW ₁₂ O ₄₀] ⁴⁻	0.264	0.225	0.175	*	*
[PW ₁₂ O ₄₀] ³⁻	0.454	-	-	-	-

2.3.2 Mo-based Keggin POMs as catalysts for nitrite reduction

Figure 2.3.5 and 2.3.6 shows CV measurements for increasing concentration of nitrite in the presence and the variation of current intensities with nitrite concentration of H₄[SiMo₁₂O₄₀] and H₃[PMo₁₂O₄₀]. Nitrite reduction current is observed on all four reduction waves of H₄[SiMo₁₂O₄₀] and increases with the concentration of NaNO₂ being added in solution (Figure 2.3.5). It can be seen that the current intensity varies almost linearly with the concentration at pH 1, while at pH 2, the intensity tends to form a plateau for higher concentrations (Figure 2.3.5). According to definition of onset potential, the obtained values are 0.59 V vs. RHE (pH 1), 0.58 V vs. RHE (pH 2), which are more positive compared to W-based Keggin POMs. Different from H₄[SiMo₁₂O₄₀], H₃[PMo₁₂O₄₀] redox waves disappear rapidly after adding nitrite, although there is still obvious nitrite reduction current. The stability of H₃[PMo₁₂O₄₀] in the presence of nitrite, especially at pH 1 is debatable as the shape of the peaks is quite altered. Especially, the first wave of H₃[PMo₁₂O₄₀] nearly disappears after the addition of 1 mM nitrite. Thus, the onset potential cannot be calculated precisely. For both pH 1 and pH 2 (Figure 2.3.6), the current intensity varies a lot for low concentrations of nitrite and starts to form a plateau for higher concentrations.

a) pH = 1



b) pH = 2

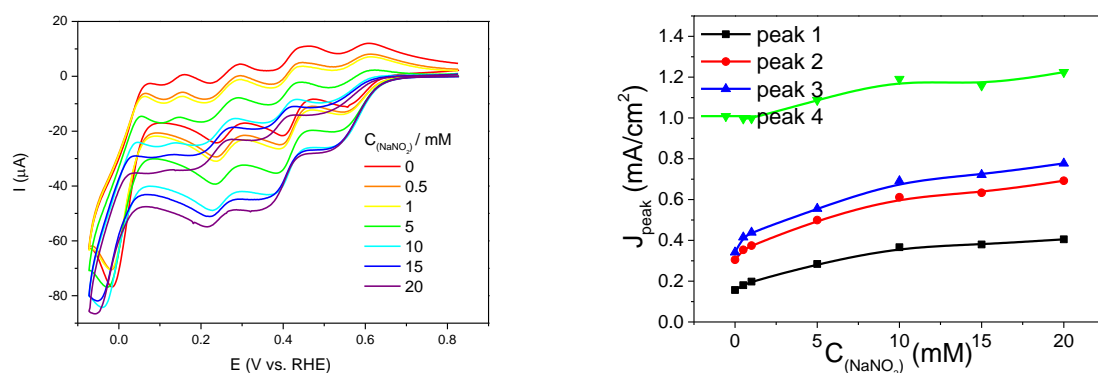
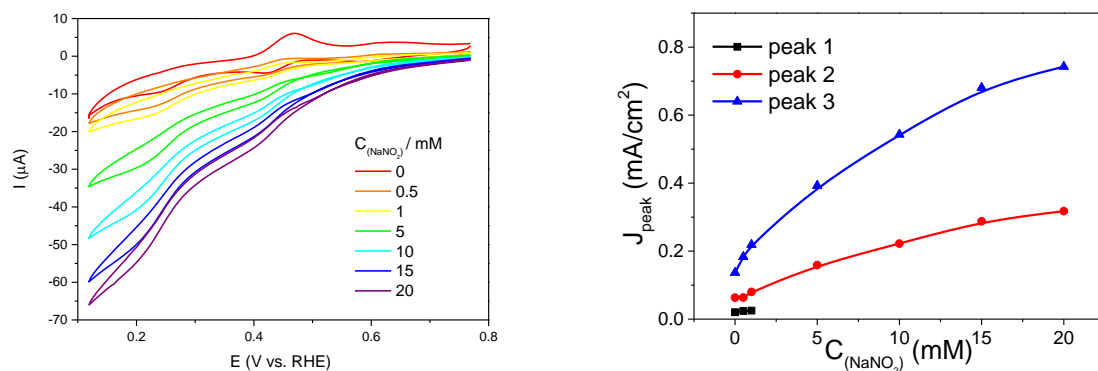


Figure 2.3.5 Cyclic voltammetry of $\text{H}_4[\text{SiMo}_{12}\text{O}_{40}]$ in the presence of different concentrations of nitrite (from 0 to 20 mM) at pH 1 and 2. Experimental conditions: $\text{H}_4[\text{SiMo}_{12}\text{O}_{40}]$, 1 mM; working electrode, glassy carbon; scan rate, 20 mVs^{-1} ; a) pH 1, 0.5 M Na_2SO_4 ; b) pH 2, 0.5 M Na_2SO_4 . Right panel: current density of the four redox peaks of $\text{H}_4[\text{SiMo}_{12}\text{O}_{40}]$ as a function of nitrite concentration.

a) pH = 1



b) pH = 2

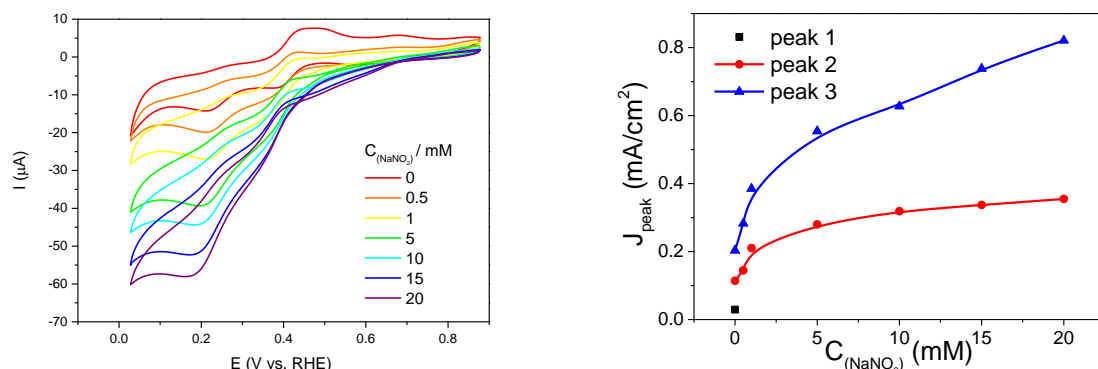


Figure 2.3.6 Cyclic voltammetry of $H_3[PMo_{12}O_{40}]$ in the presence of different concentrations of nitrite (from 0 to 20 mM) at pH 1 and 2. Experimental conditions: $H_3[PMo_{12}O_{40}]$, 1 mM; working electrode, glassy carbon; scan rate, 20 mVs⁻¹; a) pH 1, 0.5 M Na₂SO₄; b) pH 2, 0.5 M Na₂SO₄. Right panel: Current density of the two redox peaks of $H_3[PMo_{12}O_{40}]$ as a function of nitrite concentration.

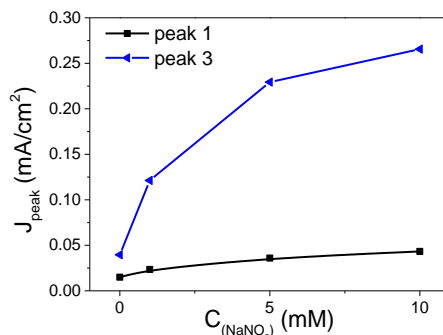
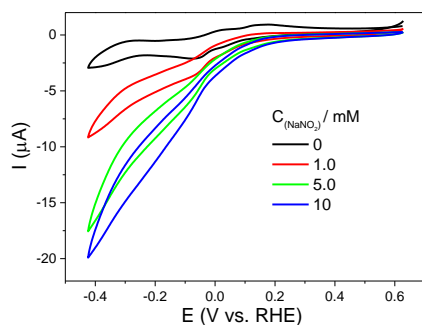
2.3.3 W-based Dawson POMs as catalysts for nitrite reduction

Figure 2.3.7 shows the CV for increasing concentrations of nitrite in the case of the four Dawson POMs: $K_6[\alpha-P_2W_{18}O_{62}]$ (P_2W_{18}) and a series of dimetal(2⁺)-substituted dimers sandwich Dawson POMs $Na_{16}[Zn_4(H_2O)_2(P_2W_{15}O_{56})_2]^{8-}$, $Na_{16}[Cd_4(H_2O)_2(P_2W_{15}O_{56})_2]^{8-}$ ($P_4W_{30}Zn_4$), $Na_{16}[Mn_4(H_2O)_2(P_2W_{15}O_{56})_2]^{21-}$ ($P_4W_{30}Mn_4$). These POMs were studied only at pH 2.

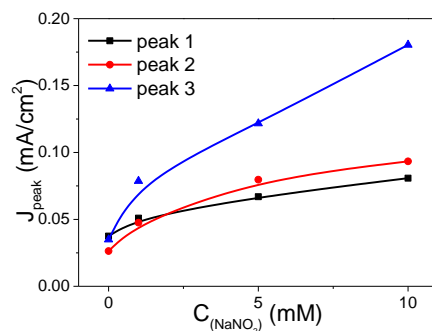
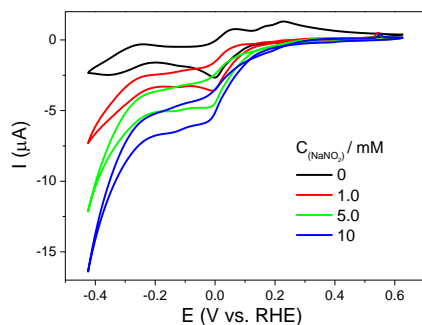
In Figure 2.3.7, it can be observed that current densities are smaller compared to other POMs. This is explained by the lower concentration of these Dawson, used in these experiments, due to a limited solubility of these compounds. As a common observation, the current intensity of peak 1 varies very little with nitrite concentration. As soon as the potential becomes negative, the current intensity of peak 2 and especially the one of peak 3 varies more intensively with nitrite concentration. The highest current density is obtained by $[Cd_4(H_2O)_2(P_2W_{15}O_{56})_2]^{16-}$ at peak 3 and this is similar to the current density of peak 4 of $[P_2W_{18}O_{62}]^{6-}$. The current density of all peak does not vary linearly with the concentration and starts to form a plateau for higher concentration, excepting for the peak 4 of $[P_2W_{18}O_{62}]^{6-}$. For better comparison of their performances, the onset potential of nitrite reduction at first

wave is arbitrarily defined at the potential where the catalytic current is $|I_{\text{HNO}_2/\text{NO}_2^-} - I_{\text{POM}}| = 0.05 \mu\text{A}$. This value is ten times lower than the one previously used because also POMs concentration is ten times less. The obtained onset potentials are summarized in Table 2.3.2. It can be observed that they are decreasing in the order $\text{P}_2\text{W}_{18}\text{O}_{62}^{6-}$, $\text{P}_4\text{W}_{30}\text{Cd}_4$, $\text{P}_4\text{W}_{30}\text{Mn}_4$, and $\text{P}_4\text{W}_{30}\text{Zn}_4$.

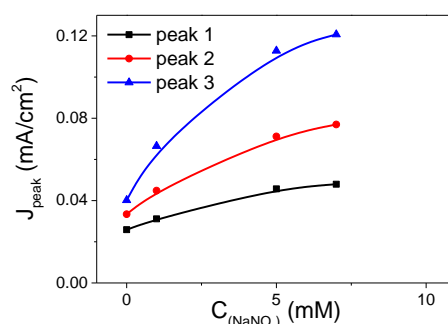
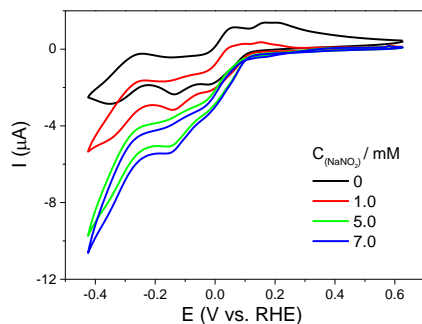
a) $[\text{Cd}_4(\text{H}_2\text{O})_2(\text{P}_2\text{W}_{15}\text{O}_{56})_2]^{16-}$



b) $[\text{Mn}_4(\text{H}_2\text{O})_2(\text{P}_2\text{W}_{15}\text{O}_{56})_2]^{16-}$



c) $[\text{Zn}_4(\text{H}_2\text{O})_2(\text{P}_2\text{W}_{15}\text{O}_{56})_2]^{16-}$



d) $\alpha\text{-}[\text{P}_2\text{W}_{18}\text{O}_{62}]^{6-}$

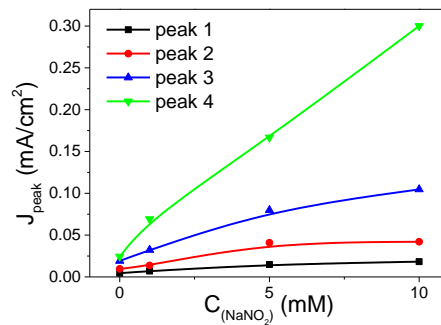
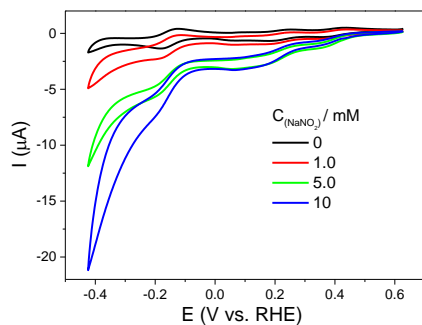


Figure 2.3.7 Cyclic voltammetry of Dawson POMs in the presence of different concentrations of nitrite (from 0 to 10 mM) at pH 2. Experimental conditions: POM: 0.1 mM; working

electrode, glassy carbon; scan rate, 20 mVs⁻¹; a) [Cd₄(H₂O)₂(P₂W₁₅O₅₆)₂]¹⁶⁻; b) [Mn₄(H₂O)₂(P₂W₁₅O₅₆)₂]¹⁶⁻; c) [Zn(H₂O)₂(P₂W₁₅O₅₆)₂]¹⁶⁻; d) α -[P₂W₁₈O₆₂]⁶⁻. Right panel: Current density of the three (four) redox peaks of α -[P₂W₁₈O₆₂]⁶⁻ as a function of nitrite concentration.

Table 2.3.2 Onset potential of different Dawson-type POMs at pH 2. (E_{onset} at |I_{HNO2/NO2-} - I_{POM}| = 0.05 μ A).

POMs	Onset potential (V vs. RHE)
[Cd(H ₂ O) ₂ (P ₂ W ₁₅ O ₅₆) ₂] ¹⁶⁻	0.157
[Mn(H ₂ O) ₂ (P ₂ W ₁₅ O ₅₆) ₂] ¹⁶⁻	0.100
[Zn(H ₂ O) ₂ (P ₂ W ₁₅ O ₅₆) ₂] ¹⁶⁻	0.070
α -[P ₂ W ₁₈ O ₆₂] ⁶⁻	0.350

2.4 Nitrite reduction catalyzed by POMs – DEMS studies

Despite several reports about nitrite reduction catalyzed by POMs, very few reports discuss about the reaction products. For example, Nadjo et al. showed that NO is converted into N₂O by a series of reduced POMs.²⁶ These studies were performed as bulk electrolysis in which POMs were reduced prior to the addition of nitrite. Nevertheless, the reaction mechanism and the relationship between POMs structure and reaction activity are still unclear. Thus, differential electrochemical mass spectroscopy (DEMS) was used to follow the formation of gaseous products depending on the applied potential. The measured signals are those of major gaseous products, i.e. m/z 31 (¹⁵NO), m/z 46 (¹⁵N₂O) and m/ 30 (¹⁵N₂). These signals are not quantitative. Thus, another parameter is required in order to compare different data sets. For this reason, the onset potential corresponding to the potential at which the product starts to form was chosen. The definition of this onset potential is specific to DEMS data, thus it is different from the definition used for CV experiments. The onset potential (P_{onset}) was chosen as the potential corresponding the signal that equals a value two times higher than the noise of the DEMS signal (2P_A). The procedure is described in Figure 2.4.1, using the signal of NO. The same procedure was used for the signal of N₂O, for which the noise is smaller.

DEMS data will be shown for each POM at pH 2. This value was selected as being common to almost all studied POMs (except [PW₁₂O₄₀]³⁻ for which pH 1 was used). For [SiW₁₂O₄₀]⁴⁻ a detailed DEMS study as function of pH was realized.

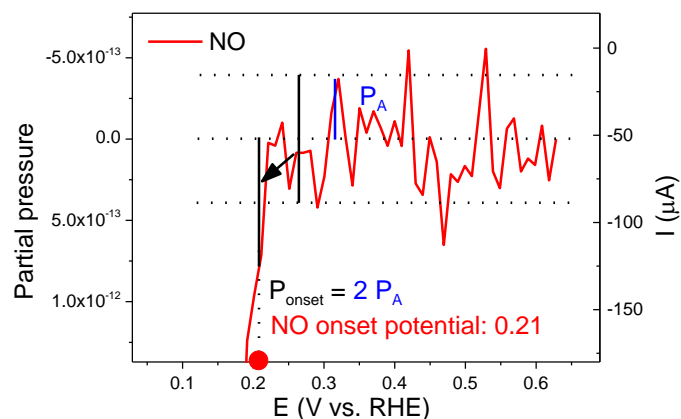


Figure 2.4.1 Procedure to measure the onset potential using DEMS data ($P_{\text{onset}} = 2 P_A$).

2.4.1 Nitrite reduction catalyzed by W-based Keggin POMs – DEMS studies

The results of DEMS experiments at pH 2 (pH 1 for $[\text{PW}_{12}\text{O}_{40}]^{3-}$) are presented in Figure 2.4.2. For the sake of simplicity, only the forward scans are showed. The red and blue curves are the ^{15}NO and $^{15}\text{N}_2\text{O}$ signal respectively. Their axes are on the left side from negative to positive values for better visual correlation with the current density data (black line). The reduction of nitrous acid at the first catalytic wave of all POMs yields ^{15}NO as product. For $[\text{H}_2\text{W}_{12}\text{O}_{40}]^{6-}$, as soon as the wave emerges, the signal of ^{15}NO appears as well. For $[\text{PW}_{12}\text{O}_{40}]^{3-}$, $[\text{SiW}_{12}\text{O}_{40}]^{4-}$, and $[\text{BW}_{12}\text{O}_{40}]^{5-}$ there is some delay, but the signal of ^{15}NO still appears during the first wave. With the potential is shifting to more negative values, ^{15}NO signal reaches a maximum value. Following this, for $[\text{H}_2\text{W}_{12}\text{O}_{40}]^{6-}$ and $[\text{BW}_{12}\text{O}_{40}]^{5-}$ the signal of ^{15}NO diminishes immediately. For $[\text{PW}_{12}\text{O}_{40}]^{3-}$ and $[\text{SiW}_{12}\text{O}_{40}]^{4-}$ the signal remains constant (a plateau) for a certain potential range. This behavior is related to the production of $^{15}\text{N}_2\text{O}$. It's very clear that the decrease of NO signal correlates to the increase of $^{15}\text{N}_2\text{O}$ signal. This leads to the assumption that ^{15}NO is reduced to $^{15}\text{N}_2\text{O}$ in the next step. Apart from $[\text{H}_2\text{W}_{12}\text{O}_{40}]^{6-}$, $^{15}\text{N}_2\text{O}$ is produced during the second wave for other POMs. For $[\text{H}_2\text{W}_{12}\text{O}_{40}]^{6-}$, $^{15}\text{N}_2\text{O}$ is detected during its first wave. This can be explained by the fact that the reduction of HNO_2 to N_2O requires two electrons and only the first reduction wave of the $[\text{H}_2\text{W}_{12}\text{O}_{40}]^{6-}$ directly undergoes two-electron reduction. The N_2O onset potential is in the middle of the first wave of $[\text{H}_2\text{W}_{12}\text{O}_{40}]^{6-}$ and in the middle of the second wave of $[\text{PW}_{12}\text{O}_{40}]^{3-}$ and $[\text{SiW}_{12}\text{O}_{40}]^{4-}$. One may inquire why the N_2O signal does not perfectly accompany the wave. Even for the first wave of $[\text{H}_2\text{W}_{12}\text{O}_{40}]^{6-}$, the electrolyte contains already a certain amount of ^{15}NO coming from the decomposition of H^{15}NO_2 . A first possible explanation is that the concentration of NO is too low and NO needs to accumulate before its subsequent reduction to N_2O . Another reasonable explanation is the existence of thermodynamic barrier for the formation of $^{15}\text{N}_2\text{O}$. Thus, NO can accumulate and even form a plateau (from 0 to -0.17 V vs. RHE for $[\text{SiW}_{12}\text{O}_{40}]^{4-}$, and from 0.26 to -0.03 V vs. RHE for $[\text{PW}_{12}\text{O}_{40}]^{3-}$) as long as this potential barrier is not overcome. These observations lead us to envisage the existence of an intermediate species issued from the reduction of NO and that could lead to the

formation of N_2O . This will be discussed in chapter 3.7. It is worth noting that the NO signal suddenly increases at the potential lower than -0.5 V vs. RHE accompanied by the decrease of N_2O for $[\text{H}_2\text{W}_{12}\text{O}_{40}]^{6-}$ and $[\text{BW}_{12}\text{O}_{40}]^{5-}$. The reasons for this are still unclear and two assumptions can be made. Firstly, hydrogen evolution, catalyzed by $[\text{BW}_{12}\text{O}_{40}]^{5-}$ and $[\text{H}_2\text{W}_{12}\text{O}_{40}]^{6-}$, may start at potentials lower than -0.5 V vs. RHE. The formation of hydrogen bubbles might enhance the removal of NO absorbed on the electrode surface, thus slowing down the conversion to N_2O . Secondly, hydrogen evolution could lead to a change of the local pH in the diffusion layer. This could cause a change in the reaction mechanism that could generate the formation of other products undetectable by DEMS, such as ammonium or hydroxylamine (NH_2OH) (this will be discussed in the chapter 3.5).

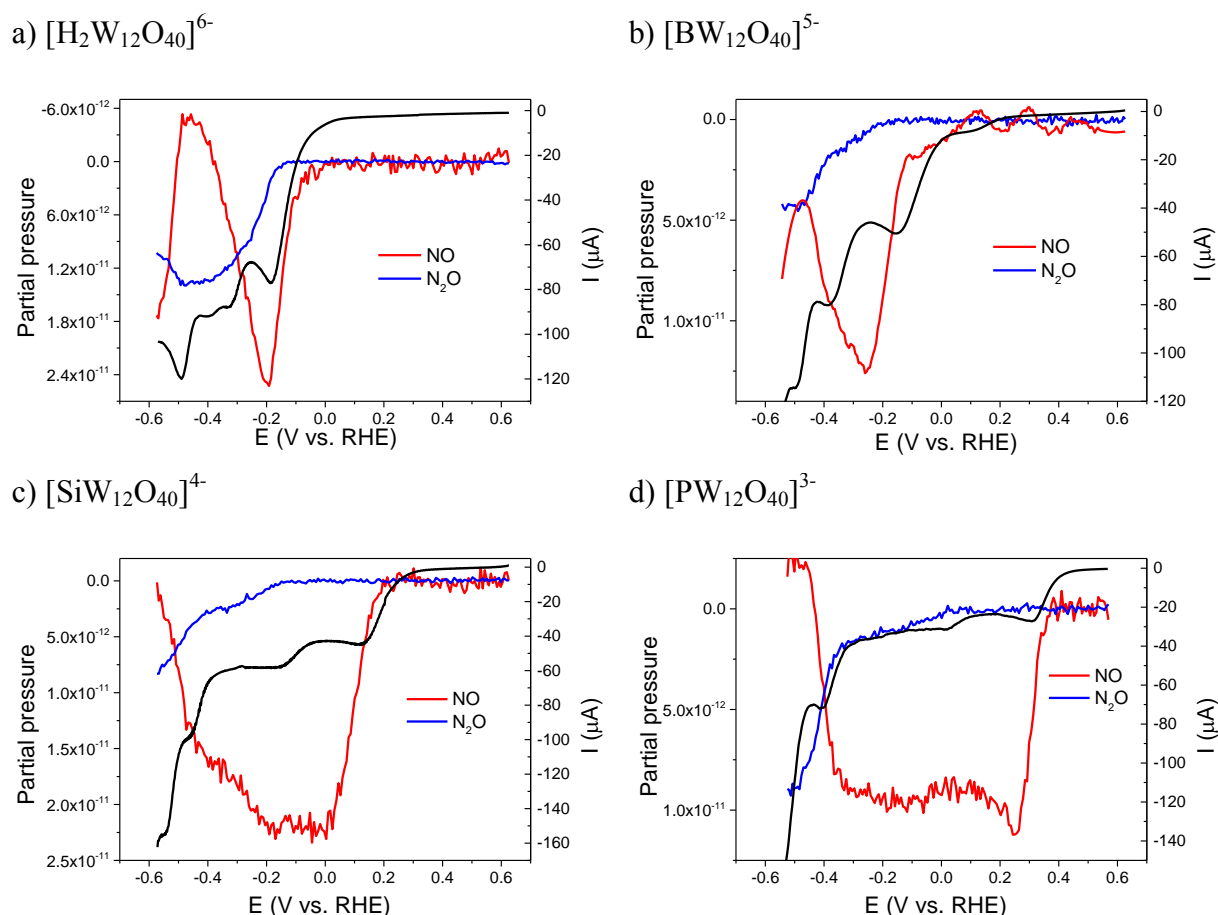


Figure 2.4.2 DEMS study of nitrite reduction catalyzed by all four POMs at pH 2 (pH 1 for $[\text{PW}_{12}\text{O}_{40}]^{3-}$). Black curve: the forward scan of cyclic voltammetry (from 0.8 V to -0.6 V vs. RHE, 0.5 mVs $^{-1}$); Red curve: the signal of m/z 31 (^{15}NO); Blue curve: the signal of m/z 46 ($^{15}\text{N}_2\text{O}$). Experimental conditions: working electrode, glassy carbon; 0.5 M Na_2SO_4 , 1 mM POM, 10 mM $\text{Na}^{15}\text{NO}_2$.

Let us carefully analyze the signal of N_2O . When the potential is scanned to more negative values, the existence of two different regions with two different slopes can be observed. For $[\text{PW}_{12}\text{O}_{40}]^{3-}$, $[\text{SiW}_{12}\text{O}_{40}]^{4-}$, and $[\text{BW}_{12}\text{O}_{40}]^{5-}$, the first region has a small slope and corresponds to the second reduction wave. When the third reduction wave is attained, a second region corresponding to a high generation of N_2O is observed. In detail, for $[\text{BW}_{12}\text{O}_{40}]^{5-}$, the small slope is between -0.26 V vs. RHE to -0.39 V vs. RHE and the higher slope is between -0.39 V vs. RHE to -0.50 V vs. RHE. For $[\text{PW}_{12}\text{O}_{40}]^{3-}$ and $[\text{SiW}_{12}\text{O}_{40}]^{4-}$,

there are respectively from -0.17 V vs. RHE to -0.48 V vs. RHE and from 0.01 V vs. RHE to -0.37 V vs. RHE for the slow slope and from -0.48 V vs. RHE to -0.56 V vs. RHE and from -0.37 V vs. RHE to -0.47 V vs. RHE for the higher slope respectively. Very intriguing and different from other POMs, for $[\text{H}_2\text{W}_{12}\text{O}_{40}]^{6-}$ a high slope is observed first (from -0.17 V vs. RHE to -0.25 V vs. RHE), followed by the small slope (from -0.26 V vs. RHE to -0.40 V vs. RHE).

At pH 5 (Figure 2.4.3), the formation of either ^{15}NO or $^{15}\text{N}_2\text{O}$ or both is specific to each POM. For $[\text{H}_2\text{W}_{12}\text{O}_{40}]^{6-}$, the first two-electron wave is divided into two partial overlapping one-electron waves. Similar to pH 2, ^{15}NO and $^{15}\text{N}_2\text{O}$ are both detected during this wave. However, at pH 5, the signal of ^{15}NO is less visible than that at pH 2, which means that ^{15}NO is rapidly consumed to form $^{15}\text{N}_2\text{O}$. For $[\text{BW}_{12}\text{O}_{40}]^{5-}$, at pH 5 the ^{15}NO and $^{15}\text{N}_2\text{O}$ appear at the same waves as at pH 2, first wave and second wave respectively, but at more positive potentials (Figure 2.4.3). Compared with other POMs, $[\text{SiW}_{12}\text{O}_{40}]^{4-}$ can produce $^{15}\text{N}_2\text{O}$ only during the third wave (Figure 2.4.3). Despite that at the second wave, the reduced POM has already accumulated enough electrons to catalyze the reaction of ^{15}NO to $^{15}\text{N}_2\text{O}$, it still requires a further reduction state in order to be able to catalyze this reaction. This reveals slower kinetics of the nitrite reduction to NO when $[\text{SiW}_{12}\text{O}_{40}]^{4-}$ is the catalyst.

The onset potentials for ^{15}NO and $^{15}\text{N}_2\text{O}$ at pH 2 and pH 5 as function of the total charge of the POM are summarized in Table 2.4.1 and in Figure 2.4.4. The onset potentials for ^{15}NO correlate to the number of charges of POMs. The onset potential of NO obtained with $[\text{PW}_{12}\text{O}_{40}]^{3-}$ is closest to the thermodynamic potential for nitrite reduction to NO (i.e. 0.990 V vs. RHE at pH 2 and 0.907 V vs. RHE at pH 5), followed by $[\text{SiW}_{12}\text{O}_{40}]^{4-}$, $[\text{BW}_{12}\text{O}_{40}]^{5-}$, and finally $[\text{H}_2\text{W}_{12}\text{O}_{40}]^{6-}$. The onset potentials of NO at pH 5 are more positive than that at pH 2. At pH 2, the onset potential of N_2O is less dependent on the charge of POMs. In fact, the potential is very similar for $[\text{SiW}_{12}\text{O}_{40}]^{4-}$, $[\text{BW}_{12}\text{O}_{40}]^{5-}$, and $[\text{H}_2\text{W}_{12}\text{O}_{40}]^{6-}$ (i.e. between -0.155 V vs. RHE to -0.220 V vs. RHE) and slightly more positive for $[\text{PW}_{12}\text{O}_{40}]^{3-}$ (0.020 V vs. RHE). This reinforces the hypothesis of an intermediate species, making the transition from NO to N_2O , having the reduction potential close to these values. At pH 5, the N_2O onset potential shifts to more negative values, suggesting a decreased reaction rate.

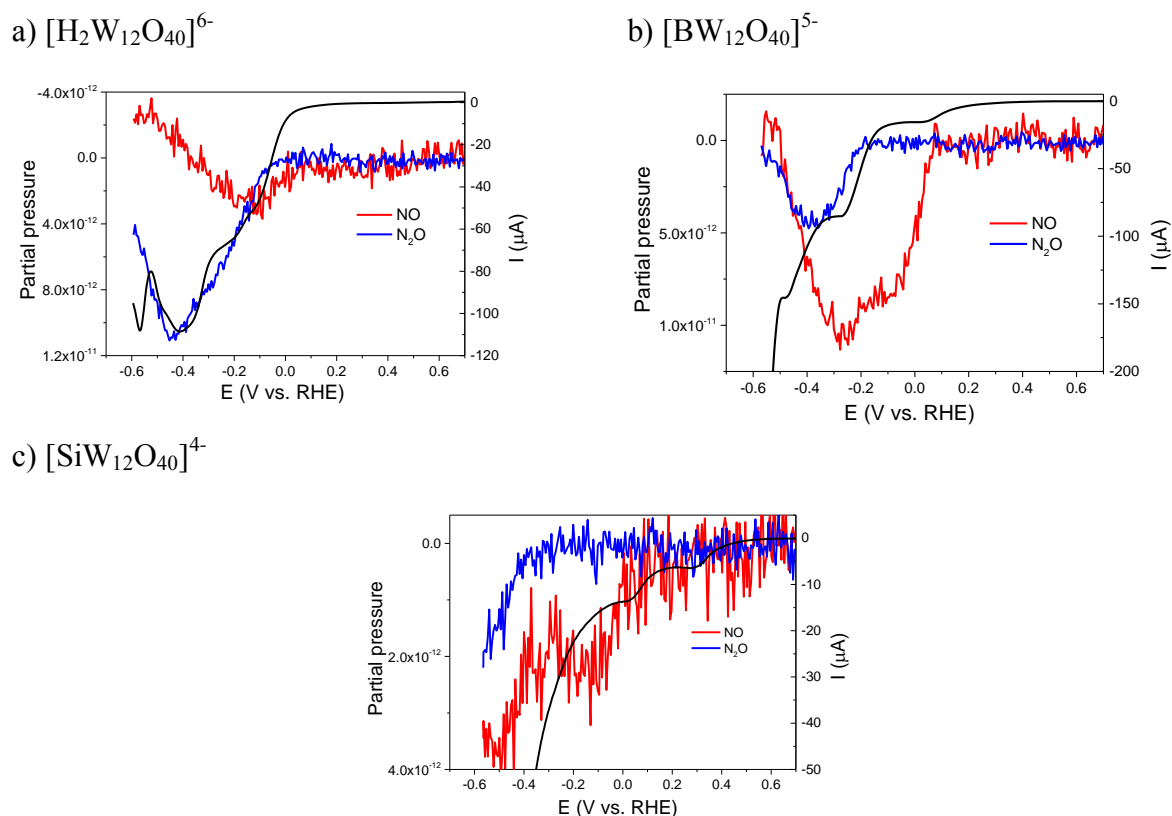


Figure 2.4.3 DEMS study of three POMs on GC electrode at pH 5. Black curve: the forward scan of cyclic voltammetry (from 0.8 V to -0.6 V vs. RHE, 0.5 mVs⁻¹); Red curve: the signal of m/z 31 (¹⁵NO); Blue curve: the signal of m/z 46 (¹⁵N₂O). Experimental conditions: working electrode, glassy carbon; 1 M CH₃COOLi pH 5, 1 mM POM, 10 mM Na¹⁵NO₂.

Table 2.4.1 Summary of DEMS data containing the onset potential on forward scan with E⁰ from before CV data.

pH	POM	E ⁰ of the first wave				
		V vs. RHE	Onset potential (V vs. RHE)	Wave (no. of electrons)	Onset potential (V vs. RHE)	Wave (no. of electrons)
2 ^a	[H ₂ W ₁₂ O ₄₀] ⁶⁻	-0.051	-0.075	First (2e ⁻)	-0.17	First (2e ⁻)
	[BW ₁₂ O ₄₀] ⁵⁻	0.076	-0.05	First (1e ⁻)	-0.22	Second (4e ⁻)
	[SiW ₁₂ O ₄₀] ⁴⁻	0.225	0.198	First (1e ⁻)	-0.155	Second (1e ⁻)
	[PW ₁₂ O ₄₀] ³⁻	0.454	0.38	First (1e ⁻)	0.02	Second (1e ⁻)
5	[H ₂ W ₁₂ O ₄₀] ⁶⁻	-0.108	0.03	First (1+1e ⁻) ^c	-0.045	First (2e ⁻)
	[BW ₁₂ O ₄₀] ⁵⁻	^b	0.08	First (1e ⁻)	-0.21	Second (5e ⁻)
	[SiW ₁₂ O ₄₀] ⁴⁻	^b	0.34	First (1e ⁻)	-0.35	Third (1e ⁻)

a) pH 1 for [PW₁₂O₄₀]³⁻

b) onset potential cannot be measured because the catalytic current is lower than the arbitrarily defined value of 0.5 μA.

c) The first wave of [H₂W₁₂O₄₀]⁶⁻ divide into two one-electron waves at pH 5.

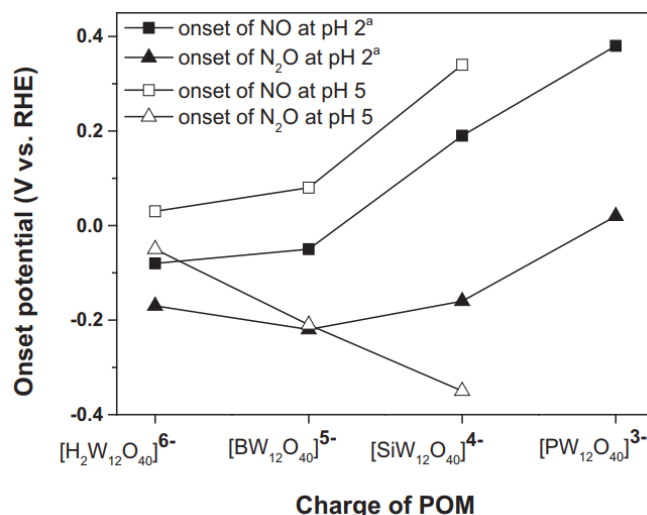


Figure 2.4.4 Variation of onset potential of ^{15}NO and $^{15}\text{N}_2\text{O}$ obtained from DEMS experiments with the total charge of the POM (pH 1 for $[\text{PW}_{12}\text{O}_{40}]^{3-}$).

For better understanding the pH influence on the reaction mechanism, DEMS analysis was conducted from pH 1 to pH 5 using $[\text{SiW}_{12}\text{O}_{40}]^{4-}$ as catalyst. The results are presented in Figure 2.4.5 and the onset potential of NO and N_2O are shown in Table 2.4.2. The POMs' first and second redox waves slightly shift to more positive potentials with the increase of pH. The onset potential of NO follows this trend, gradually shifting from 0.193 V vs. RHE at pH 1 to 0.340 at pH 5. The onset potential of N_2O remains almost unchanged between pH 1 to pH 3, i.e. -0.160 V vs. RHE. Then, it suddenly decreases to -0.27 V vs. RHE for pH 4 and to -0.350 at pH 5. Considering these data and the pK_a of HNO_2 of 3.3, it can be concluded that the reaction between the reduced POM (i.e. $[\text{SiW}^{\text{V}}\text{W}^{\text{VI}}_{11}\text{O}_{40}]^{5-}$) and HNO_2 (at pH 1 to pH 3) is faster than the one between the reduced POM and NO_2^- (at pH 4 to pH 5). **Indeed, the reaction product is NO and most probably, a minimum concentration is required before the subsequent formation of N_2O can be observed.** If the study is conducted at pH 4 or pH 5, the reaction is slow, the concentration of NO is small and thus the N_2O is only observed at higher overpotential (i.e. only when the $[\text{SiW}_2\text{W}^{\text{VI}}_{11}\text{O}_{40}]^{6-}$ is already formed). This will be discussed in detail in chapter 3.7. Moreover, the reduction reaction involves protons, thus a change in the local pH can affect the reaction kinetics.

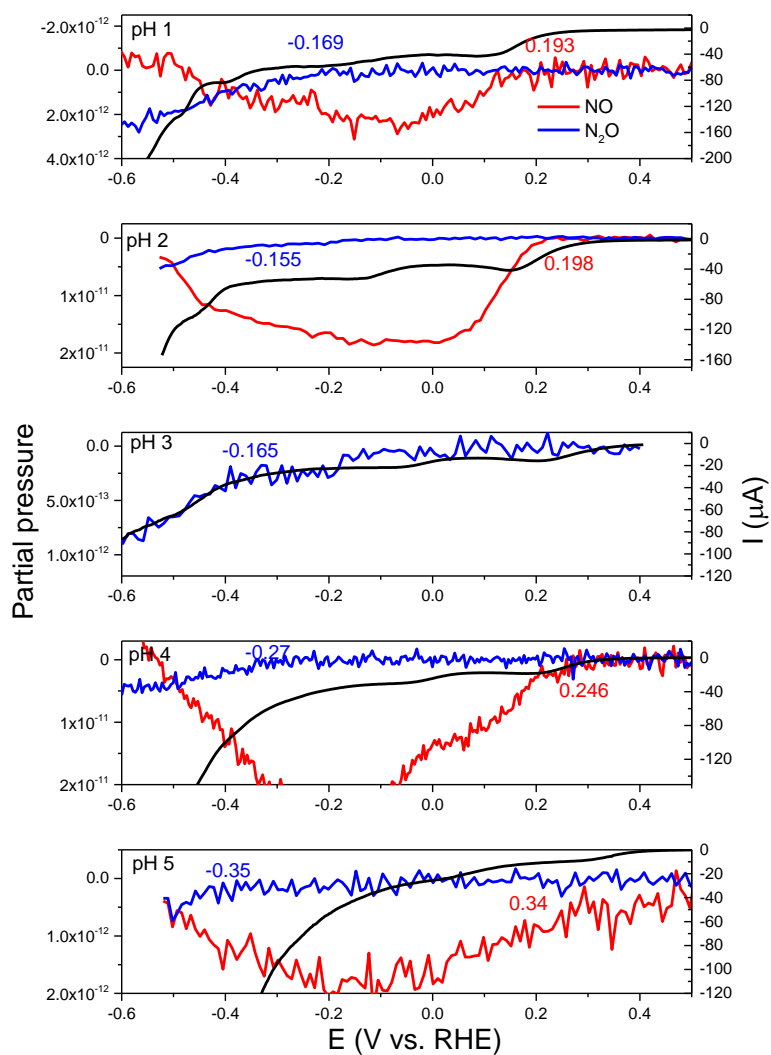
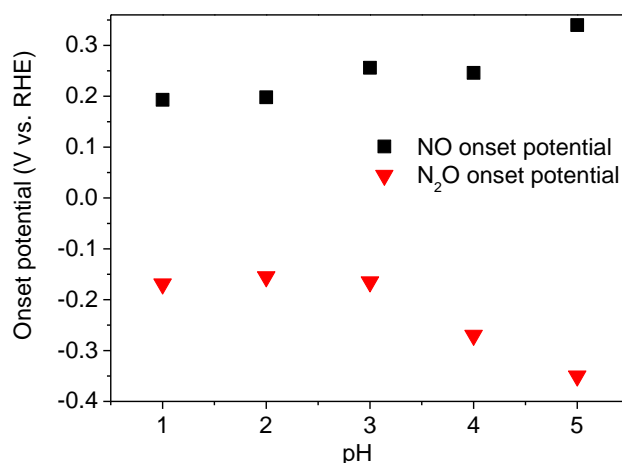


Figure 2.4.5 DEMS study of nitrite reduction catalyzed by $[\text{SiW}_{12}\text{O}_{40}]^{4-}$ from pH 1 to pH 5. Black curve: the forward scan of cyclic voltammetry (from 0.6 V to -0.5 V vs. RHE, 0.5 mVs^{-1}). Red curve: the signal of m/z 31 (^{15}NO); Blue curve: the signal of m/z 46 ($^{15}\text{N}_2\text{O}$). Experimental conditions: working electrode, glassy carbon; 1mM POM; 10 mM $\text{Na}^{15}\text{NO}_2$.

Table 2.4.2 Onset potentials of NO and N₂O obtained from Figure 2.4.5.

pH	E ⁰ of the first wave (V vs. RHE)	NO		N ₂ O	
		Onset potential (V vs. RHE)	Wave (no. of electrons)	Onset potential (V vs. RHE)	Wave (no. of electrons)
1	0.099	0.193	First (1e ⁻)	-0.169	Second (1e ⁻)
2	0.116	0.198	First (1e ⁻)	-0.155	Second (1e ⁻)
3	0.175	0.256	First (1e ⁻)	-0.165	Second (1e ⁻)
4	0.213	0.246	First (1e ⁻)	-0.270	Third (2e ⁻)
5	0.251	0.340	First (1e ⁻)	-0.350	Third (2e ⁻)

Figure 2.4.6 Onset potential of NO and N₂O obtained from nitrite reduction catalyzed by [SiW₁₂O₄₀]⁴⁻ on GC electrode from pH 1 to pH 5. Experimental conditions: see Figure 2.4.5.

2.4.2 Nitrite reduction catalyzed by Mo-based Keggin POMs – DEMS studies

From the previous described DEMS studies of nitrite reduction catalyzed by four Keggin POMs, the hypothesis of an intermediate species existing during the conversion of NO to N₂O was made. The main argument is the fact that the potential of N₂O (for a constant pH) is not depending on the global charge of the POM, i.e. it remains around -0.2 V vs. RHE, as long as the reduced POM bears two electrons. In order to bring more data to sustain this hypothesis, we have used Mo-based Keggin POMs that bear two electrons in their first reduction wave which is situated at much more positive potentials than the W-based POMs (see chapter 3.2.2 and Figure 3.2.9). Figure 2.4.7 shows DEMS data for the nitrite reduction at pH 2 catalyzed by [SiMo₁₂O₄₀]⁴⁻ and [PMo₁₂O₄₀]³⁻. The onset potential of NO is 0.63 V vs. RHE and 0.53 V vs. RHE for the reaction catalyzed by [SiMo₁₂O₄₀]⁴⁻ and [PMo₁₂O₄₀]³⁻ respectively. These values are located during the first wave of these POMs, similar to the case of W-based Keggin compounds. Very interestingly, the onset of N₂O is about -0.1 V vs. RHE in both cases. At this potential, these POMs are already bearing six electrons. ***These data sustain the hypothesis of a potential barrier required for the formation of N₂O, i.e. the existence of an intermediate species between NO and N₂O.***

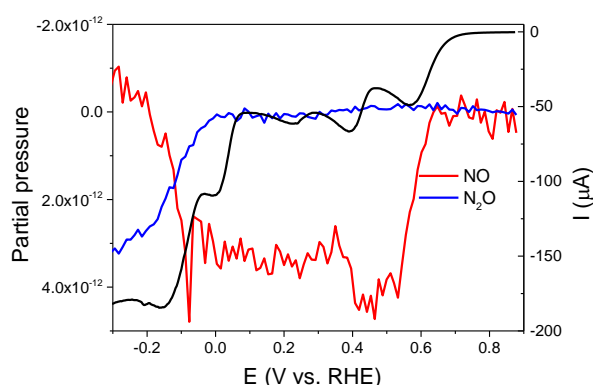
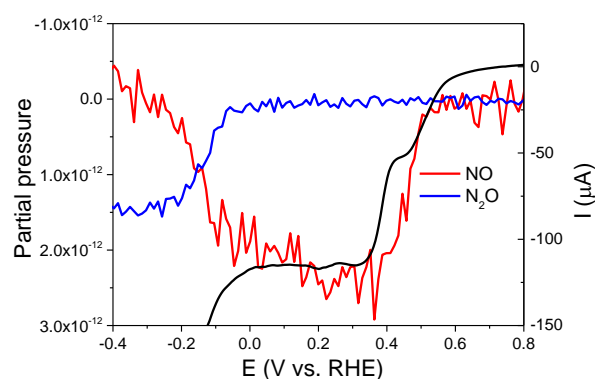
a) pH 2 $[\text{SiMo}_{12}\text{O}_{40}]^{4-}$ b) pH 2 $[\text{PMo}_{12}\text{O}_{40}]^{3-}$ 

Figure 2.4.7 DEMS study of nitrite reduction catalyzed by a) $[\text{SiMo}_{12}\text{O}_{40}]^{4-}$ and b) $[\text{PMo}_{12}\text{O}_{40}]^{3-}$ at pH 2. Black curve: the forward scan of cyclic voltammetry (from 0.5 V to -0.6 V vs. RHE, 0.5 mVs^{-1}); Red curve: the signal of m/z 31 (^{15}NO); Blue curve: the signal of m/z 46 ($^{15}\text{N}_2\text{O}$); POM concentration is 1 mM and $\text{Na}^{15}\text{NO}_2$ is 10 mM.

Table 2.4.3 Onset potential of NO and N_2O on DEMS study of Mo-based Keggin POMs at pH 2.

POMs	E^0 of the first wave (V vs. RHE)	NO		N_2O	
		Onset potential (V vs. RHE)	Wave (no. of electrons)	Onset potential (V vs. RHE)	Wave (no. of electrons)
$[\text{PMo}_{12}\text{O}_{40}]^{3-}$	-	0.53	First ($2e^-$)	-0.04	Beyond third wave
$[\text{SiMo}_{12}\text{O}_{40}]^{4-}$	0.58	0.63	First ($2e^-$)	0.02	($6e^-$)

2.4.3 Nitrite reduction catalyzed by Dawson POMs – DEMS studies

The reduction of nitrite to nitrogen requires six electrons. For this reason, we have studied the reduction of nitrite catalyzed by dimer Dawson POMs bearing four electrons for each of their three reduction waves. The following dimers sandwich Dawson POMs were used: $\text{Na}_{16}[\text{Zn}_4(\text{H}_2\text{O})_2(\text{P}_2\text{W}_{15}\text{O}_{56})_2]$ ($\text{P}_4\text{W}_{30}\text{Zn}_4$), $\text{Na}_{16}[\text{Cd}_4(\text{H}_2\text{O})_2(\text{P}_2\text{W}_{15}\text{O}_{56})_2]$ ($\text{P}_4\text{W}_{30}\text{Cd}_4$), and $\text{Na}_{16}[\text{Mn}_4(\text{H}_2\text{O})_2(\text{P}_2\text{W}_{15}\text{O}_{56})_2]$ ($\text{P}_4\text{W}_{30}\text{Mn}_4$). The results of DEMS experiments at pH 2 are presented in Figures 2.4.8-2.4.10. For the sake of comparison, DEMS analysis was performed also with the parent Dawson POM, $[\text{P}_2\text{W}_{18}\text{O}_{62}]^{6-}$ (Figure 2.4.11) that bears six electrons after the fourth reduction wave, thus accomplishing the required condition for the theoretical reduction of nitrite to nitrogen.

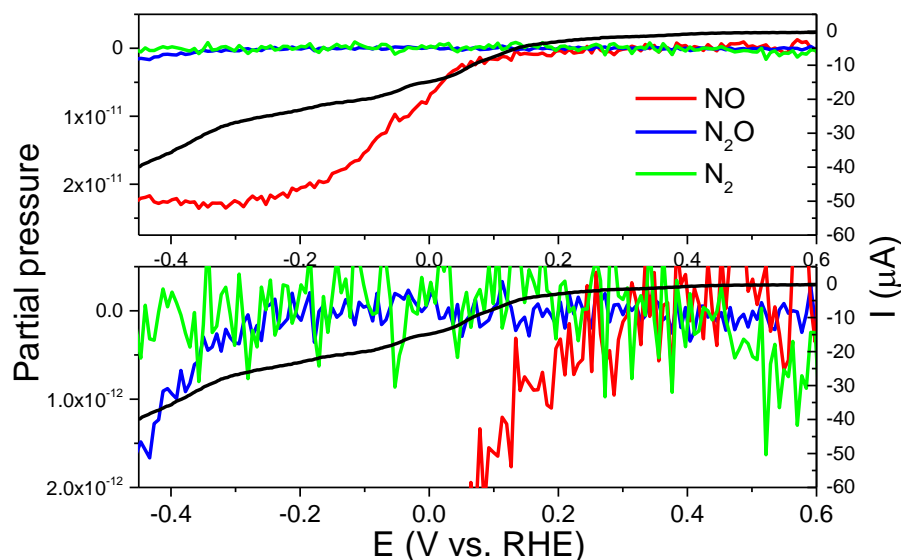


Figure 2.4.8 DEMS study of nitrite reduction catalyzed by $[\text{Cd}_4(\text{H}_2\text{O})_2(\text{P}_2\text{W}_{15}\text{O}_{56})_2]^{16-}$ at pH 2. Black curve: the forward scan of cyclic voltammetry (from 0.6 V to -0.7 V vs. RHE, 0.5 mVs^{-1}); Red curve: the signal of m/z 31 (^{15}NO); Blue curve: the signal of m/z 46 ($^{15}\text{N}_2\text{O}$). Green curve: signal of m/z 30 ($^{15}\text{N}_2$). Experimental conditions: working electrode, glassy carbon; 0.5 M Na_2SO_4 , 0.1 mM POM, 5 mM $\text{Na}^{15}\text{NO}_2$.

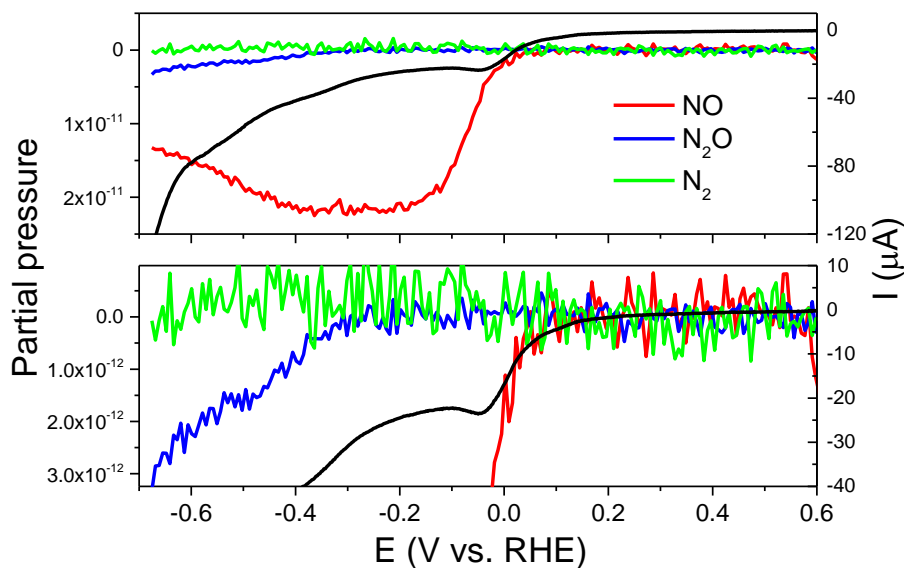


Figure 2.4.9 DEMS study of nitrite reduction catalyzed by $[\text{Mn}_4(\text{H}_2\text{O})_2(\text{P}_2\text{W}_{15}\text{O}_{56})_2]^{16-}$ at pH 2. Black curve: the forward scan of cyclic voltammetry (from 0.6 V to -0.7 V vs. RHE, 0.5 mVs^{-1}); Red curve: the signal of m/z 31 (^{15}NO); Blue curve: the signal of m/z 46 ($^{15}\text{N}_2\text{O}$). Green curve: signal of m/z 30 ($^{15}\text{N}_2$). Experimental conditions: working electrode, glassy carbon; 0.5 M Na_2SO_4 , 0.1 mM POM, 5 mM $\text{Na}^{15}\text{NO}_2$.

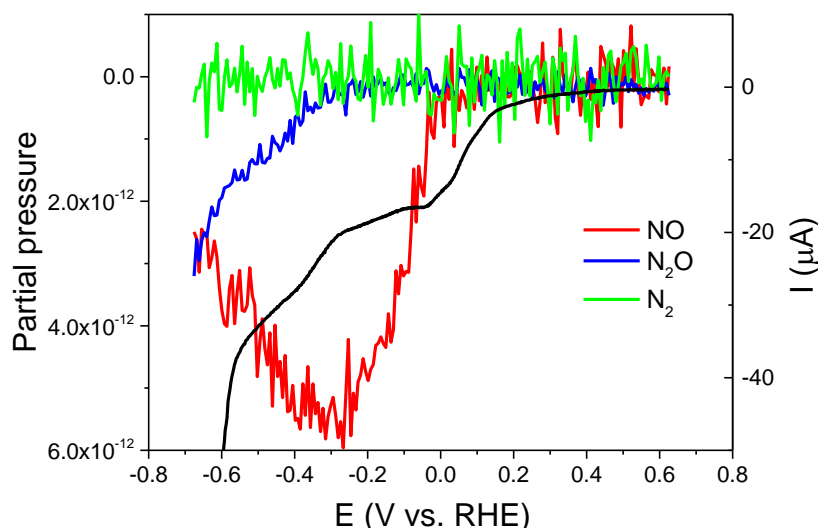


Figure 2.4.10 DEMS study of nitrite reduction catalyzed by $[\text{Zn}_4(\text{H}_2\text{O})_2(\text{P}_2\text{W}_{15}\text{O}_{56})_2]^{16-}$ at pH 2. Black curve: the forward scan of cyclic voltammetry (from 0.6 V to -0.7 V vs. RHE, 0.5 mVs^{-1}); Red curve: the signal of m/z 31 (^{15}NO); Blue curve: the signal of m/z 46 ($^{15}\text{N}_2\text{O}$). Green curve: signal of m/z 30 ($^{15}\text{N}_2$). Experimental conditions: working electrode, glassy carbon; 0.5 M Na_2SO_4 , 0.1 mM POM, 5 mM $\text{Na}^{15}\text{NO}_2$.

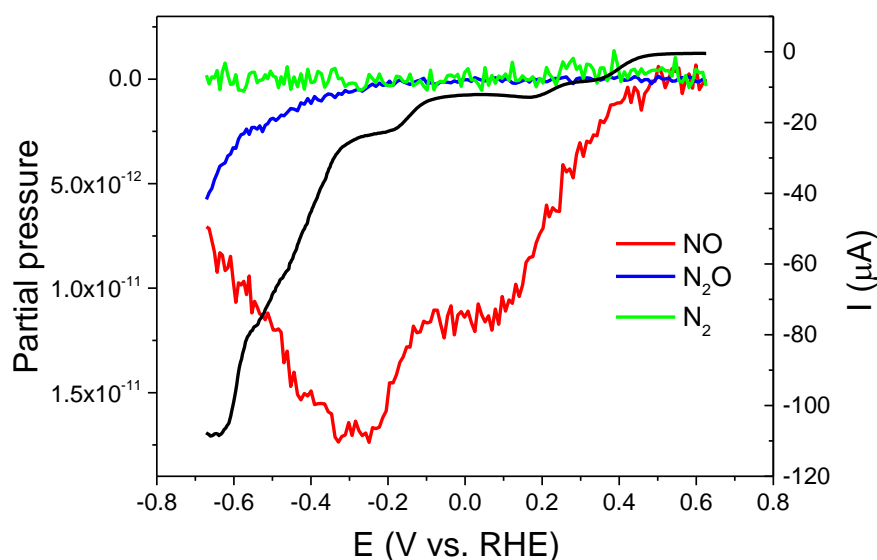


Figure 2.4.11 DEMS study of nitrite reduction catalyzed by $[\text{P}_2\text{W}_{18}\text{O}_{62}]^{6-}$ at pH 2. Black curve: the forward scan of cyclic voltammetry (from 0.63 V to -0.67 V vs. RHE, 0.5 mVs^{-1}); Red curve: the signal of m/z 31 (^{15}NO); Blue curve: the signal of m/z 46 ($^{15}\text{N}_2\text{O}$). Green curve: signal of m/z 30 ($^{15}\text{N}_2$). Experimental conditions: working electrode, glassy carbon; 0.5 M Na_2SO_4 , 0.1 mM POM, 5 mM $\text{Na}^{15}\text{NO}_2$.

The first common observation of all these data is that nitrogen production was not observed. Secondly, the ^{15}NO signal is observed at all first reduction waves of all POMs. For $\text{P}_4\text{W}_{30}\text{Zn}_4$ the onset potential of ^{15}NO is slightly more positive (0.15 V vs. RHE) than for $\text{P}_4\text{W}_{30}\text{Cd}_4$ (0.06 V vs. RHE) and $\text{P}_4\text{W}_{30}\text{Mn}_4$ (0.03 V vs. RHE). Finally, the onset potential of N_2O formation is very similar to all Dawson POMs (between -0.19 to -0.29 V vs. RHE). The

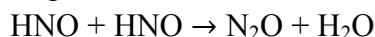
precise values are summarized in Table 2.4.4. It can be seen that all three dimers, $P_4W_{30}Zn_4$, $P_4W_{30}Cd_4$, and $P_4W_{30}Mn_4$ have very similar onset potential of N_2O (around -0.29 V vs. RHE) suggesting that the different divalent metals in these POMs doesn't have an important effect on the reduction of NO to N_2O . Moreover, at this potential value, the dimers are already bearing eight electrons. This sustains again *the hypothesis of a potential barrier required for the formation of N_2O , i.e. the existence of an intermediate species between NO and N_2O , as shown previously for Mo-based Keggin POMs*. Similarly, the onset of N_2O when parent Dawson is used is about -0.19 V, that adds another argument in the favor of the intermediate hypothesis.

Table 2.4.4 Onset potentials of NO and N_2O from DEMS studies with Dawson POMs at pH 2. Data are extracted from Figures 2.4.8 to 2.4.11.

POM	E^0 of the first wave (V vs. RHE)	NO		N_2O	
		Onset potential (V vs. RHE)	Wave (no. of electrons)	Onset potential (V vs. RHE)	Wave (no. of electrons)
$[Cd_4(H_2O)_2(P_2W_{15}O_{56})_2]^{16-}$	0.16	0.06	First ($4e^-$)	-0.28	Second ($4e^-$)
$[Mn_4(H_2O)_2(P_2W_{15}O_{56})_2]^{16-}$	0.10	0.03	First ($4e^-$)	-0.29	Second ($4e^-$)
$[Zn_4(H_2O)_2(P_2W_{15}O_{56})_2]^{16-}$	0.07	0.15	First ($4e^-$)	-0.28	Second ($4e^-$)
$[P_2W_{18}O_{62}]^{6-}$	0.35	0.46	First ($1e^-$)	-0.19	Third ($2e^-$)

2.4.4 Comparison of NO and N_2O onset potentials for all studied POMs

A summary of the onset potential for the formation of NO and N_2O , obtained from DEMS experiments, is given in Figure 2.4.12 and 2.4.13. Firstly, the NO onset potential is very dependent on the used POM. This is an expected result because the simplest step of nitrite reduction involves transfer of one electron to produce nitric oxide. As the reduction of POMs appears at a potential specific to each compound, it is natural that the onset of NO follows this trend. On the other hand, the values of N_2O onset potential are less scattered being less than 0 V. This sustains the hypothesis of a potential barrier required for the formation of N_2O . In fact, the reduction of NO could yield HNO that could further combine with a second molecule of HNO to form N_2O . In the literature, the reported values of redox potential for NO/HNO couple are very different. Recently, a value as high as -0.11 V²⁷ was reported. In this view, our values of onset potential of N_2O are quite close to this value. Thus, we conclude that the reduction of NO catalyzed by a reduced POM yields HNO and this leads to the formation of N_2O through the reaction:



Finally, we sought to correlate the NO onset potential with the “general” onset potential obtained from cyclic voltammetry data as described in previous chapters (see above for each POM). The correlation, shown in Figure 2.4.14, is quite good, with a coefficient (R^2) of 0.9. This means that the onset potential obtained from CV is in fact the onset potential for NO formation. In this case, DEMS data are useful to validate the CV analysis.

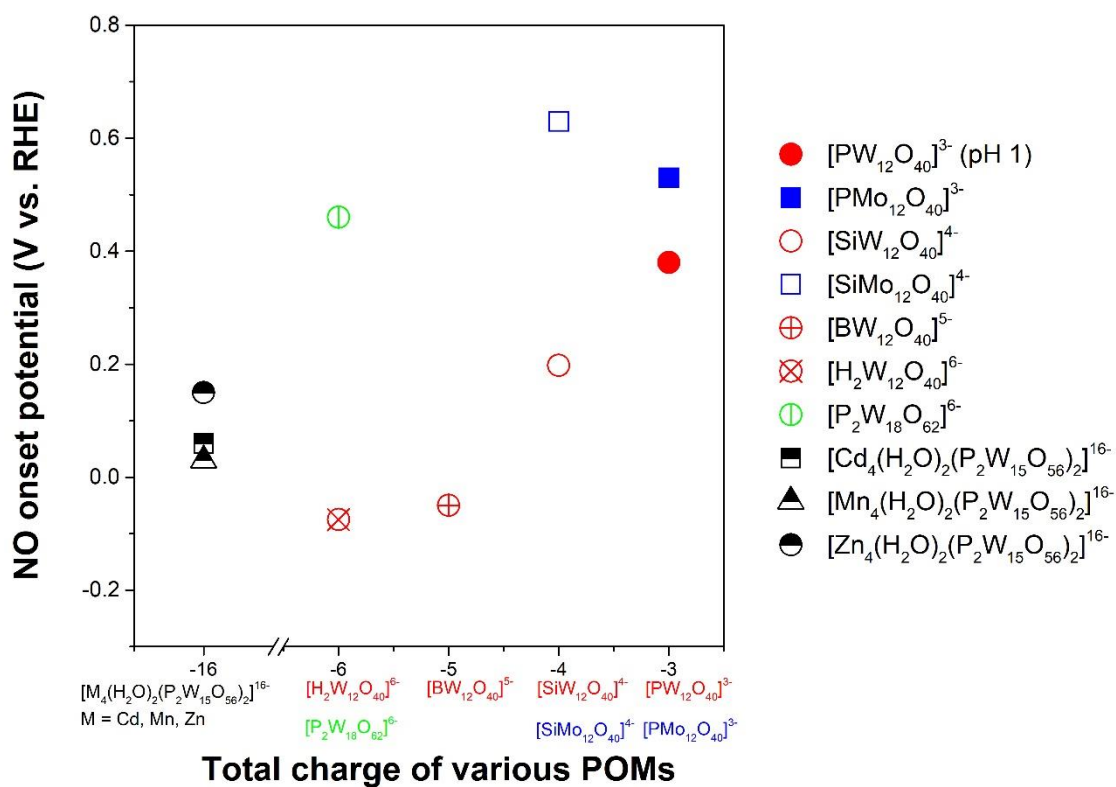


Figure 2.4.12 NO onset potential as function of the charge of various POMs at pH 2. ($[PW_{12}O_{40}]^{3-}$ at pH 1)

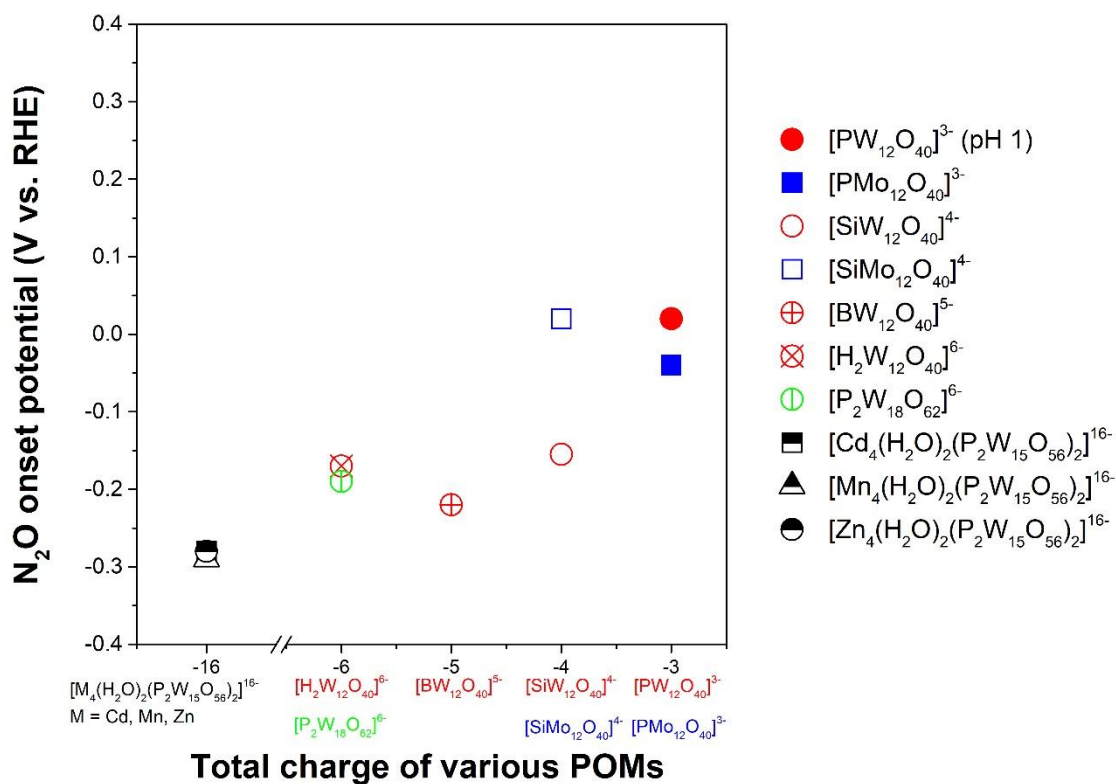


Figure 2.4.13 N_2O onset potential as function of the charge of various POMs at pH 2. ($[PW_{12}O_{40}]^{3-}$ at pH 1)

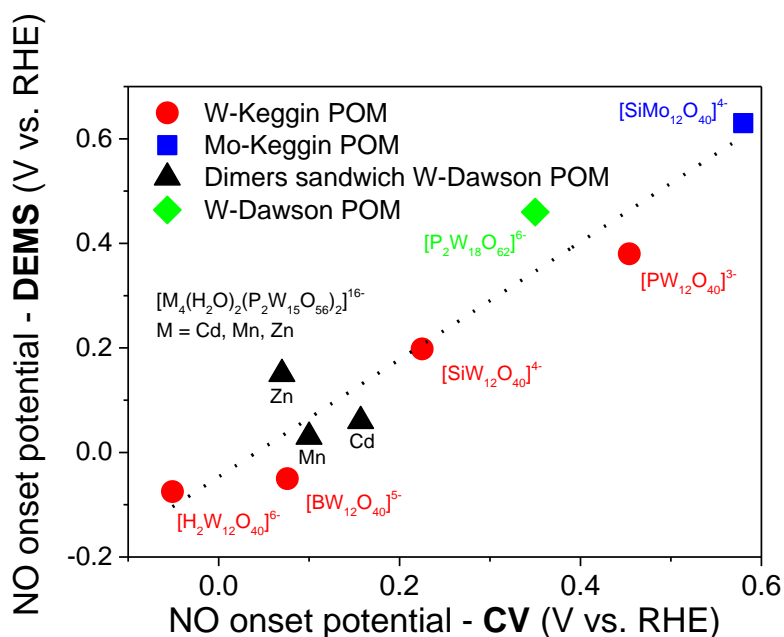


Figure 2.4.14 Onset potential on CV as function of NO onset potential with POMs at pH 2. ($[\text{PW}_{12}\text{O}_{40}]^{3-}$ at pH 1)

2.5 Investigation of other products of nitrite reduction catalyzed by POMs

As seen in chapter 3.3.1, NO signal suddenly increases at potential lower than -0.5 V vs. RHE accompanied with the decrease of N_2O when $[\text{H}_2\text{W}_{12}\text{O}_{40}]^{6-}$ and $[\text{BW}_{12}\text{O}_{40}]^{5-}$ are used as catalysts. This might suggest a change in the reaction mechanism and the formation of other products. As the formation of N_2 is excluded by running additional DEMS experiments, we have sought for the analysis of other possible products. This could be a new nitrogenous product with nitrogen atoms in a more reduced state, such as NH_4^+ or NH_2OH . Therefore, the following paragraph is dedicated to the use of DEMS to detect the NH_3 (NH_4^+) and the use of UV-Vis spectroscopy to detect hydroxylamine NH_2OH .

2.5.1 DEMS detection of NH_3 (NH_4^+)

The NH_3 (NH_4^+) detection with DEMS was performed in several experiments (Figure 2.5.1). Chronoamperometry is performed at -0.552 V vs. RHE in a solution containing 1 mM $(\text{NH}_4)_6[\text{H}_2\text{W}_{12}\text{O}_{40}]$ and 10 mM NaNO_2 (from $t = 40$ to 160 minutes) in the DEMS cell. The solution is collected into a vessel and the pH is adjusted to 13 by addition of few drops of 5 M NaOH. The new solution is reinjected into the DEMS cell at $t = 210$ minutes. A small spike in the signal of NH corresponds to a small spike in the pressure due to the manipulation of the syringe pump for changing the solutions. At $t = 240$ minutes the signal of NH suddenly increases and reaches a plateau. A first interpretation of the data is that indeed NH_3 was produced during the electroreduction of nitrite catalyzed by $[\text{H}_2\text{W}_{12}\text{O}_{40}]^{6-}$. Unfortunately, we have later realized that the counter cation of this POM is NH_4^+ . Thus, it was hypothesized that the recorded NH signal just corresponds to this cation especially due to the fact POMs

decompose at such basic pH. In order to check this, we have conducted a control experiment in which no chronoamperometry was performed, only a change of pH from acid to basic for a solution containing the POM and NO_2^- . Figure 2.5.1b illustrates the DEMS detection of NH signal. At the beginning the electrolyte in the cell contains 1 mM $(\text{NH}_4)_6[\text{H}_2\text{W}_{12}\text{O}_{40}]$ and 10 mM NaNO_2 (from 10 min to 50 min) to obtain a signal stable baseline. Further on, the pH of electrolyte in the external reservoir of the syringe pump was adjusted to 13 by addition of few drops of 5 M NaOH . It takes about 20 min to push this new electrolyte into the cell. At $t = 70$ minutes the solution reaches the cell and the signal of NH gradually increases to finally reach a plateau at $t = 80$ minutes. If we compare the two experiments, the relative increase of NH signal (from baseline to plateau) is the same, roughly 1.25×10^{-12} a.u. Thus, the NH signal recorded after the chronoamperometry experiment is, in fact, due to the counter cation of the POM. The conclusion of this experiment is that no NH_3 is produced in the electroreduction of nitrite catalyzed by POM $[\text{H}_2\text{W}_{12}\text{O}_{40}]^{6-}$. This result is not surprising given the mechanism required for conversion of nitrite to ammonia. Nitrite is first reduced to nitric oxide. The subsequent reduction of NO to NH_3 should involve several protonation steps and adsorbed species. It is rather difficult to transpose this mechanism to a homogeneous reaction involving reduced POMs and NO in solution. This experiment should be repeated with other POMs in order to make sure that ammonia is not a product of nitrite reduction catalyzed by these compounds.

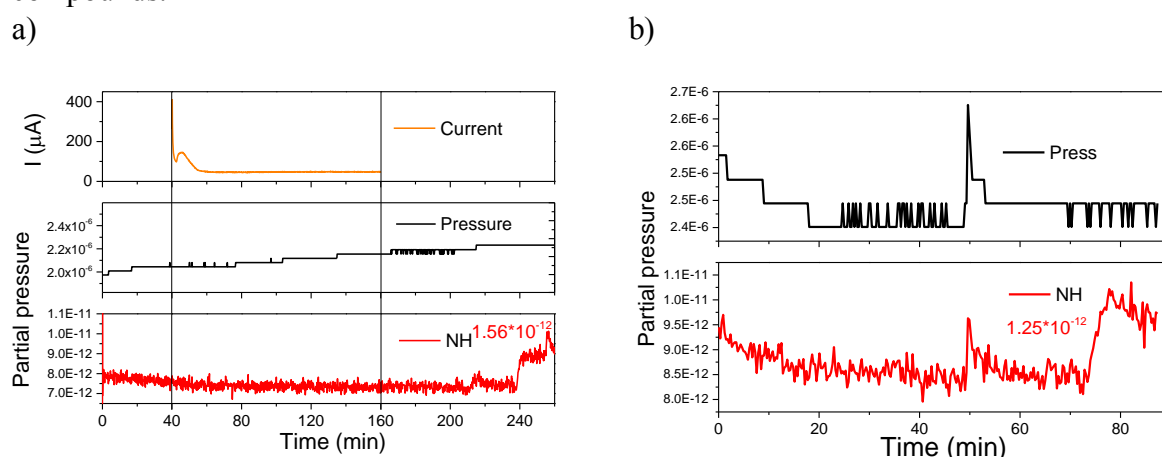


Figure 2.5.1 a) Chronoamperometry recorded with GC electrode (orange curve); Red curve is the ^{14}NH signal and total pressure inside the mass spectrometer is the black curve. Experimental conditions: pH 2, 1 mM $(\text{NH}_4)_6[\text{H}_2\text{W}_{12}\text{O}_{40}]$, 10 mM $\text{Na}^{14}\text{NO}_2$, type A DEMS cell. From $t=40$ to 160 min, the chronoamperometry was performed. b) The “no chronoamperometry” experiment, the signals of NH (red curve) and total pressure inside the mass spectrometer (black curve).

2.5.2 Detection of hydroxylamine (NH_2OH) by UV-Vis

According to previously reported data, hydroxylamine (NH_2OH) is also a possible product of electroreduction of nitrite catalyzed by noble metals.²⁸ The method to detect hydroxylamine is based on the reaction between p-nitrobenzaldehyde and oximes of less reactive carbonyl compounds. The resulting product is p-nitrobenzaldoxime, issued from the acid-catalyzed oxime exchange. The reaction is shown in Figure 2.5.2. In alkaline solution, p-nitrobenzaldoxime shows a strong yellow color with maximum absorption at 368 nm which

can be quantitatively detected by UV-Vis spectroscopy.²⁹

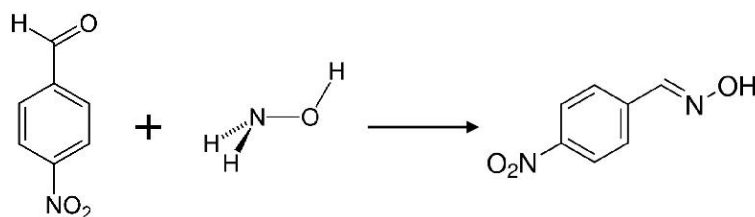


Figure 2.5.2 Acid-catalyzed oxime exchange between p-nitrobenzaldehyde and hydroxylamine yielding yellow colored p-nitrobenzaldoxime.

The following experimental steps were performed:

1. Preparation of solution A: 0.2 g p-nitrobenzaldehyde in 50 ml of ethanol was mixed with 50 ml of 0.6 M hydrochloric acid.
2. Preparation of solution B (standard solution): 0.0695 g hydroxylamine hydrochloride was dissolved in 10 ml water, then this solution was diluted to 100 mL by methanol.
3. Different volumes (0.01 mL, 0.02 mL, 0.05 mL, 0.1 mL, 0.2 mL) of solution B were mixed with 1 mL of solution A, and then enough ethanol was added to keep total volume to 2 mL.
4. Heat the above mixed solutions for 30 minutes on 90 °C.
5. Then 0.3 M NaOH was added into above hot solutions until the final volume is 2.5 mL. Cool down to room temperature.
6. Measure the sample's absorbance at 368 nm on UV spectrometer (Figure 2.5.3a). If the concentration is too high, the sample can be diluted by ethanol.

The calibration curve described in Figure 2.5.3b was obtained. The absorbance is proportional to the concentration of hydroxylamine in the standard solutions.

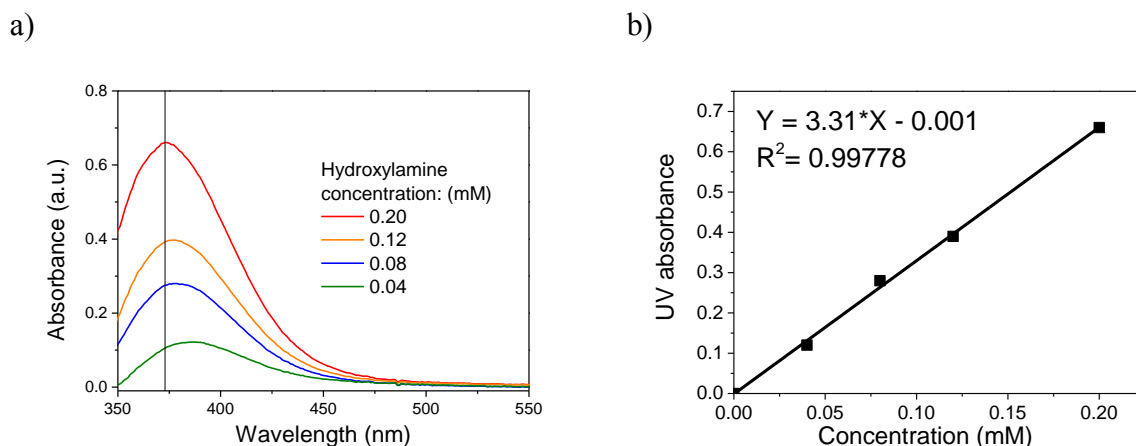


Figure 2.5.3 Calibration curve for detection of hydroxylamine using UV-Vis spectroscopy: a) UV-Vis spectra and b) calibration curve using absorbance at 368 nm from figure a).

An electrolysis experiment was performed with POM ($[\text{H}_2\text{W}_{12}\text{O}_{40}]^{6-}$) and nitrite in a two compartments cell (separated by a glass frit). Working and counter electrodes were graphite sheets (2 cm * 2 cm). The electrolyte is composed of 30 mL 0.5 M Na_2SO_4 pH 2 and contains 10 mM nitrite and 1 mM POM ($[\text{H}_2\text{W}_{12}\text{O}_{40}]^{6-}$). A constant voltage of -0.55 V vs. RHE was applied for 2 hours. The solution was sampled every 30 minutes by removing aliquots of 0.1

mL. These samples were mixed with 1 mL of solution A, and then ethanol was added to keep total volume of mixed solution to 2 mL. The analysis of products followed steps 4 to 6 described above. However, no yellow color was obtained from these the samples. One might suspect that the presence of POM could interfere in the oxime exchange that leads to the colored compound. Therefore, the following control experiments were performed in parallel:

Experiment 1: 1 mL of solution A was mixed with ethanol to 2 mL (solution B is missing).

Experiment 2: 1 mL solution A was mixed with 100 μ L of solution B containing 1 mM POM $[\text{H}_2\text{W}_{12}\text{O}_{40}]^{6-}$, then ethanol is added until the volume is 2 mL.

Experiment 3: 1 mL solution A was mixed with 100 μ L of aliquot taken after 30 min of electrolysis, then ethanol is added until the volume is 2 mL.

Experiment 4: 1 mL solution A was mixed with 100 μ L of aliquot taken after 60 min of electrolysis, then ethanol is added until the volume is 2 mL.

Experiment 5: 1 mL solution A was mixed with 100 μ L of aliquot taken after 90 min of electrolysis, then ethanol is added until the volume is 2 mL.

Experiment 6: 1 mL solution A was mixed with 100 μ L solution B, then ethanol is added until the volume is 2 mL.

As shown in Figure 2.5.4 and Figure 2.5.5, only experiment 2 and 6 have an absorption at 368 nm (yellow color). From experiment 2, it can be concluded that the presence of POM does not interfere with the mechanism of the formation of yellow colored p-nitrobenzaldoxime. For experiment 3, 4, and 5, no absorption peak at 368 nm is observed. As a conclusion, hydroxylamine is not a product of the nitrite electroreduction catalyzed by POM ($[\text{H}_2\text{W}_{12}\text{O}_{40}]^{6-}$). This experiment should be repeated with other POMs in order to make sure that hydroxylamine is not a product of nitrite reduction catalyzed by these compounds.



Figure 2.5.4 Picture of the six control experiments performed in parallel.

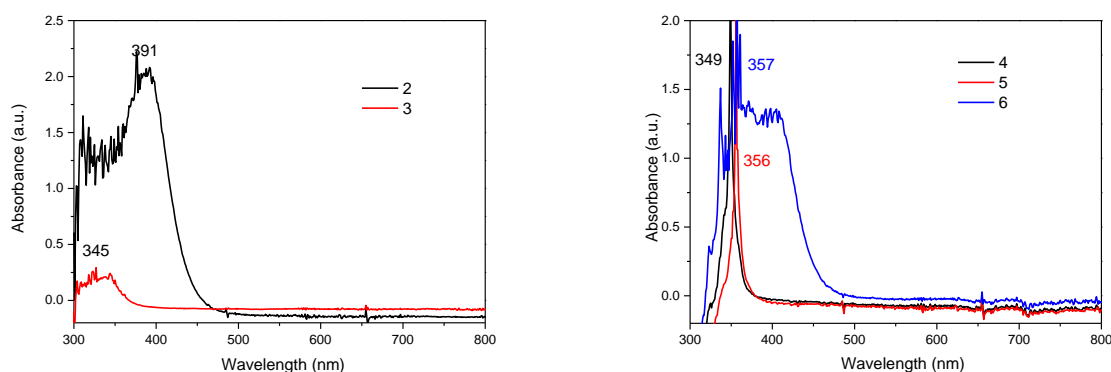


Figure 2.5.5 UV-visible absorption spectra of the six control experiments.

2.6 Reduction of nitric oxide (NO) catalyzed by POMs

Nitric oxide (NO) is one of the principal oxides of nitrogen, and is very easy to be oxidized by dioxygen to form NO₂. NO and NO₂ can also easily react to form HNO₂ in solution (see equation 1.4.26 in chapter 1.4.3). NO can be also formed from the disproportionation of HNO₂ (see equation 1.4.27 in chapter 1.4.3). The balance between HNO₂ and NO₂⁻ is set by the pK_a of 3.3. Thus, the exact composition of a NO/HNO₂/NO₂⁻/NO₂ system is very dependent on the presence of O₂, on the pH and the total concentration of nitrite. Besides, NO is an intermediate product of nitrite reduction catalyzed by POMs. Moreover, the reduction of NO catalyzed by some POMs was reported.^{2, 7} In one interesting report, when [SiMo₁₂O₄₀]⁴⁻ was used as an immobilized catalyst^{1c}, the authors have observed the same catalytic behavior for NO reduction compared to nitrite reduction. In that case, the electrolyte was 0.2 M Na₂SO₄ at pH 2 and total nitrite concentration was 10 mM. These conditions are very similar to our experiments. The authors had no explanation for the found results and they do not exclude the possibility that the actual redox species is NO⁺.

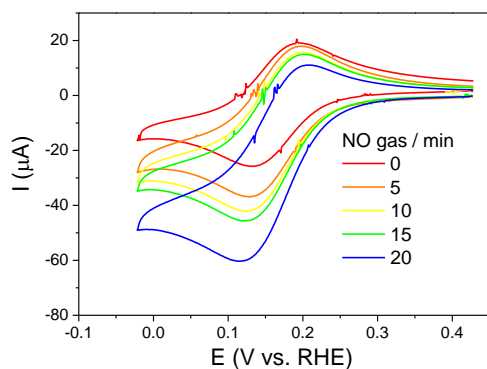
In this view, we have sought to use our DEMS setup to study the reduction of NO catalyzed by some W-based Keggin POMs. The experimental setup used for bubbling NO in the electrolyte is described in chapter 2. Argon was thoroughly bubbled through the electrolyte containers to remove traces of oxygen. Also, a container with NaOH was used as a trap of some NO₂ that could eventually form despite the efforts to remove oxygen by argon bubbling. As mentioned previously^{1c}, it is difficult to know the exact concentration of dissolved NO. Thus, by increasing the bubbling time, an increasing amount of dissolved NO was obtained, despite that the actual concentration is not known. Before performing DEMS experiments, we have traced cyclic voltammetry in the presence of [SiW₁₂O₄₀]⁴⁻. The results are depicted in Figure 2.6.1. As reported by Keita et al., we observe the same catalytic behavior for NO reduction as for nitrite reduction. In detail, the current intensity of the first reduction wave of [SiW₁₂O₄₀]⁴⁻ is already increasing with the bubbling time of NO. This wave bears only one reduction electron, thus the reduction of NO should generate a species containing a nitrogen atom with +1 oxidation state. The current intensity of the other waves is also increasing with the bubbling time of NO, suggesting a further reduction of this species. DEMS measurements were conducted for finding the gaseous products and results are shown in Figure 2.6.2. It worth mentioning that ¹⁴N isotope was used in these studies as this is the only available ¹⁴NO gas. The consequence of this is the fact that the signal of m/z = 44 is monitored, but this corresponds to N₂O and CO₂ as well. In this situation, the sensitivity for detecting N₂O is lower due to a higher baseline signal. For the sake of comparison, three different W-based Keggin POMs were used in this study, i.e. [H₂W₁₂O₄₀]⁶⁻, [BW₁₂O₄₀]⁵⁻ and [SiW₁₂O₄₀]⁴⁻. In order to have a constant concentration of NO, a fixed bubbling time of 20 minutes was set. The current intensity recorded in this case is similar to the one obtained when 1 mM of nitrite is reduced.

The most striking result is the appearance of a positive m/z 30 signal directly during the first reduction wave of all POMs (red curve in Figure 2.6.2). **This means the formation of a nitric oxide (NO) species.** The only plausible explanation is the existence of some dioxygen traces in the DEMS cell, leading to the formation of dissolved NO₂ and thus the formation of HNO₂. Then, this nitrous acid is subsequently reduced by the POMs during the first wave to form nitric oxide (NO). This hypothesis can be checked by monitoring the DEMS signal of

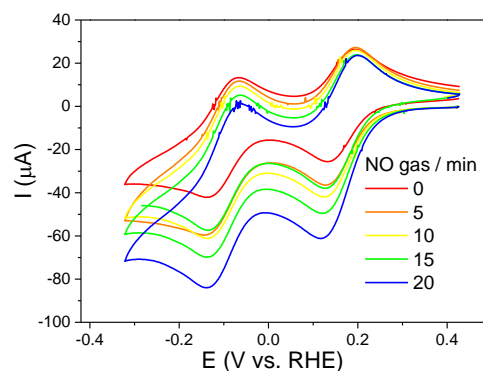
NO_2 , $m/z = 46$, shown in Figure 2.6.3. A clear correlation between the formation of NO and the consumption of NO_2 is observed. It suggests that NO_2 is consumed in the reaction with NO to form HNO_2 , as described above.

All these are quite preliminary results and measurements involving more POMs and more various experimental parameters should be run before any conclusion on the reaction mechanism can be drawn. Nevertheless, the results are intriguing enough for encouraging us to conduct more experiments in the future.

a)



b)



c)

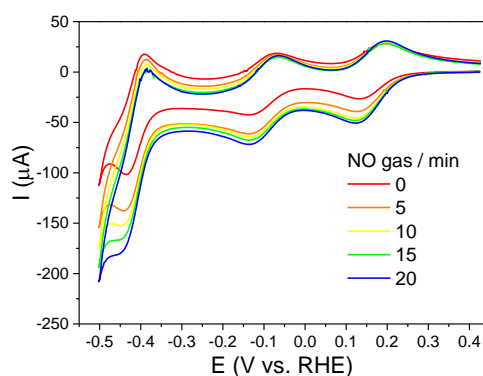


Figure 2.6.1 Cyclic voltammetry for nitric oxide reduction at pH 2 catalyzed by $[\text{SiW}_{12}\text{O}_{40}]^{4-}$. Red curve is for POM alone and other colors correspond to the different bubbling time with ^{14}NO gas: (a) first wave; (b) first and second waves; (c) all the three waves. Experimental conditions: $v = 20 \text{ mVs}^{-1}$, $0.5 \text{ M Na}_2\text{SO}_4$, 1 mM POM .

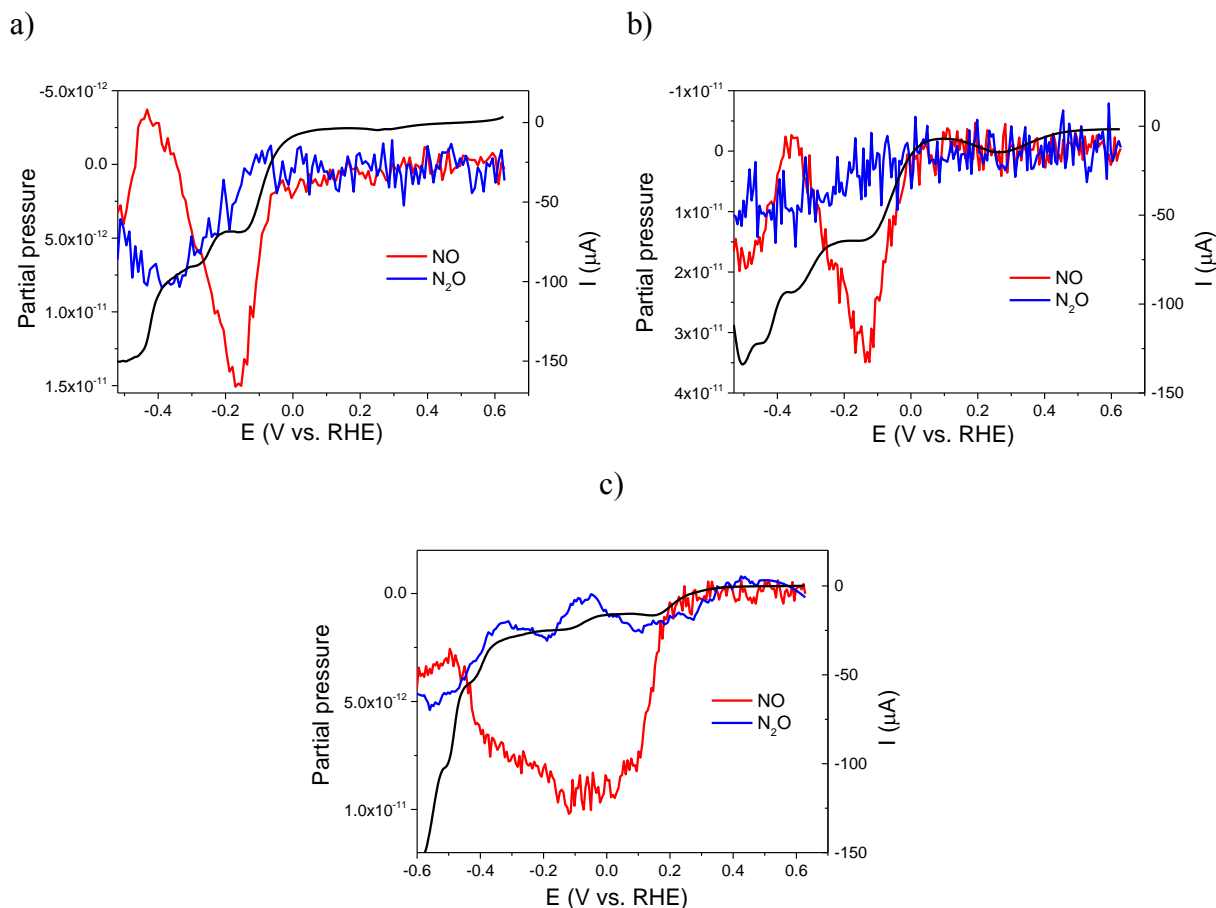


Figure 2.6.2 DEMS experiments at pH 2 after 20 minutes of bubbling with ^{14}NO gas: a) $[\text{H}_2\text{W}_{12}\text{O}_{40}]^{6-}$, b) $[\text{BW}_{12}\text{O}_{40}]^{5-}$ and c) $[\text{SiW}_{12}\text{O}_{40}]^{4-}$. Red curve: NO signal; blue curves: N_2O signal and black curves: CV curve. Experimental conditions: $v = 0.5 \text{ mVs}^{-1}$, pH 2, 0.5 M Na_2SO_4 , 1 mM POM.

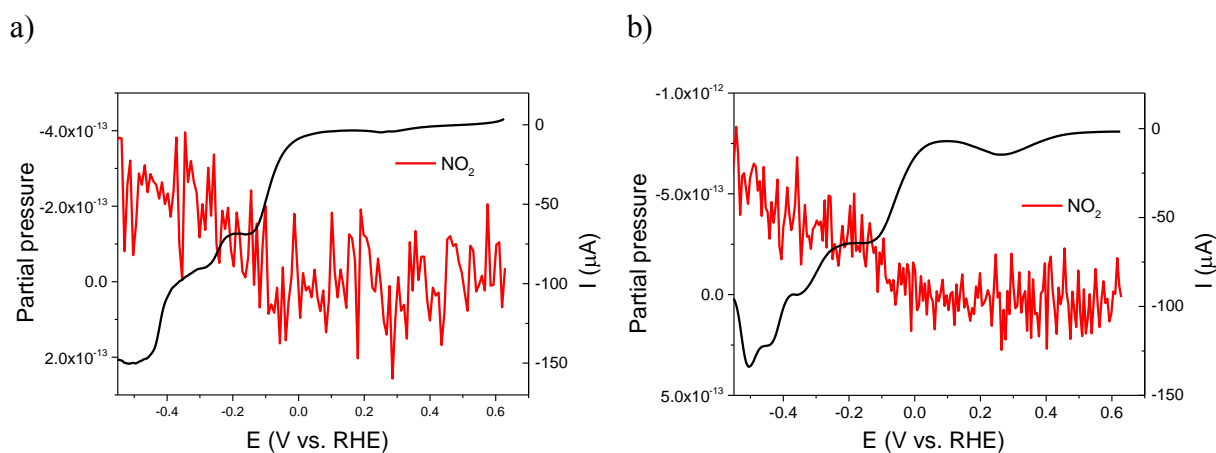


Figure 2.6.3 DEMS experiments at pH 2 with 20 min ^{14}NO gas bubbling for a), $[\text{H}_2\text{W}_{12}\text{O}_{40}]^{6-}$, b) $[\text{BW}_{12}\text{O}_{40}]^{5-}$ with $^{14}\text{NO}_2$ signals.

2.7 Kinetic studies of nitrite reduction catalyzed by POMs

A careful analysis of the DEMS curves gives some indications about the kinetics of the reaction. The correlation between the decrease in the NO signal and the increase of N_2O

signal can be interpreted also in terms of competition between the rate of NO formation and the rate of its consumption (i.e. the rate of N₂O formation). The balance between the two can be observed when the analysis of the NO signal is made compared to the baseline signal. This will be discussed individually for each POM at pH 2 and for W-based Keggin POMs at pH 5 as well. At pH 2, for [H₂W₁₂O₄₀]⁶⁻ at -0.5 V vs. RHE the ¹⁵NO signal is even lower than the baseline (taken between 0.6 V vs. RHE and 0 V vs. RHE) (Figure 2.4.2a). This suggests that the rate of NO consumption is so high that not only ¹⁵NO produced by the electrochemical reduction of H¹⁵NO₂ but also ¹⁵NO issued from the disproportionation of H¹⁵NO₂ are converted into ¹⁵N₂O. In the case of [BW₁₂O₄₀]⁵⁻, at pH 2 at -0.5 V vs. RHE, the signal of ¹⁵NO doesn't reach the baseline, suggesting that the ¹⁵NO consumption is slower and some ¹⁵NO still remains in the solution (Figure 2.4.2b). For [SiW₁₂O₄₀]⁴⁻, at pH 2 and -0.5 V vs. RHE the situation is similar to [BW₁₂O₄₀]⁵⁻, but the ¹⁵NO signal is reaching the signal of baseline at a lower potential (-0.6 V vs. RHE), suggesting that the rate of consumption is equal to the rate of production (Figure 2.4.2c). For [PW₁₂O₄₀]³⁻ the analysis was performed at pH 1, and the higher proton concentration might favor the formation of N₂O and this would explain why at -0.5 V vs. RHE the signal is already lower than the baseline (Figure 2.4.2d). At pH 5, the signal of NO is lower than the baseline only for [H₂W₁₂O₄₀]⁶⁻ (Figure 2.4.3a). For both Mo-based Keggin POMs, the signal is lower than the baseline at a potential of -0.20 V vs. RHE at pH 2 (Figures 2.4.7). For Dawson-type POMs, the signal of ¹⁵NO is never smaller than the baseline (Figures 2.4.8-2.4.11).

In order to obtain more precise information about the catalytic rates, we have computed the catalytic Tafel plots. In these plots, the turnover frequency (TOF) is related to the overpotential and these plots are recommended as key element of catalysts benchmarking.³⁰ TOF is an evaluation for catalytic activity from enzymatic kinetics, which is used both in heterogeneous and homogeneous catalysis. Although the definition of TOF is widespread, the TOF calculation processes are different according to different reaction systems that made lots of researcher wondered about its versatility on these reaction systems.³¹ However TOF is still a ubiquitous term and irreplaceable parameter in catalytic reaction. In our study, TOF was calculated using Eq. 2.7.1

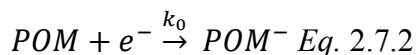
$$\text{TOF} = \frac{k_c c_0}{1 + \exp\left[\frac{F}{RT} \left(E_{\text{HNO}_2 \text{ or NO}_2^-/\text{NO}}^0 - E_{\text{POM}}^{0'}\right)\right] \exp\left(\frac{-F\eta}{RT}\right)} \quad \text{Eq. 2.7.1}$$

In the equation, k_c is second order rate constant of the catalytic reaction; $c_0 = 1.0 \text{ M}$ is the standard concentration, $E_{\text{HNO}_2/\text{NO}}^0$ is the standard redox potential of HNO₂ reduction to NO (0.990 V vs. RHE at pH 1, pH 2 and pH 3), $E_{\text{NO}_2^-/\text{NO}}^0$ is the standard redox potential of NO₂⁻ reduction to NO (0.966 V vs. RHE at pH 4, 0.907 V vs. RHE at pH 5); $E_{\text{POM}}^{0'}$ is the apparent formal potential corresponding to the first reduction wave of each POM (measured experimentally by cyclic voltammetry in a 1 mM POM solution); η is the overpotential; $F = 96485 \text{ C mol}^{-1}$ is the Faraday constant, $R = 8.314 \text{ J.K}^{-1}\text{mol}^{-1}$ is the ideal gas constant; $T = 298 \text{ K}$ is the temperature.

The rate of the catalytic reaction was obtained with the help of microkinetic simulations. At this stage, the simulations were applied only for the first catalytic wave that corresponds to the reduction of nitrite into NO (according to the DEMS results) and only for three POMs, [PW₁₂O₄₀]³⁻, [SiW₁₂O₄₀]⁴⁻, and [BW₁₂O₄₀]⁵⁻. [H₂W₁₂O₄₀]⁶⁻ is excluded from this study because a mixture of NO and N₂O is produced during the first wave. For the sake of simplicity, the kinetic model considers an EC mechanism where the POM acts as a redox

mediator, i.e. the reduced POM is reducing the nitrite in solution. In this microkinetic simulations, the model takes into account:

1. the POM / POM⁻ redox transition which occurs at the glassy carbon electrode surface (Eq. 2.7.2);
2. the diffusion of POM and POM⁻ species in solution;
3. the reaction of POM⁻ with either HNO₂ at pH 1–3 (Eq. 2.7.3) or NO₂⁻ at pH 4–5 (Eq. 2.7.4) to produce NO and regenerate POM.



Thus, this simplified model should be able to reproduce the first nitrite or nitrous acid reduction wave catalyzed by [PW₁₂O₄₀]³⁻, [SiW₁₂O₄₀]⁴⁻, and [BW₁₂O₄₀]⁵⁻. The current-potential curves can be simulated by solving the diffusion reaction equations 2.7.5-2.7.7 and using a home-made program in Scilab. A comparison between the simulated and recorded curves (Figures 2.7.1 to 2.7.3) demonstrates the relevance of the kinetic model. The visual match between the simulated and experimental curve was used to assess the quality of the fitting. The fitting is particularly good for the reduction wave, for a potential range from the beginning of the CV and down to the reduction peak. The CV curves obtained for POMs alone were fitted first (Figure. 2.7.1a-c). The CV curves obtained for POMs (1 mM) and 10 mM NaNO₂ were fitted only for the reduction currents (Figure 2.7.1d-e).

$$\frac{\delta[POM]}{\delta t} = D_p \frac{\delta^2[POM]}{\delta x^2} \text{ Eq. 2.7.5}$$

$$\frac{\delta[POM^-]}{\delta t} = D_p \frac{\delta^2[POM^-]}{\delta x^2} - k_c c[POM^-] \text{ Eq. 2.7.6}$$

$$\frac{\delta[c]}{\delta t} = D_N \frac{\delta^2[c]}{\delta x^2} - k_c [c][POM^-] \text{ Eq. 2.7.7}$$

where [c] is the nitrite or nitrous acid concentration, k_c is the reaction rate for reaction between the reduced POM⁻ and the nitrite in solution, D_p is the diffusion coefficient of the POM, D_N is the diffusion coefficient of the nitrite (or nitrous acid). The value of D_N = 1.5*10⁻⁵ cm².s⁻¹ was taken from published work.³² x is the distance to the electrode surface in the electrolyte and t is the time.

These equations are solved with the following boundary conditions:

- i) at the electrode surface, the fluxes of POM, POM⁻ and nitrite/nitrous acid are given by Equations (2.7.8) and (2.7.10); the Faradaic current density i is given by Eq. (2.7.9);
- ii) at t = 0 s, the POM concentration is spatially uniform [POM] = 1 mM and [POM⁻] = 0, c = C₀, the bulk nitrite concentration;
- iii) far from the electrode in the bulk for the solution [POM] = 1 mM and [POM⁻] = 0, c = C₀.

$$D_p = \left(\frac{\delta[POM]}{\delta x} \right)_{x=0} = -D_p \left(\frac{\delta[POM^-]}{\delta x} \right)_{x=0} = k_0([POM]_{x=0} e^{-\alpha f(E-E_{POM}^{'})}) - [POM^-]_{x=0} e^{(1-\alpha)f(E-E_{POM}^{'})} - k_c[POM^-]_{x=0}[C]_{x=0} \quad Eq. 2.7.8$$

$$i = Fk_0([POM^-]_{x=0} e^{(1-\alpha)f(E-E_{POM}^{'})} - [POM]_{x=0} e^{-\alpha f(E-E_{POM}^{'})}) \quad Eq. 2.7.9$$

$$D_N \left(\frac{\delta[C]}{\delta x} \right)_{x=0} = k_0[POM^-]_{x=0}[C]_{x=0} \quad Eq. 2.7.10$$

where $f = F/RT$, E is the electrode potential, $E_{POM}^{'}$ is the apparent formal potential of the POM/POM⁻ redox transition, k_0 its rate constant and α the charge transfer coefficient.

The values of k_0 , $E^{'}$ and D_p were first estimated by fitting the first redox wave of the POM in the absence of nitrite in solution (Figure 2.7.1a-c). Then the current potential-curves of nitrite reduction were considered and k_c was determined for each POM to reproduce the first catalytic wave of nitrite reduction (Figure 2.7.1d-e). Finally, the turnover frequency can be calculated and Tafel plots are obtained as shown in Figure 2.7.4. Table 2.7.1 summarizes all the values obtained from the simulation of CVs with the microkinetic model.

Table 2.7.1 Parameters of interest obtained from the simulation of CVs with the microkinetic model (D is the diffusion coefficient of POM k_c is second order rate constant of the catalytic reaction).

POM	pH	$D_p (10^5 \text{ cm}^2 \cdot \text{s}^{-1})$	$k_c (\text{mol}^{-1} \cdot \text{L} \cdot \text{s}^{-1})$	TOF (s^{-1}) (at η corresponding to the first wave* V vs. RHE)
[PW ₁₂ O ₄₀] ³⁻	1	0.25	2433	1119 (0.700)
	1	0.40	4900	2460 (0.855)
	2		700	363 (0.830)
[SiW ₁₂ O ₄₀] ⁴⁻	3		173	88 (0.799)
	4		15	8 (0.674)
	5		10	5 (0.612)
	1	0.52	8833	4415 (1.120)
	2		833	415 (1.094)
[BW ₁₂ O ₄₀] ⁵⁻	3		223	108 (1.050)
	4		20	10 (0.944)
	5		13	6 (0.866)

where $E_{\text{HNO}_2/\text{NO}}^{'}$ is the standard redox potential of nitrite reduction to NO (0.990 V vs. RHE at pH 1, pH 2 and pH 3) 0.966 V vs. RHE at pH 4, 0.907 V vs. RHE at pH 5); $E_{\text{NO}_2^-/\text{NO}}^{'}$ is the standard redox potential of NO₂⁻ reduction to NO (0.966 V vs. RHE at pH 4, 0.907 V vs. RHE at pH 5); $E_{POM}^{'}$ is the apparent formal potential corresponding to the first reduction wave of each POM (measured experimentally by cyclic voltammetry in a 1 mM POM solution).

*i.e. $\eta = E_{\text{HNO}_2/\text{NO}}^{'}$ or $E_{\text{NO}_2^-/\text{NO}}^{'}$ - $E_{POM}^{'}$.

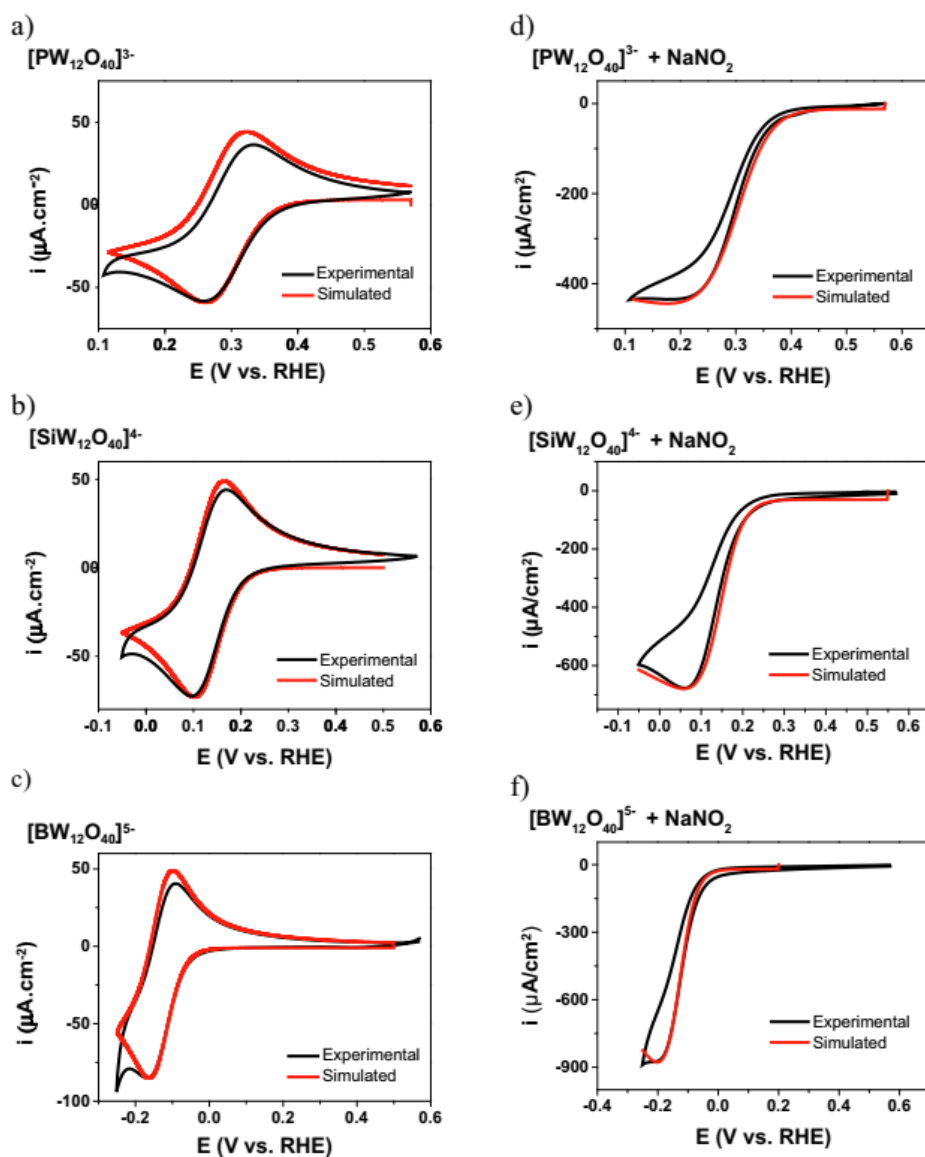
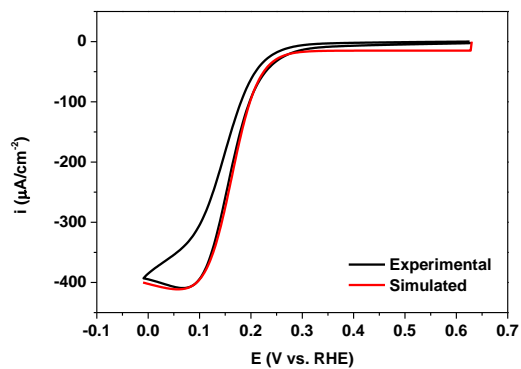
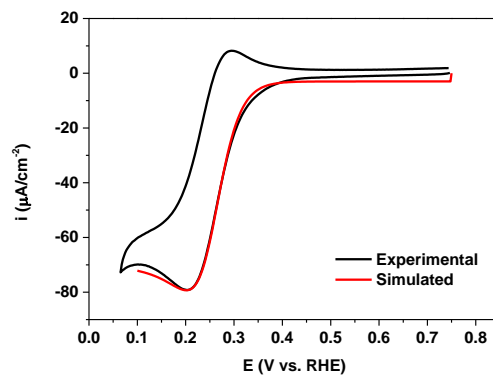


Figure 2.7.1 Comparison of experimental data of cyclic voltammetry (black curves) and simulated curve with the microkinetic model (red curves) for three POMs at pH 1 in the absence of nitrite (a-c) and in the presence of 10 mM of NaNO_2 (d-f). Experimental conditions: scan rate, 20 mVs^{-1} ; 1 mM POM; electrolyte: 0.5 M $\text{Na}_2\text{SO}_4 + \text{H}_2\text{SO}_4$, pH 1.

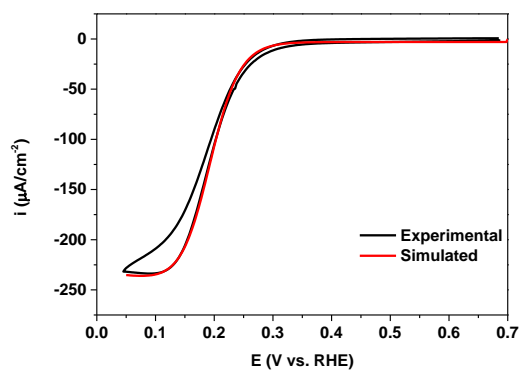
a) $[\text{SiW}_{12}\text{O}_{40}]^{4-}$ at pH 2



b) $[\text{SiW}_{12}\text{O}_{40}]^{4-}$ at pH 4



c) $[\text{SiW}_{12}\text{O}_{40}]^{4-}$ at pH 3



d) $[\text{SiW}_{12}\text{O}_{40}]^{4-}$ at pH 5

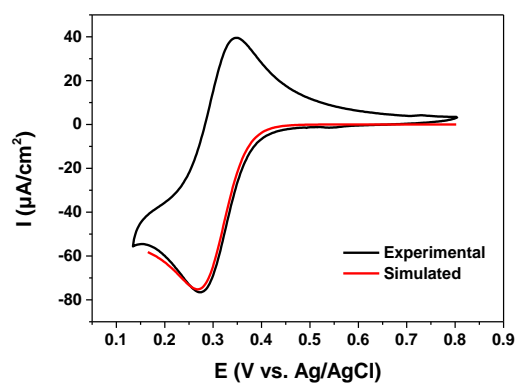


Figure 2.7.2 Comparison of experimental data of cyclic voltammetry (black curves) and data simulated with the microkinetic model (red curves) for 1 mM of $[\text{SiW}_{12}\text{O}_{40}]^{4-}$ in the presence of 10 mM NaNO_2 .

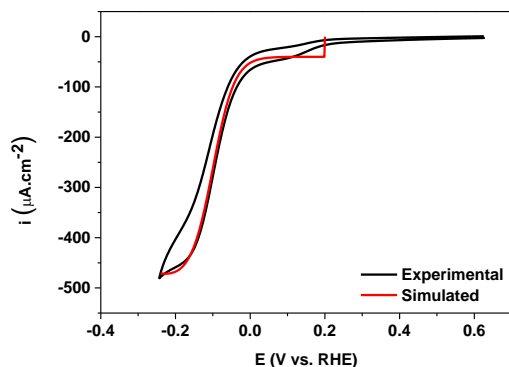
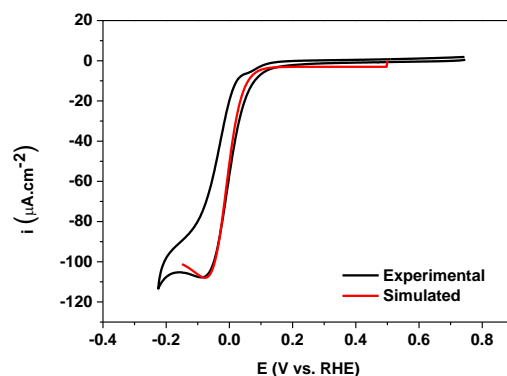
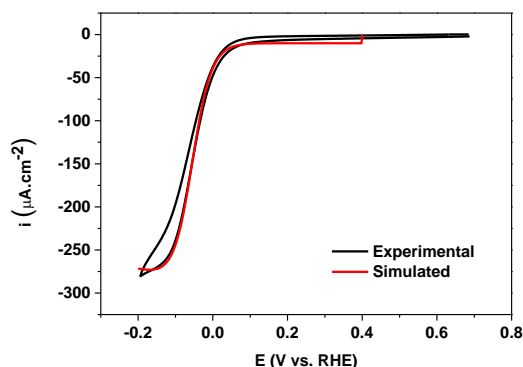
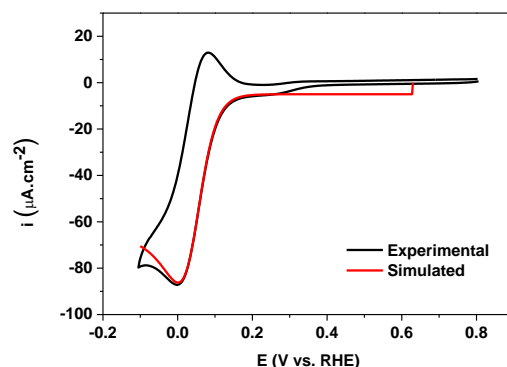
a) $[\text{BW}_{12}\text{O}_{40}]^{5-}$ at pH 2b) $[\text{BW}_{12}\text{O}_{40}]^{5-}$ at pH 4c) $[\text{BW}_{12}\text{O}_{40}]^{5-}$ at pH 3d) $[\text{BW}_{12}\text{O}_{40}]^{5-}$ at pH 5

Figure 2.7.3 Comparison of experimental data of cyclic voltammetry (black curves) and data simulated with the microkinetic model (red curves) for 1mM of $[\text{BW}_{12}\text{O}_{40}]^{5-}$ in the presence of 10 mM NaNO_2 .

$[\text{PW}_{12}\text{O}_{40}]^{3-}$ is not stable at high pH values such as pH 2, therefore the TOF comparison was only at pH 1 for these three Keggin POMs. According to the Eq. 2.7.1, the TOF value can be divided into three ranges by comparison of η with $(E^0_{\text{HNO}_2 \text{ or } \text{NO}_2^- / \text{NO}} - E^0_{\text{POM}})$. When $\eta < E^0_{\text{HNO}_2 \text{ or } \text{NO}_2^- / \text{NO}} - E^0_{\text{POM}}$, the applied potential E is higher than E^0_{POM} , the reduction of POM to POM^- is inhibited. Consequently, the nitrite reduction is nearly impossible with very small TOF values which increase with E^0_{POM} (Eq. 2.7.1) in the following order $[\text{PW}_{12}\text{O}_{40}]^{3-} > [\text{SiW}_{12}\text{O}_{40}]^{4-} > [\text{BW}_{12}\text{O}_{40}]^{5-}$. On the contrary, when $\eta > E^0_{\text{HNO}_2 \text{ or } \text{NO}_2^- / \text{NO}} - E^0_{\text{POM}}$, there is enough POM^- produced that promotes nitrite reduction. TOF is determined by the k_c values (Eq. 2.7.1). The order of POMs' TOF is reversed than before. When η is close to $E^0_{\text{HNO}_2 \text{ or } \text{NO}_2^- / \text{NO}} - E^0_{\text{POM}}$, both k_c and E^0_{POM} influence the TOF. The curves of $[\text{SiW}_{12}\text{O}_{40}]^{4-}$ and $[\text{BW}_{12}\text{O}_{40}]^{5-}$ were simulated from pH 1 to pH 5 (Figure 2.7.4b and 2.7.4c). For both POMs, TOF values are increasing with higher concentration of proton (lower pH). The variation of k_c catalytic rate constant with different pH is shown in Figure 2.7.4d. From the pH 1 to pH 3, k_c is higher at lower pH, because the pH is lower than the pK_a 3.3 of HNO_2 . In this case nitrous acid is the dominant reactant and protons are involved in the reaction (Eq. 2.7.3). In contrast, for pH 4 and 5, NO_2^- is the dominant reactant (Eq. 2.7.4) and there is no proton involved. Due to the electrostatic repulsion between the NO_2^- and the reduced POM^- , the nitrite reduction is slower at higher pH. The particular values of TOF obtained are given in Table 2.7.1 when the overpotential corresponds to the first reduction wave ($\eta = E^0_{\text{HNO}_2 \text{ or } \text{NO}_2^- / \text{NO}} - E^0_{\text{POM}}$).

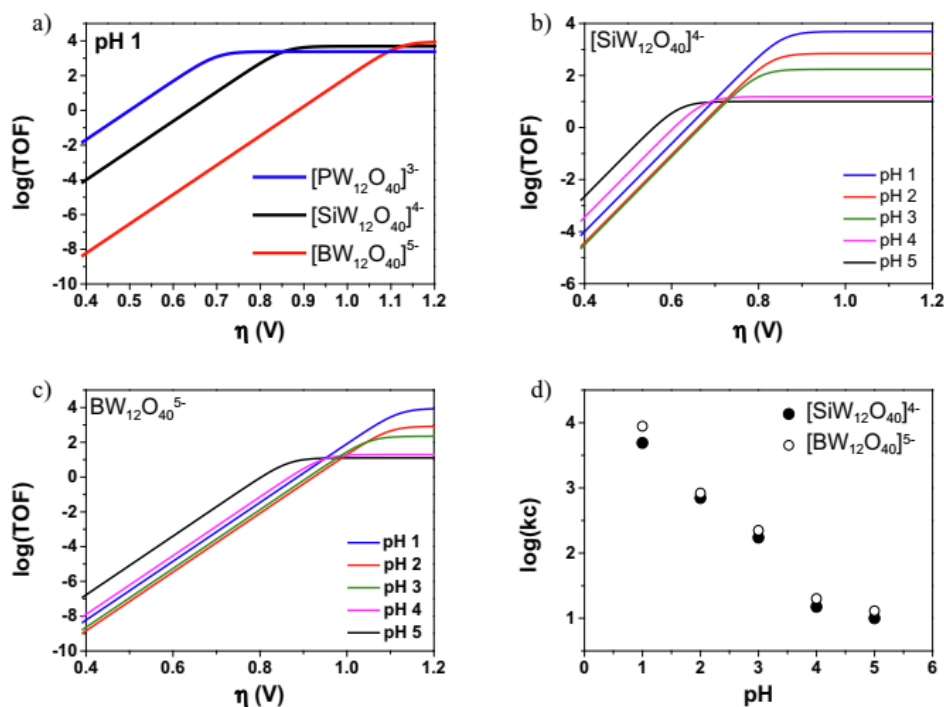


Figure 2.7.4 Catalytic Tafel plots displaying turnover frequency as function of overpotential: a) at pH 1 for $[\text{PW}_{12}\text{O}_{40}]^{3-}$ (blue line), $[\text{SiW}_{12}\text{O}_{40}]^{4-}$ (black line), $[\text{BW}_{12}\text{O}_{40}]^{5-}$ (red line); b) for $[\text{SiW}_{12}\text{O}_{40}]^{4-}$ at pH 1 to 5; c) for $[\text{BW}_{12}\text{O}_{40}]^{5-}$, at pH 1 to 5; d) influence of pH on the second order kinetic constant (k_c) for $[\text{SiW}_{12}\text{O}_{40}]^{4-}$ and $[\text{BW}_{12}\text{O}_{40}]^{5-}$. Values are obtained from modelling cyclic voltammetry data with a microkinetic model.

As a conclusion, $[\text{BW}_{12}\text{O}_{40}]^{5-}$ has highest catalysis efficiency (k_c and TOF) for conversion of nitrous acid to NO at pH 1 compared with $[\text{SiW}_{12}\text{O}_{40}]^{4-}$ and $[\text{PW}_{12}\text{O}_{40}]^{3-}$. TOF values of $[\text{BW}_{12}\text{O}_{40}]^{5-}$ and $[\text{SiW}_{12}\text{O}_{40}]^{4-}$ at pH 2 are about 70 times higher as that at pH 5, suggesting that the high proton concentration and low repulsive charges promote this reaction. A direct comparison of TOF values with data from literature is not reasonable because TOF values were computed in a different manner and for a different reaction, such as water oxidation analyzed by POMs,³³. Therefore, TOF values reported by our study should be only used as comparison criteria between our POMs in order to establish a hierarchy of their activity. It is worth to mention that another analytical model³⁰ for TOF calculation did not fit well our experimental data.

As a final discussion, the mechanism of N_2O formation is discussed tentatively. In the nitrite conversion to NO, POMs act as a redox mediator. Reduced POM^- reacts with nitrite to form NO and recycles the POM. This is a typical EC mechanism used for the kinetic model. On the basis of the DEMS experimental results, N_2O is formed during the second reduction waves of $[\text{PW}_{12}\text{O}_{40}]^{3-}$, $[\text{SiW}_{12}\text{O}_{40}]^{4-}$ and $[\text{BW}_{12}\text{O}_{40}]^{5-}$ or the first two-electron reduction wave of $[\text{H}_2\text{W}_{12}\text{O}_{40}]^{6-}$, which is concomitant to the consumption of NO. Thus, the step of reduction of POM^- to POM^{2-} is necessary as shown in Eq. 2.7.11. According to Bartberger et al.,³⁴ the reduction of NO to NO^- is unfavorable with an extremely low potential of -1.7 V vs. NHE. This reduction potential, value was recently questioned since it was shown that NO can be converted to HNO by H_2S ,³⁵ thiols³⁶ or aromatic alcohols.³⁷ These results are in agreement with $E^0_{\text{HNO/NO}} = -0.11$ V. In our experiments, the redox potentials of couple $\text{POM}^{2-}/\text{POM}^-$ are

lower than **-0.10 V for most of the studied POMs**. Therefore, an outer-sphere electron transfers between POM^{2-} and NO is thermodynamically possible and HNO is a reasonable intermediate (Eq. 2.7.12). Then, the produced HNO might convert to N_2O through a complex reaction. The simplified description is shown in Eq. 2.7.13. The entire catalytic process is schematized in Figure 2.7.5.

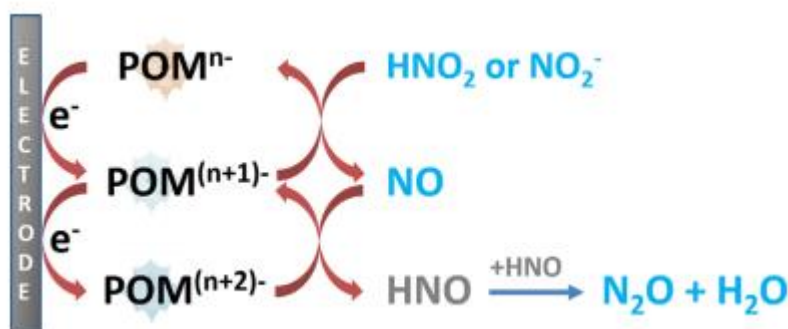
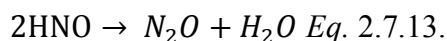
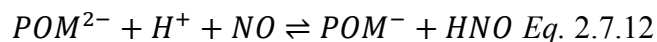
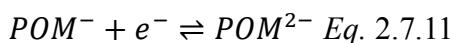


Figure 2.7.5 Catalytic redox processes of nitrite or nitrous acid electroreduction catalyzed by polyoxometalates.

2.8 Conclusion

In this chapter, we have conducted a detailed analysis of the reaction products obtained when nitrite reduction is catalyzed by various polyoxometalates (POMs). The catalysts are employed in the homogeneous phase and differential electrochemistry mass spectrometry (DEMS) was used as a complementary technique to cyclic voltammetry studies. The purpose was to understand the relation between the redox properties of the POMs and the obtained products. For this, we have studied a series of W-based Keggin POMs in which the central heteroatom is different (P, Si, B, H) and thus the total redox charge and the reduction potential is different. We have found that:

- i) when the POM undergoes a one-electron reduction, NO is produced by the reduction of HNO_2 that requires only one electron;
- ii) two molecules of two-electron reduced POMs are able to catalyze the reduction of nitrite to N_2O , as this requires four electrons;
- iii) as $POM [H_2W_{12}O_{40}]^{6-}$ is undergoing a two-electron species directly during the first wave, the production of N_2O is also observed in this first wave
- iv) the onset potential of N_2O is very little dependent on the selected POM, the value being around -0.2 V vs. RHE at pH 2
- v) at pH 5, the onset potential of N_2O becomes more negative, most probably due to the charge repulsion between the reduced POM^- anion and NO_2^- and to the reduced concentration of protons, resulting in the slowdown of NO formation.

These observations let us to the assumption that the reduction of NO firstly yields HNO because some recent studies proposed the formal potential of NO/HNO couple around -0.11 V vs. RHE. This corroborates very well with the formation of N_2O observed at -0.2 V vs.

RHE.

One way to validate this hypothesis is to study more various POMs. For this reason, we have selected two Mo-based Keggin POMs ($[\text{PMo}_{12}\text{O}_{40}]^{3-}$ and $[\text{SiMo}_{12}\text{O}_{40}]^{4-}$) that have more positive redox potentials and also are directly reduced to two-electrons in their first wave. Despite this, the onset potential of N_2O was very similar in between them, i.e. -0.1 V vs. RHE and not so different than the one of W-based Keggin POMs. The conversion of NO to N_2O via HNO is also plausible with these two POMs.

Finally, we have studied other four POMs from the Dawson family due to their high number of exchanged electrons (four for each of three waves) $[\text{Zn}_4(\text{H}_2\text{O})_2(\text{P}_2\text{W}_{15}\text{O}_{56})_2]^{16-}$, $[\text{Cd}_4(\text{H}_2\text{O})_2(\text{P}_2\text{W}_{15}\text{O}_{56})_2]^{16-}$, $[\text{Mn}_4(\text{H}_2\text{O})_2(\text{P}_2\text{W}_{15}\text{O}_{56})_2]^{16-}$ and $\alpha\text{-}[\text{P}_2\text{W}_{18}\text{O}_{62}]^{6-}$. One more time, the onset potential of N_2O is validating the hypothesis of HNO intermediate, as the value was -0.2 V vs. RHE for parent Dawson and -0.3 V vs. RHE for Sandwich dimer Dawson-type POMs. The metal atom in the core of the dimer POMs has no influence on the onset potentials. Moreover, these POMs were selected because they could provide enough electrons for the conversion of nitrite to nitrogen. But no signal of N_2 could be found in our DEMS analysis.

The detailed analysis of DEMS data indicates a potential range where nitric oxide is the soul product and this for all studied POMs. This motivated the development of a microkinetic model able to extract kinetic rate constant and turnover efficiency of the nitrite reduction to NO. For the moment, for the sake of simplicity, the model was applied only to those POMs bearing only one electron in their first wave. The model has successfully fitted the cyclic voltammetry data. In this manner, it was concluded that, at low overpotential, the values of TOF are decreasing in a trend following the redox potential of the POM: $[\text{PW}_{12}\text{O}_{40}]^{3-} > [\text{SiW}_{12}\text{O}_{40}]^{4-} > [\text{BW}_{12}\text{O}_{40}]^{5-}$ while at high overpotential the TOFs are following the reverse order. At pH 5 the values of the rate constants are about 70 times lower than at pH 2 due to the decrease in the proton concentration and to the electrostatic repulsion between the negatively charged POMs and NO_2^- .

Other possible reaction products, such as hydroxylamine and ammonia, were searched only in the case of $[\text{H}_2\text{W}_{12}\text{O}_{40}]^{6-}$. Although these products were not seen, a more systematic study should be performed with the other POMs before a general conclusion can be made.

A final study has opened the way for future experiments, that is the reduction of nitric oxide catalyzed by some POMs ($[\text{SiW}_{12}\text{O}_{40}]^{4-}$, $[\text{BW}_{12}\text{O}_{40}]^{5-}$, $[\text{H}_2\text{W}_{12}\text{O}_{40}]^{6-}$). The obtained results, both from DEMS and CV, are very similar to the reduction of nitrite described in the other chapters. One possible explanation is the existence of O_2 traces that oxidizes NO back to HNO_2 , but still the resemblance is so striking that more careful experiments should be performed in the future with other POMs before any conclusion can be drawn.

2.9 References

- (a) Imar, S.; Yaqub, M.; Maccato, C.; Dickinson, C.; Laffir, F.; Vagin, M.; McCormac, T., Nitrate and Nitrite Electrocatalytic Reduction at Layer-by-Layer Films Composed of Dawson-type Heteropolyanions Mono-substituted with Transitional Metal Ions and Silver Nanoparticles. *Electrochimica Acta* **2015**, *184*, 323-330; (b) Keita, B.; Abdeljalil, E.; Nadjo, L.; Contant, R.; Belgiche, R., First examples of efficient participation of selected metal-ion-substituted heteropolyanions in electrocatalytic nitrate reduction. *Electrochemistry communications* **2001**, *3* (2), 56-62; (c) Keita, B.; Belhouari, A.; Nadjo, L.; Contant, R., Electrocatalysis by

- polyoxometalate/vbopolymer systems: reduction of nitrite and nitric oxide. *Journal of Electroanalytical Chemistry* **1995**, 381 (1-2), 243-250; (d) Liu, H.; He, P.; Li, Z.; Sun, C.; Shi, L.; Liu, Y.; Zhu, G.; Li, J., An ionic liquid-type carbon paste electrode and its polyoxometalate-modified properties. *Electrochemistry communications* **2005**, 7 (12), 1357-1363; (e) McCormac, T.; Fabre, B.; Bidan, G., Part II. Role of pH and the transition metal for the electrocatalytic reduction of nitrite with transition metal substituted Dawson type heteropolyanions. *Journal of Electroanalytical Chemistry* **1997**, 427 (1-2), 155-159; (f) Sahraoui, Y.; Chaliaa, S.; Maaref, A.; Haddad, A.; Jaffrezic-Renault, N., An electrochemical nitrite sensor based on a multilayer film of polyoxometalate. *Journal of Sensor Technology* **2013**, 3 (03), 84; (g) Wang, B.; Cheng, L.; Dong, S., Construction of a heteropolyanion-modified electrode by a two-step sol-gel method and its electrocatalytic applications. *Journal of Electroanalytical Chemistry* **2001**, 516 (1-2), 17-22; (h) Xi, X.; Dong, S., Electrocatalytic reduction of nitrite using Dawson-type tungstodiphosphate anions in aqueous solutions, adsorbed on a glassy carbon electrode and doped in polypyrrole film. *Journal of Molecular Catalysis A: Chemical* **1996**, 114 (1-3), 257-265.
2. Ruhlmann, L.; Genet, G., Wells-Dawson-derived tetrameric complexes $\{K_{28}H_8[P_2W_{15}Ti_3O_{60.5}]_4\}$ electrochemical behaviour and electrocatalytic reduction of nitrite and of nitric oxide. *Journal of Electroanalytical Chemistry* **2004**, 568, 315-321.
 3. Imar, S.; Maccato, C.; Dickinson, C.; Laffir, F.; Vagin, M.; McCormac, T., Enhancement of nitrite and nitrate electrocatalytic reduction through the employment of self-assembled layers of nickel-and copper-substituted crown-type heteropolyanions. *Langmuir* **2015**, 31 (8), 2584-2592.
 4. (a) Jamshidi, A.; Zonoz, F. M., Synthesis, characterization, electrochemical behavior and electrocatalytical properties towards nitrate and iodate by alcohol solvated Keggin-type polyoxometalate: The effects of weak intermolecular interactions and solvent on electrocatalytical activity. *Journal of Molecular Liquids* **2017**, 242, 993-1001; (b) Oms, O.; Yang, S.; Salomon, W.; Marrot, J.; Dolbecq, A.; Rivière, E.; Bonnefont, A.; Ruhlmann, L.; Mialane, P., Heteroanionic Materials Based on Copper Clusters, Bisphosphonates, and Polyoxometalates: Magnetic Properties and Comparative Electrocatalytic NO_x Reduction Studies. *Inorganic Chemistry* **2016**, 55 (4), 1551-1561; (c) Zhou, W.; Zheng, Y.; Peng, J., Cu-containing Keggin-type polyoxometalates-based organic-inorganic hybrids with double electro-catalytic behaviors. *Journal of Solid State Chemistry* **2018**, 258, 786-791.
 5. (a) Da Cunha, M.; De Souza, J.; Nart, F., Reaction pathways for reduction of nitrate ions on platinum, rhodium, and platinum-rhodium alloy electrodes. *Langmuir* **2000**, 16 (2), 771-777; (b) De Groot, M.; Koper, M., The influence of nitrate concentration and acidity on the electrocatalytic reduction of nitrate on platinum. *Journal of Electroanalytical Chemistry* **2004**, 562 (1), 81-94; (c) Dima, G.; De Voos, A.; Koper, M., Electrocatalytic reduction of nitrate at low concentration on coinage and transition-metal electrodes in acid solutions. *Journal of Electroanalytical Chemistry* **2003**, 554, 15-23; (d) Duca, M.; Cucarella, M. O.; Rodriguez, P.; Koper, M. T., Direct reduction of nitrite to N₂ on a Pt (100) electrode in alkaline media. *Journal of the American Chemical Society* **2010**, 132 (51), 18042-18044; (e) Nishimura, K.; Machida, K.; Enyo, M., On-line mass spectroscopy applied to electroreduction of nitrite and nitrate ions at porous Pt electrode in sulfuric acid solutions. *Electrochimica acta* **1991**, 36 (5-6), 877-880; (f) Pérez-Gallent, E.; Figueiredo, M. C.; Katsounaros, I.; Koper, M. T., Electrocatalytic reduction of Nitrate on Copper single crystals in acidic and alkaline solutions. *Electrochimica Acta* **2017**, 227, 77-84.
 6. Debiemme-Chouvy, C.; Cachet, H.; Folcher, G.; Deslouis, C., Electrocatalytic reduction of HNO₂ by a silicomolybdate polyanion: a differential electrochemical mass spectrometry study. *Electroanalysis: An International Journal Devoted to Fundamental and Practical Aspects of Electroanalysis* **2007**, 19 (23), 259-262.
 7. Ruhlmann, L.; Nadjo, L.; Canny, J.; Contant, R.; Thouvenot, R., Di- and Tetranuclear Dawson-Derived Sandwich Complexes: Synthesis, Spectroscopic Characterization, and Electrochemical Behavior. *European Journal of Inorganic Chemistry* **2002**, 2002 (4), 975-986.

8. Finke, R. G.; Droege, M. W.; Domaille, P. J., Trivacant heteropolytungstate derivatives. 3. Rational syntheses, characterization, two-dimensional tungsten-183 NMR, and properties of tungstometallophosphates $P_2W_{18}M_4(H_2O)_2O_{68}^{10-}$ and $P_4W_{30}M_4(H_2O)_2O_{112}^{16-}$ (M= cobalt, copper, zinc). *Inorganic Chemistry* **1987**, 26 (23), 3886-3896.
9. (a) Mbomekallé, I.-M.; López, X.; Poblet, J. M.; Sécheresse, F.; Keita, B.; Nadjo, L., Influence of the heteroatom size on the redox potentials of selected polyoxoanions. *Inorganic chemistry* **2010**, 49 (15), 7001-7006; (b) Pope, M. T.; Varga Jr, G. M., Heteropoly blues. I. Reduction stoichiometries and reduction potentials of some 12-tungstates. *Inorganic Chemistry* **1966**, 5 (7), 1249-1254.
10. Prenzler, P. D.; Boskovic, C.; Bond, A. M.; Wedd, A. G., Coupled electron-and proton-transfer processes in the reduction of α - $[P_2W_{18}O_{62}]^{6-}$ and α - $[H_2W_{12}O_{40}]^{6-}$ as revealed by simulation of cyclic voltammograms. *Analytical chemistry* **1999**, 71 (17), 3650-3656.
11. Baker, L. C.; Glick, D. C., Present general status of understanding of heteropoly electrolytes and a tracing of some major highlights in the history of their elucidation. *Chemical Reviews* **1998**, 98 (1), 3-50.
12. Dong, S.; Xi, X.; Tian, M., Study of the electrocatalytic reduction of nitrite with silicotungstic heteropolyanion. *Journal of Electroanalytical Chemistry* **1995**, 385 (2), 227-233.
13. (a) Himeno, S.; Takamoto, M.; Ueda, T., Synthesis, characterisation and voltammetric study of a β -Keggin-type $[PW_{12}O_{40}]^{3-}$ complex. *Journal of Electroanalytical Chemistry* **1999**, 465 (2), 129-135; (b) Ueda, T.; Kodani, K.; Ota, H.; Shiro, M.; Guo, S.-X.; Boas, J. F.; Bond, A. M., Voltammetric and Spectroscopic Studies of α - and β - $[PW_{12}O_{40}]^{3-}$ Polyoxometalates in Neutral and Acidic Media: Structural Characterization as Their $[(n-Bu_4N)_3][PW_{12}O_{40}]$ Salts. *Inorganic Chemistry* **2017**, 56 (7), 3990-4001.
14. Włodarczyk, R.; Chojak, M.; Miecznikowski, K.; Kolary, A.; Kulesza, P. J.; Marassi, R., Electroreduction of oxygen at polyoxometallate-modified glassy carbon-supported Pt nanoparticles. *Journal of power sources* **2006**, 159 (2), 802-809.
15. (a) Matsui, T.; Morikawa, E.; Nakada, S.; Okanishi, T.; Muroyama, H.; Hirao, Y.; Takahashi, T.; Eguchi, K., Polymer electrolyte fuel cells employing heteropolyacids as redox mediators for oxygen reduction reactions: Pt-free cathode systems. *ACS applied materials & interfaces* **2016**, 8 (28), 18119-18125; (b) Lewera, A.; Chojak, M.; Miecznikowski, K.; Kulesza, P. J., Identification and electroanalytical characterization of redox transitions in solid-state kegggin type phosphomolybdic acid. *Electroanalysis: An International Journal Devoted to Fundamental and Practical Aspects of Electroanalysis* **2005**, 17 (15-16), 1471-1476.
16. Jürgensen, A.; Moffat, J., The stability of 12-molybdosilicic, 12-tungstosilicic, 12-molybdophosphoric and 12-tungstophosphoric acids in aqueous solution at various pH. *Catalysis letters* **1995**, 34 (1), 237-244.
17. (a) Maeda, K.; Himeno, S.; Osakai, T.; Saito, A.; Hori, T., A voltammetric study of Keggin-type heteropolymolybdate anions. *Journal of Electroanalytical Chemistry* **1994**, 364 (1-2), 149-154; (b) Himeno, S.; Takamoto, M.; Ueda, T., Cation effects on the voltammetric behavior of α -Keggin-type $[SiMo_{12}O_{40}]^{4-}$ and $[PMo_{12}O_{40}]^{3-}$ complexes in CH_3COCH_3 and CH_3CN . *Journal of Electroanalytical Chemistry* **2000**, 485 (1), 49-54.
18. Barcza, L.; Pope, M. T., Heteroconjugation of inorganic anions in nonaqueous solvents. III. Complexes of polymolybdates and-tungstates with chloral hydrate. *The Journal of Physical Chemistry* **1975**, 79 (1), 92-93.
19. Ghali, M.; Benlifa, M.; Brahmi, C.; Elbassi, L.; Dumur, F.; Simonnet-Jégat, C.; Bousselmi, L.; Lalevée, J., LED and solar photodecomposition of erythrosine B and rose Bengal using $H_3PMo_{12}O_{40}$ /polymer photocatalyst. *European Polymer Journal* **2021**, 159, 110743.
20. Finke, R. G.; Droege, M. W., Trivacant heteropolytungstate derivatives. 2. Synthesis, characterization, and tungsten-183 NMR of $P_4W_{30}M_4(H_2O)_2O_{112}^{16-}$ (M= Co, Cu, Zn). *Inorganic Chemistry* **1983**, 22 (6), 1006-1008.
21. Liu, J.; Dong, T.; Li, S.; Ma, H.; Liu, B., Fabrication and Properties of a Nanocomposite Multilayer Film Based on a Polyoxometalate. *Zeitschrift für Naturforschung B* **2012**, 67 (7), 673-677.
22. (a) Ciabrini, J.-P.; CONSTANT, R., Mixed heteropolyanions. Synthesis and formation constants of Cerium

- (III) and Cerium (IV) complexes with lacunary tungstophosphates. *Journal of chemical research. Synopses (Print)* **1993**, (10); (b) Gómez-García, C.; Borrás-Almenar, J.; Coronado, E.; Delhaes, P.; Garrigou-Lagrange, C.; Baker, L., Organic-inorganic salts made by TTF and magnetic clusters. *Synthetic metals* **1993**, 56 (1), 2023-2027; (c) Kirby, J.; Baker, L. In *The effect of counterion on electron transfer rates in bridged heteropolyanions: A further limitation on a general method of rate determination*, ABSTRACTS OF PAPERS OF THE AMERICAN CHEMICAL SOCIETY, AMER CHEMICAL SOC 1155 16TH ST, NW, WASHINGTON, DC 20036: 1996; pp 16-INOR; (d) Kirby, J. F.; Baker, L. C., Evaluations of a general NMR method, based on properties of heteropoly blues, for determining rates of electron transfer through various bridges. New mixed-valence complexes. *Journal of the American Chemical Society* **1995**, 117 (40), 10010-10016; (e) Weakley, T. J.; Finke, R. G., Single-crystal X-ray structures of the polyoxotungstate salts $K_{8.3}Na_{1.7}[Cu_4(H_2O)_2(PW_9O_{34})_2] \cdot 24H_2O$ and $Na_{14}Cu[Cu_4(H_2O)_2(P_2W_{15}O_{56})_2] \cdot 53H_2O$. *Inorganic Chemistry* **1990**, 29 (6), 1235-1241; (f) Zhang, X.; Anderson, T. M.; Chen, Q.; Hill, C. L., A Baker-Figgis Isomer of Conventional Sandwich Polyoxometalates. $H_2Na_{14}[Fe^{III}_2(NaOH_2)_2(P_2W_{15}O_{56})_2]$, a Diiron Catalyst for Catalytic H_2O_2 -Based Epoxidation. *Inorganic Chemistry* **2001**, 40 (3), 418-419; (g) Zhang, X.; Chen, Q.; Duncan, D. C.; Campana, C. F.; Hill, C. L., Multiiron Polyoxoanions. Syntheses, Characterization, X-ray Crystal Structures, and Catalysis of H_2O_2 -Based Hydrocarbon Oxidations by $[Fe^{III}_4(H_2O)_2(P_2W_{15}O_{56})_2]^{12-}$. *Inorganic Chemistry* **1997**, 36 (19), 4208-4215.
23. (a) Baker, L. In *Plenary Lecture*, Proc. XV Int. Conf. on Coordination Chemistry proceedings, Moscow, 1973; (b) Lyon, D. K.; Miller, W. K.; Novet, T.; Domaille, P. J.; Evitt, E.; Johnson, D. C.; Finke, R. G., Highly oxidation resistant inorganic-porphyrin analog polyoxometalate oxidation catalysts. 1. The synthesis and characterization of aqueous-soluble potassium salts of α_2 - $P_2W_{17}O_{61} (M^{n+}OH_2)^{(n-10)}$ and organic solvent soluble tetra-n-butylammonium salts of α_2 - $P_2W_{17}O_{61} (M^{n+}Br)^{(n-11)}$ ($M = Mn^{3+}, Fe^{3+}, Co^{2+}, Ni^{2+}, Cu^{2+}$). *Journal of the American Chemical Society* **1991**, 113 (19), 7209-7221.
24. Mughal, N. S.; Walsh, D. A.; Newton, G. N., Functionalization of Carbon Surfaces Tunes the Redox Stability of Polyoxometalate@ Carbon Electrodes. *ACS Applied Energy Materials* **2020**, 3 (12), 12308-12315.
25. Belhouari, A.; Keita, B.; Nadjio, L.; Contant, R., Efficient conversion of NO into N_2O by selected electroreduced heteropolyanions. *New Journal of Chemistry* **1998**, 22 (2), 83-86.
26. (a) Kakhki, S.; Shams, E.; Barsan, M. M., Fabrication of carbon paste electrode containing a new inorganic-organic hybrid based on $[SiW_{12}O_{40}]^{4-}$ polyoxoanion and Nile blue and its electrocatalytic activity toward nitrite reduction. *Journal of Electroanalytical Chemistry* **2013**, 704, 80-85; (b) Khadro, B.; Baroudi, I.; Goncalves, A.-M.; Berini, B.; Pegot, B.; Nouar, F.; Le, T. N. H.; Ribot, F.; Gervais, C.; Carn, F., Interfacing a heteropolytungstate complex and gelatin through a coacervation process: design of bionanocomposite films as novel electrocatalysts. *Journal of Materials Chemistry A* **2014**, 2 (24), 9208-9220; (c) Li, S.; Ma, H.; Pang, H.; Zhang, L.; Zhang, Z.; Lin, H., The first 3D POMOF based on α -metatungstate and mixed-ligand. *Inorganic Chemistry Communications* **2014**, 44, 15-19; (d) Wang, C.-J.; Yao, S.; Chen, Y.-Z.; Zhang, Z.-M.; Wang, E.-B., Assembly of polyoxometalates and Ni-bpy cationic units into the molecular core-shell structures as bifunctional electrocatalysts. *RSC advances* **2016**, 6 (101), 99010-99015; (e) Zhang, P.; Peng, J.; Shen, X.; Han, Z.; Tian, A.; Pang, H.; Sha, J.; Chen, Y.; Zhu, M., A twofold interpenetrating framework based on the α -metatungstates. *Journal of Solid State Chemistry* **2009**, 182 (12), 3399-3405; (f) Zhang, Z.; Sun, X.; Ma, H.; Pang, H.; Li, S.; Zhao, C., Two hybrid compounds constructed from Ni-tris(imidazolyl) complexes and Keggin clusters: Syntheses, structures and electrochemical properties. *Journal of Molecular Structure* **2016**, 1116, 174-179.
27. Flores-Santana, W.; Salmon, D. J.; Donzelli, S.; Switzer, C. H.; Basudhar, D.; Ridnour, L.; Cheng, R.; Glynn, S. A.; Paolucci, N.; Fukuto, J. M., The specificity of nitroxyl chemistry is unique among nitrogen oxides in biological systems. *Antioxidants & redox signaling* **2011**, 14 (9), 1659-1674.
28. (a) Duca, M.; Van Der Klugt, B.; Hasnat, M.; Machida, M.; Koper, M., Electrocatalytic reduction of nitrite on a polycrystalline rhodium electrode. *Journal of Catalysis* **2010**, 275 (1), 61-69; (b) Duca, M.; Kavvadia, V.;

- Rodriguez, P.; Lai, S.; Hoogenboom, T.; Koper, M., New insights into the mechanism of nitrite reduction on a platinum electrode. *Journal of Electroanalytical Chemistry* **2010**, *649* (1-2), 59-68.
29. Johnson, D. P., Spectrophotometric determination of oximes and unsubstituted hydroxylamine. *Analytical Chemistry* **1968**, *40* (3), 646-648.
30. Costentin, C.; Passard, G.; Savéant, J.-M., Benchmarking of homogeneous electrocatalysts: Overpotential, turnover frequency, limiting turnover number. *Journal of the American Chemical Society* **2015**, *137* (16), 5461-5467.
31. Kozuch, S.; Martin, J. M., "Turning over" definitions in catalytic cycles. ACS Publications: 2012; Vol. 2, pp 2787-2794.
32. Alam, M. S.; Rahman, M. M.; Marwani, H. M.; Hasnat, M. A., Insights of temperature dependent catalysis and kinetics of electro-oxidation of nitrite ions on a glassy carbon electrode. *Electrochimica Acta* **2020**, *362*, 137102.
33. Xing, X.; Wang, M.; Liu, R.; Zhang, S.; Zhang, K.; Li, B.; Zhang, G., Highly efficient electrochemically driven water oxidation by graphene-supported mixed-valent Mn₁₆-containing polyoxometalate. *Green Energy & Environment* **2016**, *1* (2), 138-143.
34. Bartberger, M. D.; Liu, W.; Ford, E.; Miranda, K. M.; Switzer, C.; Fukuto, J. M.; Farmer, P. J.; Wink, D. A.; Houk, K. N., The reduction potential of nitric oxide (NO) and its importance to NO biochemistry. *Proceedings of the National Academy of Sciences* **2002**, *99* (17), 10958-10963.
35. Eberhardt, M.; Dux, M.; Namer, B.; Miljkovic, J.; Cordasic, N.; Will, C.; Kichko, T. I.; De La Roche, J.; Fischer, M.; Suárez, S. A., H₂S and NO cooperatively regulate vascular tone by activating a neuroendocrine HNO–TRPA1–CGRP signalling pathway. *Nature communications* **2014**, *5* (1), 1-17.
36. Suarez, S. A.; Muñoz, M.; Alvarez, L.; Venâncio, M. F.; Rocha, W. R.; Bikiel, D. E.; Martí, M. A.; Doctorovich, F., HNO Is Produced by the Reaction of NO with Thiols. *Journal of the American Chemical Society* **2017**, *139* (41), 14483-14487.
37. Suarez, S. A.; Neuman, N. I.; Muñoz, M.; Álvarez, L. a.; Bikiel, D. E.; Brondino, C. D.; Ivanović-Burmazović, I.; Miljkovic, J. L.; Filipovic, M. R.; Martí, M. A., Nitric oxide is reduced to HNO by proton-coupled nucleophilic attack by ascorbate, tyrosine, and other alcohols. A new route to HNO in biological media? *Journal of the American Chemical Society* **2015**, *137* (14), 4720-4727.

Chapter III: Nitrite electroreduction catalyzed by a series of Keggin polyoxometalates and Ag materials

3.1 Introduction

Transition metals have been tested for nitrite reduction, displaying different behaviors. For example, noble metals (Pt, Ru, Pd, Rh, Ir)¹ are catalyzing the reduction of HNO₂ to hydrogenated species while coinage metals (Cu, Ag, Au) are catalyzing the reduction of HNO₂ to NO and the subsequent conversion of NO to N₂O.^{1b, 1d, 2} Nitric oxide reduction on transition-metal electrodes was also investigated by online electrochemical mass spectrometry (OLEMS). When NO is available in the solution phase, the mechanism involves the combination of a surface-bonded NO to a dissolved NO with a simultaneous proton-electron transfer. The assumed intermediate is a dimer, HN₂O_{2, ads} and its formation is the rate determining step. The product obtained via this mechanism is mainly N₂O. The formation of NH₃ requires only the reduction of a surface-bonded NO and takes place only in the low potential range. It is worth to mention here that polycrystalline silver was not tested in these OLEMS studies. The formation of NO dimer from loosely bounded NO on silver has been documented both by experimental and theoretical studies³.

In chapter 3, it has been discussed the influence of the redox properties of four different Keggin type POMs on the electrochemical reduction of nitrous acid. With help of the differential electrochemical mass spectrometry (DEMS) it was observed that, as long as the POM is in a one electron reduced state (POM¹⁻), nitrous acid is electroreduced to NO. Moreover, N₂O formation is correlated to NO consumption, suggesting that the second electron reduced POM²⁻ is able to convert aqueous NO into N₂O, probably via an HNO intermediate.

In this chapter, the studied POMs [H₂W₁₂O₄₀]⁶⁻, [BW₁₂O₄₀]⁵⁻, [SiW₁₂O₄₀]⁴⁻ and [PW₁₂O₄₀]³⁻ are accompanied by Ag electrode to form a mixed homogeneous-heterogeneous catalysis. The purpose is to search a possible synergy between POMs and silver for nitrite reduction. The motivation of this study was to make a bridge between studies of POMs alone and the results reported for metallic catalysts. The choice of silver electrode is justified by the well-known interaction between POMs and this metal. In detail, different POMs have been used as reducing agent and stabilizer in the synthesis of silver nanoparticles. Several reports describe the formation of Ag nanoparticles capped by POMs, denoted Ag@POM. For example, as early as 1952, [PW₁₂O₄₀]³⁻ was used to reduce silver ions to metallic silver.⁴ In 2001, Keggin POMs [PW₁₂O₄₀]³⁻ and [SiW₁₂O₄₀]⁴⁻ as well as Dawson [P₂Mo₁₈O₆₂]⁶⁻ were used for the photocatalytic recovery of different metals ions.⁵ In 2022, the study was completed by the addition of more POMs and especially by the possibility of obtaining metallic nanoparticles.⁶ During the photoreduction of POM, propan-2-ol or 2,4-dichlorophenol are electrons donor. The surface of Ag nanoparticles is covered by POMs and the charge repulsion between these anions prevents the agglomeration of nanoparticles.⁷ Our group has also shown the formation of silver nanoparticles with two isomers of the tetracobalt Dawson-derived sandwich complexes, *αββα*-Na₁₇[Co₄(H₂O)(OH)(P₂W₁₅O₅₆)₂] and *ααβα*-Na₁₆[Co₄(H₂O)₂(OH)(P₂W₁₅O₅₆)₂].⁸ Despite this, there is no report about nitrite reduction catalyzed by Ag NPs stabilized by POMs. Thus, in the second part of this chapter,

we have used Ag@POM nanoparticles as homogeneous catalysts for nitrite reduction. The nanoparticles are used directly after their synthesis, meaning they are dispersed in solution. In a future work, they will be immobilized on an inert electrode, such as a glassy carbon electrode.

3.2 Cyclic voltammetry studies

The electrochemical properties of $[\text{SiW}_{12}\text{O}_{40}]^{4-}$, $[\text{BW}_{12}\text{O}_{40}]^{5-}$, and $[\text{H}_2\text{W}_{12}\text{O}_{40}]^{6-}$ in solution with silver as a bulk working electrode were studied by cyclic voltammetry at different pH values. Because Ag electrode has also a certain activity for the electroreduction of nitrite, we have conducted also experiments using only this electrode alone.

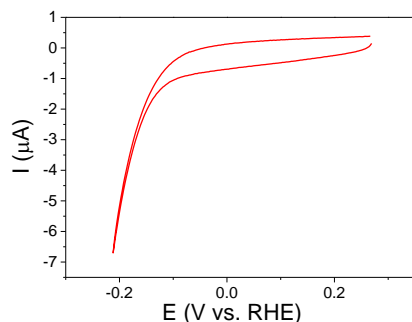
3.2.1 Electrochemical properties of Ag electrode

Cyclic voltammograms of Ag electrode alone are displayed in Figure 3.2.1. The range of potential is limited from 0.30 to -0.40 V *vs.* RHE (pH 1, pH 2 and pH 5) to avoid electrode oxidation. At pH 1, Ag electrode has an electric double layer current of 0.5 μA until the potential is about -0.2 V *vs.* RHE, when the current intensity increases rapidly due to the hydrogen evolution reaction (HER) (Figure 3.2.1a). Upon addition of different concentration of nitrite, the current intensity increases in the entire potential range as reported previously.^{1d} It must be noted that nitrite reduction was previously studied at polycrystalline electrode using a perchlorate based electrolyte. Adsorption of sulfate anions on silver electrode is potential dependent, being more obvious in the region where electrode oxidation appears.⁹ Also, Ag (111) facets are more prone to sulfate poisoning than other orientations.¹⁰ Our DEMS analysis will show how this phenomenon impacts nitrite reduction. From CV analysis alone, the onset potential of the catalytic reduction ($E_{\text{Nitrite onset}}$) is defined at the potential where $|I_{\text{absence of nitrite}} - I_{\text{HNO}_2/\text{NO}_2}| = 0.5 \mu\text{A}$ (in the presence of 1 mM of $\text{HNO}_2/\text{NO}_2^-$ in the solution). The onset potential is more positive than 0.260 V *vs.* RHE at pH 1 (beginning of the CV), -0.078 V *vs.* RHE at pH 2 and -0.263 V *vs.* RHE at pH 5. The onset potential of HER ($E_{\text{HER onset}}$) is defined at the potential where the $|I_{\text{HER}} - I_{\text{Electric double layer}}| = 0.5 \mu\text{A}$ in the absence of nitrite solution. In this way, it can be observed that, at each pH, there is a potential range between $E_{\text{Nitrite onset}}$ and $E_{\text{HER onset}}$ where the reduction current is specific to nitrite reduction. At pH 1, it's from 0.260 to -0.130 V *vs.* RHE, at pH 2, it's from -0.078 to -0.200 V *vs.* RHE. However, at pH 5, $E_{\text{Nitrite onset}}$ is more negative than $E_{\text{HER onset}}$. These values are summarized in Table 3.2.1.

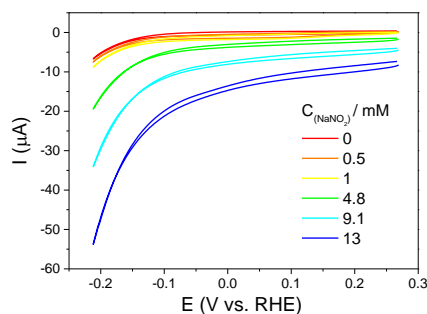
Table 3.2.1 Summary of hydrogen evolution onset potential and nitrite reduction onset potential at different pH values using Ag as working electrode.

pH	Onset of hydrogen evolution ($E_{\text{HER-onset}}$ / V vs. RHE)	Onset of nitrite reduction ($E_{\text{Nitrite onset}}$ / V vs. RHE)	Selectivity for nitrite reduction
1	-0.130	> 0.260	Yes
2	-0.200	-0.078	Yes
5	-0.240	-0.263	No

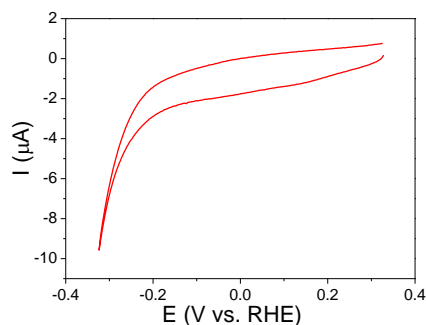
a) pH 1, in absence of nitrite



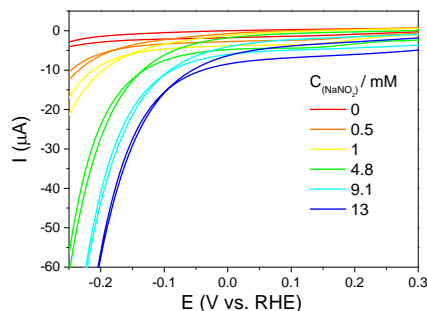
b) pH 1, nitrite additions



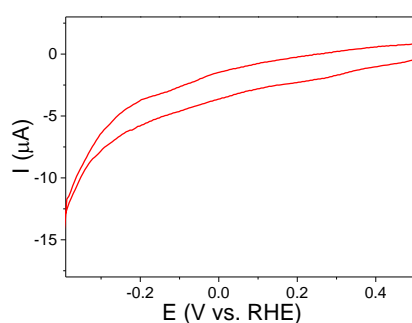
c) pH 2, in absence of nitrite



d) pH 2, nitrite additions



e) pH 5, in absence of nitrite



f) pH 5, nitrite additions

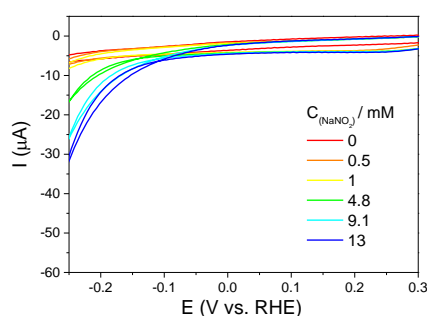
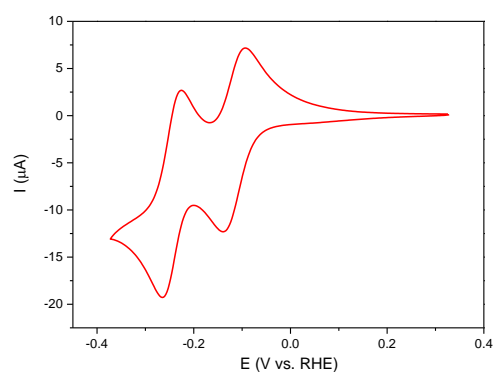


Figure 3.2.1 Cyclic voltammetry of Ag electrode in the absence and in the presence of different concentrations of nitrite at pH 1, pH 2 and pH 5. Experimental conditions: scan rate, 20 mVs^{-1} ; electrolyte: a) and b) $0.5 \text{ M Na}_2\text{SO}_4$ pH 1; c) and d) $0.5 \text{ M Na}_2\text{SO}_4$ pH 2; e) and f) $1 \text{ M CH}_3\text{COOLi}$ pH 5.

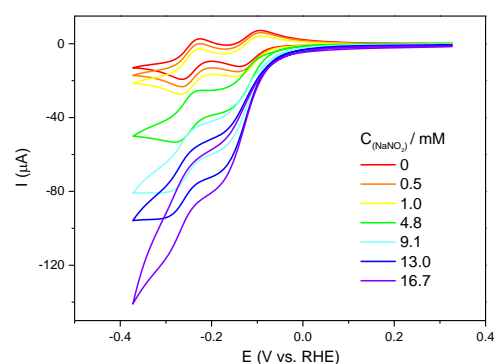
3.2.2 Electrochemical and electrocatalytic properties of POMs on Ag electrode

The electrochemical properties of $[\text{H}_2\text{W}_{12}\text{O}_{40}]^{6-}$ (Figure 3.2.2), $[\text{BW}_{12}\text{O}_{40}]^{5-}$ (Figure 3.2.3), $[\text{SiW}_{12}\text{O}_{40}]^{4-}$ (Figure 3.2.4) and $[\text{PW}_{12}\text{O}_{40}]^{3-}$ (Figure 3.2.5) in solution using silver bulk as a working electrode were studied with cyclic voltammetry at different pH values, both in the absence and in the presence of different concentrations of nitrite. In order to avoid HER, the potential range is limited. As a consequence, for $[\text{BW}_{12}\text{O}_{40}]^{5-}$, $[\text{SiW}_{12}\text{O}_{40}]^{4-}$ and $[\text{PW}_{12}\text{O}_{40}]^{3-}$ the second or third wave respectively are not visible. The formal potential of the waves is recorded in Table 3.2.2. The values are similar to those obtained when glassy carbon is used as a working electrode (chapter 2). The number of electrons of each redox process is the same. For example, $[\text{H}_2\text{W}_{12}\text{O}_{40}]^{6-}$ still displays two waves which overlap at pH 2 and divide into two one-electron waves at pH 5. Experiments with increasing concentration of nitrite were performed at pH 2 and pH 5. The onset potentials of nitrite reduction are summarized in Table 3.2.3. Except when $[\text{PW}_{12}\text{O}_{40}]^{3-}$ and $[\text{SiW}_{12}\text{O}_{40}]^{4-}$ are used, the onset potential slightly shifts positively when compared with the case when GC is the working electrode and POMs are in solution. The difference might not be significant. When compared to the use of Ag alone, the onset potentials are significantly more positive, except for $[\text{H}_2\text{W}_{12}\text{O}_{40}]^{6-}$ for which the values are similar (i.e. -0.078 V *vs.* RHE for Ag alone and -0.038 V *vs.* RHE for $[\text{H}_2\text{W}_{12}\text{O}_{40}]^{6-}$). This indicates that the reaction catalyzed by POMs, i.e. nitrite reduction, happens in a potential range where Ag electrode is not acting as a catalyst. This potential range corresponds to the first wave of each POM.

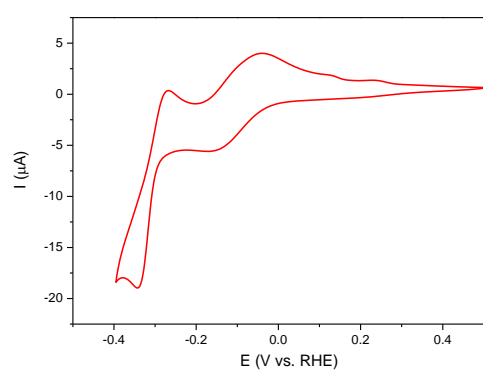
a) pH 2 in absence of nitrite



b) pH 2 nitrite additions



c) pH 5 in absence of nitrite



d) pH 5 nitrite additions

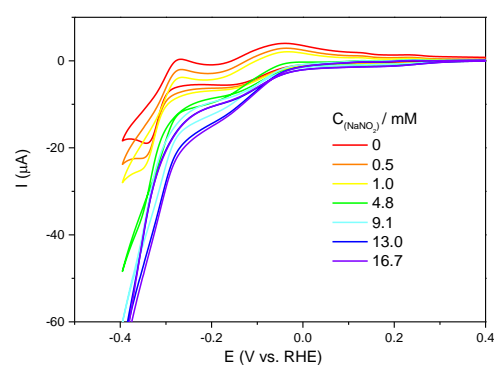
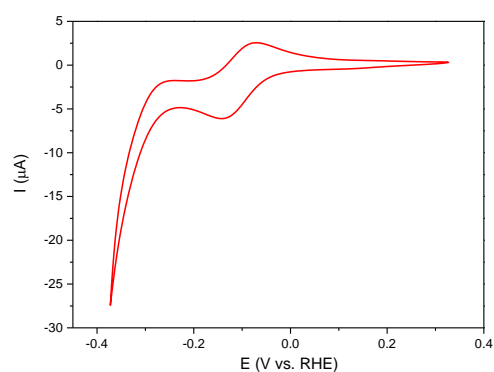
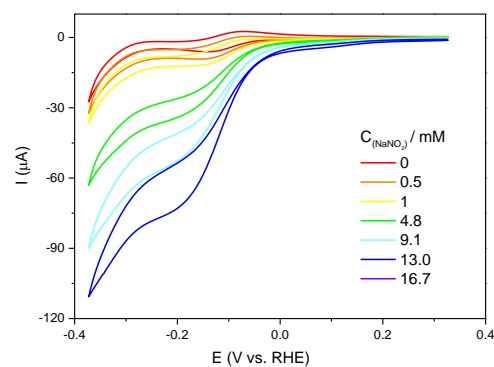


Figure 3.2.2 Cyclic voltammetry of $[\text{H}_2\text{W}_{12}\text{O}_{40}]^{6-}$ on Ag electrode at a) pH 2 and c) pH 5 in the absence of nitrite and b) and d) for different concentrations of nitrite. Experimental conditions: working electrode, Ag; scan rate, 20 mVs^{-1} ; 1 mM POM; electrolyte: a) and b) 0.5 M Na_2SO_4 pH 2; c) and d) 0.5 M CH_3COOLi pH 5.

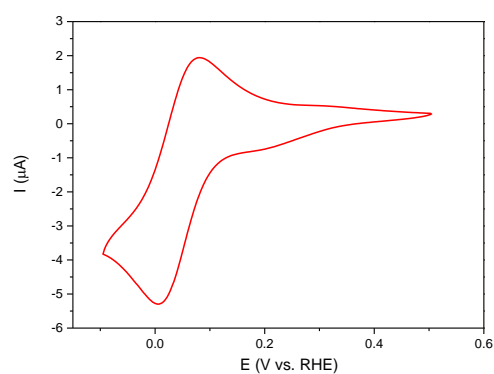
a) pH 2 in absence of nitrite



b) pH 2 nitrite additions



c) pH 5 in absence of nitrite



d) pH 5 nitrite additions

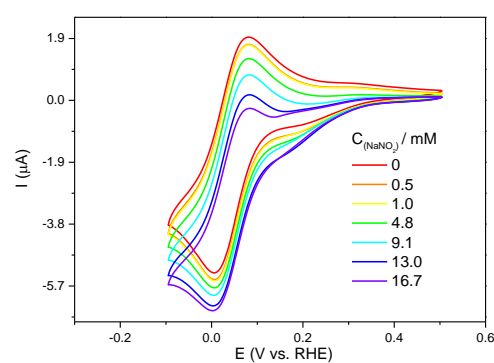
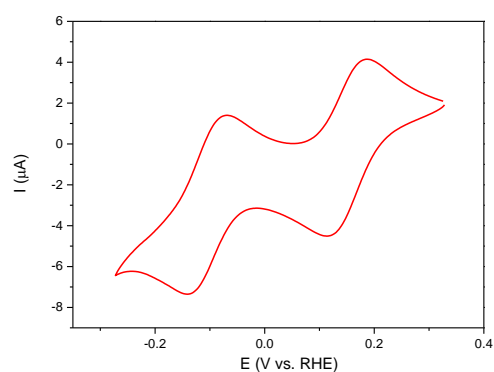
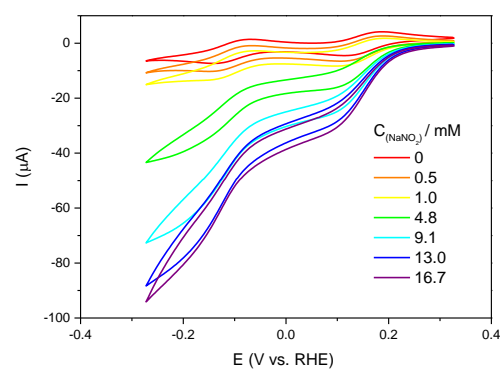


Figure 3.2.3 Cyclic voltammetry of $[\text{BW}_{12}\text{O}_{40}]^{5-}$ on Ag electrode at a) pH 2 and c) pH 5 in the absence of nitrite and b) and d) for different concentrations of nitrite. Experimental conditions: working electrode, Ag; scan rate, 20 mVs^{-1} ; 1 mM POM; electrolyte: a) and b) $0.5 \text{ M Na}_2\text{SO}_4$ pH 2; c) and d) $0.5 \text{ M CH}_3\text{COOLi}$ pH 5.

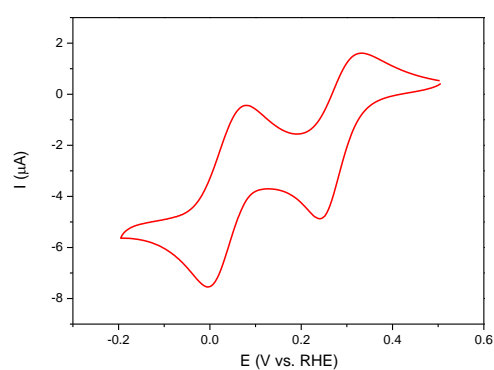
a) pH 2 in absence of nitrite



b) pH 2 nitrite additions



c) pH 5 in absence of nitrite



d) pH 5 nitrite additions

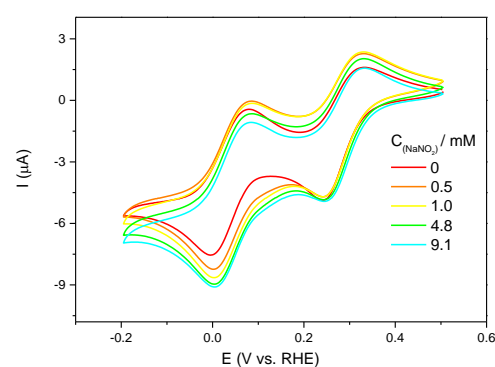
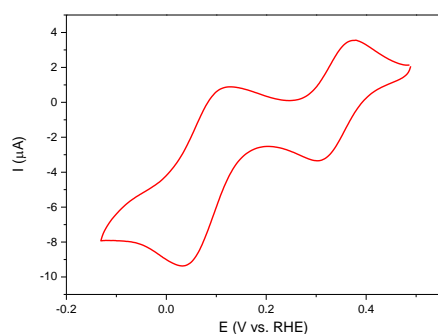


Figure 3.2.4 Cyclic voltammetry of $[\text{SiW}_{12}\text{O}_{40}]^{4-}$ on Ag electrode at a) pH 2 and c) pH 5 in the absence of nitrite and b) and d) for different concentrations of nitrite. Experimental conditions: working electrode, Ag; scan rate, 20 mVs^{-1} ; 1 mM POM; electrolyte: a) and b) 0.5 M Na_2SO_4 pH 2; c) and d) 0.5 M CH_3COOLi pH 5.

a) pH 1 in absence of nitrite



b) pH 1 nitrite additions

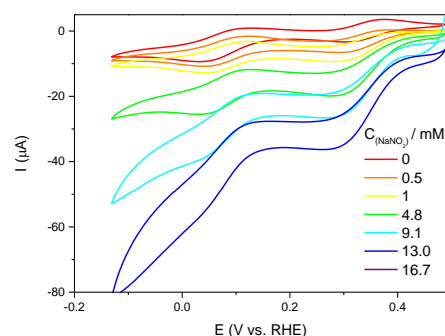


Figure 3.2.5 Cyclic voltammetry of $[\text{PW}_{12}\text{O}_{40}]^{4-}$ on Ag electrode at pH 1: a) in the absence of nitrite and b) for different concentrations of nitrite. Experimental conditions: working electrode, Ag; scan rate, 20 mVs^{-1} ; 1 mM POM; electrolyte, 0.5 M Na_2SO_4 .

Table 3.2.2 Details of redox behavior of studied POMs with Ag electrode: apparent formal potential and number of electrons¹¹ for each wave for all studied POMs.

pH	POM	$E^0/\text{V vs. RHE}$ (no. of electrons)		
		I st wave	II nd wave	III rd wave
pH 1	$[\text{PW}_{12}\text{O}_{40}]^{3-}$	0.315 ($1e^-$)	-0.036 ($1e^-$)	-
	$[\text{H}_2\text{W}_{12}\text{O}_{40}]^{6-}$	- 0.139 ($2e^-$)	- 0.262 ($2e^-$)	-
pH 2	$[\text{BW}_{12}\text{O}_{40}]^{5-}$	- 0.140 ($1e^-$)	-	-
	$[\text{SiW}_{12}\text{O}_{40}]^{4-}$	0.114 ($1e^-$)	-0.142 ($1e^-$)	-
pH 5	$[\text{H}_2\text{W}_{12}\text{O}_{40}]^{6-}$	-0.162 ($2e^-$)	- 0.343 ($2e^-$)	-
	$[\text{BW}_{12}\text{O}_{40}]^{5-}$	0.00 ($1e^-$)	-	-
	$[\text{SiW}_{12}\text{O}_{40}]^{4-}$	0.24 ($1e^-$)	-0.004 ($1e^-$)	-

Table 3.2.3 Onset potential of nitrite reduction catalyzed by different Keggin POMs and Ag electrode at different pH. (*: the catalytic current is lower than the standard $|I_{\text{POM}} - I_{\text{HNO}_2/\text{NO}_2}| = 0.5 \mu\text{A}$). (Red: positive shift compared with GC electrode; Blue: negative shift compared with GC electrode)

Electrode	Onset potential of nitrite reduction (and potential shift with respect to GC electrode) (V vs. RHE)		
	pH 1	pH 2	pH 5
Ag electrode only	0.260	-0.078	-0.253
$[\text{H}_2\text{W}_{12}\text{O}_{40}]^{6-}$	-	-0.038 (0.013)	-0.012 (0.096)
$[\text{BW}_{12}\text{O}_{40}]^{5-}$	-	0.123 (0.047)	*
$[\text{SiW}_{12}\text{O}_{40}]^{4-}$	-	0.177 (-0.048)	*
$[\text{PW}_{12}\text{O}_{40}]^{3-}$	0.408 (-0.046)	-	-

3.3 DEMS studies of nitrite reduction

3.3.1 Catalysis by Ag electrode alone

OLEMS (on-line electrochemical mass spectrometry) was previously used to characterize nitrite reduction catalyzed by noble metals (see chapter 1) but only at pH 2 and using perchloric acid as electrolyte.^{1a, 1b, 1d, 12} As mentioned by several authors, perchlorate anions are the least adsorbed on metals, compare to other anions such as sulfate¹³. For this reason, our DEMS results are quite different than the reported OLEMS results. Figure 3.3.1 shows OLEMS data for nitrite reduction catalyzed by bulk silver electrode. The onset potential of NO formation is about 0.1 V vs. RHE and the maximum of the signal is reached at -0.2 V vs. RHE. Below to this value, the signal starts to decrease. This corresponds to the onset of HER, indicated by the dash dotted line. The onset of N₂O formation is -0.1 V vs. RHE

Our DEMS results using Ag electrode at pH 2 are presented in Figure 3.3.2. In Figure 3.3.2a, the m/z signal corresponding to molecular hydrogen was also followed (green curve). The most striking observation is for the signal of NO for which only a decrease, compared to the baseline is observed. In other words, **the formation of NO is not observed**. The coupling between the consumption of NO and the formation of N₂O is visible in Figure 3.3.2b where different concentrations of nitrite have been used. The onset potential of N₂O becomes more positive as the concentration of nitrite increases (Nernstian behavior). It must be noted that in Figure 3.3.2b **some NO formation is observed** when the NaNO₂ concentration is 10 mM. In fact, after repeating this experiment, the conclusion is that the amount of NO formed from the reduction of HNO₂ at pH 1 or pH 2 is very little. Moreover, at these pH values, the amount of NO coming from the disproportionation of HNO₂ is quite high. For this reason, the signal of NO formation is small and difficult to be observed.

A second difference is the onset of hydrogen formation for which a more negative potential, i.e. -0.4 V vs. RHE is observed. While sulfate adsorption can partially explain this, another explanation is the experimental setup used in our case. Indeed, the thin layer design with a long distance between the electrode and the membrane could delay the detection of hydrogen gas, thus inducing false “more negative” onset potential. Despite this, another difference is that the signal of N₂O is not decreasing in the same time as the formation of hydrogen.

A possible reason that could explain these differences is the catalyzed reaction which is not the same. In OLEMS data^{1d}, as explained by the authors, silver is reducing nitrous acid (HNO₂) to NO (hence NO formation is observed). Subsequently, NO is reduced to N₂O, probably via the formation of an adsorbed intermediate HN₂O₂ (see Equation 3.3.1).¹⁴ In our data, NO formation is difficult to be observed. **Thus, HNO₂ direct reduction is heavily hindered in the presence of sulfate anions while the subsequent NO reduction to N₂O is more visible** (the source of NO is the disproportionation of HNO₂).

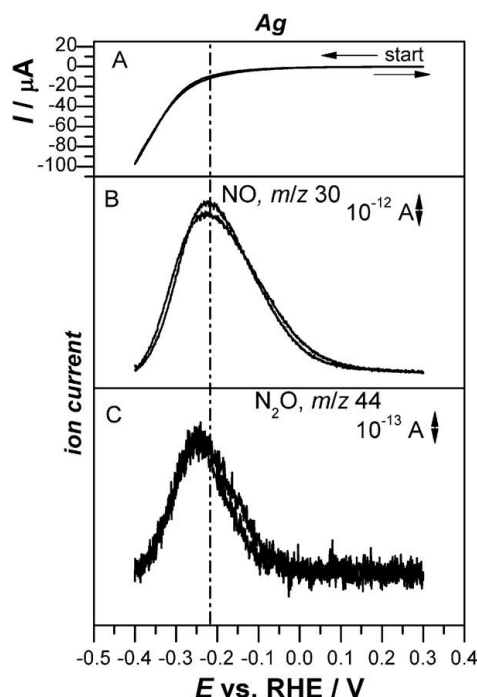
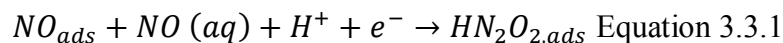
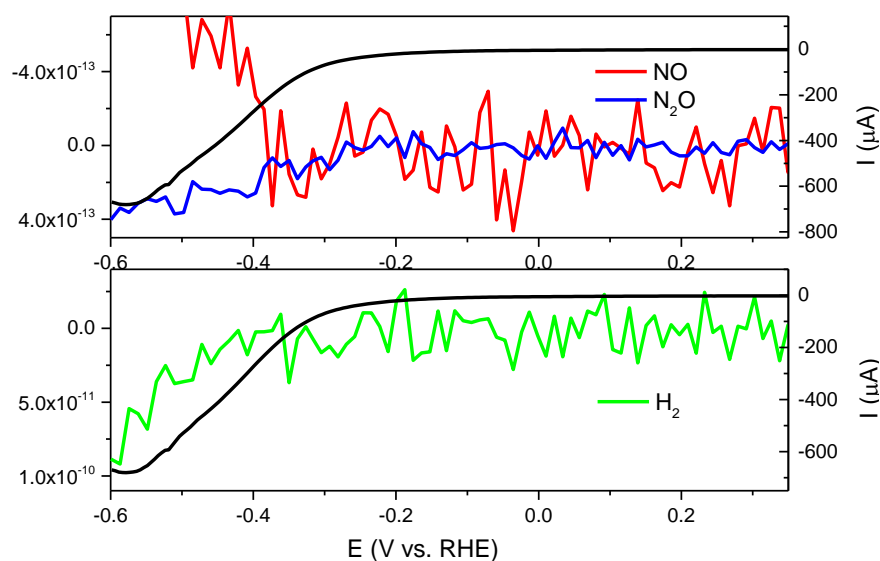


Figure 3.3.1 Cyclic voltammetry during OLEMS measurements (A) and ion current profiles for $m/z = 30$ (B) and $m/z = 44$ (C) in 0.1 M HClO_4 containing 1.6 mM NaNO_2 . The working electrode is a polycrystalline Ag bead electrode, $v = 1 \text{ mVs}^{-1}$. The dashed dotted line indicates the onset potential for hydrogen evolution. The arrows indicate the direction of the potential sweep.^{1d}

The potential of NO consumption is about -0.20 V. This is close to the onset potential obtained from CV measurements (-0.078 V in Table 3.3.1) at pH 2. We have called this the onset potential of nitrite reduction, but DEMS data indicate that, in fact, it is the onset potential of nitric oxide (NO) reduction to N_2O . As nitrite concentration increases, so the concentration of NO issued from the disproportionation is increasing. Thus, the total reduction current from the CV experiments is increasing (Figure 2.2.1d), and the onset potential of nitric oxide reduction is more positive (Figure 3.3.2b, Nernstian behavior).

a)



b)

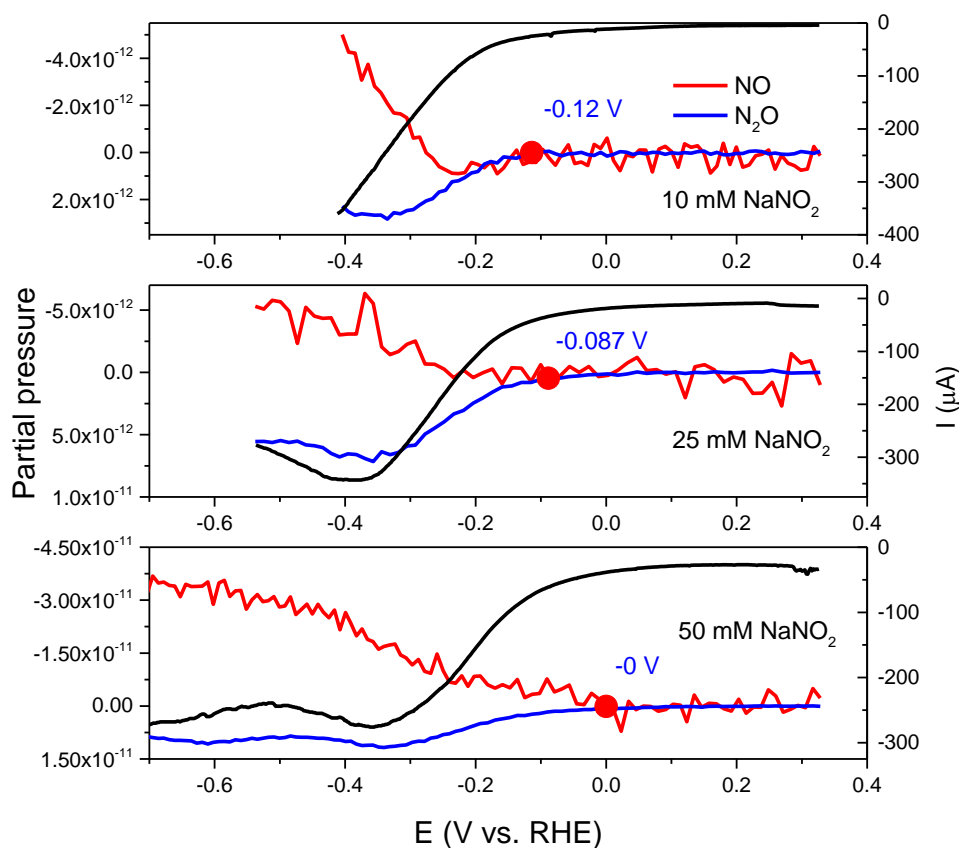


Figure 3.3.2 DEMS study of nitrite reduction catalyzed by Ag electrode alone at pH 2. a) 10 mM NaNO₂; b) Different concentration of nitrite (10 mM, 25 mM and 50 mM). Black curve: the forward scan of cyclic voltammetry (0.5 mVs⁻¹); Red curve: the signal of m/z 31 (¹⁵NO); Blue curve: the signal of m/z 46 (¹⁵N₂O); Green curve: the signal of m/z 2 (H₂); Electrolyte: 0.5 M Na₂SO₄.

The influence of pH was studied (Figure 3.3.3). Taken into account the pK_a of nitrous acid (3.3), the ratio of $\text{HNO}_2/\text{NO}_2^-$ is constantly changing between pH 1 to pH 5. Moreover, the disproportionation of HNO_2 is pH dependent, being more intense at low pH. As a consequence, the amount of NO in solution is very pH dependent. Based on our findings, and using also data from literature, the following observations can be made:

- at pH 1, when using sulfate as electrolyte, Ag electrode is preferentially catalyzing the reduction of NO to N_2O (the direct reduction of HNO_2 to NO is barely observed).
- at pH 2 and pH 3, the amount of NO in solution is lower than at pH 1. A shift towards negative value for the NO reduction should be observed. DEMS data in Figure 3.3.3 indicate very similar potentials of NO consumption (around -0.2 V vs. RHE) and N_2O formation, probably due to a lack of sensitivity.
- from pH 4 to pH 5, the catalyzed reaction gradually changes to NO_2^- reduction. At pH 5, the DEMS data are noisy because the amount of NO and N_2O gaseous species is very low. For this reason, the measured potentials are less precise. The gaseous N_2O observed is most probably a minor species, as the reaction mechanism changes towards the formation of ammonia.^{1d}

Table 3.3.1 Summary of different potentials of nitrite reduction using Ag electrode at different pH values. Data are extracted from Figure 3.3.3

pH	Onset potential obtained from CV (E / V vs. RHE)	NO formation potential (E / V vs. RHE)	NO consumption potential (E / V vs. RHE)	N_2O onset potential (E / V vs. RHE)
1	-0.13	Not observed	-0.2	-0.25
2	-0.078	-0.150*	-0.2	-0.18
3	n.d.	Not observed	-0.2	-0.2
4	n.d.	Not observed	-0.3	-0.22
5	-0.24	Not observed	-0.4	-0.35

n.d. not determined; * very difficult to be observed

If a comparison is made with the onset potentials obtained from cyclic voltammetry, it can be observed that the values of NO consumption obtained from DEMS data are more negative. This is somewhat expected, as the consumption of NO appears only after some time required to consume the initial amount of NO existing in the solution before the start of the experiment. Here again, DEMS data are useful to comfort the values obtained from CV, while still adding a supplementary information about the reaction mechanism.

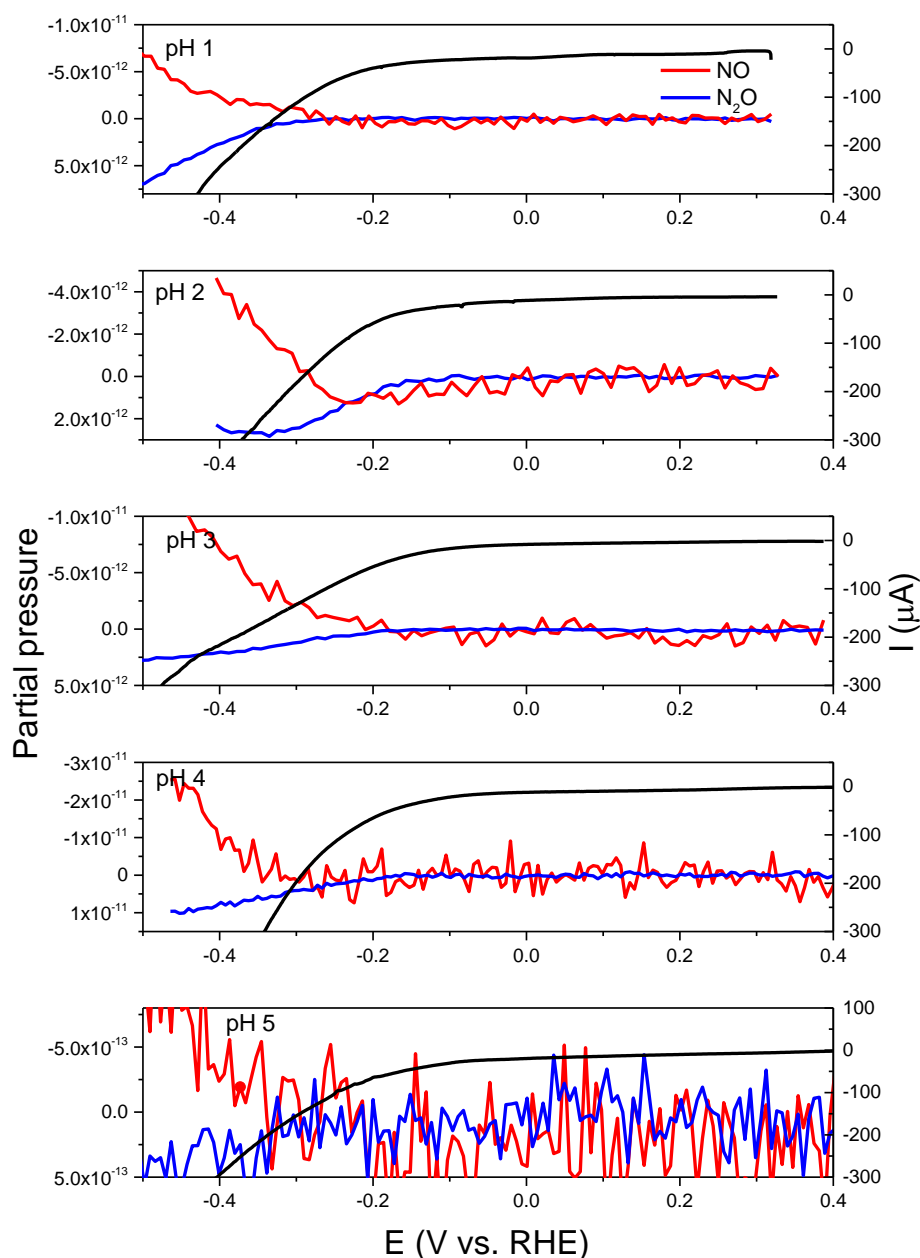


Figure 3.3.3 DEMS study of nitrite reduction using Ag electrode at different pH values (from pH 1 to pH 5). Black curve: the forward scan of cyclic voltammetry (0.5 mVs^{-1}); Red curve: the signal of m/z 31 (^{15}NO); Blue curve: the signal of m/z 46 ($^{15}\text{N}_2\text{O}$). Electrolyte: a) pH 1, $0.5 \text{ M Na}_2\text{SO}_4$; b) pH 2, $0.5 \text{ M Na}_2\text{SO}_4$; c) pH 3, $0.3 \text{ M Na}_3\text{C}_6\text{H}_5\text{O}_7$; d) pH 4, $1 \text{ M CH}_3\text{COOLi}$; e) pH 5 $1 \text{ M CH}_3\text{COOLi}$; $10 \text{ mM Na}^{15}\text{NO}_2$.

3.3.2 Catalysis by Keggin POMs and Ag electrode

DEMS analysis including POMs and silver electrode was run in $0.5 \text{ M Na}_2\text{SO}_4$ at pH 1, pH 2 and pH 5 electrolyte and results are shown in Figure 3.3.4, 3.3.5 and 3.3.6 respectively. Anions adsorption can easily modify the activity of metals towards reduction of different

species, such as HNO_2 , HNO_3 or even NO .^{1a, 1d, 12, 15} By choosing our electrolyte Na_2SO_4 , we have deliberately diminished the HNO_2 reduction on silver electrode, allowing only the contribution of homogeneous catalysis sustained by POMs.

At pH 1, a small signal of NO formation is observed for all POMs, while the signal is more obvious for $[\text{PW}_{12}\text{O}_{40}]^{3-}$. For this POM, the NO formation is visible directly from the beginning of the CV, suggesting that this POM is very active for nitrite reduction (black curve in Figure 3.3.4). The onset potential of NO formation is summarized in Table 3.3.2, together with the shift compared to the values obtained when glassy carbon is the working electrode and the POMs are in solution (homogenous catalysis). No significantly different values are obtained. This comforts the hypothesis that in the mixed system (silver and POMs in solution) only POMs are active for the reduction of HNO_2 to NO. The same conclusions are drawn for DEMS data at pH 2 (Figure 3.3.5). For both pH 1 and pH 2, the NO signal becomes smaller than the baseline, suggesting that NO reduction is so fast, that NO issued from the disproportionation of HNO_2 (the baseline) is also reduced to N_2O . At pH 5, the NO signals are very noisy and difficult to interpret. For $[\text{SiW}_{12}\text{O}_{40}]^{4-}$ and $[\text{BW}_{12}\text{O}_{40}]^{5-}$, the formation of NO can be observed and the onset values are similar to the GC electrode (same observations as at pH 1 and pH 2). As a general observation, the NO onset becomes more positive as the total charge of the POM becomes smaller, as already explained in chapter 3 when glassy carbon was used as working electrode. In Figure 3.3.7 a, c and e the variation of NO onset potential both with the pH for Ag and GC electrode is shown. These figures visually shows that there is no significant difference between Ag and GC electrode (any difference of less than 0.1 V is not considered as being significantly different due to small fluctuations of the pH and the use of multiple reference electrodes throughout the entire studies).

The most interesting results concern the formation of N_2O . The onset potential of N_2O formation is summarized in Table 3.3.3, together with the shift compared to the values obtained when glassy carbon is the working electrode and the POMs are in solution (homogenous catalysis). Also, in Figure 3.3.7 b, d and f the variation of N_2O onset potential both with the pH for Ag and GC electrode is shown. We can identify that for some POMs and some pH values, the N_2O onset potential is at least with 0.1 V more positive than when Ag electrode is used. In detail, this is not observed for $[\text{H}_2\text{W}_{12}\text{O}_{40}]^{6-}$ at any pH nor for $[\text{BW}_{12}\text{O}_{40}]^{5-}$ at pH 1. For all the other conditions, i.e. for $[\text{BW}_{12}\text{O}_{40}]^{5-}$ at pH 2 and pH 5, for $[\text{SiW}_{12}\text{O}_{40}]^{4-}$ and $[\text{PW}_{12}\text{O}_{40}]^{3-}$ at all pH values this observation is valid. This positive shift suggests that the local concentration of NO is higher, because, as shown in Figure 3.3.2 when higher concentrations of HNO_2 are used, the onset of N_2O formation is more positive (Nernstian behavior). But in all these experiments the concentration of HNO_2 was the same.

Thus, the following interpretation of the data is made:

- 1) POMs are acting as catalysts for conversion of HNO_2 into NO.
- 2) As a consequence, the concentration of dissolved NO is increased.
- 3) Silver electrode acts as a catalyst for the conversion of NO to N_2O , while GC electrode is not a good catalyst for this reaction.

- 4) As a consequence, the onset potential of N_2O is more positive in the presence of POMs and Ag electrode compared to the Ag electrode alone and also compared to the case of POMs and GC electrode.

Moreover, in chapter 3, the hypothesis of the conversion of NO into N_2O via and HNO intermediate was sustained by the onset potential of N_2O that was close to the reported values of -0.11 V *vs.* RHE for the NO/ HNO redox couple.¹⁶ The values of N_2O onset in this chapter, when Ag electrode is used, are too positive to accept this hypothesis, especially at pH 1 and pH 2 (i.e. 0.12 V and 0.15 V *vs.* RHE for $[\text{SiW}_{12}\text{O}_{40}]^{4-}$ and $[\text{PW}_{12}\text{O}_{40}]^{3-}$ respectively, see table 3.3.3). Based on these DEMS data, we can conclude on **a tandem catalysis between silver electrode and two POMs, $[\text{SiW}_{12}\text{O}_{40}]^{4-}$ and $[\text{PW}_{12}\text{O}_{40}]^{3-}$** . In other words, POMs are catalyzing the conversion of HNO_2 to NO and, in a subsequent step, silver adsorbs NO and promote the formation of N_2O via a “NO” dimer. This last step is happening on silver alone but at a more negative potential (starting at -0.18 V *vs.* RHE, table 3.3.1).

Figure 3.3.8 contains a scheme that illustrates the tandem mechanism proposed from the DEMS data. As a comparison, Figure 3.7.5 in chapter 3 describes the mechanism on GC electrode and POMs in solution. One may inquire if this tandem catalysis is not due to an interaction between these POMs and Ag electrode. Indeed, in the literature there are several reports regarding the particular adsorption of $[\text{SiW}_{12}\text{O}_{40}]^{4-}$ on silver followed by the immediate reduction of the POM. This was modelled by DFT and classical molecular dynamics simulations on Ag (100).¹⁷ If silver is poised in the cathodic region, ordered multilayers of $[\text{SiW}_{12}\text{O}_{40}]^{4-}$ are electrostatically assembled on the electrode (this is not observed on gold or carbon electrodes).¹⁸ Finally, there is the use of $[\text{SiW}_{12}\text{O}_{40}]^{4-}$ and $[\text{PW}_{12}\text{O}_{40}]^{3-}$ as reducing and stabilizing agents in the formation of silver nanoparticles $\text{Ag}@\text{[SiW}_{12}\text{O}_{40}]$.^{6-7, 19} One method to decide if the tandem catalysis is due to a particular interaction between the POMs and silver is to increase the number of studied POMs. Thus, we have conducted a similar study by using a Mo-based POM, i.e. $[\text{SiMo}_{12}\text{O}_{40}]^{4-}$. The electrochemical behavior on silver is similar to the one when GC electrode is used (data not shown here). Figure 3.3.9 displays the DEMS data obtained with this POM and silver electrode (at pH 1 and pH 2). The onset potential of NO is 0.58 V *vs.* RHE and 0.60 V *vs.* RHE at pH 1 and pH 2 respectively and the onset of N_2O is 0.26 V *vs.* RHE and 0.30 V *vs.* RHE at pH 1 and pH 2 respectively. Based on the data described in chapter 2 (Table 2.4.3), the onset of NO is very similar, while a shift of N_2O onset potential equal to 0.30 V at pH 1 and 0.28 V at pH 2 is observed. These values confirm again the tandem catalysis between silver electrode and POMs. Nevertheless, it is possible that the rates of each reaction steps (conversion of HNO_2 to NO and subsequent conversion of NO to N_2O) are specific to each couple POM-silver, as the DEMS profiles are different from a POM to another. For example, at pH 1, the NO signal is becoming smaller than the baseline quite easily for $[\text{SiW}_{12}\text{O}_{40}]^{4-}$ compared to $[\text{PW}_{12}\text{O}_{40}]^{3-}$ or to $[\text{SiMo}_{12}\text{O}_{40}]^{4-}$. Moreover, the signal of N_2O is more intense for $[\text{SiW}_{12}\text{O}_{40}]^{4-}$ and $[\text{PW}_{12}\text{O}_{40}]^{3-}$ compared to $[\text{SiMo}_{12}\text{O}_{40}]^{4-}$. This is only a qualitative description and other methodology should be used for a quantitative comparison.

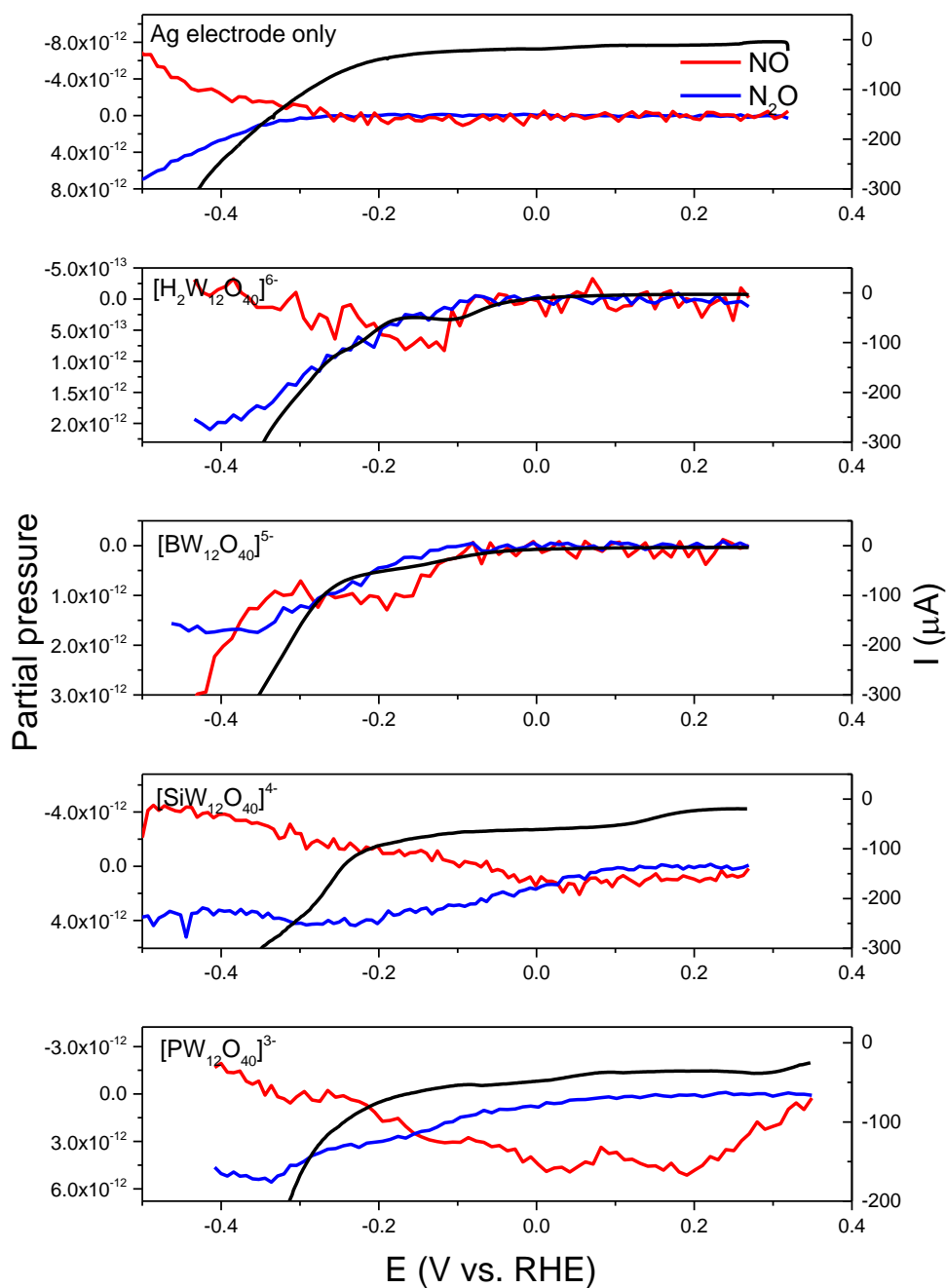


Figure 3.3.4 DEMS study of all four POMs and Ag electrode at pH 1. Black curve: the forward scan of cyclic voltammetry (0.5 mVs^{-1}); Red curve: the signal of m/z 31 (^{15}NO); Blue curve: the signal of m/z 46 ($^{15}\text{N}_2\text{O}$). Electrolyte: pH 1, 0.5 M Na_2SO_4 ; 10 mM $\text{Na}^{15}\text{NO}_2$ and 1 mM POM.

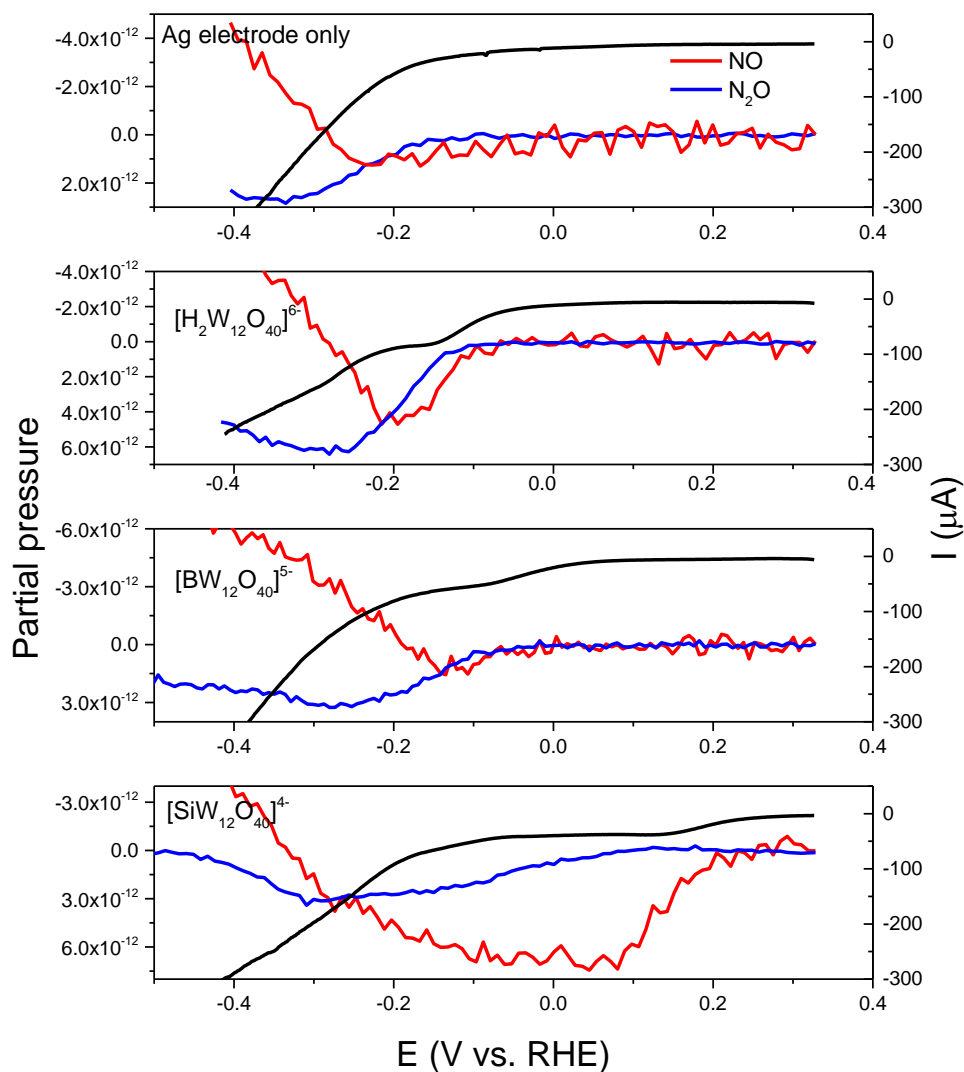


Figure 3.3.5 DEMS study of all three POMs with Ag electrode at pH 2. Black curve: the forward scan of cyclic voltammetry (0.5 mVs^{-1}); Red curve: the signal of m/z 31 (^{15}NO); Blue curve: the signal of m/z 46 ($^{15}\text{N}_2\text{O}$). Electrolyte: pH 2, $0.5 \text{ M Na}_2\text{SO}_4$; $10 \text{ mM Na}^{15}\text{NO}_2$ and 1 mM POM .

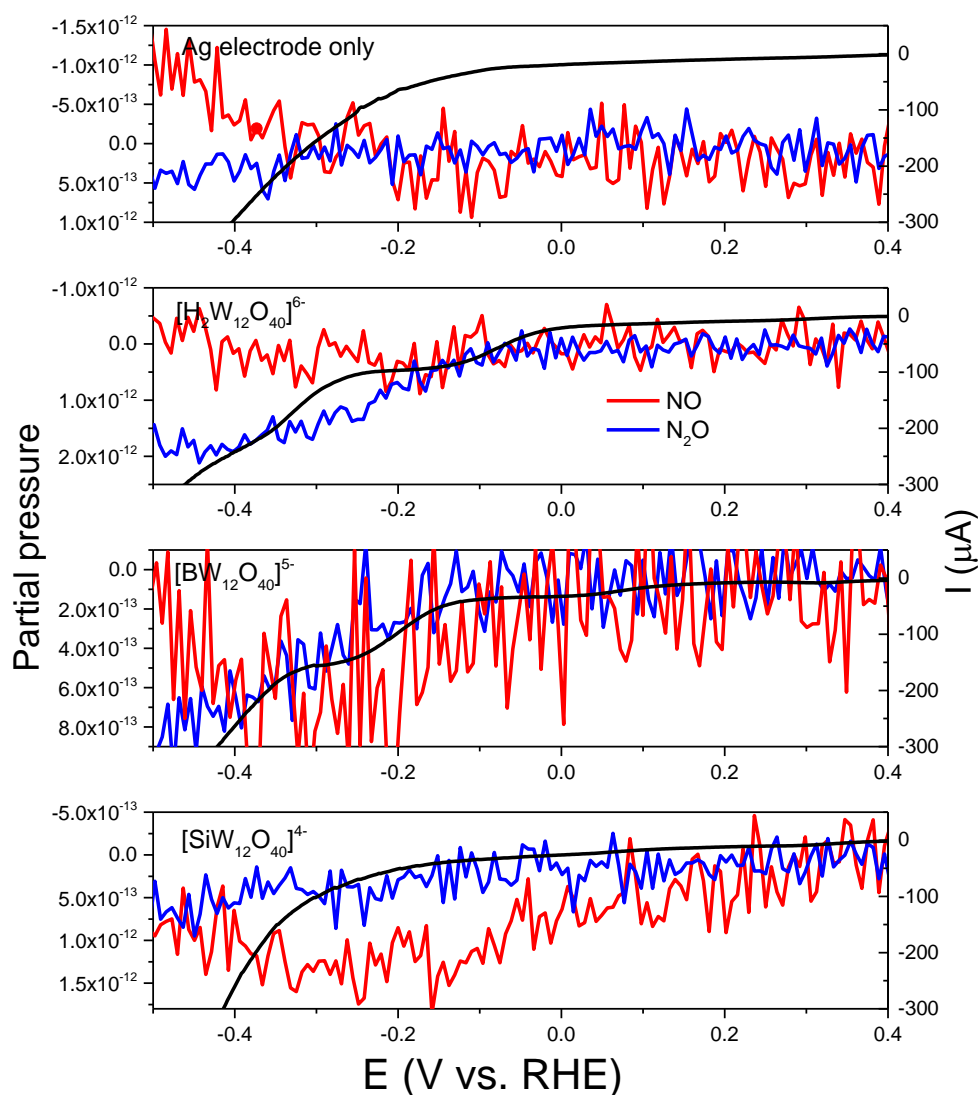


Figure 3.3.6 DEMS study of three POMs on Ag electrode at pH 5. Black curve: the forward scan of cyclic voltammetry (0.5 mVs^{-1}); Red curve: the signal of m/z 31 (^{15}NO); Blue curve: the signal of m/z 46 ($^{15}\text{N}_2\text{O}$). Electrolyte: pH 5, 1 M CH_3COOLi ; 10 mM $\text{Na}^{15}\text{NO}_2$ and 1 mM POM.

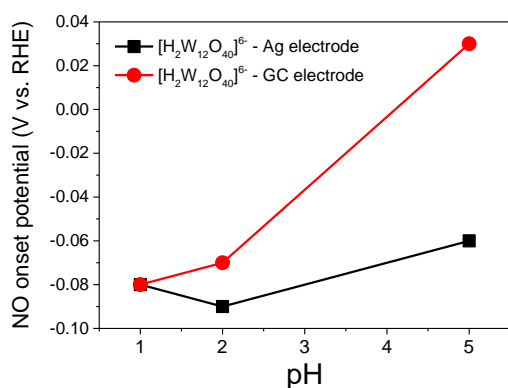
Table 3.3.2 DEMS NO onset potential (V vs. RHE) and shift compared to the NO onset on GC electrode ($E_{\text{NO-shift}} = E_{\text{NO-Ag}} - E_{\text{NO-GC}}$)

POM	$E_{\text{NO-onset}} (E_{\text{NO-shift}}): (\text{V vs. RHE})$				
	pH 1	pH 2	pH 3	pH 4	pH 5
$[\text{H}_2\text{W}_{12}\text{O}_{40}]^{6-}$	-0.08 (0)	-0.09 (-0.02)	-	-	-0.06 (-0.09)
$[\text{BW}_{12}\text{O}_{40}]^{5-}$	-0.05 (0.04)	-0.01 (0.04)	-	-	0.02 (-0.06)
$[\text{SiW}_{12}\text{O}_{40}]^{4-}$	0.27 (0.08)	0.22 (0.02)	0.35 (0.09)	0.23 (-0.02)	0.26 (-0.08)
$[\text{PW}_{12}\text{O}_{40}]^{3-}$	0.36 (0.02)	-	-	-	-

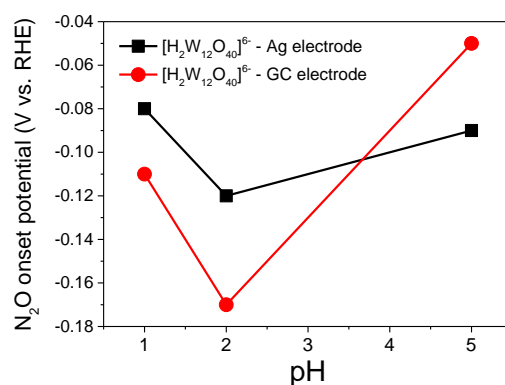
Table 3.3.3 DEMS N₂O onset potential (V *vs.* RHE) and shift compared to N₂O onset on GC electrode $E_{\text{N}_2\text{O-shift}} = E_{\text{N}_2\text{O-Ag}} - E_{\text{N}_2\text{O-GC}}$

POM	$E_{\text{N}_2\text{O-onset}} (E_{\text{N}_2\text{O-shift}}): (\text{V vs. RHE})$				
	pH 1	pH 2	pH 3	pH 4	pH 5
[H ₂ W ₁₂ O ₄₀] ⁶⁻	-0.08 (0.03)	-0.12 (0.05)	-	-	-0.09 (-0.04)
[BW ₁₂ O ₄₀] ⁵⁻	-0.09 (0.02)	-0.04 (0.18)	-	-	-0.10 (0.11)
[SiW ₁₂ O ₄₀] ⁴⁻	0.12 (0.29)	0.12 (0.27)	-0.05 (0.12)	-0.06 (0.21)	-0.15 (0.21)
[PW ₁₂ O ₄₀] ³⁻	0.15 (0.13)	-	-	-	-

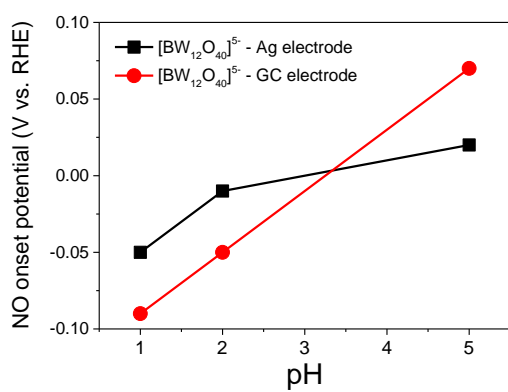
a) NO onset potential with $[\text{H}_2\text{W}_{12}\text{O}_{40}]^{6-}$



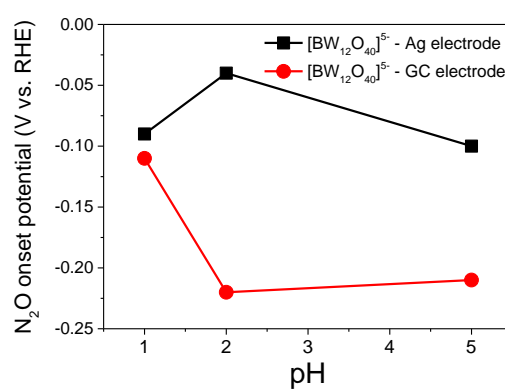
b) N_2O onset potential with $[\text{H}_2\text{W}_{12}\text{O}_{40}]^{6-}$



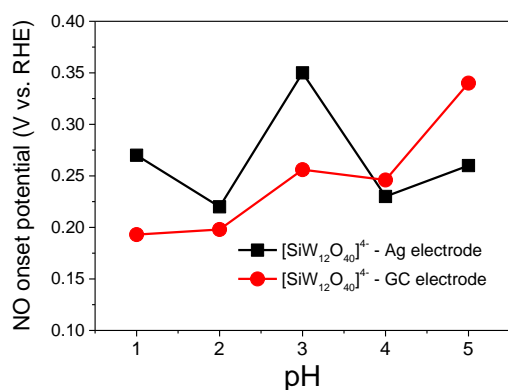
c) NO onset potential with $[\text{BW}_{12}\text{O}_{40}]^{5-}$



d) N_2O onset potential with $[\text{BW}_{12}\text{O}_{40}]^{5-}$



e) NO onset potential with $[\text{SiW}_{12}\text{O}_{40}]^{4-}$



f) N_2O onset potential with $[\text{SiW}_{12}\text{O}_{40}]^{4-}$

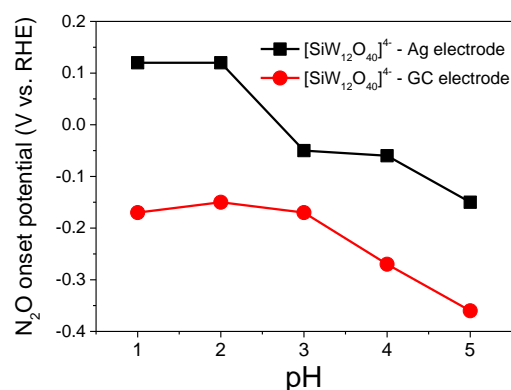


Figure 3.3.7 NO and N_2O onset potential as a function of different pH. Black curve: Ag electrode; Red Curve: GC electrode. (a) NO onset potential with $[\text{H}_2\text{W}_{12}\text{O}_{40}]^{6-}$; (b) N_2O onset potential with $[\text{H}_2\text{W}_{12}\text{O}_{40}]^{6-}$; (c) NO onset potential with $[\text{BW}_{12}\text{O}_{40}]^{5-}$; (d) N_2O onset potential with $[\text{BW}_{12}\text{O}_{40}]^{5-}$; (e) NO onset potential with $[\text{SiW}_{12}\text{O}_{40}]^{4-}$; (f) N_2O onset potential with $[\text{SiW}_{12}\text{O}_{40}]^{4-}$.

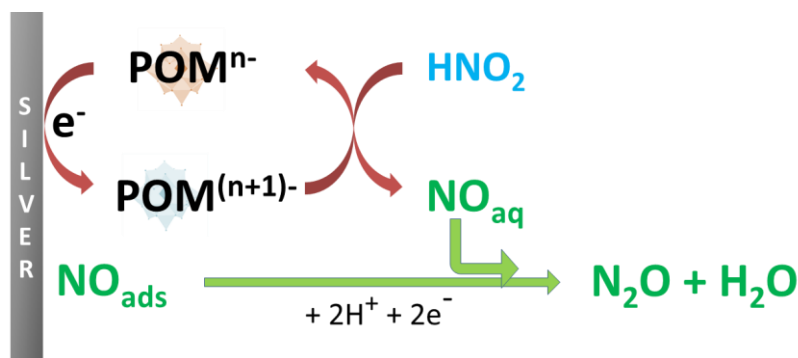
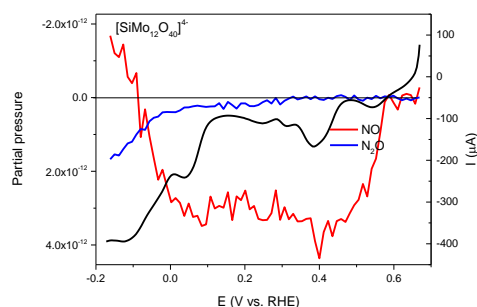


Figure 3.3.8 Proposed mechanism of HNO_2 reduction to N_2O catalyzed by silver electrode and Keggin polyoxometalates.

a) pH 1



b) pH 2

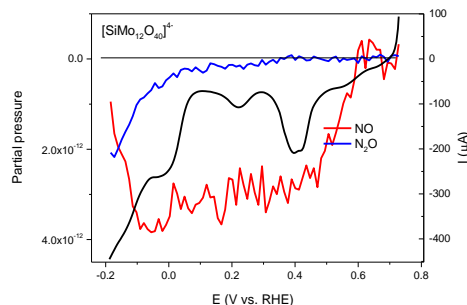


Figure 3.3.9. DEMS study of $[\text{SiMo}_{12}\text{O}_{40}]^{4-}$ with Ag electrode. Black curve: the forward scan of cyclic voltammetry (0.5 mVs^{-1}); Red curve: the signal of m/z 31 (^{15}NO); Blue curve: the signal of m/z 46 ($^{15}\text{N}_2\text{O}$). Electrolyte: a) pH 1; b) pH 2, $0.5 \text{ M Na}_2\text{SO}_4$; $10 \text{ mM Na}^{15}\text{NO}_2$ and 1 mM POM . The black horizontal line is only for visual guidance.

3.4 Nitrite reduction catalyzed by Ag nanoparticles stabilized by POMs (Ag@POM)

3.4.1 Synthesis of Ag@POM nanoparticles

3.4.1.1 Synthesis of Ag@POM nanoparticles using photoreduced POM

A solution of $1 \text{ mM } [\text{SiW}_{12}\text{O}_{40}]^{4-}$ is mixed with 1 M propan-2-ol as the electron donor. The concentration of POM and propan-2-ol can be adjusted if necessary. Three mL of above solution are loaded into quartz cuvette and exposed to a light source for 30 min to 2 h (a distance of 20 cm between separates the cuvette and light source). A 300 W Xe arc lamp provides the illumination and a water-based filter is used to absorb the near-IR radiation that could excessively heat the cuvette. Before the illumination, the solution is degassed by argon bubbling for more than 30 minutes. During the illumination, the solution was kept under

argon atmosphere. UV-vis absorption spectra were recorded to follow the reduction of POM to $\text{POM}^{\text{n-}}$. Before reduction, POMs have an absorption band in the UV region (below 370 nm). With prolonged illumination, a wide absorption band in the Visible region (about 700 nm, between 600 nm to 800 nm) increases gradually until all POM in solution is reduced. The final solution has a deep blue color. Different reduced POMs have similar absorption bands which can be attributed to the d-d transitions and tungsten-to-tungsten charge transfer ($\text{W}^{5+}\text{-O-W}^{6+}$ CT), so these bands are also called intervalence bands.

In the following step, 0.3 mL of deaerated 1 mM Ag_2SO_4 solution were added into the above blue solution with stirring. The blue solution will transform to green solution (mixed solution of yellow Ag nanoparticles and blue reduced POMs). On the UV-vis absorption spectra, a well-known plasmon absorption band of silver nanoparticles around 407 nm is obtained.²⁰ This band generally corresponds to spherical AgNPs with the average sizes of 20 - 30 nm.²¹ In the same time, the wide absorption band in the UV region (about 700 nm) decreased a lot. If the solution is kept under argon atmosphere, the solution remains green. However, if the solution is exposed to air, the solution will turn to yellow (characteristic to Ag nanoparticles), and the second absorption band (intervalence band) disappears indicating that the reduced POM is oxidized by O_2 . After 1 week, the Ag NPs band at 400 nm has only a slight decrease, which means that Ag@POM NPs are stable in solution, in a closed vessel. As a result, the solution contains 0.2 mM of Ag@POMs and 1 mM POM. This experimental protocol is pictured in Figure 3.4.1 and was applied for $[\text{PW}_{12}\text{O}_{40}]^{3-}$, $[\text{SiW}_{12}\text{O}_{40}]^{4-}$, and $[\text{BW}_{12}\text{O}_{40}]^{5-}$ as shown in Figure 3.4.2.

Although our experiments are based on previously published experimental methods, we have notice that the speed of addition of Ag^+ solution into photoreduced POM solution greatly influences the color (and hence the size) of the obtained nanoparticles. Figure 3.4.3 shows a picture of Ag@[$\text{PW}_{12}\text{O}_{40}$]³⁻ nanoparticles obtained when the entire volume of Ag^+ solution is added in 3 min (i.e. very slowly), in 1 min (i.e. slowly) and in couple of seconds (i.e. quickly). We conclude that the nanoparticles are smaller when the solution of Ag^+ is added as quickly as possible, a missing information in previously published protocols. For this reason, all the other synthesis of Ag@POMs has been realized in this manner.

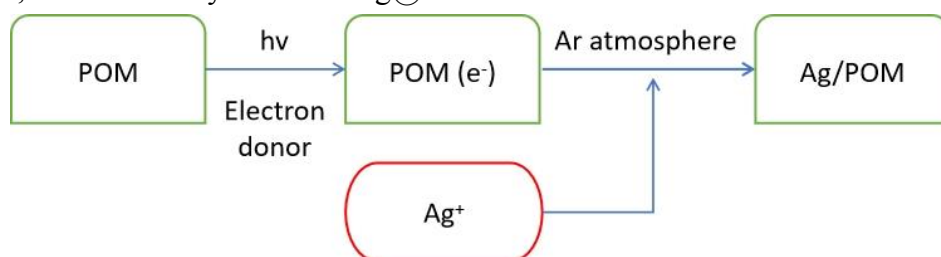


Figure 3.4.1 Experimental steps for the synthesis of Ag@POM using photoreduced POMs.

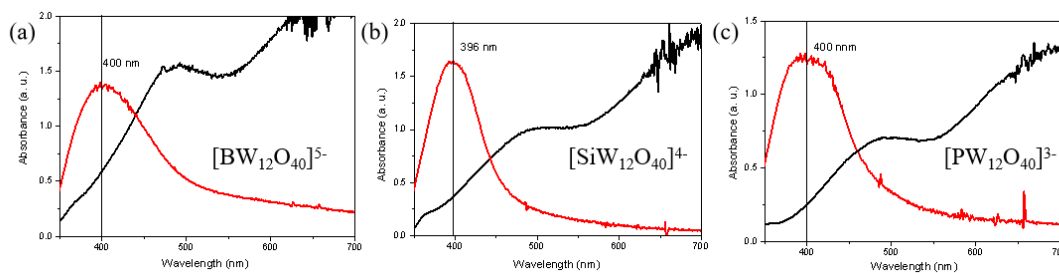


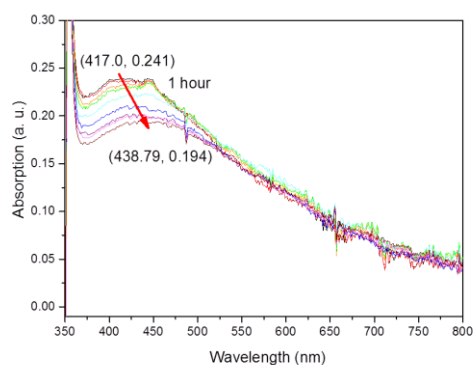
Figure 3.4.2 The UV-vis spectroscopy of $[\text{PW}_{12}\text{O}_{40}]^{3-}$, $[\text{SiW}_{12}\text{O}_{40}]^{4-}$, and $[\text{BW}_{12}\text{O}_{40}]^{5-}$. The red curve is from the Ag NPs solution exposed to air for a week. The black curve is the POMs solution after illumination before adding Ag_2SO_4 solution.



Figure 3.4.3 Picture of $\text{Ag}@[\text{PW}_{12}\text{O}_{40}]^{3-}$ NPs obtained with a different addition time of the Ag^+ solution into the photoreduced POM solution.

The above protocol was applied also for $[\text{H}_2\text{W}_{12}\text{O}_{40}]^{6-}$ but several differences are observed. Firstly, the photoreduction requires higher concentrations of POM and propanol and smaller concentration of Ag^+ . Secondly, the color of $\text{Ag}@[\text{H}_2\text{W}_{12}\text{O}_{40}]^{6-}$ is different compared to other particles. Finally, these nanoparticles are far less stable; their color is changing a little after 1 hour and a lot after several days (Figure 3.4.4). For this reason, $\text{Ag}@[\text{H}_2\text{W}_{12}\text{O}_{40}]^{6-}$ is produced by a completely different manner, by using $[\text{H}_2\text{W}_{12}\text{O}_{40}]^{6-}$ reduced in an electrochemical reaction (see next section). Table 3.4.1 and Figure 3.4.5 show a comparison of experimental conditions and results of the four $\text{Ag}@\text{POM}$ nanoparticles.

a)



b)

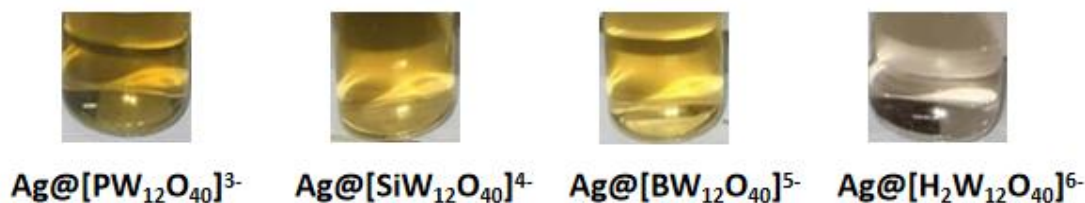


Figure 3.4.4 a) UV-Vis spectra of $\text{Ag}@\text{[H}_2\text{W}_{12}\text{O}_{40}]^{6-}$ NPs during 1 h after synthesis. b) Picture of $\text{Ag}@\text{[H}_2\text{W}_{12}\text{O}_{40}]^{6-}$ NPs after several minutes and several days after synthesis.

Table 3.4.1 Summary of experimental conditions for synthesis of four $\text{Ag}@\text{POM}$ NPs

POM	POM (mM)	Propanol (M)	Ag_2SO_4 (mM)	Ratio POM^-/Ag^+	Wavelength (nm)	Abs (a.u.)
$[\text{PW}_{12}\text{O}_{40}]^{3-}$	1	1	1	5.5	408	1.370
$[\text{SiW}_{12}\text{O}_{40}]^{4-}$	1	1	1	5.1	397	1.650
$[\text{BW}_{12}\text{O}_{40}]^{5-}$	1	1	1	3.8	401	1.250
$[\text{H}_2\text{W}_{12}\text{O}_{40}]^{6-}$	8	4	0.2	28.8	453	0.144

a)



b)

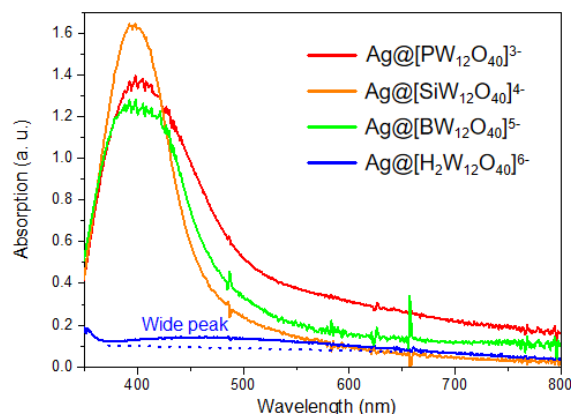


Figure 3.4.5 a) Picture of four solutions containing Ag@POM NPs. B) UV-Vis spectra of solution in a).

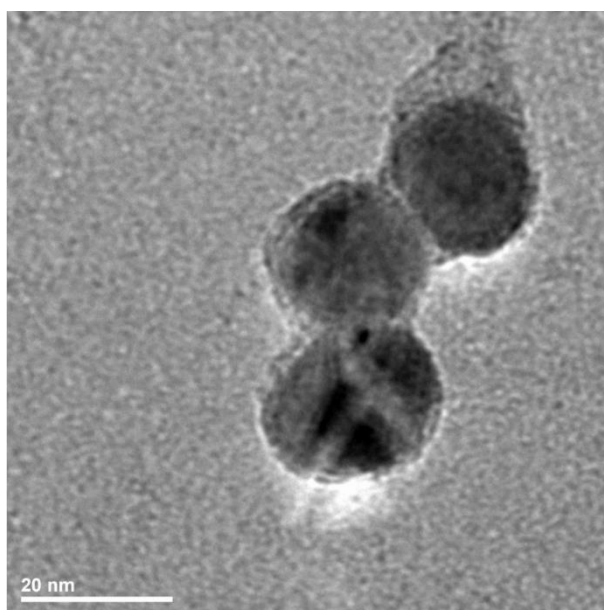


Figure 3.4.6 TEM image of $\text{Ag@[PW}_{12}\text{O}_{40}]^{3-}$ from photoreduction method.

3.4.1.2 Synthesis of Ag@POM using electroreduced POM

Compared with photoreduction, POM electroreduction do not need extra organic electron donor. The hypothesis is that reduced $[\text{H}_2\text{W}^{\text{V}}\text{W}^{\text{VI}}_{12}\text{O}_{40}]^{7-}$ is able to reduce Ag^+ and produce stable $\text{Ag@[H}_2\text{W}_{12}\text{O}_{40}]^{6-}$ NPs. The H-type electrochemical reactor is shown in Figure 3.4.7, the anode and cathode compartments being separated by a glass frit. The catholyte is 30 mL 4 mM degassed $[\text{H}_2\text{W}_{12}\text{O}_{40}]^{6-}$ solution and the anolyte is 10 mL pH 2 0.125 M Na_2SO_4 solution. Working electrode is a square 2 cm * 2 cm glassy carbon.

Reference electrode is Ag/AgCl/3 M KCl. Counter electrode is a graphite sheet (1 cm * 4 cm). Before electroreduction, the anolyte and catholyte are bubbled with argon for more than 30 minutes and kept on argon atmosphere. During the reaction a constant voltage of -0.50 V vs. RHE was applied for 2 hours with stirring. The catholyte changed quickly from colorless to blue. UV-vis absorption spectra were also recorded to follow the reduction to POM⁻. Every 30 mins, an aliquot of 1 mL catholyte was sampled out. A wide absorption band in the UV region (about 700 nm, between 600 nm to 800 nm) increases gradually with longer time until all POM is reduced and the solution becomes deep blue, as shown on Figure 3.4.9a.

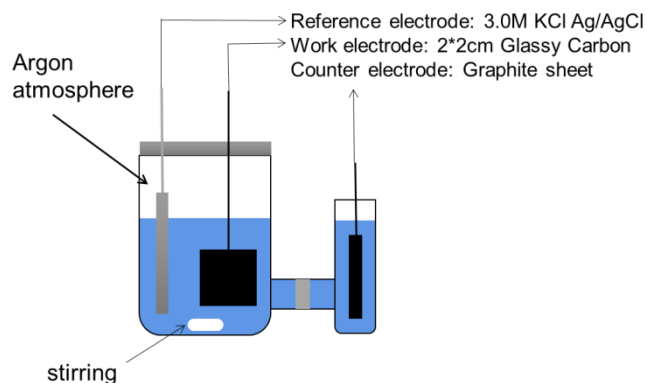


Figure 3.4.7 Electrochemical H-type reactor for POM electroreduction.

In the following step, 3 mL of 10 mM Ag₂SO₄ solution (degassed by argon) was added while stirring. The solution turns to green (mixed Ag nanoparticles and reduced POM) (Figure 3.4.8 and Figure 3.4.9b). After 1 night, the solution turns to yellow because the reduced POM will be oxidized by O₂ in air. Finally, the colloidal solution of Ag@[H₂W₁₂O₄₀]⁶⁻ NPs is obtained. Most probably some unreacted POM remains in the colloidal solution. A dialysis experiment could separate the nanoparticles, but this was not performed in this thesis. The concentration of thus obtained Ag@POM solution is very high. This leads to aggregation of nanoparticles, as shown by orange curve in Figure 3.4.10. After dilution of this aged solution, the absorbance at 400 nm is low. Instead, if the solution is diluted directly after the synthesis (dilution of 20% with water), the aggregation is avoided and the absorbance of the solution after 3 days is in a good range (back curve in Figure 3.4.10). In conclusion, this synthesis method provides more stable Ag@[H₂W₁₂O₄₀]⁶⁻ nanoparticles. This synthesis method was also used for Ag@[SiW₁₂O₄₀]⁴⁻ nanoparticles. TEM images of Ag@[SiW₁₂O₄₀]⁴⁻ and Ag@[H₂W₁₂O₄₀]⁶⁻ from electroreduction method are shown in Figure 3.4.11. Ag@[SiW₁₂O₄₀]⁴⁻ NPs are more uniform in size and shape while Ag@[H₂W₁₂O₄₀]⁶⁻ NPs are more heterogeneous in size and shape and tend to aggregate.

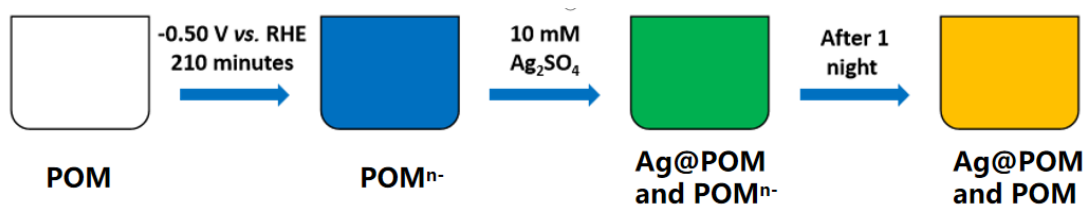


Figure 3.4.8 Scheme for preparation of Ag@[H₂W₁₂O₄₀]⁶⁻ using previously reduced [H₂W₁₂O₄₀]⁷⁻.

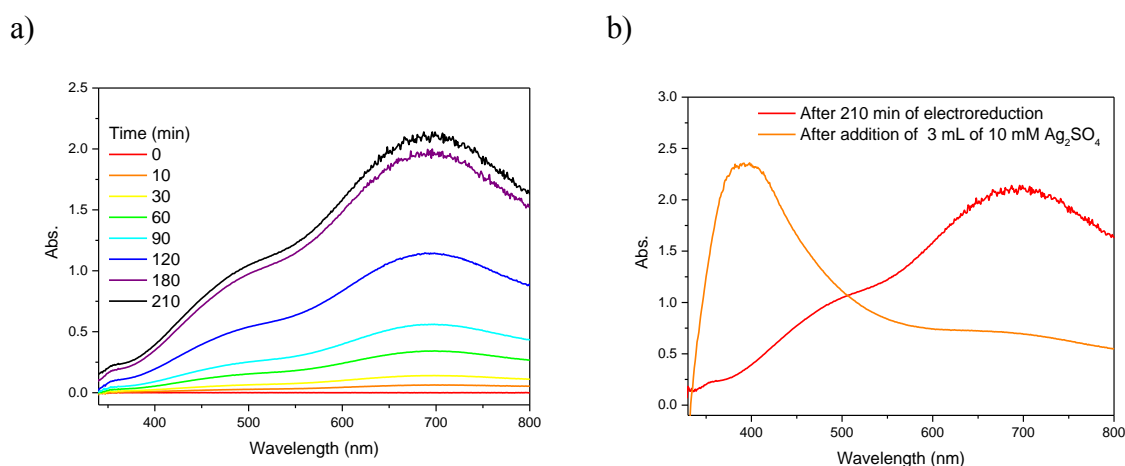


Figure 3.4.9 a) UV-vis spectra of 2 mM [H₂W₁₂O₄₀]⁶⁻ with different electroreduction time; b) UV-vis spectra after 210 minutes of electroreduction and before and after the addition of 10 mM Ag₂SO₄ (added volume, 3 mL).

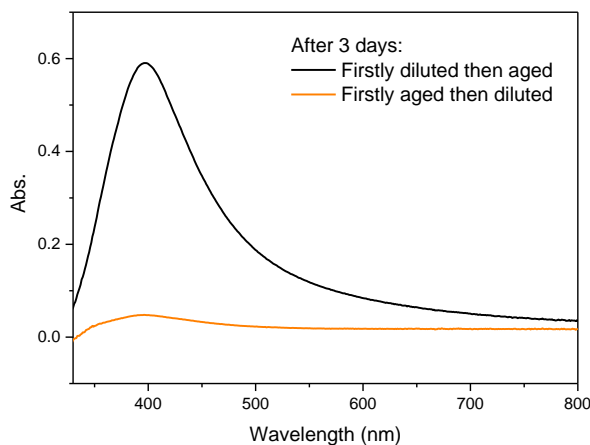


Figure 3.4.10 The UV-vis spectroscopy of Ag@[H₂W₁₂O₄₀]⁶⁻ 3 days after preparation. Black curve: 20 % diluted Ag@[H₂W₁₂O₄₀]⁶⁻ solution; Orange curve: keep 3 days without dilution then dilute the solution by water to 20%.

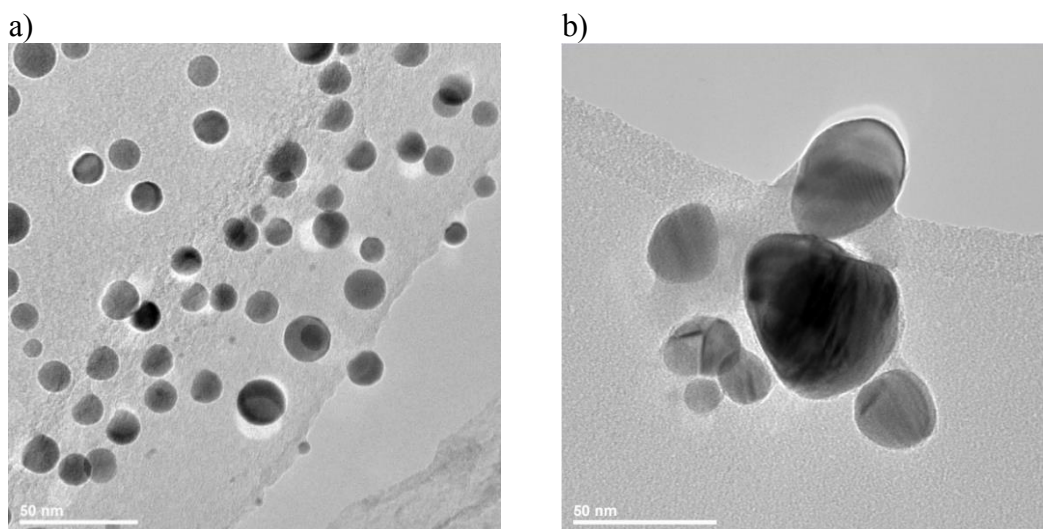


Figure 3.4.11 TEM images of (a) $\text{Ag}@\text{[SiW}_{12}\text{O}_{40}]^{4-}$ and (b) $\text{Ag}@\text{[H}_2\text{W}_{12}\text{O}_{40}]^{6-}$ from electroreduction method.

3.4.2 DEMS analysis of nitrite reduction catalyzed by $\text{Ag}@\text{POM}$

In this part, the $\text{Ag}@\text{POM}$ nanoparticles were tested in solution phase, right after their synthesis. In the experiments described below a certain dilution with the desired electrolyte solution was achieved. In future experiments, an immobilization method will be employed.

3.4.2.1 Performance of $\text{Ag}@\text{[SiW}_{12}\text{O}_{40}]^{4-}$ prepared by photoreduction

During the synthesis of $\text{Ag}@\text{[SiW}_{12}\text{O}_{40}]^{4-}$ an excess of propan-2-ol was used as an electron donor. After the synthesis, the remaining propan-2-ol is not removed. Thus, one would like to verify that propan-2-ol has no influence on the electrochemical behavior of $\text{Ag}@\text{[SiW}_{12}\text{O}_{40}]^{4-}$. The following values of propan-2-ol concentration, but also those of POM and $\text{Ag}@\text{[SiW}_{12}\text{O}_{40}]^{4-}$ correspond to the initial value before the synthesis started. Especially, the “concentration” of $\text{Ag}@\text{[SiW}_{12}\text{O}_{40}]^{4-}$ corresponds to the concentration of Ag^+ at the beginning of the synthesis.

The first series of DEMS experiments was conducted at pH 2 (Figure 3.4.12). Table 3.4.2 summarizes the experimental conditions of four different manipulations. Experiment 1 contains the $\text{Ag}@\text{[SiW}_{12}\text{O}_{40}]^{4-}$ diluted in pH 2 electrolyte (v/v: 1/9) and using GC as working electrode. Experiment 2 is using an analog concentration of $\text{[SiW}_{12}\text{O}_{40}]^{4-}$, propan-2-ol and GC as working electrode. Experiments 3 and 4 are the conventional experiments (as described in the first part of this chapter and in chapter 3), meaning with only $\text{[SiW}_{12}\text{O}_{40}]^{4-}$ in solution and using either Ag or GC as working electrode. It can be observed that NO onset potential is the same in all conditions, and N_2O onset potential is more positive only in experiment 3, as described above. It can be concluded that the presence of propan-2-ol is not deleterious to our experiments. Unfortunately, no catalytic effect from the presence of $\text{Ag}@\text{[SiW}_{12}\text{O}_{40}]^{4-}$ is observed. This triggered the hypothesis that the nanoparticles are not stable in these experimental conditions. Indeed, Figure 3.4.13 displays the UV-Vis spectra

obtained by mixing, during three independent experiments, the solution of $\text{Ag}@\text{[SiW}_{12}\text{O}_{40}]^{4-}$ with different concentration of sodium nitrite, prepared at pH 2 (only 0.01 M H_2SO_4). It can be observed the rapid decrease of plasmon intensity (at 400 nm). Already after 10 minutes, no more plasmon is observed. These results explain very well the before described DEMS experiment in which the $\text{Ag}@\text{[SiW}_{12}\text{O}_{40}]^{4-}$ had no particular catalytic effect, because the particles were not stable for the “long” time scale (40 minutes) required by the slow recording of the cyclic voltammetry. In conclusion, for further experiments, higher pH values are recommended.

a) $[\text{SiW}_{12}\text{O}_{40}]^{4-}$ and propan-2-ol

b) $\text{Ag}@\text{[SiW}_{12}\text{O}_{40}]^{4-}$ and propan-2-ol

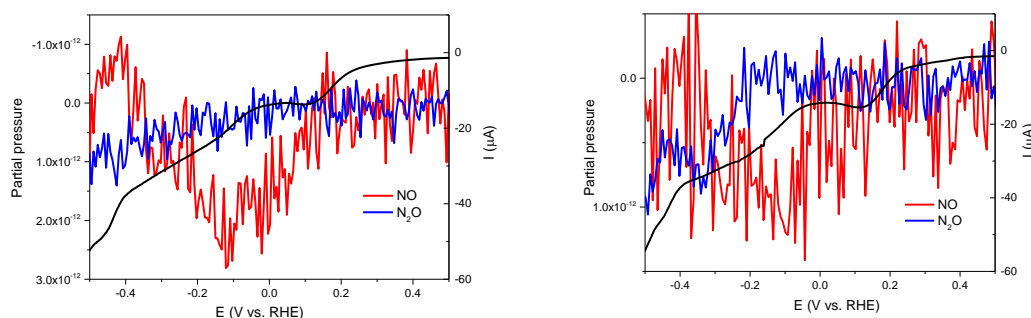


Figure 3.4.12 DEMS study of nitrite reduction at pH 2 catalyzed by: a) $[\text{SiW}_{12}\text{O}_{40}]^{4-}$ at GC electrode; b) $\text{Ag}@\text{[SiW}_{12}\text{O}_{40}]^{4-}$ at GC electrode. Black curve: the forward scan of cyclic voltammetry (0.5 mVs^{-1}); Red curve: the signal of m/z 31 (^{15}NO); Blue curve: the signal of m/z 46 ($^{15}\text{N}_2\text{O}$). Experimental conditions: a) 0.1 mM $[\text{SiW}_{12}\text{O}_{40}]^{4-}$ and 0.1 M 2-propanol; b) 0.02 mM of $\text{Ag}@\text{[SiW}_{12}\text{O}_{40}]^{4-}$, 0.1 mM $[\text{SiW}_{12}\text{O}_{40}]^{4-}$, and 0.1 M 2-propanol. For both a) and b) 10 mM $\text{Na}^{15}\text{NO}_2$ and pH 2, 0.5 M Na_2SO_4 .

Table 3.4.2 Experimental conditions and onset potential of NO and N_2O of four different manipulations

Experiment	2-propanol (M)	Ag NPs (mM)	Concentration of POM (mM)	Electrode	Onset potential (V vs. RHE)	
					NO	N_2O
1	0.1	0.02	0.1	GC	0.22	-0.14
2	0.1	0	0.1	GC	0.19	-0.12
3	0	0	1	Ag	0.22	0.12
4	0	0	1	GC	0.20	-0.15

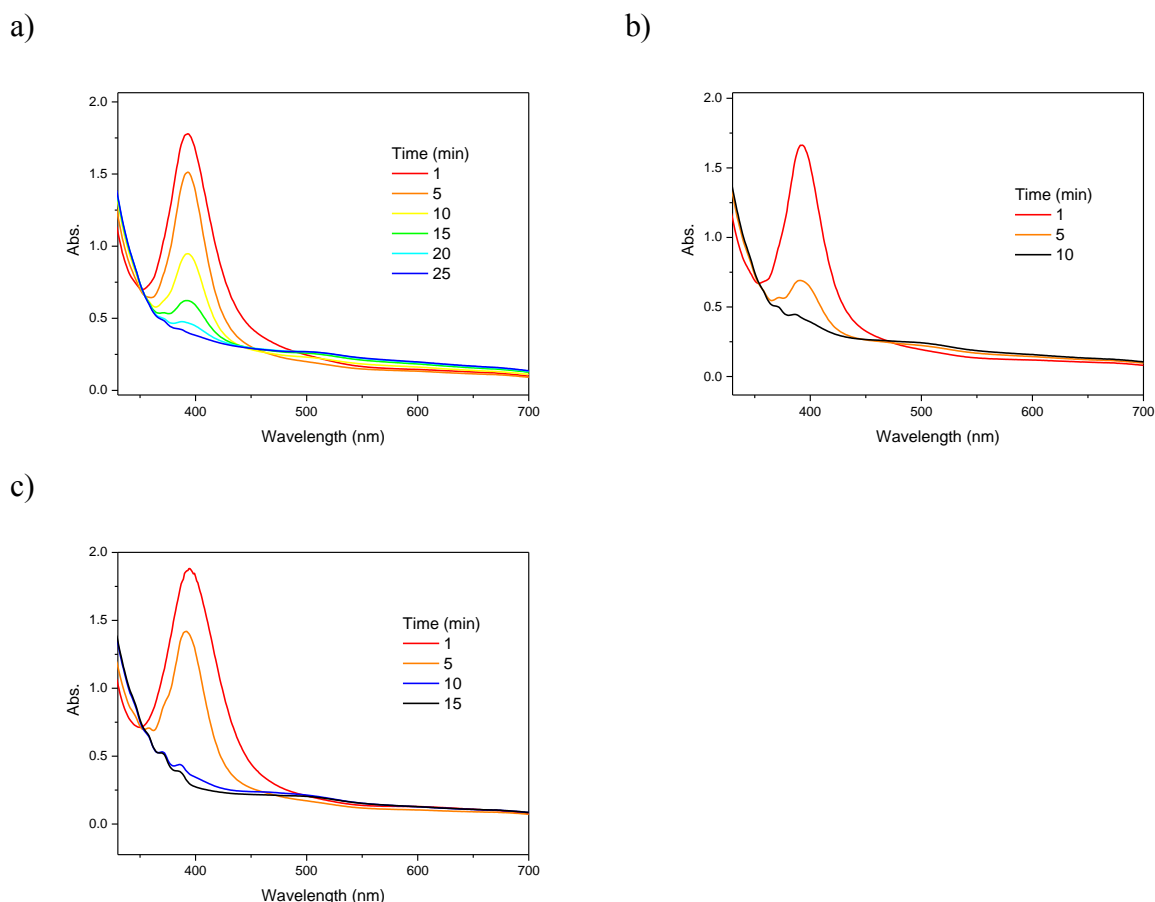


Figure 3.4.13 UV-vis spectra of 0.02 mM $\text{Ag}@\text{[SiW}_{12}\text{O}_{40}]^{4-}$ solution at pH 2 in the presence of different concentration of nitrite (NaNO_2): a) 1.25 mM; b) 2.5 mM; c) 5.0 mM.

3.4.2.2 Performance of $\text{Ag}@\text{[SiW}_{12}\text{O}_{40}]^{4-}$ prepared by electroreduction

As previously discussed, the low pH and high electrolyte concentration (pH 2, 0.5 M Na_2SO_4) lead to the precipitation of the $\text{Ag}@\text{[SiW}_{12}\text{O}_{40}]^{4-}$ nanoparticles. In this view, we have used the $\text{Ag}@\text{[SiW}_{12}\text{O}_{40}]^{4-}$ NPs prepared by electroreduction and made the dilution with a pH 4.5 solution (water adjusted with CH_3COOH to reach desired pH). DEMS result is shown in the Figure 3.4.14. The N_2O signal shows no variation while the NO signal starts to decrease at 0.2 V vs. RHE. This case was not previously observed neither with Ag electrode nor with the POM in solution. Before some reasonable explanation could be found, it was observed that, even in this condition, the $\text{Ag}@\text{[SiW}_{12}\text{O}_{40}]^{4-}$ NPs are not stable, as the plasmon intensity is still decreasing. For the following experiment, we sought to reduce the concentration of nitrite. DEMS result is shown in Figure 3.4.15a and UV-Vis spectra of the $\text{Ag}@\text{[SiW}_{12}\text{O}_{40}]^{4-}$ NPs in Figure 3.4.15b. DEMS data are almost the same, while the stability of the NPs seems to be improved, but still the intensity of the plasmon is decreasing.

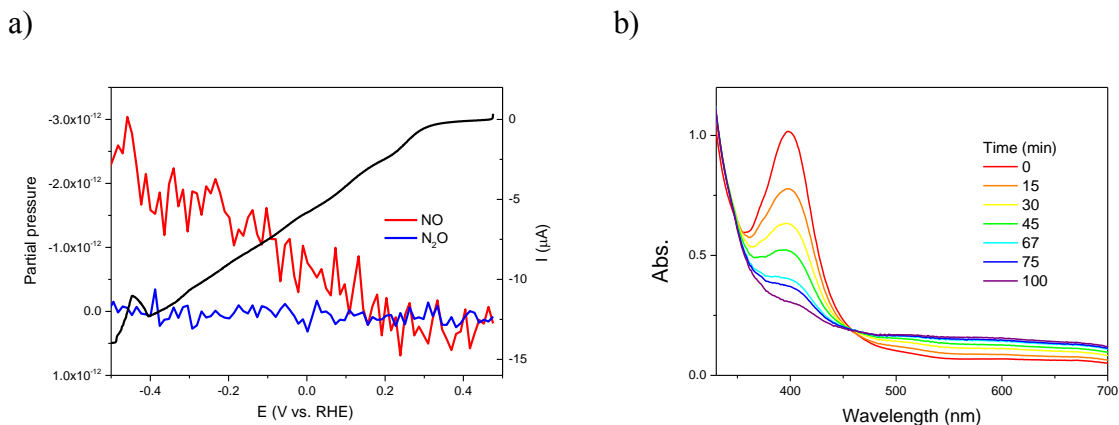


Figure 3.4.14 a) DEMS study of nitrite reduction with $\text{Ag}@\text{[SiW}_{12}\text{O}_{40}]^{4-}$ in solution and GC electrode at pH 4.5 with 10 mM $\text{Na}^{15}\text{NO}_2$; b) UV-vis spectra of $\text{Ag}@\text{[SiW}_{12}\text{O}_{40}]^{4-}$ in solution at pH 4.5 and in the presence of 10 mM $\text{Na}^{15}\text{NO}_2$; For all the experiments: 0.5 mM $\text{[SiW}_{12}\text{O}_{40}]^{4-}$ and 0.133 mM Ag NPs. Black curve: the forward scan of cyclic voltammetry (0.5 mVs^{-1}); Red curve: the signal of m/z 31 (^{15}NO); Blue curve: the signal of m/z 46 ($^{15}\text{N}_2\text{O}$).

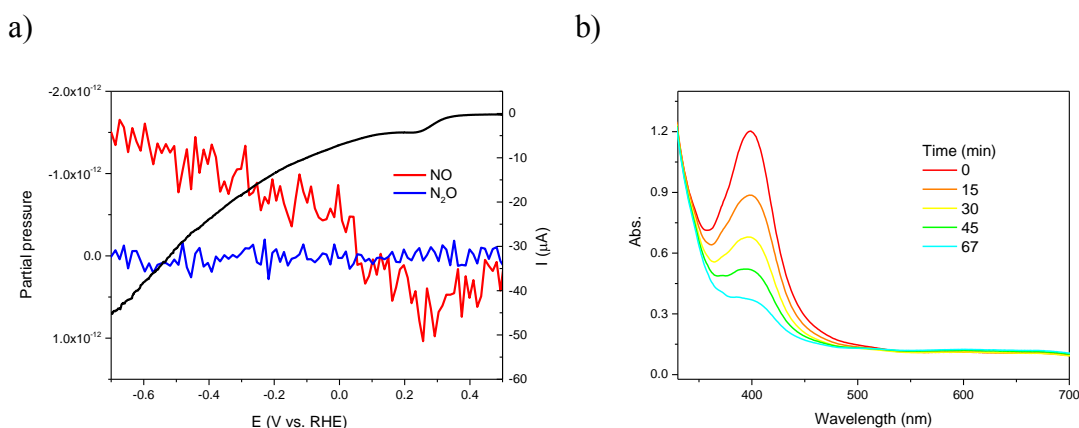
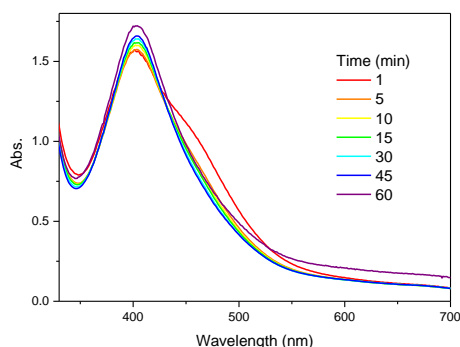


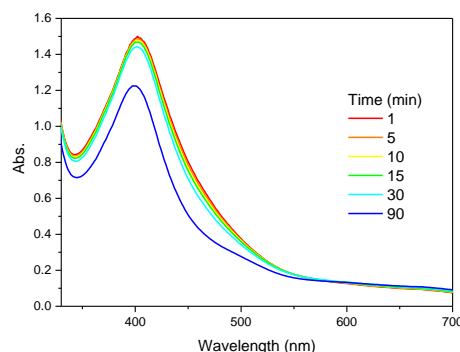
Figure 3.4.15 (a) DEMS study of nitrite reduction with $\text{Ag}@\text{[SiW}_{12}\text{O}_{40}]^{4-}$ solution and GC electrode at pH 4.5 with 3.33 mM $\text{Na}^{15}\text{NO}_2$; (b) UV-vis spectra of $\text{Ag}@\text{[SiW}_{12}\text{O}_{40}]^{4-}$ solution at pH 4.5. Electrolyte contains totally 0.667 mM $\text{[SiW}_{12}\text{O}_{40}]^{4-}$ and 0.178 mM $\text{Ag}@\text{[SiW}_{12}\text{O}_{40}]^{4-}$ NPs. Black curve: the forward scan of cyclic voltammetry (0.5 mVs^{-1}); Red curve: the signal of m/z 31 (^{15}NO); Blue curve: the signal of m/z 46 ($^{15}\text{N}_2\text{O}$).

In this view, the final experiments were conducted in the presence of pectin, a polysaccharide with high molecular weight previously used as a stabilizer of nanoparticles.²² The stability of $\text{Ag}@\text{[SiW}_{12}\text{O}_{40}]^{4-}$ NPs at pH 5 in the presence of nitrite is greatly improved as shown by UV-Vis spectra in Figure 3.4.16 a and b. Subsequently, DEMS experiment was performed and result is shown in Figure 3.4.16c. Although the reduction peaks of $\text{[SiW}_{12}\text{O}_{40}]^{4-}$ are clearly visible, the reduction potential is shifted to more negative values (i.e. -0.2 V and -0.4 V vs. RHE for the first and second wave, corresponding to a shift of -0.4V compared to $\text{[SiW}_{12}\text{O}_{40}]^{4-}$ alone). Moreover, there is no signal for NO and N_2O .

a) no nitrite



b) with nitrite



c)

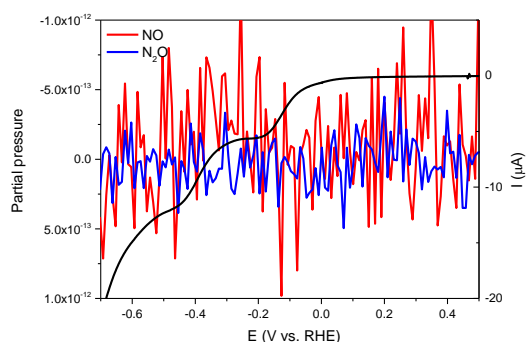


Figure 3.4.16 UV-vis spectra of $\text{Ag}@\text{[SiW}_{12}\text{O}_{40}]^{4-}$ solution at pH 5 containing totally 0.5 mM $\text{[SiW}_{12}\text{O}_{40}]^{4-}$ and 0.133 mM Ag NPs mixed with 1.0 mg/mL pectin: a) in the absence of nitrite; b) with 10 mM of NaNO_2 ; c) DEMS study of $\text{Ag}@\text{[SiW}_{12}\text{O}_{40}]^{4-}$ solution with GC electrode at pH 5 with 10 mM nitrite. DEMS study of $\text{Ag}@\text{[SiW}_{12}\text{O}_{40}]^{4-}$ solution with GC electrode at pH 5 with 10 mM nitrite

We suppose that the concentration of pectin (1 mg/mL) is too high. We have thus performed an optimization study to find the lowest concentration of pectin that could still prevent the nanoparticles from agglomeration. For this, UV-Vis spectra were recorded for mixtures of $\text{Ag}@\text{[SiW}_{12}\text{O}_{40}]^{4-}$ in the presence of nitrite and different concentration of pectin (Figure 3.4.17). It can be observed that the nanoparticles are very stable even in the presence of low concentration of pectin, as low as 0.005 mg/mL. Nevertheless, after an optical inspection of the solution (before the addition of nitrite, Figure 3.4.17), the solution with the lowest concentration of pectin is not perfectly clear. It is interesting to notice how the solutions have a lighter color after the addition of nitrite (Figure 3.4.17 lower picture), suggesting that the nanoparticles are still affected by the addition of nitrite. For this reason, the concentration of 0.2 mg/mL was chosen for the final experiment. The results are shown in Figure 3.4.19. First of all, the redox behavior of $\text{[SiW}_{12}\text{O}_{40}]^{4-}$ is restored, as the values of the reduction potential are the ones expected for this POM at pH 5. Upon addition of several concentrations of nitrite, the catalytic current increases only for the third wave as expected. But the onset of N_2O (-0.38 V vs. RHE) is similar to the case when $\text{[SiW}_{12}\text{O}_{40}]^{4-}$ is used in

solution with GC electrode. Thus, the presence of silver nanoparticles does not contribute to the reduction of nitrite. This is unexpected because we have shown previously that silver bulk electrode can catalyze the reaction in tandem with the POM (even though the tandem catalysis works better at pH 2). The fact that the signal of NO shows no variation (and it is very noisy), might suggest that this species is too strongly adsorbed at the surface of the nanoparticles.²³ As a consequence, the formation of N₂O happens at higher overpotential and no nitric oxide is present in the solution as free species.

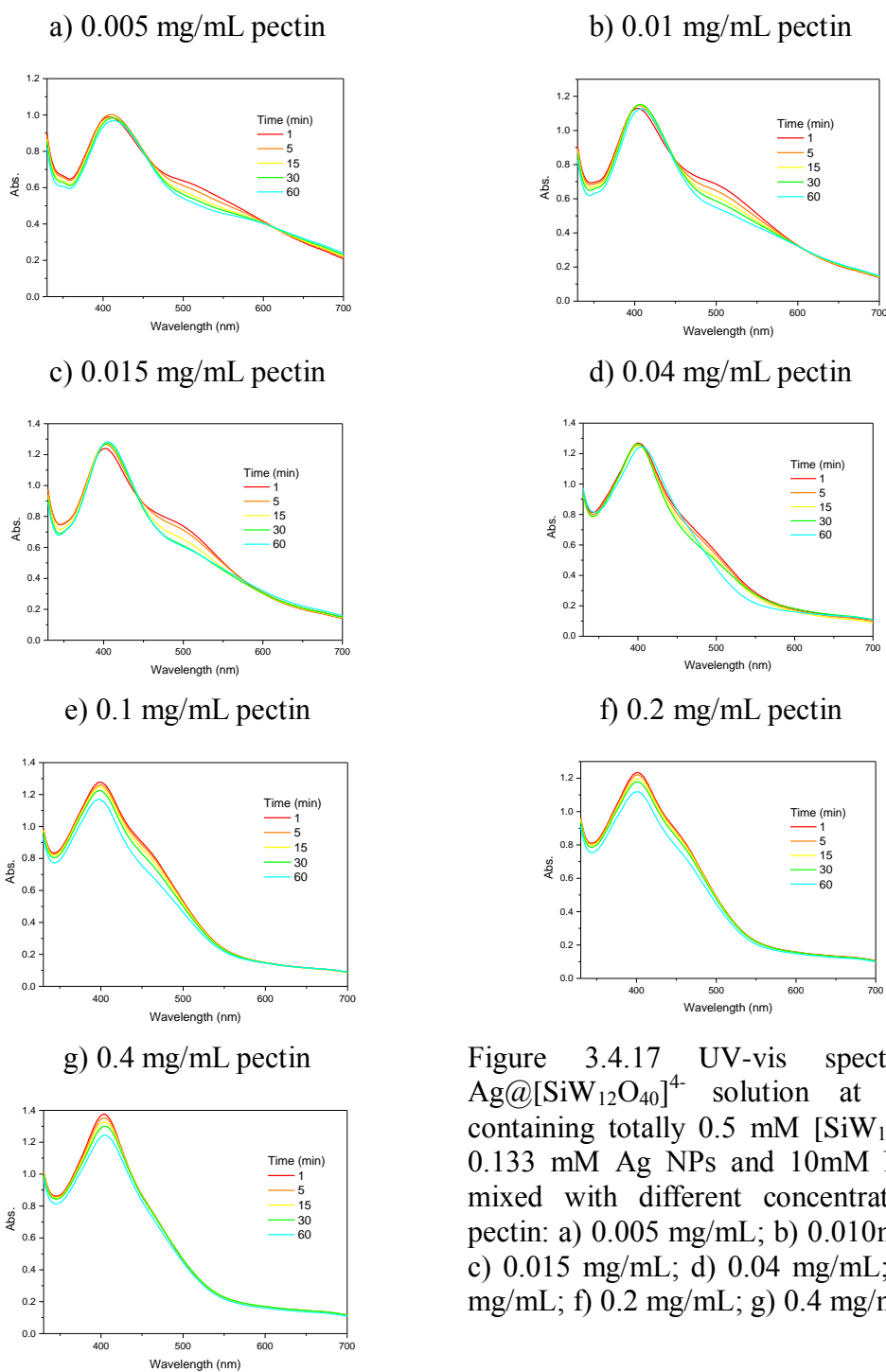


Figure 3.4.17 UV-vis spectra of $\text{Ag}@\text{[SiW}_{12}\text{O}_{40}]^{4-}$ solution at pH 5 containing totally 0.5 mM $\text{[SiW}_{12}\text{O}_{40}]^{4-}$, 0.133 mM Ag NPs and 10mM NaNO_2 mixed with different concentration of pectin: a) 0.005 mg/mL; b) 0.010mg/mL; c) 0.015 mg/mL; d) 0.04 mg/mL; e) 0.1 mg/mL; f) 0.2 mg/mL; g) 0.4 mg/mL.

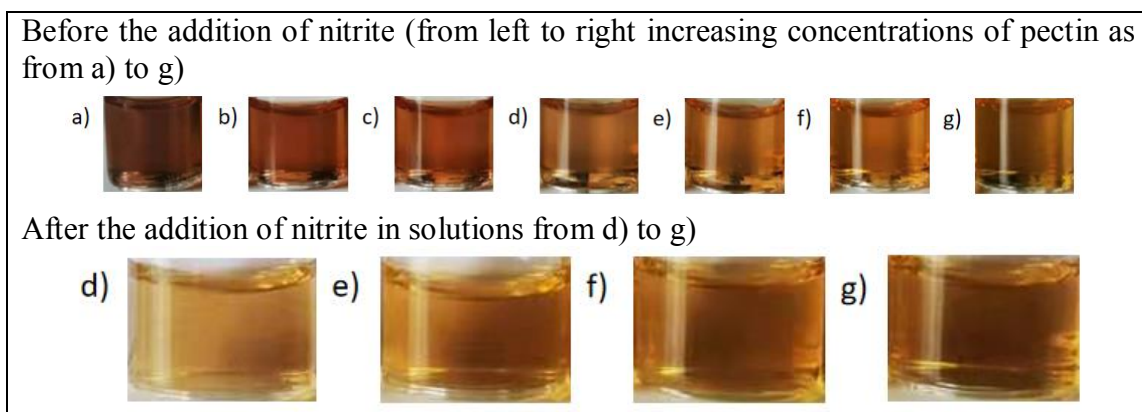


Figure 3.4.18 Optical images of solutions containing the $\text{Ag}@\text{[SiW}_{12}\text{O}_{40}]^{4-}$ as described in Figure 3.4.15. Upper panel, before the addition of nitrite, lower panel after the addition of nitrite.

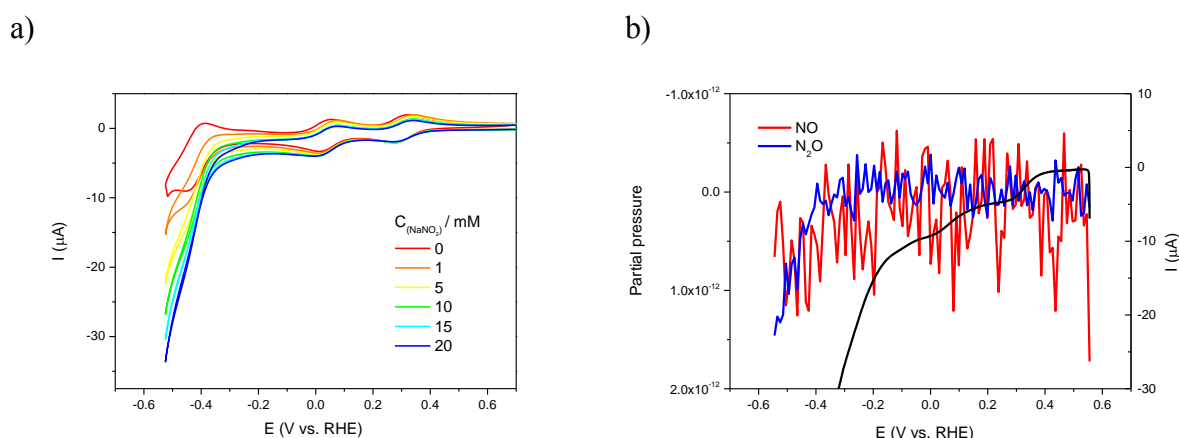


Figure 3.4.19 a) Cyclic voltammetry of $\text{Ag}@\text{[SiW}_{12}\text{O}_{40}]^{4-}$ solution with GC electrode at pH 5 and increasing concentration of nitrite. Experimental conditions: scan rate, 20 mVs^{-1} ; pH 5, 1 M CH_3COOLi . Electrolyte contains totally 0.5 mM $\text{[SiW}_{12}\text{O}_{40}]^{4-}$, 0.133 mM, $\text{Ag}@\text{[SiW}_{12}\text{O}_{40}]^{4-}$ NPs and 0.2 mg/mL pectin; b) DEMS study of nitrite reduction with $\text{Ag}@\text{[SiW}_{12}\text{O}_{40}]^{4-}$ and GC electrode. Experimental conditions: scan rate, 0.5 mV s^{-1} ; pH 5, 1 M CH_3COOLi . Electrolyte contains totally 0.5 mM $\text{[SiW}_{12}\text{O}_{40}]^{4-}$, 0.133 mM, $\text{Ag}@\text{[SiW}_{12}\text{O}_{40}]^{4-}$ NPs and 0.2 mg/mL pectin

3.5 Conclusion

In this chapter, the tandem catalysis of nitrous acid (HNO_2) reduction to N_2O is performed by silver electrode and Keggin polyoxometalates (POMs). Differential electrochemical mass spectrometry (DEMS) was used to measure the gaseous products (NO , N_2O). Catalysis performed by silver electrode alone was compared with the one performed by Keggin polyoxometalates alone (using a glassy carbon electrode) and with the one performed by the same POMs and silver electrode together (mixed homogenous-heterogeneous catalysis). The following conclusions can be drawn:

1. The HNO_2 reduction to NO is diminished when silver alone is used as working electrode in a sulfate electrolyte.

2. The HNO_2 reduction to NO is catalyzed by the studied POMs in the same manner irrespective of the type of working electrode (Ag or GC).

3. A tandem catalysis was obtained when the POMs having the most positive redox potentials (i.e. $[\text{SiW}_{12}\text{O}_{40}]^{4-}$, $[\text{PW}_{12}\text{O}_{40}]^{3-}$ and $[\text{SiMo}_{12}\text{O}_{40}]^{4-}$) are used with Ag working electrode. This is sustained by a positive shift of the N_2O onset potential. This is explained by the increase in the local concentration of nitric oxide as a consequence of the nitrite reduction catalyzed by POMs. In the same time, silver electrode is promoting the formation of N_2O formation via a NO dimer, a mechanism completely different than the one involving the HNO intermediate.

In the second part of this chapter, silver nanoparticles stabilized by POMs ($[\text{H}_2\text{W}_{12}\text{O}_{40}]^{6-}$ and $[\text{SiW}_{12}\text{O}_{40}]^{4-}$) were synthesized using two methods: i) with a previously photoreduced POM and ii) with a previously electroreduced POM. In the electrochemical experiments, the Ag@POM NPs were used dispersed in solution, after dilution with the desired electrolyte. The stability of these NPs is very poor, being affected by the low pH, by the high concentration of the electrolyte and by the concentration of nitrite. The use of pectin allowed the stabilization of these NPs, but no tandem catalysis between the silver core and the surrounding POM was observed for nitrite reduction at pH 5. It is supposed that the key species, nitric oxide, is too strongly adsorbed on the nanoparticles to allow a synergy effect to appear.

3.6 References

1. (a) De Groot, M.; Koper, M., The influence of nitrate concentration and acidity on the electrocatalytic reduction of nitrate on platinum. *Journal of Electroanalytical Chemistry* **2004**, 562 (1), 81-94; (b) Dima, G.; De Voos, A.; Koper, M., Electrocatalytic reduction of nitrate at low concentration on coinage and transition-metal electrodes in acid solutions. *Journal of Electroanalytical Chemistry* **2003**, 554, 15-23; (c) Rosca, V.; Koper, M. T., Mechanism of electrocatalytic reduction of nitric oxide on Pt (100). *The Journal of Physical Chemistry B* **2005**, 109 (35), 16750-16759; (d) Duca, M.; Van der Klugt, B.; Koper, M., Electrocatalytic reduction of nitrite on transition and coinage metals. *Electrochimica Acta* **2012**, 68, 32-43; (e) Duca, M.; Van Der Klugt, B.; Hasnat, M.; Machida, M.; Koper, M., Electrocatalytic reduction of nitrite on a polycrystalline rhodium electrode. *Journal of Catalysis* **2010**, 275 (1), 61-69; (f) Duca, M.; Cucarella, M. O.; Rodriguez, P.; Koper, M. T., Direct reduction of nitrite to N_2 on a Pt (100) electrode in alkaline media. *Journal of the American Chemical Society* **2010**, 132 (51), 18042-18044.
2. De Voos, A.; Beltramo, G.; Van Riet, B.; Van Veen, J.; Koper, M., Mechanisms of electrochemical reduction and oxidation of nitric oxide. *Electrochimica Acta* **2004**, 49 (8), 1307-1314.
3. (a) Hara, K.; Kamata, M.; Sonoyama, N.; Sakata, T., Electrocatalytic reduction of NO on metal electrodes and gas diffusion electrodes in an aqueous electrolyte. *Journal of Electroanalytical Chemistry* **1998**, 451 (1-2), 181-186; (b) Jigato, M. P.; King, D. A.; Yoshimori, A., The chemisorption of spin polarised NO on Ag {111}. *Chemical physics letters* **1999**, 300 (5-6), 639-644; (c) Brown, W. A.; King, D. A., NO chemisorption and reactions on metal surfaces: a new perspective. ACS Publications: 2000; Vol. 104, pp 2578-2595; (d) Liu, Z.-P.; Jenkins, S. J.; King, D. A., Car exhaust catalysis from first principles: selective NO reduction under excess O_2 conditions on Ir. *Journal of the American Chemical Society* **2004**, 126 (34), 10746-10756; (e) Gómez, R.;

- Weaver, M. J., Electrochemical infrared studies of monocrystalline iridium surfaces. 3. Adsorbed nitric oxide and carbon monoxide as probes of Ir (100) interfacial structure. *The Journal of Physical Chemistry B* **1998**, *102* (19), 3754-3764.
4. Chalkley, L., The extent of the photochemical reduction of phosphotungstic acid. *The Journal of Physical Chemistry* **1952**, *56* (9), 1084-1086.
5. Troupis, A.; Hiskia, A.; Papaconstantinou, E., Reduction and recovery of metals from aqueous solutions with polyoxometallates. *New Journal of Chemistry* **2001**, *25* (3), 361-363.
6. Troupis, A.; Hiskia, A.; Papaconstantinou, E., Synthesis of metal nanoparticles by using polyoxometalates as photocatalysts and stabilizers. *Angewandte Chemie International Edition* **2002**, *41* (11), 1911-1914.
7. Troupis, A.; Triantis, T.; Hiskia, A.; Papaconstantinou, E., Rate-Redox-Controlled Size-Selective Synthesis of Silver Nanoparticles Using Polyoxometalates. Wiley Online Library: 2008.
8. Costa-Coquelard, C.; Schaming, D.; Lampre, I.; Ruhlmann, L., Photocatalytic reduction of Ag_2SO_4 by the Dawson anion $\alpha\text{-}[\text{P}_2\text{W}_{18}\text{O}_{62}]^{6-}$ and tetracobalt sandwich complexes. *Applied Catalysis B: Environmental* **2008**, *84* (3-4), 835-842.
9. Horanyi, G.; Rizmayer, E.; Konya, J., Radiotracer study of anion adsorption at silver electrodes in acidic medium. *Journal of electroanalytical chemistry and interfacial electrochemistry* **1984**, *176* (1-2), 339-348.
10. Smoliński, S.; Zelenay, P.; Sobkowski, J., Effect of surface order on adsorption of sulfate ions on silver electrodes. *Journal of Electroanalytical Chemistry* **1998**, *442* (1-2), 41-47.
11. (a) Mbomekallé, I.-M.; López, X.; Poblet, J. M.; Sécheresse, F.; Keita, B.; Nadjó, L., Influence of the heteroatom size on the redox potentials of selected polyoxoanions. *Inorganic chemistry* **2010**, *49* (15), 7001-7006; (b) Pope, M. T.; Varga Jr, G. M., Heteropoly blues. I. Reduction stoichiometries and reduction potentials of some 12-tungstates. *Inorganic Chemistry* **1966**, *5* (7), 1249-1254.
12. Pérez-Gallent, E.; Figueiredo, M. C.; Katsounaros, I.; Koper, M. T., Electrocatalytic reduction of Nitrate on Copper single crystals in acidic and alkaline solutions. *Electrochimica Acta* **2017**, *227*, 77-84.
13. Milhano, C.; Pletcher, D., The electrochemistry and electrochemical technology of nitrate. In *Modern Aspects of Electrochemistry*, No. 45, Springer: 2009; pp 1-61.
14. De Voors, A.; Koper, M.; Van Santen, R.; Van Veen, J., Mechanistic study on the electrocatalytic reduction of nitric oxide on transition-metal electrodes. *Journal of Catalysis* **2001**, *202* (2), 387-394.
15. Duca, M.; Kavvadia, V.; Rodriguez, P.; Lai, S.; Hoogenboom, T.; Koper, M., New insights into the mechanism of nitrite reduction on a platinum electrode. *Journal of Electroanalytical Chemistry* **2010**, *649* (1-2), 59-68.
16. Flores-Santana, W.; Salmon, D. J.; Donzelli, S.; Switzer, C. H.; Basudhar, D.; Ridnour, L.; Cheng, R.; Glynn, S. A.; Paolucci, N.; Fukuto, J. M., The specificity of nitroxyl chemistry is unique among nitrogen oxides in biological systems. *Antioxidants & redox signaling* **2011**, *14* (9), 1659-1674.
17. Fang, Y.; Zheng, Y.; Fang, T.; Chen, Y.; Zhu, Y.; Liang, Q.; Sheng, H.; Li, Z.; Chen, C.; Wang, X., Photocatalysis: an overview of recent developments and technological advancements. *Science China Chemistry* **2020**, *63* (2), 149-181.
18. Kim, J.; Lee, L.; Niece, B. K.; Wang, J. X.; Gewirth, A. A., Formation of ordered multilayers from polyoxometalates and silver on electrode surfaces. *The Journal of Physical Chemistry B* **2004**, *108* (23), 7927-7933.
19. (a) Zoladek, S.; Blicharska-Sobolewska, M.; Krata, A. A.; Rutkowska, I. A.; Wadas, A.; Miecznikowski, K.; Negro, E.; Vezzù, K.; Di Noto, V.; Kulesza, P. J., Heteropolytungstate-assisted fabrication and deposition of

- catalytic silver nanoparticles on different reduced graphene oxide supports: electroreduction of oxygen in alkaline electrolyte. *Journal of Electroanalytical Chemistry* **2020**, 875, 114694; (b) Troupis, A.; Gkika, E.; Hiskia, A.; Papaconstantinou, E., Photocatalytic reduction of metals using polyoxometallates: recovery of metals or synthesis of metal nanoparticles. *Comptes Rendus Chimie* **2006**, 9 (5-6), 851-857.
20. Lu, X.; Rycenga, M.; Skrabalak, S. E.; Wiley, B.; Xia, Y., Chemical synthesis of novel plasmonic nanoparticles. *Annual review of physical chemistry* **2009**, 60, 167-192.
21. Agnihotri, S.; Mukherji, S.; Mukherji, S., Size-controlled silver nanoparticles synthesized over the range 5–100 nm using the same protocol and their antibacterial efficacy. *Rsc Advances* **2014**, 4 (8), 3974-3983.
22. (a) Nemiwal, M.; Zhang, T. C.; Kumar, D., Pectin modified metal nanoparticles and their application in property modification of biosensors. *Carbohydrate Polymer Technologies and Applications* **2021**, 2, 100164; (b) Ahmed, H. B.; Zahran, M.; Emam, H. E., Heatless synthesis of well dispersible Au nanoparticles using pectin biopolymer. *International journal of biological macromolecules* **2016**, 91, 208-219; (c) Mani, V.; Devasenathipathy, R.; Chen, S.-M.; Vasantha, V.; Ali, M. A.; Huang, S.-T.; Al-Hemaid, F. M., A simple electrochemical platform based on pectin stabilized gold nanoparticles for picomolar detection of biologically toxic amitrole. *Analyst* **2015**, 140 (16), 5764-5771; (d) Devasenathipathy, R.; Karuppiah, C.; Chen, S.-M.; Mani, V.; Vasantha, V. S.; Ramaraj, S., Highly selective determination of cysteine using a composite prepared from multiwalled carbon nanotubes and gold nanoparticles stabilized with calcium crosslinked pectin. *Microchimica Acta* **2015**, 182 (3), 727-735; (e) Zahran, M.; Ahmed, H. B.; El-Rafie, M., Facile size-regulated synthesis of silver nanoparticles using pectin. *Carbohydrate polymers* **2014**, 111, 971-978; (f) Devasenathipathy, R.; Mani, V.; Chen, S.-M.; Arulraj, D.; Vasantha, V., Highly stable and sensitive amperometric sensor for the determination of trace level hydrazine at cross linked pectin stabilized gold nanoparticles decorated graphene nanosheets. *Electrochimica Acta* **2014**, 135, 260-269.
23. (a) Rodriguez-Gattorno, G.; Diaz, D.; Rendon, L.; Hernandez-Segura, G., Metallic nanoparticles from spontaneous reduction of silver (I) in DMSO. Interaction between nitric oxide and silver nanoparticles. *The Journal of Physical Chemistry B* **2002**, 106 (10), 2482-2487; (b) Citra, A.; Andrews, L., A spectroscopic and theoretical investigation of charge transfer complexes between silver and nitric oxide: Infrared spectra and density functional calculations of $\text{AgNO}^{+0,-}$ and $\text{Ag}_x(\text{NO})_y$ clusters (x, y= 1, 2) in solid argon and neon. *The Journal of Physical Chemistry A* **2001**, 105 (13), 3042-3051; (c) Carley, A.; Davies, P.; Roberts, M.; Santra, A.; Thomas, K., Coadsorption of carbon monoxide and nitric oxide at Ag (111): evidence for a CO–NO surface complex. *Surface science* **1998**, 406 (1-3), L587-L591; (d) Ludviksson, A.; Huang, C.; Jänsch, H.; Martin, R., Isotopic studies of the reaction of NO on silver surfaces. *Surface science* **1993**, 284 (3), 328-336.

**Chapter IV: Nitrite electroreduction catalyzed
by hybrid compounds of Keggin
polyoxometalates and 1-butyl-3-
vinylimidazolium**

4.1 Introduction

In this chapter, we describe an immobilization method of four Keggin-type POMs by using the reaction with an ionic liquid, 1-butyl-3-vinylimidazolium (BVIM) bromide. The reaction yields an insoluble salt that is mixed with carbon powder and Nafion in order to prepare an ink. This ink is casted on glassy carbon electrodes and the electrochemical activity for nitrite reduction is measured.

Indeed, the reaction between POMs and ionic liquid has been proposed for several examples, but only the Mo-based Keggin POM ($[\text{PMo}_{12}\text{O}_{40}]^{3-}$) was used in development of sensors for nitrite reduction. As ionic liquid, the following compounds were tested: 1-n-Butyl-3-methylimidazolium tetrafluoroborate (BMIMBF_4)¹, 1-methyl-3-methylimidazolium tetrafluoroborate (EMIMBF_4), their bromide analogues², and N-dodecyl pyridinium hexafluorophosphate ($[\text{C}_{12}\text{Py}]\text{PF}_6$)³. When used as binder in the construction of a carbon paste electrode, the ionic liquid contributed to the enhancement of conductivity and behaved as a charge-transfer bridge, facilitating the electrons intake from the POM¹. It was also shown that the hydrophobic alkyl chain of ($[\text{C}_{12}\text{Py}]\text{PF}_6$) strongly interacts with MWNCTs, thus reducing the charge transfer resistance between the immobilized POM and the electrode.³

In our work, we have chosen another ionic liquid, BVIM, for its ability to polymerize. Indeed, using a radical polymerization of the vinyl group, a polymerized ionic liquid (PIL) containing onium cations fixed on the main chain is obtained.⁴ This PIL was used for immobilization of glucose oxidase⁵ and hemoglobin⁶, based on self-assembly between positive groups of the polymer and negative groups of the biological macromolecule. In fact, we have conducted preliminary work to immobilize our POMs by using this PIL (and reduced graphene oxide). Nevertheless, the obtained electrodes suffered from a very high capacitive current and high charge transfer resistance, mostly due to a dramatic decrease of the ionic conductivity of the PIL. This phenomenon is well documented⁴ and it is ascribed to the reduced number of mobile ions and to an important increase of glass transition temperature (TG). Based on this, we have decided to immobilize our POMs by using the simple and direct reaction with BVIM, in which the exchange of POMs inherent cation (Na^+ , K^+ , NH_4^+) with the imidazolium cation leads to an insoluble salt.

4.2 Synthesis of hybrid compounds BVIM-POM

The solubility of POM can be altered by changing the counter-cation, especially by using bulky cations such as tetra-alkyl ammonium. Another option is the use of ionic liquids.⁷ In our method, we have used 1-butyl-3-vinylimidazolium (BVIM) cation with the following protocol:

- Solution A: 3 mL containing 3×10^{-5} moles of Keggin POMs ($[\text{PW}_{12}\text{O}_{40}]^{3-}$, $[\text{SiW}_{12}\text{O}_{40}]^{4-}$, $[\text{BW}_{12}\text{O}_{40}]^{5-}$, and $[\text{H}_2\text{W}_{12}\text{O}_{40}]^{6-}$)
- Solution B: 1 mL containing 2.4×10^{-4} moles (56 mg) 1-butyl-3-vinylimidazolium bromide [BVIM]Br
- Mix solution A and B. Some white precipitate is formed immediately.
- The mixed solution is stirred for 15 mins then filtered. The white precipitate is washed by deionized water several times to remove excess ions.
- The collected precipitate was naturally air-dried at room temperature. BVIM-POM salt is thus synthesized.

CHNS elemental analysis was used to compute the percentage of C and N in the final BVIM-POM salts. For all the four salts the values correspond to the complete replacement of initial cations by the BVIM (Table 4.2.1). Thus, the final composition is (BVIM)₆[H₂W₁₂O₄₀], (BVIM)₅[BW₁₂O₄₀], (BVIM)₄[SiW₁₂O₄₀], and (BVIM)₃[PW₁₂O₄₀].

Table 4.2.1 Results of CHNS analysis of BVIM-POMs

Compound	% C calculated (found)	% H calculated (found)	% N calculated (found)
(BVIM) ₆ [H ₂ W ₁₂ O ₄₀]	17.3 (17.1)	2.4 (2.5)	4.5 (4.0)
(BVIM) ₅ [BW ₁₂ O ₄₀]	14.9 (14.9)	2.1 (2.1)	3.9 (3.6)
(BVIM) ₄ [SiW ₁₂ O ₄₀]	12.4 (12.3)	1.7 (1.8)	3.2 (2.7)
(BVIM) ₃ [PW ₁₂ O ₄₀]	9.7 (9.8)	1.4 (1.4)	2.5 (2.2)

4.3 Characterization of BVIM-POM

4.3.1 FT-IR characterization of BVIM-POM

Firstly, Figure 4.3.1 shows the FT-IR spectrum of the 1-butyl-3-vinylimidazolium bromide (BVIMBr) alone. The characteristic bands of imidazolium ring are:

- C-H in imidazole ring stretching between 2775-3187 cm⁻¹,
- Ring stretching 1567, 1543, 1465 cm⁻¹,
- H-C-C and H-C-N in imidazole ring bending 1161-1171 cm⁻¹,
- In-plane imidazole ring bending 881 cm⁻¹,
- Out of plane C-H bending of imidazolium ring 738 cm⁻¹,
- Imidazolium C-N-C 657 cm⁻¹.

Our BVIMBr contains a vinyl group for which the characteristic band are observed at 1652 cm⁻¹ (C=C stretching) and 927 cm⁻¹ (=C-H bending). The broad band at 3400 cm⁻¹ corresponds to water as the compound presents a lot of moisture at room temperature.

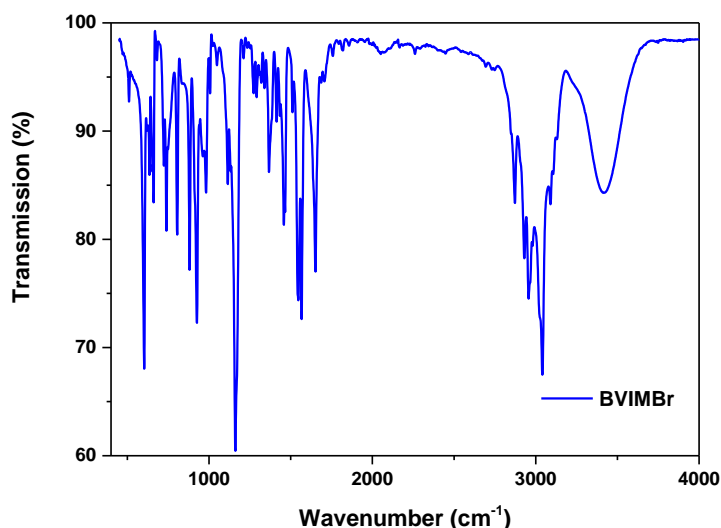


Figure 4.3.1 FT-IR spectrum of 1-butyl-3-vinylimidazolium bromide (BVIMBr).

The characteristic bands of $[\text{H}_2\text{W}_{12}\text{O}_{40}]^{6-}$ cluster are:

- W-O_{terminal} stretching 927 cm^{-1} ,
- edge sharing W-O-W stretching 860 cm^{-1} ,
- corner sharing W-O-W stretching 720 cm^{-1} .

The Heteroatom-Oxygen stretching bond is different in each POM, thus appearing at different positions. For $[\text{BW}_{12}\text{O}_{40}]^{5-}$ and $[\text{SiW}_{12}\text{O}_{40}]^{4-}$, the B-O and Si-O bonds are hidden by the W-O-W stretching, for $[\text{PW}_{12}\text{O}_{40}]^{3-}$ the P-O stretching is visible at 1548 cm^{-1} . For $(\text{NH}_4)_6[\text{H}_2\text{W}_{12}\text{O}_{40}]$, there is no heteroatom -oxygen bond, but the N-H stretching in ammonium group is visible at 1400 cm^{-1} . A strong adsorption band corresponding to O-H bending at $\sim 1610\text{ cm}^{-1}$ is visible for $[\text{PW}_{12}\text{O}_{40}]^{3-}$, $[\text{SiW}_{12}\text{O}_{40}]^{4-}$ and $[\text{BW}_{12}\text{O}_{40}]^{5-}$ and less visible for $[\text{H}_2\text{W}_{12}\text{O}_{40}]^{6-}$ (this compound contains less crystalline water). Actually, the constitution water molecules were determined from TGA analysis (vide infra) as shown in Figures 4.3.2 and 4.3.3. FT-IR spectra of the hybrid materials prove that the structure of both 1-butyl-3-vinylimidazolium cation and the POM anion (Figures 4.3.2 and 4.3.3) are preserved because several characteristic bands of both POMs and BVIM^+ are visible:

- Ring stretching $1567, 1543, 1465\text{ cm}^{-1}$,
- 1652 cm^{-1} (C=C stretching of vinyl group),
- Imidazole H-C-C and H-C-N bending $1159 - 1171\text{ cm}^{-1}$,
- W-O_{terminal} stretching 923 cm^{-1} ,
- Edge sharing W-O-W stretching 867 cm^{-1} ,
- Corner sharing W-O-W stretching 753 cm^{-1} .

Interestingly, the water content of hybrid materials is reduced in a POM dependent manner. For example, for $(\text{BVIM})_6[\text{H}_2\text{W}_{12}\text{O}_{40}]$ and $(\text{BVIM})_4[\text{SiW}_{12}\text{O}_{40}]$ the large band at 3400 cm^{-1} is almost completely disappeared. This phenomenon was observed for other POM-ionic liquid hybrid materials, such as the one resulting from pairing $[\text{H}_4\text{PW}_{18}\text{O}_{62}]^{7-}$ or $[\text{P}_2\text{W}_{18}\text{O}_{60}]^{6-}$ with 1-butyl-3-methylimidazolium $[\text{BMIM}]^+$ cation.⁷ But for $(\text{BVIM})_5[\text{BW}_{12}\text{O}_{40}]$ and $(\text{BVIM})_3[\text{PW}_{12}\text{O}_{40}]$ the water is still present, especially in the second compound. The reason for this is not clear, but it can be noted that parent POMs of these two compounds initially contain a higher number of constitution water molecules as determined from TG analysis (see below).

Table 4.3.1 Summary of FT-IR spectra of POMs and hybrid materials peak vibration mode

BVIMBr	$(\text{NH}_4)_6\text{H}_2\text{W}_{12}\text{O}_{40} \cdot 4\text{H}_2\text{O}$	$(\text{BVIM})_6\text{H}_2\text{W}_{12}\text{O}_{40}$	$\text{K}_5\text{BW}_{12}\text{O}_{40} \cdot 7\text{H}_2\text{O}$	$(\text{BVIM})_5\text{BW}_{12}\text{O}_{40}$	Vibration mode
3400	3543	3524 (shoulder)	3554	3550	Water
2775-3187	n.a.	2775-3197	n.a.	2787-3204	C-H stretching in imidazole ring
n.a.	1600	n.v.	1608	n.a.	O-H bending
1652	n.a.	1652	n.a.	1651	C=C
1567, 1543, 1465	n.a.	1566, 1543, 1460	n.a.	1567, 1574, 1463	Imidazole ring stretching
n.a.	1400	n.v.	n.a.	n.a.	-N-H (from NH_4^+) stretching
1161-1171	n.a.	1166	n.a.	1668	Imidazole H-C-C and H-C-N bending
n.a.	n.a.	n.a.	n.a.	n.a.	P-O stretching
n.a.	927	923	952	949	W-O _{terminal} str
n.a.	860	867	888	892	Edge sharing W-O-W str
n.a.	720	753	795	797	Corner W-O-W str

Table 4.3.1 Summary of FT-IR spectra of POMs and hybrid materials peak vibration mode (follow up)

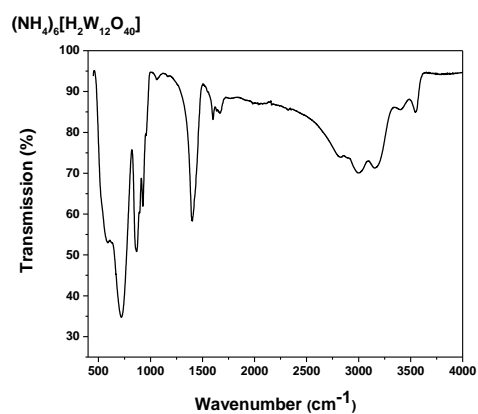
$\text{K}_4\text{SiW}_{12}\text{O}_{40} \cdot 4\text{H}_2\text{O}$	$(\text{BVIM})_4\text{SiW}_{12}\text{O}_{40}$	$\text{Na}_3\text{PW}_{12}\text{O}_{40} \cdot 12\text{H}_2\text{O}$	$(\text{BVIM})_3\text{PW}_{12}\text{O}_{40}$	Vibration mode
3582	3507 (shoulder)	3527	3379 (strong)	Water
n.a.	2777-3214	n.a.	2874-3183	C-H stretching in imidazole ring
1617	n.v.	1612	n.v.	O-H bending
n.a.	1652	n.a.	1649	C=C
n.a.	1569, 1547, 1460	n.a.	1568, 1547, 1461	Imidazole ring stretching
n.a.	n.a.	n.a.	n.a.	-N-H (from NH_4^+) stretching
n.a.	1167	n.a.	1167	Imidazole H-C-C and H-C-N bending
n.a.	n.a.	1548	1547	P-O stretching
977	969	1057	1007	W-O _{terminal} str
910	915	974	908	Edge sharing W-O-W str
744	771	781	789	Corner W-O-W str

n.a. = not applicable

n.v. = not visible

str = stretching

a)



b)

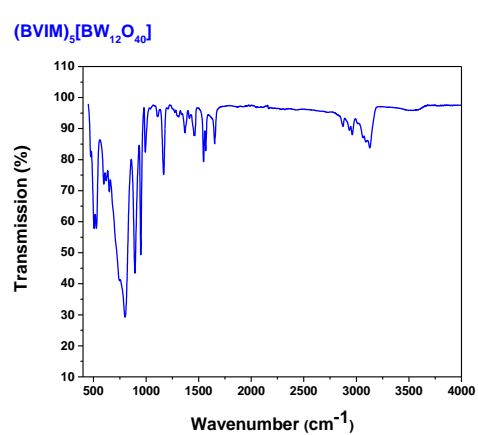
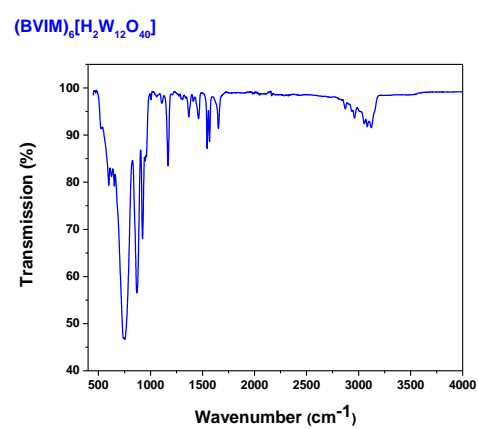
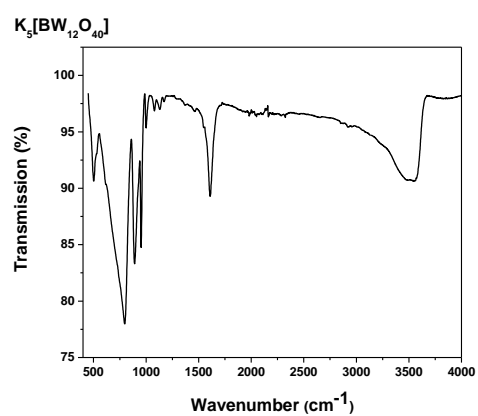
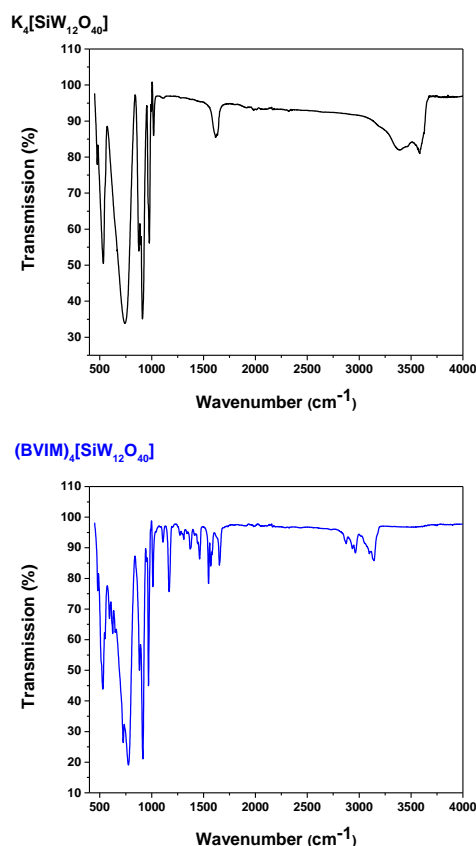


Figure 4.3.2 FT-IR spectra of POMs and hybrid materials: a) $(\text{NH}_4)_6[\text{H}_2\text{W}_{12}\text{O}_{40}]$ and $(\text{BVIM})_6[\text{H}_2\text{W}_{12}\text{O}_{40}]$, b) $\text{K}_5[\text{BW}_{12}\text{O}_{40}]$ and $(\text{BVIM})_5[\text{BW}_{12}\text{O}_{40}]$.

a)



b)

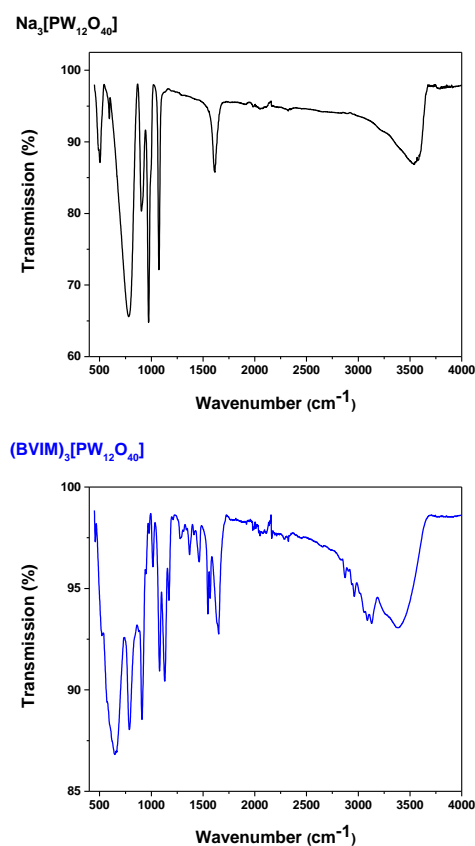


Figure 4.3.3 FT-IR spectra of POMs and hybrid materials: a) $K_4[SiW_{12}O_{40}]$ and $(BVIM)_4[SiW_{12}O_{40}]$, b) $Na_3[PW_{12}O_{40}]$ and $(BVIM)_3[PW_{12}O_{40}]$.

4.3.2 TGA characterization of BVIM-POM

The thermogravimetric behavior of BVIM, parent POMs and hybrid materials is displayed in Figures 4.3.4, 4.3.5 and 4.3.6. The TGA curve of BVIMBr shows a total weight loss starting at 300 °C and completing at 600 °C. This is attributed to the decomposition of ionic liquid. Thermal analysis of all parent POMs shows an initial mass loss from about 100 °C to 300 °C corresponding to the water loss since all POMs contain constitution water molecules. Besides, this analysis gives the possibility to compute exactly how many water molecules are present. Thus, we obtain $(NH_4)_6[H_2W_{12}O_{40}] \cdot 4H_2O$, $K_5[BW_{12}O_{40}] \cdot 7H_2O$, $K_4[SiW_{12}O_{40}] \cdot 4H_2O$ and $Na_3[PW_{12}O_{40}] \cdot 12H_2O$. Thus, the water loss is accounted for 3%, 4%, 2% and 7% respectively. Interestingly, this happens in two steps (as shown by two endothermic pics on the heat flow axis) for all POMs except $K_4[SiW_{12}O_{40}] \cdot 4H_2O$ for which only one step is visible. Above 300 °C a slight slow decomposition of POMs is observed, except for $(NH_4)_6[H_2W_{12}O_{40}] \cdot 3H_2O$ for which a clear decomposition from 300 to 400 °C (endothermic peak), accounting for 4 % of mass loss is observed. This is probably associated to the decomposition of accompanying ammonium cation happening before the decomposition of the Keggin anion. For all hybrid materials, the thermal stability is improved as no mass loss is observed up to 300 °C. This is explained by the fact that almost no water is available in the hybrid materials. This corroborates with the FT-IR spectra that

show a clear decrease in the water content (vide supra). Above 300 °C a significant weight loss of about 24%, 20%, 16% and 13% is observed for the hybrid materials. This is associated with the decomposition of the organic cation and corresponds to the theoretical percentage of the cation in the BVIM-POM materials.

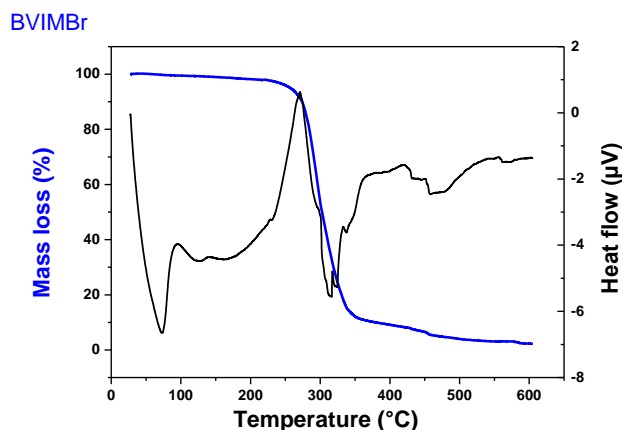
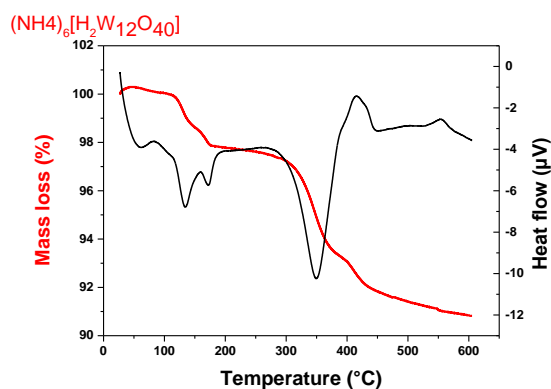


Figure 4.3.4 TG analysis of 1-butyl-3-vinylimidazolium bromide (BVIMBr).

a)



b)

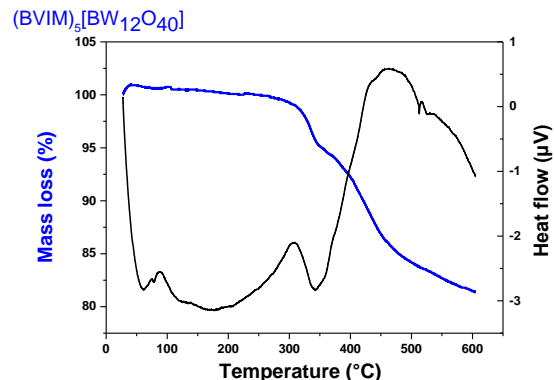
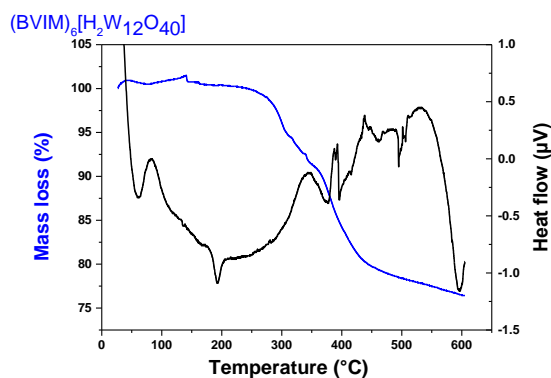
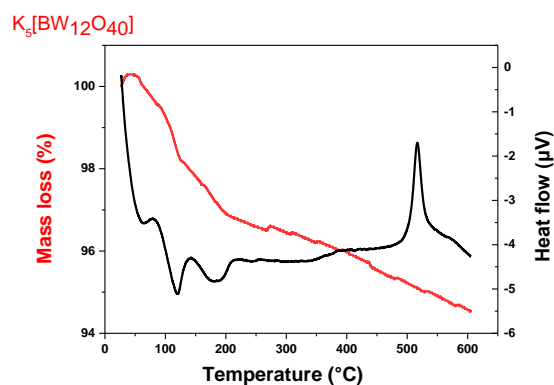


Figure 4.3.5 TG analysis of POMs and hybrid materials: a) $(\text{NH}_4)_6[\text{H}_2\text{W}_{12}\text{O}_{40}]$ and $(\text{BVIM})_6[\text{H}_2\text{W}_{12}\text{O}_{40}]$, b) $\text{K}_5[\text{BW}_{12}\text{O}_{40}]$ and $(\text{BVIM})_5[\text{BW}_{12}\text{O}_{40}]$.

a)

b)

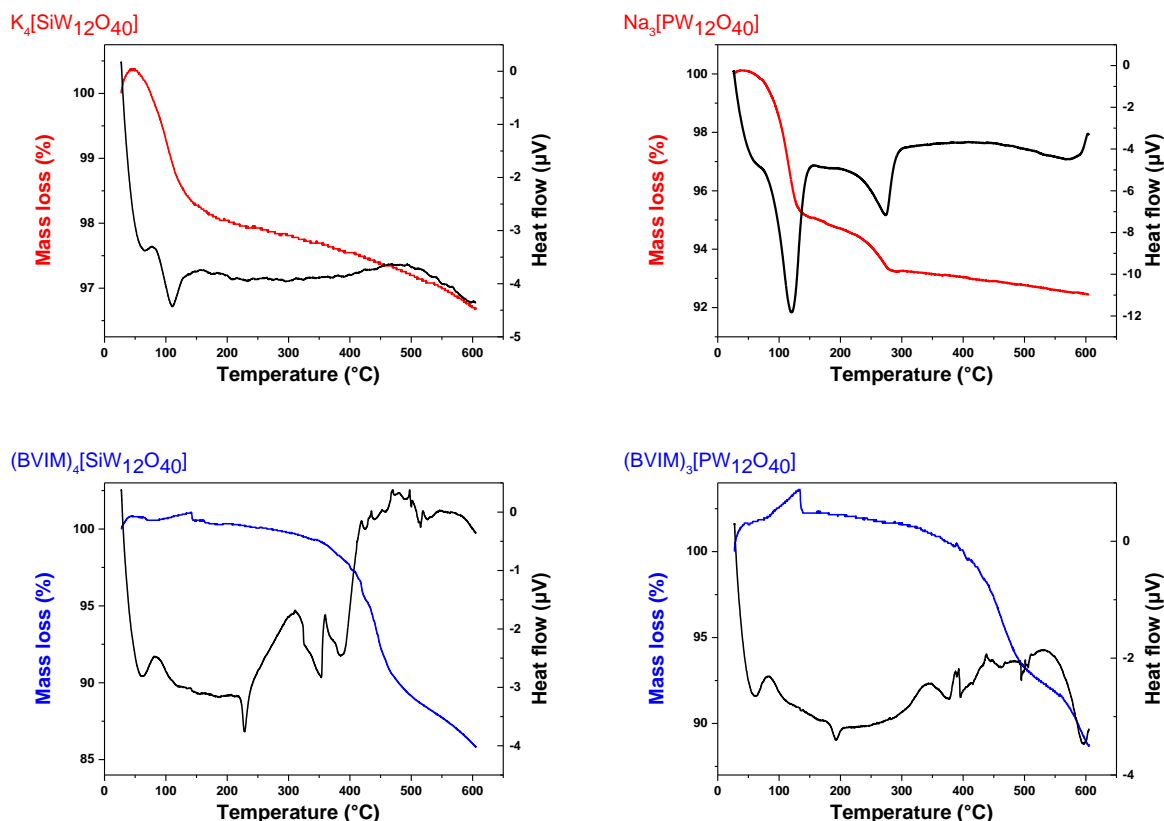
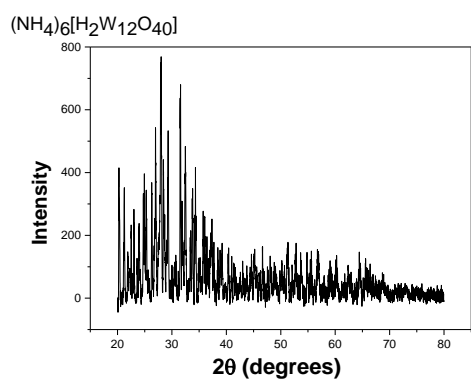


Figure 4.3.6 TG analysis of a) $K_4[SiW_{12}O_{40}]$ and $(BVIM)_4[SiW_{12}O_{40}]$, b) $Na_3[PW_{12}O_{40}]$ and $(BVIM)_3[PW_{12}O_{40}]$.

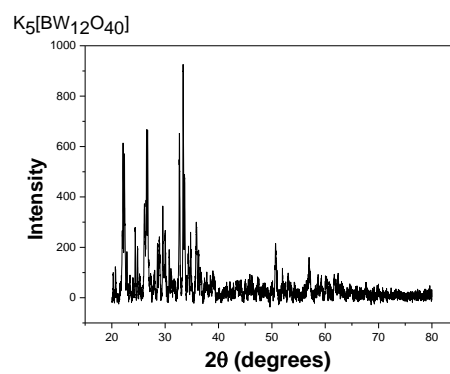
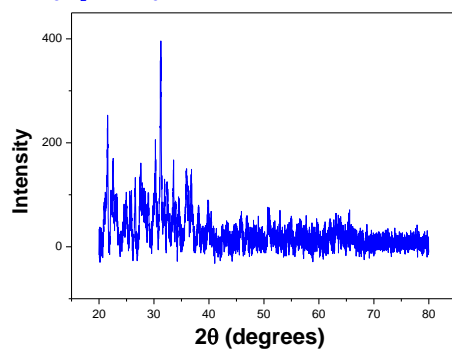
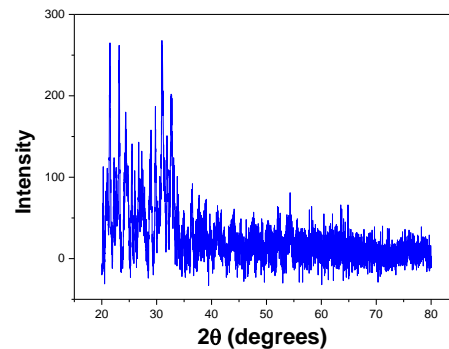
4.3.3 XRD characterization of BVIM-POM

Figure 4.3.7 shows the powder X-ray diffraction pattern of parent POMs and hybrid materials. Figure 4.3.8 shows XRD spectra obtained from references in literature mainly for the acid form of the POMs. Our XRD patterns show that pure Keggin salts have a better defined structure compared to hybrid BVIM-POM materials. This can be explained by the changes in the secondary structure of the POMs induced by the ionic liquid. These changes are explained with the removal of constitution water molecules but also by the replacement of small cations (NH_4^+ , K^+ , Na^+) with a bulkier cation ($BVIM^+$). A similar behavior was observed for other examples of hybrid materials, such as the ones obtained from Dawson-type POMs $K_7[H_4PW_{18}O_{62}]$ and $K_6[P_2W_{18}O_{62}]$ and 1-butyl-3-methylimidazolium tetrafluoroborate.⁷ Particularly for $(BVIM)_3[PW_{12}O_{40}]$ the structure is completely amorphous.

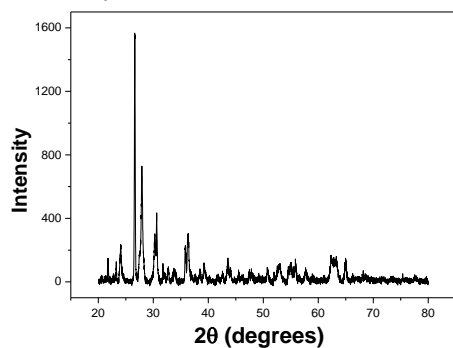
a)



b)

(BVIM)₆[H₂W₁₂O₄₀](BVIM)₃[PW₁₂O₄₀]

c)

 $\text{K}_4[\text{SiW}_{12}\text{O}_{40}]$ 

d)

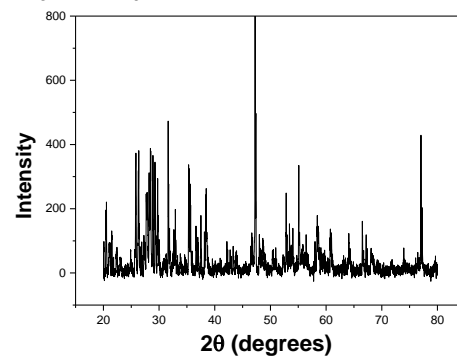
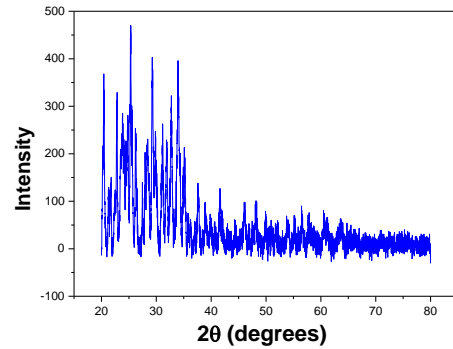
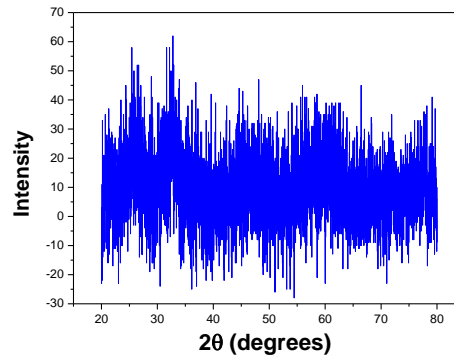
 $\text{Na}_3[\text{PW}_{12}\text{O}_{40}]$ (BVIM)₄[SiW₁₂O₄₀](BVIM)₃[PW₁₂O₄₀]

Figure 4.3.7 XRD spectra of parent POMs and hybrid BVIM-POMs.

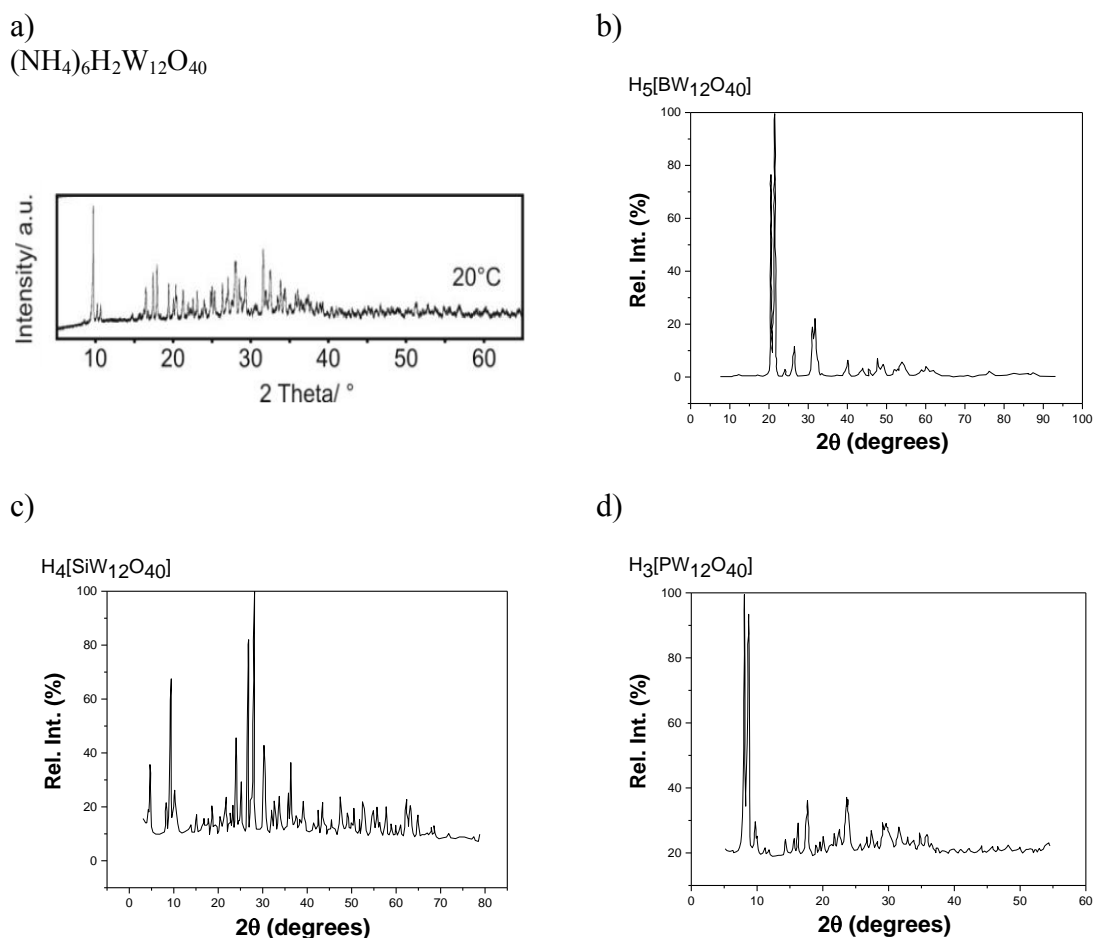


Figure 4.3.8 XRD spectra of various form of Keggin POMs from references: a) $(\text{NH}_4)_6\text{H}_2\text{W}_{12}\text{O}_{40}$ and acid form;⁸ b) $\text{H}_5\text{BW}_{12}\text{O}_{40}$;⁹ c) $\text{H}_4\text{SiW}_{12}\text{O}_{40}$;¹⁰ d) $\text{H}_3\text{PW}_{12}\text{O}_{40}$.¹¹

4.4 Preparation of BVIM-POM/C electrodes

The obtained BVIM-POM salt white powder was barely dispersed in water (10 mg/mL) using ultrasonic bath. In order to obtain an ink that could be cast on the electrode surface, carbon black was firstly dispersed in water (3 mg/mL) containing 10 % Nafion (Nafion stock solution is 5. wt.% dispersion in low aliphatic alcohols and water (15 - 20 %)). This suspension was mixed with BVIM-POM solution in a 1:2 v/v ratio. From this ink, 5 μL ink were dropped evenly on the surface of the glassy carbon electrode and dried in air. Then, extra 5 μL of stock Nafion solution were dropped on the electrode and dried in air. Then BVIM-POM/C electrode is ready for use. All four hybrid materials were used to obtain these electrodes. As some small amount of the hybrid material may not be strongly fixed on the electrode surface, cyclic voltammetry was run in clean electrolyte for several cycles until the CV curve is stable. Then it can be assumed that the remaining ink on the surface of the GC electrode is stable. Subsequent DEMS and classic electrochemical runs were run in a pH 1 0.5 M Na_2SO_4 electrolyte containing only 10 mM $\text{Na}^{15}\text{NO}_2$.

4.5 Electrochemical behavior of GC/C/BVIM-POM electrodes

After the immobilization on glassy carbon electrode, it is important to notice the number of redox peaks and, if possible, the number of exchanged electrons. Figure 4.5.1 shows the cyclic voltammetry of immobilized BVIM-POMs (blue curves) in comparison with parent POMs in solution (black curves). For $(\text{BVIM})_6[\text{H}_2\text{W}_{12}\text{O}_{40}]$ two pairs of peaks, with similar current intensities, are observed. This is similar to parent $(\text{NH}_4)_6[\text{H}_2\text{W}_{12}\text{O}_{40}]$, suggesting that each peak corresponds to two exchanged electrons. For $(\text{BVIM})_5[\text{BW}_{12}\text{O}_{40}]$, only one pair of peaks is observed. The potential was not scanned to lower values because this leads to a degradation of the first pair of peaks. The parent $\text{K}_5[\text{BW}_{12}\text{O}_{40}]$ displays one electron wave followed by a five electrons wave at much lower potentials. It is possible that this is the case also for $(\text{BVIM})_5[\text{BW}_{12}\text{O}_{40}]$. For $(\text{BVIM})_4[\text{SiW}_{12}\text{O}_{40}]$, two pairs of peaks, with similar current intensities, are observed. This is similar to parent $\text{K}_4[\text{SiW}_{12}\text{O}_{40}]$, suggesting that each peak corresponds to one exchanged electron. The third pair of peaks could again not be observed because potential was not scanned to lower values to avoid a degradation of the first two pairs of peaks. Finally, for $(\text{BVIM})_3[\text{PW}_{12}\text{O}_{40}]$ two pairs of peaks are observed but with different current intensities (the first pair is smaller than the second one). It thus must be noted the peculiar redox behavior of the immobilized $(\text{BVIM})_3[\text{PW}_{12}\text{O}_{40}]$ (vide infra).

The redox behavior of immobilized hybrid BVIM-POMs is also analyzed by measuring the peak-to-peak separation (ΔE) (Table 4.5.1). For $(\text{BVIM})_6[\text{H}_2\text{W}_{12}\text{O}_{40}]$ and $(\text{BVIM})_5[\text{BW}_{12}\text{O}_{40}]$ values closed to zero are obtained, which is characteristic to a fully reversible redox system. For the other two hybrid POMs, values are around 0.020V, suggesting a small deviation from the reversible behavior. The quantity of immobilized BVIM-POMs was calculated from the total charge (Q) exchanged during the first cathodic wave (by computing the area of this peak) (Table 4.5.1). Very similar values were obtained for three BVIM-POMs, while the amount of immobilized $(\text{BVIM})_3[\text{PW}_{12}\text{O}_{40}]$ is smaller.

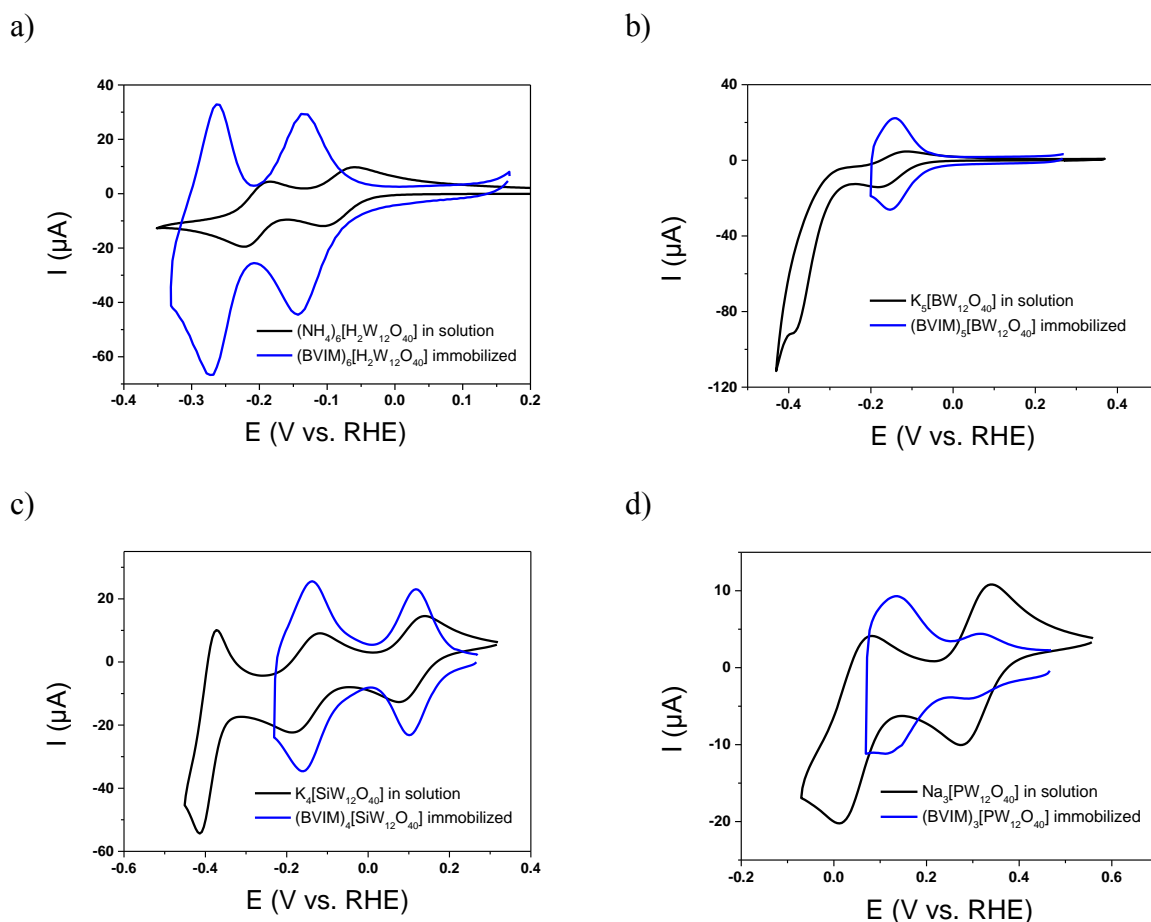


Figure 4.5.1 Cyclic voltammetry of immobilized hybrid BVIM-POM (blue line) compared to parent POM in solution (black line): a) $(\text{BVIM})_6[\text{H}_2\text{W}_{12}\text{O}_{40}]$, b) $(\text{BVIM})_5[\text{BW}_{12}\text{O}_{40}]$, c) $(\text{BVIM})_4[\text{SiW}_{12}\text{O}_{40}]$, d) $(\text{BVIM})_3[\text{PW}_{12}\text{O}_{40}]$. Experimental conditions: scan rate, 20 mVs^{-1} ; electrolyte, $0.5 \text{ M Na}_2\text{SO}_4$, pH 1; 1 mM POM (only for CV with POM in solution, black line).

Table 4.5.1 Peak to peak separation ($\Delta E = E_{\text{pa}} - E_{\text{pc}}$) and surface coverage for immobilized BVIM-POMs

POM	$\Delta E \text{ (V)}$ I st wave	$\Delta E \text{ (V)}$ II nd wave	Surface coverage ($\Gamma/\text{mol cm}^{-2}$)
$(\text{BVIM})_6[\text{H}_2\text{W}_{12}\text{O}_{40}]$	0.007	0.009	$5.8 \cdot 10^{-8}$
$(\text{BVIM})_5[\text{BW}_{12}\text{O}_{40}]$	0.009	n.d.	$6.8 \cdot 10^{-8}$
$(\text{BVIM})_4[\text{SiW}_{12}\text{O}_{40}]$	0.017	0.020	$7.2 \cdot 10^{-8}$
$(\text{BVIM})_3[\text{PW}_{12}\text{O}_{40}]$	0.023	0.019	$1.3 \cdot 10^{-8}$

A comparison between the redox behavior of hybrid BVIM-POM immobilized on glassy carbon electrode and the parent POMs dissolved in solution is made also via the formal peak potential, E° , computed as the average of anodic (E_{pa}) and cathodic peak (E_{pc}). The values are listed in Table 4.5.2. A slight negative shift is observed for almost all BVIM-POMs that may be related to a local small pH increase. For $(\text{BVIM})_3[\text{PW}_{12}\text{O}_{40}]$ a slight positive shift is observed. This indicates one more time the special redox behavior of this immobilized POM, but the reason for this is unknown.

Table 4.5.2 Formal peak potentials (E°) of POMs free in solution and BVIM-POMs immobilized. $E^{\circ} = (E_{pa} + E_{pc}) / 2$ (n.d. not determined)

POM	E ^o / V vs. RHE				Peak shift (E ^o _{immobilized} - E ^o _{sn solution}) (V)	
	Free in solution		Immobilized (BVIM-POM)			
	I st wave	II nd wave	I st wave	II nd wave		
(BVIM) ₆ [H ₂ W ₁₂ O ₄₀]	-0.084	-0.204	-0.140	-0.268	-0.056	-0.064
(BVIM) ₅ [BW ₁₂ O ₄₀]	-0.128	-0.305	-0.159	n.d.	-0.031	n.d.
(BVIM) ₄ [SiW ₁₂ O ₄₀]	0.132	-0.123	0.099	-0.163	-0.033	-0.040
(BVIM) ₃ [PW ₁₂ O ₄₀]	0.291	0.032	0.305	0.107	0.014	0.075

Finally, the redox behavior of immobilized hybrid BVIM-POMs was studied by increasing the scan rate, as shown in Figure 4.5.2 and 4.5.3. It can be seen that both reduction and oxidation currents of the first redox peak are increasing with scan rate. In Figure 4.5.2 and 4.5.3, panels in the middle and right-hand side show variation of cathodic peak intensity with scan rate and square root of scan rate, respectively. Red lines represent the linear fit and black is only uniting the experimental points for better eye guidance. It can be seen that at lower scan rate ($v < 40\text{mV/s}$) the intensity varies linearly with scan rate which illustrates a surface-controlled redox process. At higher scan rate ($v > 40\text{mV/s}$), the intensity varies linearly with the square root of the scan rate which implies a diffusion control mechanism. In both cases, correlation coefficient (R^2) is higher than 0.998. This change was already described for the incorporation of a similar ionic liquid, i.e. 1-butyl-3-methylimidazolium in a carbon paste electrode.^{1a} In that case, the authors interpreted their data as a proof of increase in the conductivity of the electrode due to extra ionic sources. Thus, that modified electrode is able to perform fast charge-transfer kinetics even at higher scan rate. It is important to note here than when our parent POMs were analyzed dissolved in solution, only the diffusion control of the redox behavior was observed (i.e. the current varied linearly only with the square root of the scan rate). Another possible explanation would be a slight mobility of BVIM-POMs inside the immobilized film. When the scan rate is low, all BVIM-POMs participate at the redox process, while at high scan rate, the current is limited by the diffusion of the BVIM-POMs in the film.

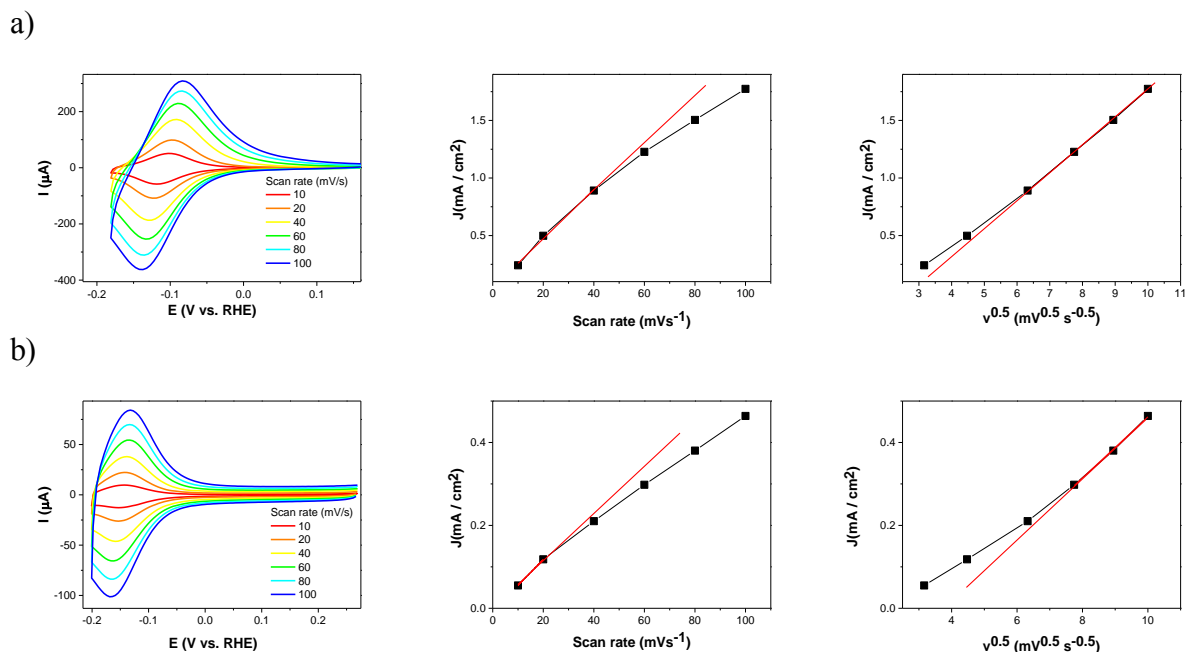


Figure 4.5.2 Cyclic voltammetry of immobilized hybrid BVIM-POM at different scan rates: a) $(\text{BVIM})_6[\text{H}_2\text{W}_{12}\text{O}_{40}]$, b) $(\text{BVIM})_5[\text{BW}_{12}\text{O}_{40}]$. Panels in the middle and right-hand side show variation pour reduction peak intensity with scan rate and square root of scan rate, respectively. Red lines represent the linear fit and black is only uniting the experimental point for better eye guidance. Experimental conditions: electrolyte, 0.5 M Na_2SO_4 , pH 1.

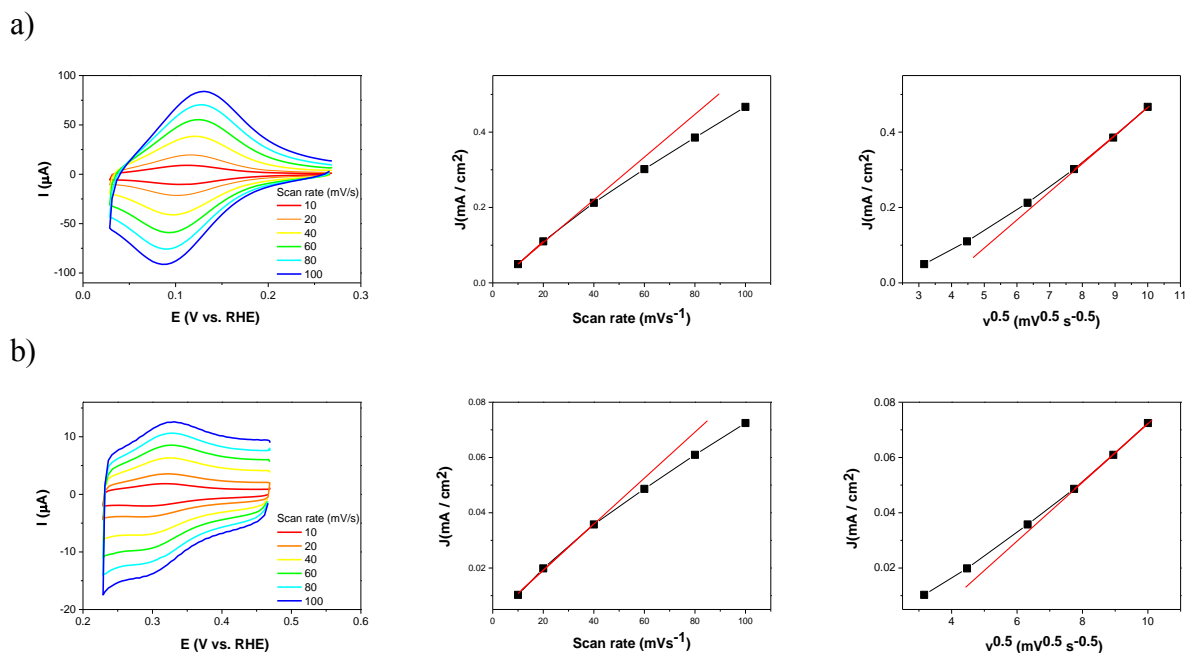


Figure 4.5.3 Cyclic voltammetry of immobilized hybrid BVIM-POM at different scan rates: a) $(\text{BVIM})_4[\text{SiW}_{12}\text{O}_{40}]$, b) $(\text{BVIM})_3[\text{PW}_{12}\text{O}_{40}]$. Panels in the middle and right-hand side show the variation of reduction peak intensity with scan rate and square root of scan rate, respectively. Red lines represent the linear fit and black is only uniting the experimental point for better eye guidance. Experimental conditions: electrolyte, 0.5 M Na_2SO_4 , pH 1.

4.6 Electrocatalytic behavior of GC/C/BVIM-POM electrodes

The ability of immobilized hybrid BVIM-POMs to catalyze the electrochemical

reduction of nitrite was first tested with cyclic voltammetry. Figure 4.6.1 shows the CVs before addition of nitrite (red curve), followed by subsequent additions of HNO_2 , from 1 to 20 mM. An increase of the reduction current is observed each time, suggesting an electrocatalytic effect. Nevertheless, it can be observed that the reduction current increases right from the beginning of the scan, before even reaching the potential range of BVIM-POM reduction. This phenomenon was already reported in literature in the case of $[\text{SiMo}_{12}\text{O}_{40}]^{4-}$ immobilized in a polypyrrole matrix, but the authors gave no explanation (see Figure 1.5.1 in chapter 1).¹²

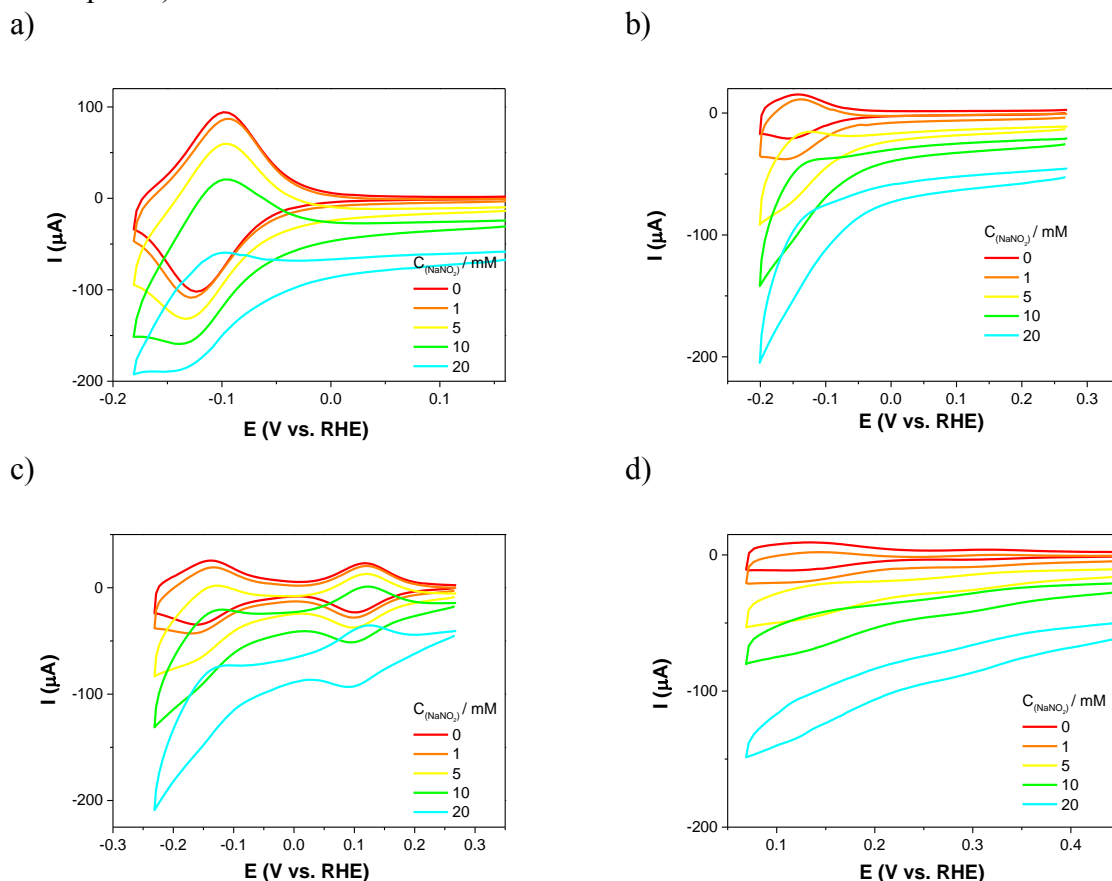


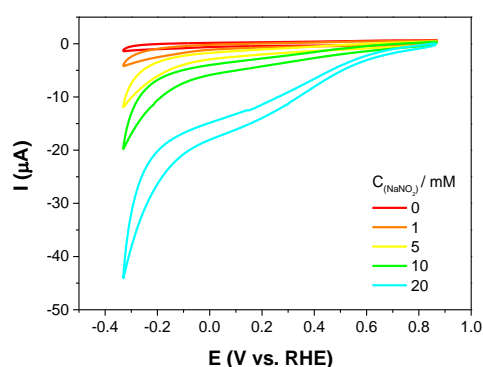
Figure 4.6.1 Cyclic voltammetry for immobilized BVIM-POMs before and after the addition of increasing concentrations of nitrite: a) $(\text{BVIM})_6[\text{H}_2\text{W}_{12}\text{O}_{40}]$, b) $(\text{BVIM})_5[\text{BW}_{12}\text{O}_{40}]$, c) $(\text{BVIM})_4[\text{SiW}_{12}\text{O}_{40}]$, d) $(\text{BVIM})_3[\text{PW}_{12}\text{O}_{40}]$. Experimental conditions: electrolyte, 0.5 M Na_2SO_4 , pH 1.

In order to try to explain this phenomenon, some control experiments were performed. First, one might inquire about the influence of the ionic liquid on the electrocatalytic behavior of the POMs. Thus, CV was performed with a clean glassy carbon alone and also with ionic liquid dissolved in the electrolyte (Figure 4.6.2a and b) in the absence and in the presence of nitrite. From Figure 4.6.2a for a glassy carbon electrode (GC), it can be seen that the reduction current increases already at 0.7 V vs. RHE (almost immediately after the start of the scan, i.e. 0.8 V vs. RHE), but overall reduction current is lower than -50 μA for the entire potential range (for 20 mM NaNO_2). In the presence of BVIM^+ in solution, a very similar behavior is observed, even though the upper limit potential was only 0.5 V vs. RHE. To better see if BVIM^+ plays a role in the electron transfer between the nitrite and GC electrode, two measurements were done. Figure 4.6.2c shows bare GC electrode (black curve) and bare GC electrode with BVIM^+ in solution (red curve). It can be observed that the capacitive current is decreased in the second case. Subsequently, nitrite was added in solution

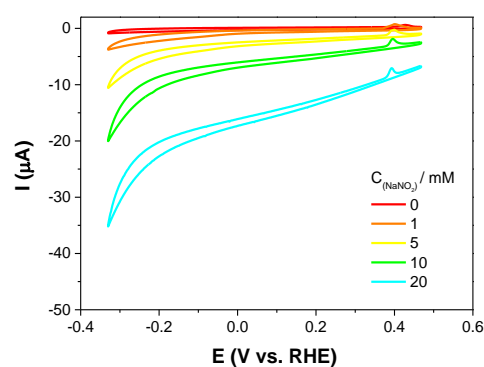
and results are depicted in Figure 4.6.2d. The black dash curve is only GC electrode with nitrite, while the red dash curve is GC electrode with BVIM⁺ and nitrite in solution. The presence of BVIM⁺ seems to help the electron transfer between the nitrite and the electrode, but the effect is not very strong. A similar experiment was performed with glassy carbon electrode modified with the carbon ink (GC/C) and also with ionic liquid dissolved in the electrolyte (Figure 4.6.3a and b) in the absence and in the presence of nitrite. In both cases, the reduction current in the presence of nitrite increases directly from the beginning of the scan, i.e. 0.8 V *vs.* RHE. When BVIM⁺ is in solution (Figure 4.6.3b), the reduction currents are smaller. The presence of BVIM⁺ in solution does not reduce the capacitive current (Figure 4.6.3c) as seen for GC electrode (Figure 4.6.2.c). Moreover, a small reduction peak was observed at -0.1 V *vs.* RHE (Figure 4.6.3c red curve), but we haven't attributed this peak to any redox couple. When data from Figures 4.6.3a and 4.6.3b are compared in Figure 4.6.3d, it can be seen that the reduction current for 10 mM of NaNO₂ is smaller in the presence of BVIM⁺. This is contrary to the observation made for GC electrode and BVIM⁺ in solution (Figure 4.6.2d). Thus, the effect of BVIM⁺ on the reduction of nitrite is not conclusive. Probably a more comprehensive study employing different ionic liquids could make clear the role of these compounds for the reduction of nitrite.

Secondly, one might inquire about the role of carbon ink in the reduction of nitrite. A simple comparison is made between glassy carbon electrode (GC) and glassy carbon modified with carbon ink (GC/C) in the absence of nitrite (Figure 4.6.4a). It is observed that the carbon powder greatly increases the capacitive current, probably due to the high surface of this material. The faradic current obtained for nitrite reduction is greatly increased as well (Figure 4.6.4b).

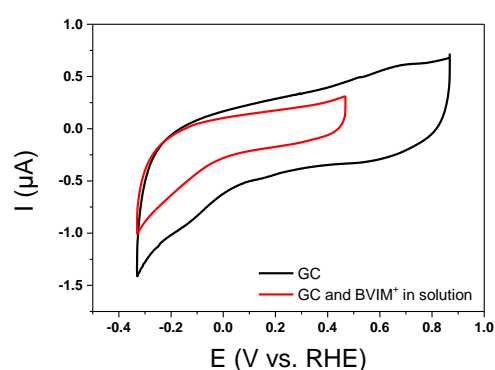
a) GC alone



b) GC and ionic liquid in solution



c)



d)

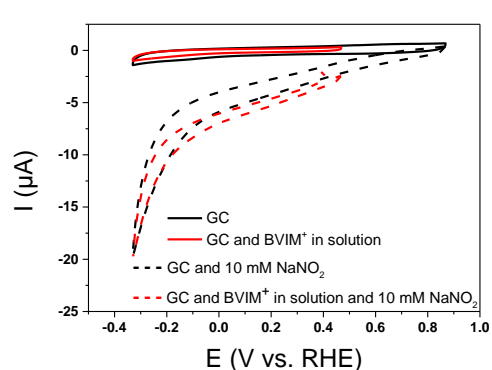
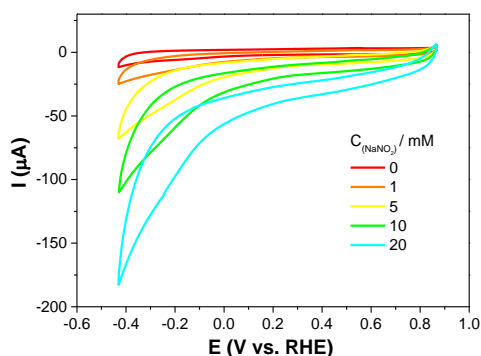
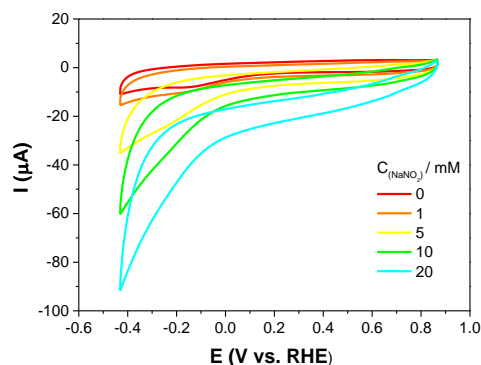


Figure 4.6.2 Cyclic voltammetry for glassy carbon (GC) alone and in the presence of BVIM⁺ in solution. a) Increasing concentrations of nitrite with a GC alone; b) Increasing concentrations of nitrite with a GC and 1 mM of BVIM⁺; c) comparison between GC alone (black curve) and GC in presence of BVIM⁺ (red curve); d) like c) but after addition of 10 mM NaNO₂ (dashed curves). Experimental conditions: electrolyte, 0.5 M Na₂SO₄, pH 1; scan rate, 20 mVs⁻¹.

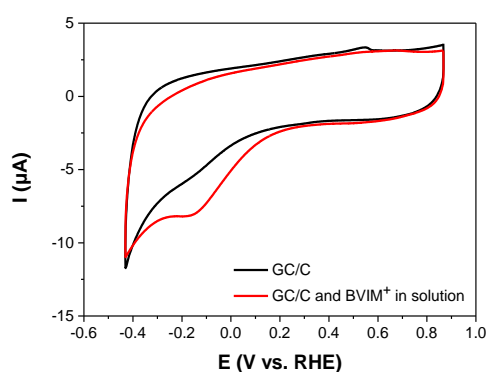
a) GC/C alone



b) GC/C and ionic liquid in solution



c)



d)

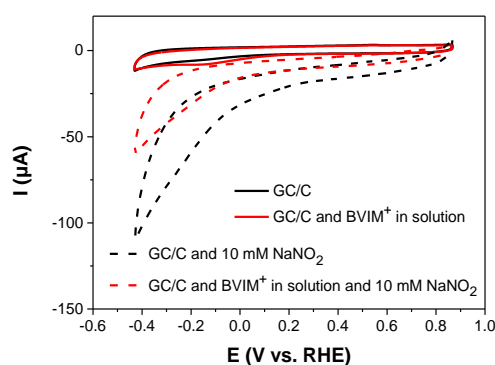
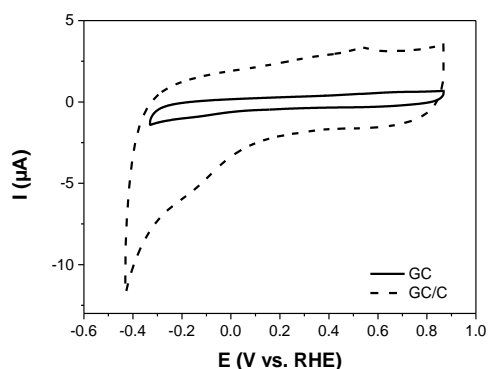


Figure 4.6.3 Cyclic voltammetry for glassy carbon modified with carbon powder (GC/C) alone and in the presence of BVIM^+ in solution. a) Increasing concentrations of nitrite with a GC/C alone; b) Increasing concentrations of nitrite with a GC/C and 1 mM of BVIM^+ ; c) comparison between GC/C alone (black curve) and GC/C in presence of BVIM^+ (red curve); d) like c) but after addition of 10 mM NaNO_2 (dashed curves). Experimental conditions: electrolyte, 0.5 M Na_2SO_4 , pH 1; scan rate, 20 mVs^{-1} .

a)



b)

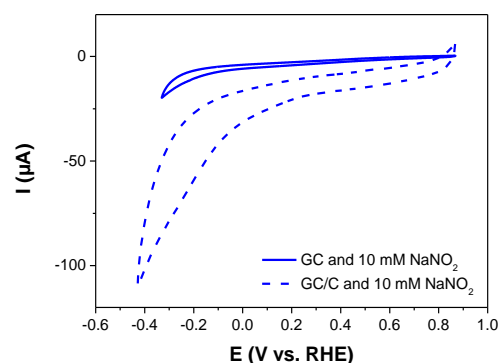


Figure 4.6.4 Cyclic voltammetry for glassy carbon (GC) and glassy carbon modified with carbon powder (GC/C) alone (a) and in the presence of 10 mM of NaNO_2 in solution (b). Experimental conditions: electrolyte, 0.5 M Na_2SO_4 , pH 1; scan rate, 20 mVs^{-1} .

The final comparison is made between a GC modified with carbon powder (GC/C) and with BVIM^+ in solution and a GC/C electrode modified with the hybrid materials BVIM^+ -

POMs (black and blue curves respectively in Figure 4.6.5). The overall reduction current is increased. More precisely the reduction current recorded at the beginning of the scan (from 0.2 V to 0.5 V vs. RHE, depending on the POM) is three times higher than the one recorded only with GC/C and BVIM⁺ and almost no variation on the used BVIM-POM is observed (Table 4.6.1). For the reduction current recorded at the potential of the first reduction of each BVIM-POM, an increase of 5 to 6 times is observed (Table 4.6.1). It must be noted here, though, that the cathodic peaks of the BVIM-POMs have a very similar intensity to the anodic ones. This is not expected for a catalytic process, setting a doubt about the POMs acting as catalysts when immobilized. This observation is sustained by the DEMS data described below, where the actual catalysis of nitrite conversion to NO could not be evidenced in the presence of POMs. It is probable that BVIM-POMs actually reduce the hydrophobicity of the carbon inks and thus allowing an increase in the overall reduction current.

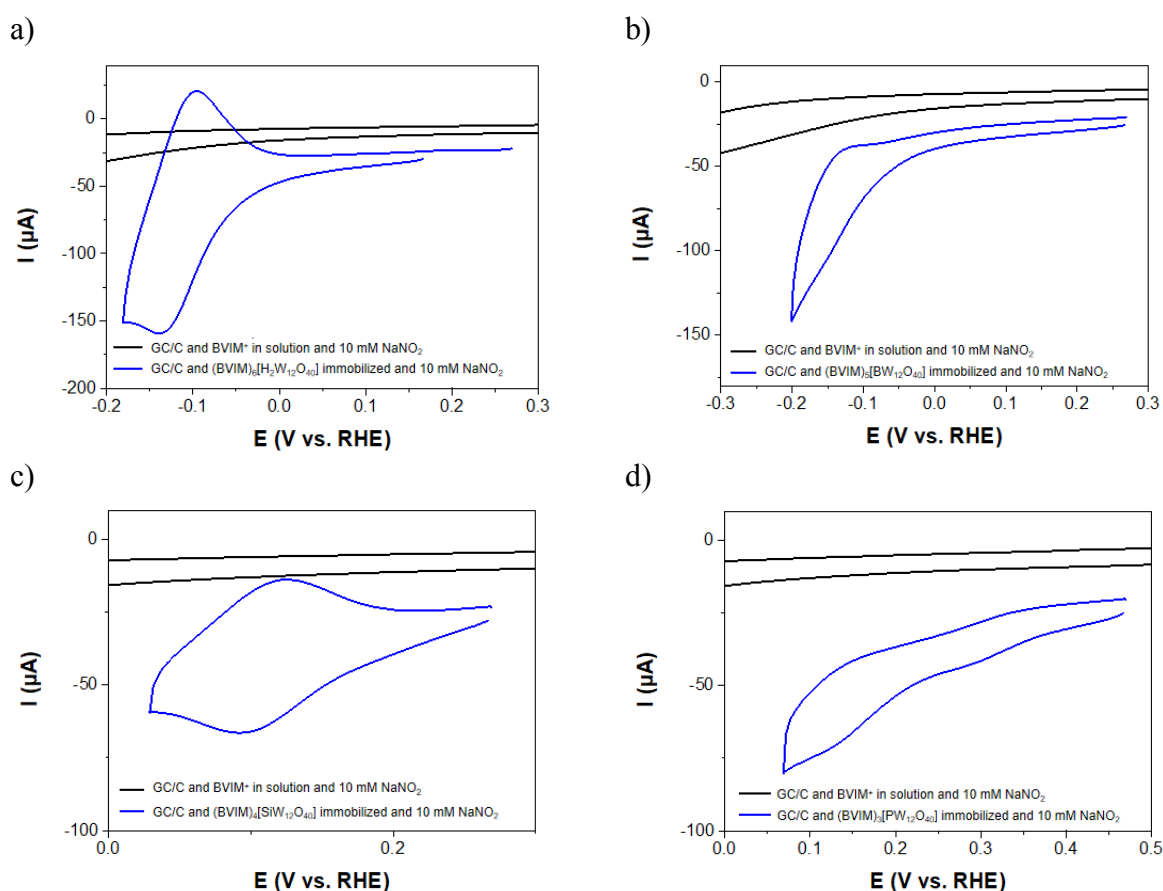


Figure 4.6.5 Cyclic voltammetry obtained at two different electrodes in the presence of nitrite: glassy carbon and carbon powder (GC/C) electrode with BVIM⁺ in solution (black) curve and GC/C modified with hybrid BVIM-POMs (blue curve). Experimental conditions: electrolyte, 0.5 M Na₂SO₄, pH 1; scan rate, 20 mV s⁻¹; 10 mM NaNO₂.

Table 4.6.1 Reduction currents in the presence of nitrite, extracted from CV in Figure 4.6.5.

POM	At BVIM-POM I st reduction potential			At beginning of the scan		
	I _{BVIM-POM} (μA)	I _{BVIM⁺} (μA)	$\frac{I_{BVIM-POM}}{I_{BVIM^+}}$	I _{BVIM-POM} (μA)	I _{BVIM⁺} (μA)	$\frac{I_{BVIM-POM}}{I_{BVIM^+}}$
(BVIM) ₆ [H ₂ W ₁₂ O ₄₀]	-159	-24	6.6	-30	-12	2.5
(BVIM) ₅ [BW ₁₂ O ₄₀]	-117	-27	4.3	-26	-10	2.6
(BVIM) ₄ [SiW ₁₂ O ₄₀]	-66	-13	5.1	-28	-10	2.8
(BVIM) ₃ [PW ₁₂ O ₄₀]	-42	-10	4.2	-25	-9	2.8

4.7 DEMS analysis of nitrite reduction catalyzed by GC/C/BVIM-POM electrodes

DEMS analysis of nitrite reduction was performed using immobilized BVIM-POMs. The purpose is to compare the gaseous products and their onset potential with those obtained when POMs are free in solution (chapter 3.4). The results are shown in Figure 4.7.1. The first striking observation is for the signal of NO (red curve). For all four BVIM-POMs, after a stable zero baseline, the signal decreases. Moreover, this decrease is very well correlated with the increase of the N₂O signal. The explanation for this is that NO is consumed to produce N₂O. The source of NO is most probably the disproportionation of HNO₂. This behavior is completely different with the case of POMs in solution, where a formation of NO, from the catalyzed reduction of HNO₂, is observed. One possible explanation is that the immobilized BVIM-POMs are not catalyzing the reduction of HNO₂ to NO or, if this reaction happens, NO is entrapped inside the ink and cannot be detected by DEMS. The latter case is somewhat less probable because N₂O is also a gaseous product but it is not entrapped inside the ink and it is detected by DEMS.

At this stage, we can compare our results with the only published paper so far, that is the nitrite reduction catalyzed by H₄[SiMo₁₂O₄₀] immobilized in a poly-pyrrole matrix on a platinum electrode (chapter 1.5).¹² In that case, DEMS analysis showed the consumption of NO and the formation of N₂O, similar to our case. Nevertheless, when H₄[SiMo₁₂O₄₀] was used free in the solution, only the formation of NO was observed (not the formation of N₂O). This is different that the behavior of our POMs in solution (support electrode, glassy carbon). We have to emphasize that the support electrode may change the reaction mechanism¹³, especially due to different adsorption behaviors of NO on platinum *versus* glassy carbon electrode. In fact, little is known about the reduction of NO (or HNO₂) on glassy carbon and thus we have performed DEMS studies for nitrite reduction on this electrode (see below data).

A second striking observation from Figure 4.7.1 is the lack of dependence of the onset of N₂O formation on the used BVIM-POMs. Table 4.7.1 contains the onset potentials of NO and N₂O obtained from DEMS measurements. The values of N₂O onset potentials are comprised between 0.10 and 0.15 V *vs.* RHE, thus the difference is not significant. More intriguing is the fact that these values are located before the first reduction wave of two BVIM-POMs ((BVIM)₆[H₂W₁₂O₄₀] and (BVIM)₅[BW₁₂O₄₀]), in the first reduction wave for (BVIM)₄[SiW₁₂O₄₀] and in the second reduction wave of (BVIM)₃[PW₁₂O₄₀]. In order to understand this, we have performed some control experiments.

First of all, one may inquire about the role of carbon powder used to prepare the ink. We have described above that reduction of nitrite of a GC/C electrode starts at a very positive potential, i.e. 0.8 V *vs.* RHE (CV runs). From Figure 4.7.2a (and Table 4.7.1) it can be seen that the onset potential of N₂O is around 0.05 V *vs.* RHE. Thus, the reduction current observed at the beginning of the CV scans (i.e. 0.8V *vs.* RHE in Figure 4.6.3a, b, and d) is not associated to the reduction of NO into N₂O. When compared to the GC/C/BVIM-POMs,

the onset potential of N_2O is very similar, though slightly more negative. Also, there is no formation of NO. We have also compared these data with DEMS analysis for glassy carbon electrode alone (Figure 4.7.2b). The onset of N_2O is quite different and much more negative, i.e. -0.15 V vs. RHE, as expected for this type of electrode. In the same time, NO formation is not observed. By comparing these two electrodes, we can conclude that the carbon electrode has an important catalytic behavior, most probably due to its large surface. Another possible explanation would be the existence of some trace metals in the composition of the carbon powder. We have thus pre-treated this material by dipping in concentrated sulfuric acid for 3 days and measured DEMS for nitrite reduction afterwards (Figure 4.7.2c). The obtained behavior is very similar, that is we observe NO consumption and onset of N_2O at 0.10 V vs. RHE. This result excludes the possibility of attributing the catalytic activity of carbon powder to some trace metals.

Nafion was used to prepare the carbon and BVIM-POMs based inks and served to their fixation on the glassy carbon electrode. Nafion is a copolymer composed of perfluorovinylether groups terminated with sulfonate groups and a tetrafluoroethylene (PTFE) backbone. This polymer has a very high ionic conductivity that increases with hydration. At nanometer length scale, there are hydrophilic domains which allow movement of water and cations. In order to understand if the use of Nafion on our inks could influence nitrite reduction, we have drop-casted Nafion on glassy carbon electrode and perform DEMS analysis (Figure 4.7.2d). The results are very similar to GC alone (no NO formation, onset of N_2O at -0.15 V), thus the use of Nafion has no influence on nitrite reduction.

Finally, we have conducted a last control experiment, in the absence of POMs. We have used a GC electrode and a GC/C electrode with the BVIM^+ in solution (Figure 4.7.2e and f, respectively). The results are similar with the respective experiments in the absence of BVIM^+ (Figure 4.7.2a and b), but DEMS data are more noisy and absolute values are smaller.

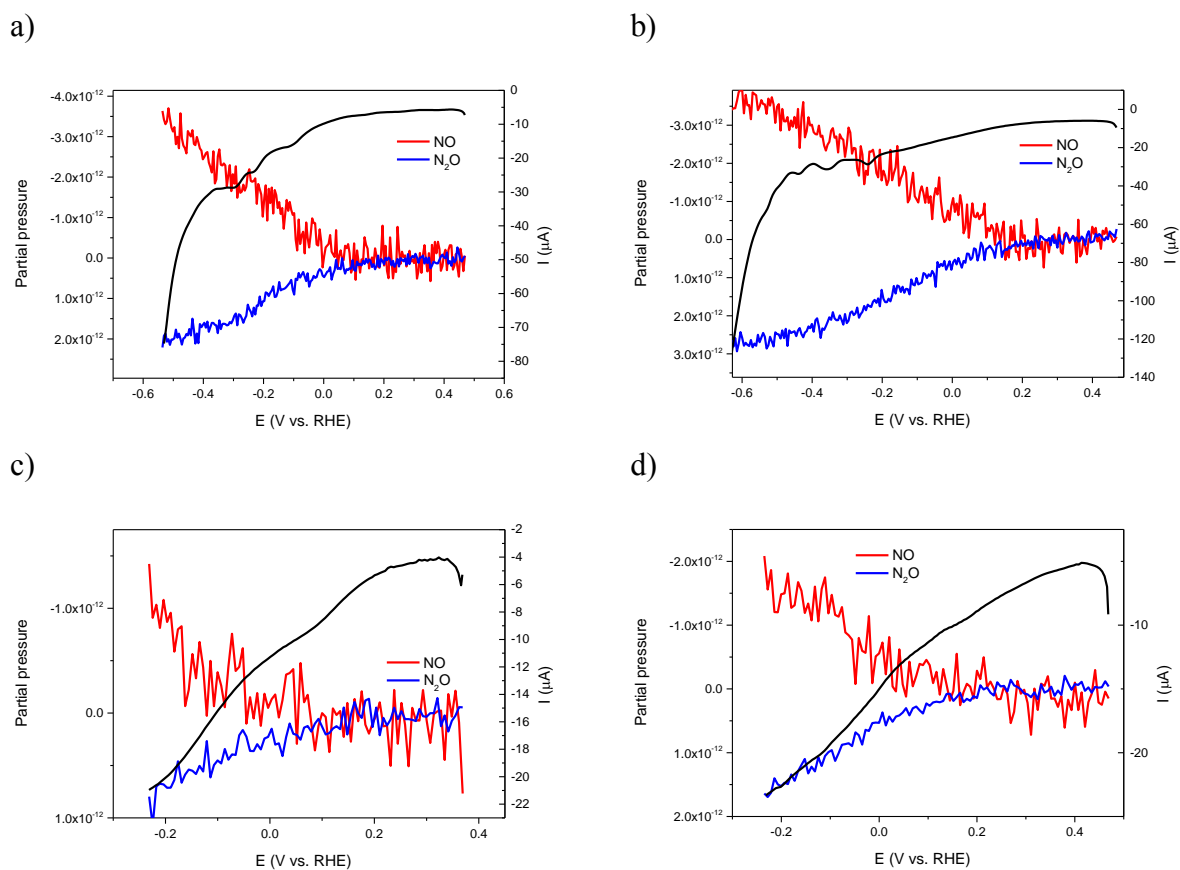
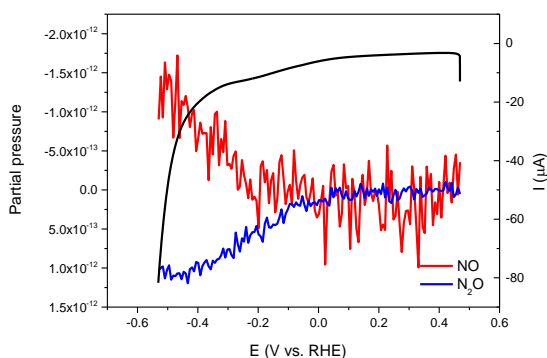
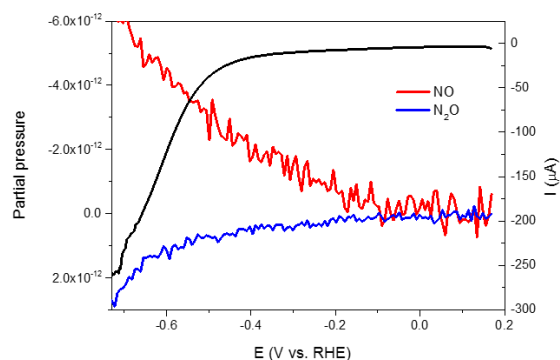


Figure 4.7.1 DEMS analysis of nitrite reduction catalyzed by immobilized BVIM-POMs. a) $(\text{BVIM})_6[\text{H}_2\text{W}_{12}\text{O}_{40}]$, b) $(\text{BVIM})_5[\text{BW}_{12}\text{O}_{40}]$, c) $(\text{BVIM})_4[\text{SiW}_{12}\text{O}_{40}]$, d) $(\text{BVIM})_3[\text{PW}_{12}\text{O}_{40}]$. Experimental conditions: electrolyte, 0.5 M Na_2SO_4 , pH 1; scan rate, 0.5 mVs^{-1} ; 10 mM $\text{Na}^{15}\text{NO}_2$.

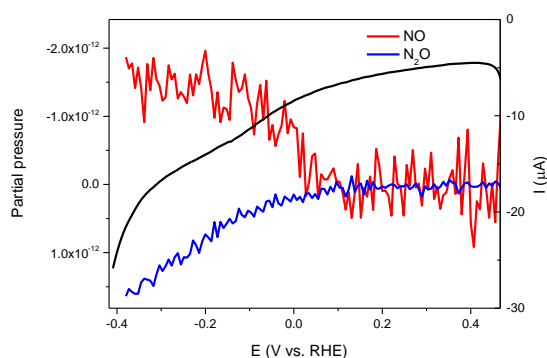
a) carbon powder (GC/C)



b) glassy carbon (GC)



c) pre-treated carbon powder (GC/C cleaned)



d) GC covered by Nafion

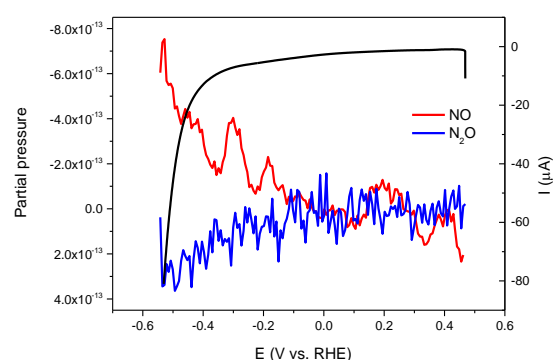
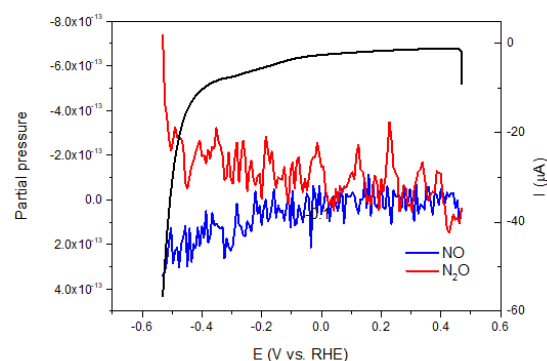
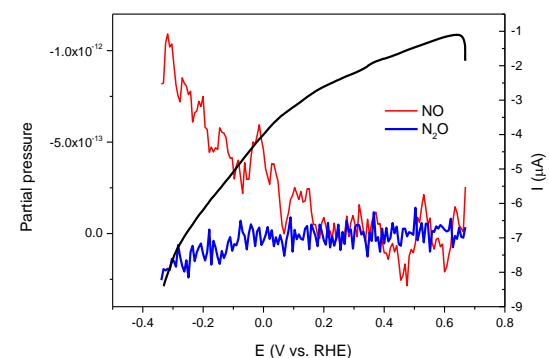
e) GC and BVIM⁺ in solutionf) GC/C and BVIM⁺ in solution

Figure 4.7.2 DEMS analysis of nitrite reduction, in the absence of POM, on a) glassy carbon electrode modified with carbon ink (no POM); b) glassy carbon alone (no POM); c) carbon powder cleaned in concentrated sulfuric acid (no POM); d) glassy carbon covered by a Nafion layer (no POM); e) glassy carbon electrode and BVIM⁺ in solution (no POM); f) glassy carbon electrode modified with carbon ink and BVIM⁺ in solution (no POM). Experimental conditions: electrolyte, 0.5 M Na₂SO₄, pH 1; scan rate, 0.5 mVs⁻¹; 10 mM Na¹⁵NO₂.

To sum up, the positive values of N₂O onset observed with GC/C/BVIM-POMs are partially explained by the use of the carbon ink, but a contribution of immobilized POMs makes this value even more positive (Table 4.7.1). The values are much more positive compared with the POMs in solution (Figure 4.7.3). This excludes the mechanism of N₂O

formation via an HNO intermediate. The other mechanism can be proposed, based on the reaction between one adsorbed molecule of NO and one molecule of NO in the solution phase, leading to the $\text{HN}_2\text{O}_{2\text{ads}}$ dimer. But it is also difficult to assume this mechanism because of the improbability of having NO adsorbed on a carbonaceous material. Thus, at this stage the mechanism remains unknown and other spectroscopic techniques are required in order to clarify it. A final advantage brought by the use of POMs in the hybrid materials is the increase of the reduction current. In Figure 4.7.4, the comparison of CV (obtained during the DEMS analysis described above) show that the reduction current of nitrite is higher at the GC/C/BVIM-POMs compared to GC/C and GC electrode.

Table 4.7.1 Summary of onset potentials obtained from DEMS analysis.

Catalysts	Electrode	Onset NO (V vs. RHE)	Onset N_2O (V vs. RHE)	Shift of N_2O onset (GC/C/BVIM-POM – GC/POM)
POMs in solution	$\text{GC}/[\text{H}_2\text{W}_{12}\text{O}_{40}]^{6-}$	-0.07	-0.12	0.22
	$\text{GC}/[\text{BW}_{12}\text{O}_{40}]^{5-}$	-0.09	-0.11	0.22
	$\text{GC}/[\text{SiW}_{12}\text{O}_{40}]^{4-}$	0.12	-0.09	0.22
	$\text{GC}/[\text{PW}_{12}\text{O}_{40}]^{3-}$	0.42	0.02	0.13
				Shift of N_2O onset (GC/C/BVIM-POM – GC/C)
Immobilized POMs (BVIM-POMs)	$\text{GC}/\text{C}/(\text{BVIM})_6[\text{H}_2\text{W}_{12}\text{O}_{40}]$	Not observed	0.10	0.05
	$\text{GC}/\text{C}/(\text{BVIM})_5[\text{BW}_{12}\text{O}_{40}]$		0.11	0.06
	$\text{GC}/\text{C}/(\text{BVIM})_4[\text{SiW}_{12}\text{O}_{40}]$		0.13	0.08
	$\text{GC}/\text{C}/(\text{BVIM})_3[\text{PW}_{12}\text{O}_{40}]$		0.15	0.10
No POMs	GC	Not observed	-0.32	Not applicable
	GC/BVIM^+		-0.10	
	GC/C		0.05	
	$\text{GC}/\text{C}/\text{BVIM}^+$		-0.01	

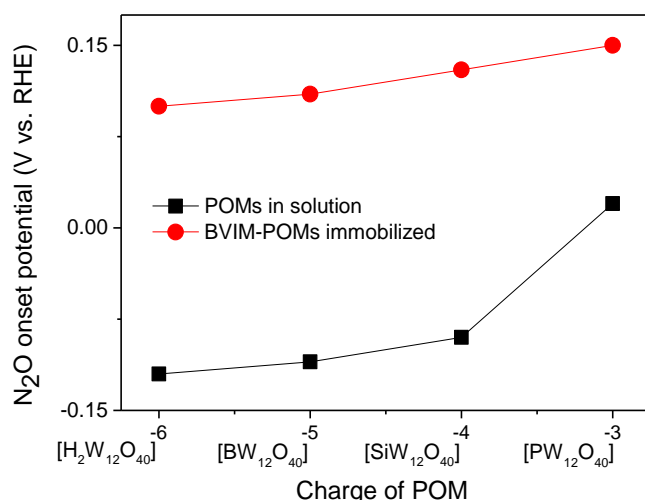


Figure 4.7.3 Comparison of N_2O onset potential obtained from DEMS data for electrodes with POMs in solution (black squares) and for electrodes modified with hybrid immobilized BVIM-POMs materials (red circles).

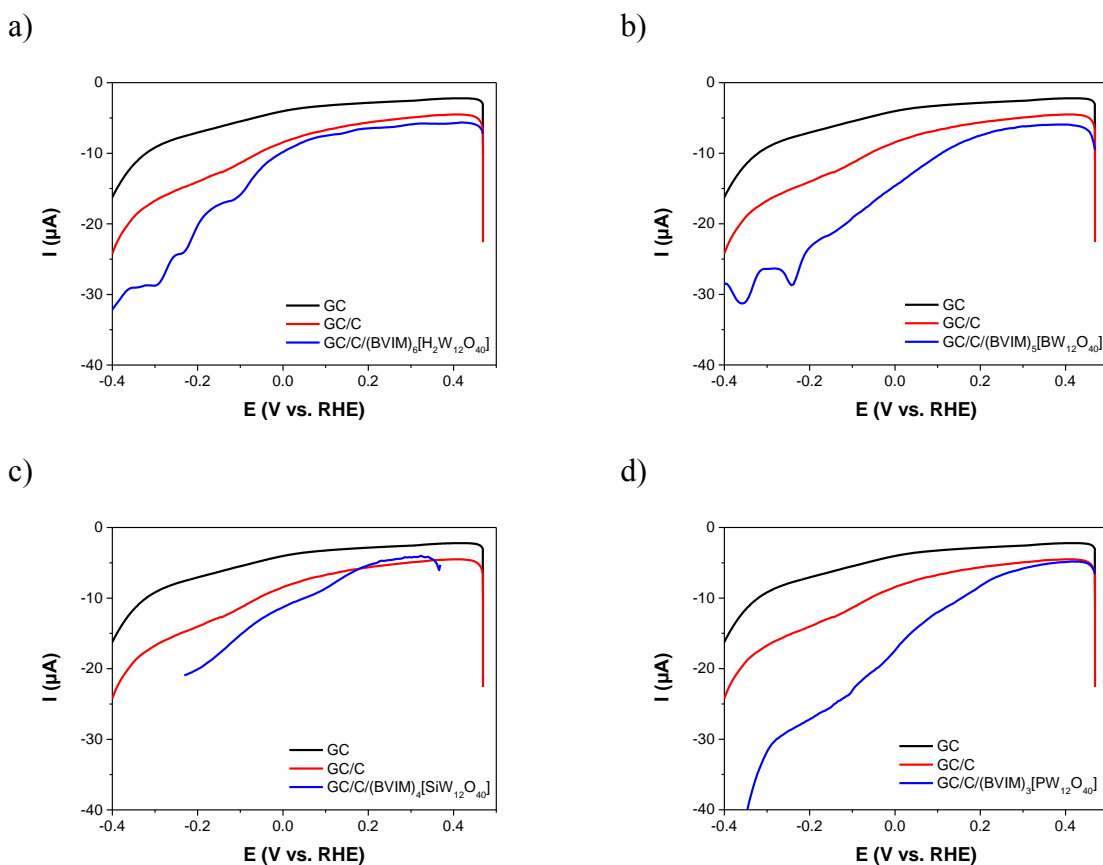


Figure 4.7.4 Comparisons of CV data obtained from DEMS analysis from Figure 4.7.1 and Figures 4.7.2 a and b. Experimental conditions: electrolyte, 0.5 M Na_2SO_4 , pH 1; scan rate, 0.5 mVs^{-1} ; 10 mM $\text{Na}^{15}\text{NO}_2$.

4.8 Conclusion

In this chapter, we have described the synthesis and electrochemical properties of new hybrid materials obtained by the reaction of four Keggin-type POMs with the ionic liquid, 1-butyl-3-vinyl-imidazolium bromide (BVIM). Several physico-chemical characterization techniques (FT-IR, TGA, XRD) have been used to show that POMs preserve their structure in the hybrid materials, although with a reduced water content and reduced crystallinity. The redox behavior of immobilized hybrid BVIM-POM is similar to the one of parent compounds, with the exception of (BVIM)₃PW₁₂O₄₀ for which a shift to more positive potentials was observed. The hybrid materials contribute to the increase of the current of nitrite reduction, although a different mechanism is supposed. This is sustained by DEMS analysis from which a very positive onset of N₂O formation was observed. It was also found that carbon ink displays an unexpected catalytic behavior because the N₂O onset was also observed at more positive potential when compared to glassy carbon alone. For a better understanding, some other spectroscopic techniques should be used in the future. Also, a higher variety of the ionic liquids should be tested in order to fully describe the influence of such compounds on the nitrite reduction.

4.9 References

1. (a) Liu, H.; He, P.; Li, Z.; Sun, C.; Shi, L.; Liu, Y.; Zhu, G.; Li, J., An ionic liquid-type carbon paste electrode and its polyoxometalate-modified properties. *Electrochemistry communications* **2005**, 7 (12), 1357-1363; (b) Huang, B.-Q.; Wang, L.; Shi, K.; Xie, Z.-X.; Zheng, L.-S., A new strategy for the fabrication of the phosphor polyoxomolybdate modified electrode from ionic liquid solutions and its electrocatalytic activities. *Journal of Electroanalytical Chemistry* **2008**, 615 (1), 19-24.
2. Wang, R.; Jia, D.; Cao, Y., Facile synthesis and enhanced electrocatalytic activities of organic-inorganic hybrid ionic liquid polyoxometalate nanomaterials by solid-state chemical reaction. *Electrochimica acta* **2012**, 72, 101-107.
3. Feizy, S.; Haghighi, B., A survey on the effect of ionic liquid on electrochemical behavior and electrocatalytic activity of a phosphomolybdic acid-ionic liquid-MWCNT-modified glassy carbon electrode. *Journal of Solid State Electrochemistry* **2019**, 23 (5), 1339-1350.
4. Ohno, H. In *Design of ion conductive polymers based on ionic liquids*, Macromolecular Symposia, Wiley Online Library: 2007; pp 551-556.
5. Zhang, Q.; Wu, S.; Zhang, L.; Lu, J.; Verproot, F.; Liu, Y.; Xing, Z.; Li, J.; Song, X.-M., Fabrication of polymeric ionic liquid/graphene nanocomposite for glucose oxidase immobilization and direct electrochemistry. *Biosensors and Bioelectronics* **2011**, 26 (5), 2632-2637.
6. Zhang, Q.; Lv, X.; Qiao, Y.; Zhang, L.; Liu, D. L.; Zhang, W.; Han, G. X.; Song, X. M., Direct electrochemistry and electrocatalysis of hemoglobin immobilized in a polymeric ionic liquid film. *Electroanalysis: An International Journal Devoted to Fundamental and Practical Aspects of Electroanalysis* **2010**, 22 (9), 1000-1004.
7. Ammam, M.; Fransaer, J., Synthesis and characterization of hybrid materials based on 1-butyl-3-

methylimidazolium tetrafluoroborate ionic liquid and Dawson-type tungstophosphate $K_7[H_4PW_{18}O_{62}] \cdot 18H_2O$ and $K_6[P_2W_{18}O_{62}] \cdot 13H_2O$. *Journal of Solid State Chemistry* **2011**, *184* (4), 818-824.

8. Hunyadi, D.; Sajó, I.; Szilágyi, I. M., Structure and thermal decomposition of ammonium metatungstate. *Journal of Thermal Analysis and Calorimetry* **2014**, *116* (1), 329-337.

9. Adameczyk, L.; Miecznikowski, K., Solid-state electrochemical behavior of Keggin-type borotungstic acid single crystal. *Journal of Solid State Electrochemistry* **2013**, *17* (4), 1167-1173.

10. Lesbani, A.; Setyowati, M.; Mohadi, R.; Rohendi, D., OXIDATION OF CYCLOHEXANE TO CYCLOHEXANOL AND CYCLOHEXANONE USING $H_4\alpha-SiW_{12}O_{40}/Zr$ AS CATALYST. *Molekul* **2016**, *11* (1), 53-60.

11. Liu, M.; Yu, F.; Yuan, B.; Xie, C.; Yu, S., Oxidation of 1-propanol to propionic acid with hydrogen peroxide catalysed by heteropolyoxometalates. *BMC chemistry* **2021**, *15* (1), 1-8.

12. Debiemme-Chouvy, C.; Cachet, H.; Folcher, G.; Deslouis, C., Electrocatalytic reduction of HNO_2 by a silicomolybdate polyanion: a differential electrochemical mass spectrometry study. *Electroanalysis: An International Journal Devoted to Fundamental and Practical Aspects of Electroanalysis* **2007**, *19* (2-3), 259-262.

13. Duca, M.; Kavvadia, V.; Rodriguez, P.; Lai, S.; Hoogenboom, T.; Koper, M., New insights into the mechanism of nitrite reduction on a platinum electrode. *Journal of Electroanalytical Chemistry* **2010**, *649* (1-2), 59-68.

Conclusion

This thesis reports and compares the performance of a series of polyoxometalates (POMs) and hybrid POMs materials for the electrocatalytic reduction of nitrite with the use of Differential electrochemical mass spectrometry (DEMS) as main electroanalytical tool for the detection of reaction products. The analysis indicates a potential range where nitric oxide is the soul product, followed by N_2O at more negative potential and this for all studied POMs. No presence of N_2 could be detected by our DEMS analysis. Additional tests were performed to detect two other liquid phase products, hydroxylamine and ammonia, but these species were not found in the case of one tested POM, i.e. $[\text{H}_2\text{W}_{12}\text{O}_{40}]^{6-}$.

Four Keggin type W-POMs were studied in solution (homogeneous catalysis) to discuss the relation between the redox properties of the POMs and the obtained products. These POMs are $[\text{H}_2\text{W}_{12}\text{O}_{40}]^{6-}$, $[\text{BW}_{12}\text{O}_{40}]^{5-}$, $[\text{SiW}_{12}\text{O}_{40}]^{4-}$ and $[\text{PW}_{12}\text{O}_{40}]^{3-}$. The onset potential of NO obtained with $[\text{PW}_{12}\text{O}_{40}]^{3-}$ is closest to the thermodynamic potential for nitrite reduction to NO, followed by $[\text{SiW}_{12}\text{O}_{40}]^{4-}$, $[\text{BW}_{12}\text{O}_{40}]^{5-}$, and finally $[\text{H}_2\text{W}_{12}\text{O}_{40}]^{6-}$. The onset potential of N_2O is very little dependent on the selected POM, the value being around -0.2 V vs. RHE at pH 2 for all Keggin type W-POMs POMs. At pH 5, the onset potential of N_2O becomes more negative, most probably due to the charge repulsion between the reduced POM^- anion and NO_2^- and to the reduced concentration of protons, resulting in the slowdown of NO formation. A microkinetic model was develop to extract kinetic rate constant and turnover efficiency of the nitrite reduction to NO. At low overpotential, the values of TOF are decreasing in a trend following the redox potential of the POM: $[\text{PW}_{12}\text{O}_{40}]^{3-} > [\text{SiW}_{12}\text{O}_{40}]^{4-} > [\text{BW}_{12}\text{O}_{40}]^{5-}$ while at high overpotential the TOFs are following the reverse order. At pH 5 the values of the rate constants are about 70 times lower than at pH 2. A reaction mechanism based on the HNO intermediate is sustained by our data, since the formation of N_2O observed at -0.2 V vs. RHE, a value that is close to the redox potential of NO/HNO couple. More evidence data is brought when other POMs, that is $[\text{PMo}_{12}\text{O}_{40}]^{3-}$, $[\text{SiMo}_{12}\text{O}_{40}]^{4-}$, $\alpha\text{-}[\text{P}_2\text{W}_{18}\text{O}_{62}]^{6-}$, $[\text{Cd}_4(\text{H}_2\text{O})_2(\text{P}_2\text{W}_{15}\text{O}_{56})_2]^{16-}$, $[\text{Mn}_4(\text{H}_2\text{O})_2(\text{P}_2\text{W}_{15}\text{O}_{56})_2]^{16-}$ and $[\text{Zn}_4(\text{H}_2\text{O})_2(\text{P}_2\text{W}_{15}\text{O}_{56})_2]^{16-}$ having various redox properties, were used as catalysts. While the formation of NO is dependent on these properties, the potential of N_2O formation is very similar, confirming the existence of a potential barrier explained by the formation of HNO intermediate.

This mechanism changes completely when a silver electrode is used as working electrode and POMs are in solution (mixed heterogeneous-homogeneous catalysis). In fact, DEMS data evidenced a tandem catalysis between the two systems, since the potential of N_2O formation is much reduced. In fact, nitrite reduction to NO is catalyzed by the studied POMs ($[\text{SiW}_{12}\text{O}_{40}]^{4-}$, $[\text{PW}_{12}\text{O}_{40}]^{3-}$ and $[\text{SiMo}_{12}\text{O}_{40}]^{4-}$) in the same manner irrespective of the type of working electrode (Ag or GC). But the subsequent reduction of NO to N_2O is assisted by silver electrode via the formation of an adsorbed intermediate, HN_2O_2 . This tandem catalysis can work only if POMs have quite high redox potentials, that is their reduction happens before the reduction of nitrite on silver electrode.

As a comparison, silver nanoparticles stabilized by POMs ($[\text{H}_2\text{W}_{12}\text{O}_{40}]^{6-}$ and $[\text{SiW}_{12}\text{O}_{40}]^{4-}$) were synthesized using two methods: i) with a previously photoreduced POM and ii) with a previously electroreduced POM. However, the stability of these NPs is very poor, being affected by the low pH, by the high concentration of the electrolyte and by the concentration of nitrite. The use of pectin allowed the stabilization of these NPs, but no tandem catalysis between the silver core and the surrounding POM was observed for nitrite reduction at pH 5. It is supposed that the key species, nitric oxide, is too strongly adsorbed on

the nanoparticles to allow a synergy effect to appear.

Finally, a complete heterogeneous catalysis of nitrite reduction by new hybrid inorganic-organic materials has been studied. The materials are obtained by the reaction of four Keggin-type POMs with the ionic liquid, 1-butyl-3-vinylimidazolium bromide (BVIM). Several physico-chemical characterization techniques (FT-IR, TGA, XRD) have been used to show that POMs preserve their structure in the hybrid materials, although with a reduced water content and reduced crystallinity. The redox behavior of immobilized hybrid BVIM-POM is similar to the one of parent compounds, with the exception of (BVIM)₃PW₁₂O₄₀ for which a shift to more positive potentials was observed. The hybrid materials contribute to the increase of the current of nitrite reduction, although a different mechanism is supposed. This is sustained by DEMS analysis from which a very positive onset of N₂O formation was observed. It was also found that carbon ink displays an unexpected catalytic behavior because the N₂O onset was also observed at more positive potential when compared to glassy carbon alone.

In conclusion, the work of this thesis was dedicated to the study of nitrite reduction catalyzed by various POMs, either alone or combined with silver or an ionic liquid. As perspective, more various POMs should be tested in order to bring even more evidence data for the proposed mechanisms. Plus, the influence of the type of ionic liquid should be studied, perhaps using other spectroscopic techniques, since this mechanism is not yet fully understood.

Appendix

A.1 Reagents

All POMs used in this study were synthesized previously in our laboratory following well known protocols¹ except $(\text{NH}_4)_6[\text{H}_2\text{W}_{12}\text{O}_{40}]$ that was purchased from Sigma. All the other reagents were purchased from Sigma and used as received. NO gas was provided by Air Liquide (France).

Synthesis of BPOM $\text{K}_5\text{BW}_{12}\text{O}_{40}$. During the time course of this thesis, the synthesis of $\text{K}_5\text{BW}_{12}\text{O}_{40}$ was necessary as the previous product run out. While trying to find a precise protocol for the synthesis, it was observed that some important information such as precise pH and reaction time are not always provided. After some trial and error, a clear protocol was established. The success of obtaining the right isomer was checked by FT-IR spectroscopy (using characteristic features described in literature). The starting salt $\text{Na}_2\text{WO}_4 \cdot 2 \text{H}_2\text{O}$ (20 g) was dissolved at 70 °C in 20 mL of distilled hot water with stirring. Then, H_3BO_3 (1 g) was added into above solution with vigorous stirring. After the salts are dissolved, the pH is adjusted to 6 by addition of 6 M HCl and boiled for 6 h. During this time, water was added from time to time in order to keep the same initial volume. The obtained solution was cooled down. After one day $\text{Na}_{10}\text{W}_{12}\text{O}_{41} \cdot x\text{H}_2\text{O}$ was precipitated and filtered off. The filtrate solution was acidified by 6 M HCl to pH 2 and boiled for 30 minutes. 0.4 g of solid KCl was added into above boiled solution with stirring. Then, the obtained solution was cooled down on fridge for 6 h and wait for $\alpha\text{-K}_5[\text{BW}_{12}\text{O}_{40}]$ to precipitate. The solid was washed with ethanol. Crude product was obtained and recrystallized in 3 mL of water at 80 °C.¹

A.2 Cyclic voltammetry

Cyclic voltammetry was conducted in a classic three electrode cell. Working electrode is either a glassy carbon (GC) disk or silver disk (3 mm diameter). GC electrode was mechanically polished by using 6 μm , 3 μm and 1 μm diamond paste, then the electrode was rinsed with distilled water and cleaned in an ultrasound bath. Platinum wire is the counter electrode. The reference electrode is Ag/AgCl/3 M KCl. For this cell, Autolab 12-potentiostat was used. The electrolyte pH ranges from 1 to 5. For pH 1 and 2, the electrolyte is 0.5 M Na_2SO_4 adjusted with H_2SO_4 . For pH 3 the electrolyte is a sodium citrate solution 0.3 M $\text{Na}_3\text{C}_6\text{H}_5\text{O}_7$ adjusted with H_2SO_4 . For pH 4 the electrolyte is 1 M CH_3COOLi adjusted with H_2SO_4 . For pH 5 the electrolyte is 1 M CH_3COOLi adjusted CH_3COOH . All the solutions were degassed with an argon flow. POMs' concentration is 1 mM and sodium nitrite concentration is from 0 mM to 20 mM. The scan rate is 20 mV/s.

When nitrite solution was replaced by NO saturated solutions, the electrolyte was bubbled by pure NO for different amount of time (from 0 to 30 min). Nitric oxide is a very reactive gas, thus eliminating oxygen from the solution is a very important task. Figure a.1 displays our home-made bubbling setup. Before bubbling, the system was ventilated by Ar gas for 20 mins to remove air and to prevent NO oxidization. Another concern is the presence of other gases (such as N_2O and NO_2) in the NO bottle. Thus, two washing bottles, one containing H_2O and another one with 1 M NaOH, were used to remove these gases. After NO gas goes through the desired electrolyte (is 0.5 M Na_2SO_4 , pH 2) the waste gas was

harmlessly treated by three washing bottles containing 0.1 M KMnO_4 and 30 mM NaOH .

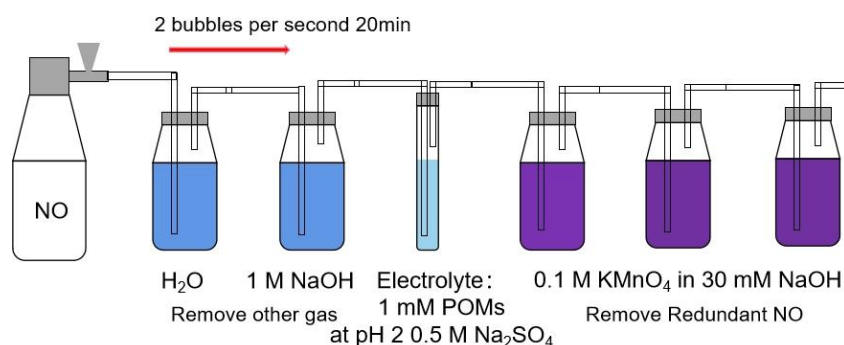


Figure A.1 Experimental design for safely bubbling of NO into a POM containing electrode.

A.3 DEMS experimental setup

DEMS (Differential electrochemical mass spectrometry) experiments were performed with a commercial setup (Hidden Analytical, UK), as shown in Figure a.2. PAR potentiostat (Princeton Applied Research Model 263A) or SP300 (Biologic, France) were used in conjunction with the mass spectrometer. The two devices are controlled separately. DEMS electrochemical cell is type A cell (Hidden Analytical, UK). Glassy carbon or silver electrodes (5 mm diameter) and leakless $\text{Ag}/\text{AgCl}/3\text{ M KCl}$ reference electrode were provided by Hidden Analytical. Platinum counter electrode was placed in the outlet channel of the cell. Therefore, the products obtained from the counter oxidation reactions cannot be detected by the mass spectrometer and they cannot interfere with the reduction reaction at the working electrode. The same electrolytes as in classic cyclic voltammetry experiments were used (vide supra). The flow rate of electrolyte is 0.5 mL/h. A syringe pump (Fusion 200, KR Analytical, UK) was used for this purpose. The volume of the cell is about 0.11 mL. In this manner the electrolyte is renewed every 14 mins. DEMS cyclic voltammetry was run at 0.5 mV/s. Acquisition of mass spectrometry points was achieved every 14s. Nitrite salt containing 98% of isotope ^{15}N and was purchased from Sigma and used only for DEMS experiments. Therefore, the m/z signals for ^{15}NO (31), $^{15}\text{N}_2\text{O}$ (46), and $^{15}\text{N}_2$ (30) are specific to these species and interference from atmospheric nitrogen is avoided. The signal of ^{15}NO was corrected by subtracting the m/z 31 fragment coming from $^{15}\text{N}_2\text{O}$ using reference data.³

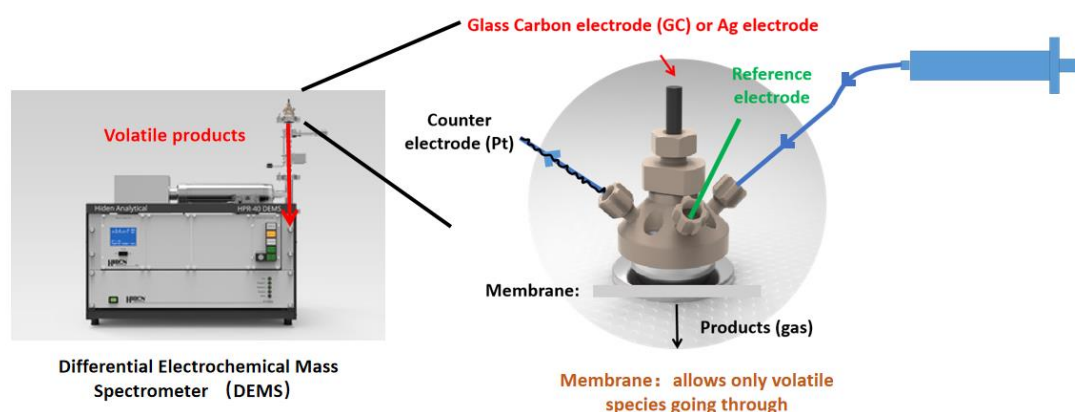


Figure A.2 DEMS experimental setup (left side) and the electrochemical cell (right side).

According to literature data, ammonia is also a possible product of nitrite

electroreduction.² However the pK_a of NH₃ is 9. Thus, in our experimental conditions, i.e. pH 2 or 5, the main species is ammonium ion NH₄⁺. Therefore, detection of this species by DEMS directly in our electrolyte is not possible. To overcome this problem, one possibility is to perform electrolysis and increase the pH above 9 afterwards. Nevertheless, the question is what fragment should be used because m/z of NH₃ is equal to m/z of OH (17), that is an important fragment of H₂O. Moreover, isotope ¹⁵N cannot be used due to an overlap of ¹⁵NH₃ with m/z 18 of H₂O. For these reasons, the only specific fragment is NH (m/z = 15 for ¹⁴N isotope) but its theoretical intensity is only of 7% of the one of main fragment m/z = 17. For this reason, the sensitivity is quite low. In this view, only the detection of NH₃ eventually produced by the nitrite reduction catalyzed by one POM, H₂W₁₂O₄₀ was tested in this thesis.

A.4 Apparatus of other physicochemical characterizations

CHNS-O analyzer (FlashEA 1112 series) was used for elemental analysis. Infrared spectra were acquired with Jasco FT/IR-4600 device. UV-vis absorption spectra have been recorded on an Agilent 8453 spectrophotometer. For illumination of POMs solution in the photocatalytic experiments, a 300 W Xe arc lamp, equipped with a water cell filter to absorb the near-IR radiation, was used. TGA analysis were performed with Perkin analyzer. X-ray diffraction spectra have been acquired with a Bruker D8 Advance equipped with a non-monochromatic copper radiation (K α = 0.154056 nm) and a Sol-X detector in the 20-70° 2 θ range with a scan step of 0.016°. High-purity silicon powder (a = 0.543082 nm) was systematically used as an internal standard.

A.5 Reference

1. Rocchiccioli-Deltcheff, C.; Fournier, M.; Franck, R.; Thouvenot, R., Vibrational investigations of polyoxometalates. 2. Evidence for anion-anion interactions in molybdenum (VI) and tungsten (VI) compounds related to the Keggin structure. *Inorganic Chemistry* **1983**, 22 (2), 207-216.
2. (a) Duca, M.; Van Der Klugt, B.; Hasnat, M.; Machida, M.; Koper, M., Electrocatalytic reduction of nitrite on a polycrystalline rhodium electrode. *Journal of Catalysis* **2010**, 275 (1), 61-69; (b) Duca, M.; Kavvadia, V.; Rodriguez, P.; Lai, S.; Hoogenboom, T.; Koper, M., New insights into the mechanism of nitrite reduction on a platinum electrode. *Journal of Electroanalytical Chemistry* **2010**, 649 (1-2), 59-68.
3. NIST WebBook, (n.d.). <https://webbook.nist.gov/cgi/cbook.cgi?Formula=N2O&NoIon=on&Units=SI>.

LISTE DES PRÉSENTATIONS :

1. POM-BASICS: Summer School in “Polyoxometalates Chemistry for Fundamentals and Applications” (13 – 15 June 2022, La Rochelle, France)

Communication par affiche

Titre: “Differential electrochemical mass spectrometry studies of nitrite reduction catalyzed by Keggin polyoxometalates”

Auteurs: Yulin Zhou, Antoine Bonnefont, Laurent Ruhlmann, Vasilica Badets

2. 73rd Annual Meeting of the International Society of Electrochemistry (12 – 16 September 2022, online) a poster with 5 minutes online oral-presentation.

Communication par affiche

Titre: “Immobilized Keggin W POMs - Ionic Liquid Hybrid Materials for electroreduction of HNO₂”

Auteurs: Yulin Zhou, Corinne Boudon, Antoine Bonnefont, Laurent Ruhlmann, Vasilica Badets

3. 72nd Annual Meeting of the International Society of Electrochemistry (29 August – 3 September 2021, Jeju Island, Korea Hybrid Meeting, online) a poster with 5 minutes online oral-presentation.

Présentation orale

Titre: “Differential Electrochemical Mass Spectrometry (DEMS) studies of nitrite reduction catalyzed by Keggin W polyoxometalates and silver”

Auteurs: Yulin Zhou, Francois Bihl, Antoine Bonnefont, Laurent Ruhlmann, Vasilica Badets

4. 29th Topical meeting of the International society of Electrochemistry (18 – 21 April 2021, Mikulov, Czech Republic, online)

Communication par affiche

Titre: “Differential Electrochemical Mass Spectrometry Study of Nitrite Reduction Catalyzed by Silver Foams”

Auteurs: Jing Sun, Yulin Zhou, Antoine Bonnefont, Laurent Ruhlmann, Vasilica Badets

5. Journées Scientifiques Institut de Chimie Strasbourg, UMR 7177 CNRS- Unistra (14 – 15 March 2021, Strasbourg, France, online)

Présentation orale

Titre: “NO₂⁻ (HNO₂) electrocatalytic reduction by Keggin polyoxometalates”

Auteurs: Yulin Zhou, Antoine Bonnefont, Laurent Ruhlmann, Vasilica Badets

6. 71st Annual Meeting of the International Society of Electrochemistry (31 August – 4 September 2020, Belgrad, Serbia, online)

Communication par affiche

Titre: “Differential electrochemical mass spectrometry studies of nitrite reduction catalyzed by Keggin polyoxometalates”

Auteurs: Yulin Zhou, Antoine Bonnefont, Laurent Ruhlmann, Vasilica Badets

LISTE DES PUBLICATIONS

1. Y. Zhou, A. Bonnefont, C. Boudon, L. Ruhlmann, V. Badets, “Nitrite reduction catalysed by Keggin polyoxometalates: a DEMS study of the volatile products.”, *J. of Catalysis*. **2022**, 405, 212-223. doi.org/10.1016/j.jcat.2021.11.037

Études par spectrométrie de masse électrochimique différentielle (DEMS) de la réduction des nitrites catalysée par les polyoxométallates, une électrode d'argent et des matériaux hybrides à base de liquide ionique

Résumé

La réduction électrochimique du nitrite est catalysée, entre autres, par les polyoxométallates (POMs), une classe d'agrégats d'oxydes métalliques inorganiques solubles en milieu aqueux. Le travail effectué dans cette thèse est axé sur l'étude des produits de la réaction par la technique « Spectrométrie de masse différentielle couplée à l'électrochimie » (DEMS). Les produits gazeux sont l'oxyde nitrique (NO) et l'oxyde nitreux (N_2O) et leur potentiel de formation est étroitement lié aux propriétés électrochimiques des POMs sélectionnés. La modélisation microcinétique a été utilisée pour établir une hiérarchie des efficacités électrocatalytiques d'une série de POMs du type Keggin où la charge du POM a été modulée. Un mécanisme de réaction impliquant HNO comme intermédiaire est fortement soutenu par les résultats obtenus. Dans une deuxième partie, la catalyse en tandem entre les POMs et une électrode de travail en argent a été étudiée. Les études DEMS ont mis en évidence la synergie entre les deux systèmes, responsable pour la diminution de la surtension nécessaire à la formation du N_2O . Le mécanisme de réaction implique un intermédiaire de type HN_2O_2 adsorbé sur l'électrode d'argent. La dernière partie décrit la catalyse hétérogène réalisée par une série de POMs hybrides obtenus en remplaçant les contre-cations par un cation issu du liquide ionique. Les résultats DEMS sont inattendus car la surtension nécessaire à la formation du N_2O est encore diminuée.

Mots clés : Electroréduction des nitrites, polyoxométallates, Spectroscopie de masse électrochimique différentielle (DEMS), Etudes cinétiques, synergie, Nanoparticules d'Ag, Liquide ionique, matériaux hybrides.

Résumé en Anglais

The electrochemical reduction of nitrite is catalyzed by polyoxometalates (POMs), a class of inorganic metal oxide aggregates soluble in aqueous media. This thesis is focused on the study of the reaction products detected by the technique "Differential Electrochemical mass spectrometry" (DEMS). The gaseous products are nitric oxide (NO) and nitrous oxide (N_2O) and their formation potential is closely related to the electrochemical properties of the selected POMs. Microkinetic modeling was used to establish a hierarchy of electrocatalytic efficiencies of a series of Keggin-type POMs where the POM charge was modulated. The reaction mechanism involves HNO as intermediate species. In a second part, tandem catalysis between POMs and a silver working electrode was studied. DEMS studies have highlighted the synergy between the two systems, responsible for the reduction of the overvoltage necessary for the formation of N_2O . The reaction mechanism involves the HN_2O_2 dimer adsorbed on the silver surface. The last part describes the heterogeneous catalysis achieved by a series of hybrid POMs obtained by replacing the counter-cations with a cation from the ionic liquid. The DEMS results are unexpected because the overvoltage necessary for the formation of N_2O is further reduced.

Keywords: Nitrite electroreduction, Polyoxometalates, Differential Electrochemical Mass Spectroscopy (DEMS), Kinetic studies, synergy, Ag nanoparticles, Ionic liquid, hybrid materials.